Reda, Kamel (2019) ***Measurement of Rotational Speed and Vibration Through Electrostatic Sensing and Digital Signal Processing.*** **Doctor of Philosophy (PhD) thesis, University of Kent,.**

MEASUREMENT OF ROTATIONAL SPEED AND VIBRATION THROUGH ELECTROSTATIC SENSING AND DIGITAL SIGNAL PROCESSING

A Thesis Submitted to the University of Kent
For the Degree of PhD
In Electronic Engineering

By

Kamel Reda

September 2019

Abstract

Rotating machines exist in a wide variety of industrial processes such as power generation, vehicle transportation, manufacturing and other industries. Often, they operate continuously for a long time and under a variety of harsh conditions. Thus, they are prone to failure in one or more of their components, causing a decrease in system efficiency and, ultimately, a complete breakdown. It is well known that when a machine component begins to deteriorate, its dynamic behaviour changes. Monitoring relevant parameters allows rapid identification of any changes that are taking place and possible failure modes. Rotational speed and vibration are key parameters in the condition monitoring of rotating machinery. These parameters usually contain abundant fault-related information about the machines.

A literature review is conducted to examine all existing techniques for rotational speed and vibration measurements. Advantages and existing limitations of the reviewed techniques are discussed. Consequently, a technical strategy, incorporating electrostatic sensing and digital signal processing techniques is proposed. Mathematical modelling is established and used to determine the characteristics of electrostatic sensors. The results of the model are used to optimise the electrode and markers design.

A novel electrostatic measurement system, including sensing electrodes, signal conditioning circuit and signal processing unit, has been designed and implemented to provide a solution to a robust online monitoring of rotational speed and vibration of rotating metallic shafts.

Extensive evaluations of the prototype system were conducted on purpose-built laboratory scale test rigs. Experimental results from the rotational speed measurement suggest that the measurement error is within ±0.2% over the speed range from 40 rpm to 3000 rpm with a repeatability less than 0.7%. Results obtained from the vibration displacement measurement of an unbalanced metallic shafts with 0.5mm eccentricity have demonstrated that the measurement system has a relative error no greater than ±0.6% under all test conditions. The developed measurement system can potentially be incorporated into a condition monitoring system, integrated with fault detection and diagnosis algorithms, to assess the working condition of rotating machinery, detect incipient faults and allow repairs to be scheduled.

Acknowledgements

The author wishes to express his gratefulness and thanks to all the people who have, in numerous ways, contributed to this research:

Professor Yong Yan	My supervisor whose experience, insight and advice have been invaluable in giving direction and form to the work, as well as helping to overcome the difficulties encountered along the way.
Dr. Lijuan Wang	for her advice and guidance on electrostatic sensors, and for her collaboration in joint papers.
Dr. Mark Price	for his assistance in scanning the surface of PTFE samples using SEM equipment.
Tony Brazier	whose technical advice in mechanical design was greatly appreciated and the excellent machining skills helped produce the test rigs involved in the research.
University of Kent	for providing research facilities as well as professional and supportive staff.

Acknowledgement is also made to Dr. Sebastien Boisseau at CEA-France (Atomic Energy and Alternative Energies Commission) for his cooperation in providing the electret materials in this research.

Content

List of Tables

List of Figures

Nomenclature

Symbol	Meaning
μ_0	Magnetic permeability
A	open-loop gain of an amplifier
A_s	Surface area
A_0	Equivalent cross-sectional area
B	Bandwidth of the signal
C	Capacitance of a capacitor
C_0	Initial capacitance
C_f	Feedback capacitor
C_{in}	Total input capacitance
D	Diameter of the cylinder
D_o	D-operator
e	Eccentricity of the shaft
E_r	Relative error
E_f	Electric flux
F	Coriolis force
f_c	Cut-off frequency
f_s	Sampling frequency
f_{sc}	Frequency at the spectrum crest
f_v	Electrostatic field of view

G	Gain of the conditioning circuit
G_{inst}	Gain of the instrumentation amplifier
$H(s)$	Transfer function of the filter
H_m	Angular momentum
I_{in}	Current source
K_s	Spring constant
L	Length of the electrode
l_0	Length of the gap
L_m	Length of the marker
M_i	Moment of inertia
M_n	Electret Markers
$n(t)$	Periodic noise
N	Length of data
N_{max}	Number of data points at maximum transit time
N_{mmax}	Maximum number of markers
q	Point charge
$Q(\theta)$	Induced charge
Q_0	Inducing charge
r	Repeatability of the measurement system
R_a	Autocorrelation function
R_c	Cross-correlation function
R_f	Feedback resistor

R_i	Input resistance
R_{in}	Total input resistance
R_{mod}	Modified correlation function
s	Displacement between the shaft and the sensor
S_h	Power spectrum of the impulse response
$S(k)$	Digital signal
$S(t)$	Analogue signal
$S_1(t)$	Noise-free upstream signal
$S_{1n}(t)$	Noisy upstream signal
$S_2(t)$	Noise-free downstream signal
$S_{2n}(t)$	Noisy downstream signal
S_c	Closed surface
S_{max}	Maximum rotational speed
S_{min}	Minimum rotational speed
S_{rpm}	Rotational speed
$S_s(\theta)$	Spatial sensitivity
T	Period of the rotation motion
T_a	Acquisition time
t_p	Duration of charge passing the electrode
$u(t)$	Output signal
V_f	Voltage of Capacitor
V_g	Voltage on the grid

V_{in}	Voltage between the two inputs of the op-amp
V_{out}	Output voltage
V_p	Voltage on the marker points
V_{ref}	Voltage reference
W	Width of the electrode
W_m	Width of the marker
Z_{in}	Input impedance
βv	Viscous damping coefficient
δ	Tolerance of the transit time
Δt	Sampling period
ε_r	Relative permittivity of the dielectric material
ε_0	Permittivity of free space (8.85 pF/m)
ϑ	Angular deflection
θ_m	Central angle corresponding to the width of the marker
v_m	Instantaneous velocity of the masses
σ	Surface charge density of the electrode
σ_m	Surface charge density of the marker
τ	Time delay
φ	Angular spacing between the two sensors
Φ	voltage induced on an electrode
ω	Angular speed
ω_{min}	Minimum angular speed

List of Abbreviations

Abbreviation	**Meaning**
AC	Alternating Current
ADC	Analogue-to-Digital Converter
AFM	Atomic Force Microscopy
CCD	Charge-Coupled Device
DC	Direct Current
FEP	Fluorinated Ethylene Propylene
FET	Field Effect Transistor
LCD	Liquid Crystal Display
LED	Light-Emitting Diode
MEMS	Micro-Electro-Mechanical Systems
Op-amp	Operational Amplifier
PC	Personal Computer
PCB	Printed Circuit Board
RMS	Root Mean Square
RMSE	Root Mean Square Error
RPM	Revolutions Per Minute
S/N	Signal-to-Noise ratio
TIA	Transimpedance Amplifier

Chapter 1

Introduction

1.1 Background and Motivation

Rotating machinery is extensively used in a range of mechanical systems and plays an important role in industrial applications. Rotating machinery components such as shafts, bearings and gearboxes, degrade under severe working environments and during long-term operation in industrial plants. The degradation and deterioration of such critical components cause rotating machinery to fail unexpectedly, reducing machinery reliability [1]-[3]. To keep machinery functioning at optimal levels, fault and failure detection of vital components at an early stage is important, as any mechanical degradation or wear, if is not impeded in time, will often progress to more serious damage affecting the operational performance of the machine. This requires far more costly repairs than simply replacing a part. Moreover, unexpected machinery failure may decrease the safety in industrial plants because machines often fail catastrophically causing injury to personnel. Wind farms are one of the key applications where it is important to monitor the operating performance of turbines in real-time and detect potential faults at an early stage [4]-[6]. According to a new research by Wood Mackenzie Power & Renewables, 57% of maintenance costs are due to unscheduled maintenance.

The aforementioned requirements has motivated researchers and engineers to develop online condition monitoring schemes and fault detection technologies for early forewarning of incipient mechanical faults [7]-[12]. Reliable and robust monitoring systems can lead to planned corrective maintenance actions before complete component failure occurs, thereby minimizing collateral damage to adjacent components. Planned maintenance can cover all preventive maintenance, including routine checks, periodic maintenance and periodic testing.

There are numerous condition monitoring techniques being used to assess the performance of rotating machinery including vibration and rotational speed analysis [13]-[16], temperature analysis [17], [18], current signature analysis [19], oil debris analysis

[20]-[22], and acoustic emission signal based techniques [23], [24]. Among these techniques, vibration and rotational speed based techniques are the most widely used in rotating machine fault detection and diagnosis. A variety of rotational speed measurement techniques based on optical and electromagnetic principles have been developed. Digital image processing techniques have also been used to measure rotational speed. In recent years the estimation of instantaneous rotational speed, based on vibration signal measurement, has been studied by many researches [25], [26]. However, all the existing measurement techniques have their limitations in operation in industrial environments, such as low measurement accuracy, narrow measuring range, and unsuitability for applications in a hostile environment and for higher speed measurement.

Rotating machine vibrations are likely to convey a great deal of information about the internal forces in the system. These internal forces are often related to some fault mechanisms and exhibit distinctive vibration symptoms widely referred as mechanical signatures [1]-[3]. Vibration is measured as an acceleration, velocity, or displacement. Conventional contact type sensors, such as accelerometers and velocity transducers, are unsuitable for rotating shafts due to the impractical requirement of physical contact of the sensors with the moving surface. Hence, non-contact type sensors, such as proximity sensors, are required in this case. Several types of proximity sensors based on inductive (e.g. Eddy-current) and capacitive principles are often used to measure the relative vibration of rotating shafts [27].

In this study, electrostatic sensors are developed as sensing devices, in conjunction with permanently charged markers, for the condition monitoring of metallic rotating machinery. Electrostatic sensors have been used extensively in flow measurement, especially for the velocity measurement of pneumatically conveyed particles [28]-[31]. They have advantages of non-contact measurement, low cost, simple structure and suitability for hostile environments. The resulting signals from the electrostatic sensors are electronically integrated to obtain the overall operating conditions of the machinery, including the measurements of rotational speed and vibration displacement of rotating shafts. An indication of the current state of the machinery can be provided through the analysis of the sensors outputs and diagnosis algorithm.

1.2 Technical Challenges in the Use of Electrostatic Sensors

In view of the sensing principle of electrostatic sensors and the operating conditions of rotating machinery, the development of electrostatic sensors based measurement system for rotational speed and vibration measurement faces a number of technical challenges.

The main technical challenges that have been identified are as follows:

- **Charge stability:** The sensing principle of electrostatic sensors is based on the phenomenon of electrostatic induction of charged markers, fixed around the shaft, on the electrode of the sensor. Although the charge magnitude on the markers is quasi-permanent (electret material), they are, however, limited and susceptible to environmental conditions such as relative humidity and temperature. Moreover, the level of charge on the markers depends also on the rotational speed due to the triboelectric effect between the dielectric charged markers and the air. Consequently, signal amplitude parameters cannot be used to achieve an absolute measurement due to the uncertain amount of charge on the markers.

- **Sensitivity:** This is one of the most important characteristics which affects the dynamic performance of the sensor. The sensitivity to the inducing charge increases with respect to the magnitude of the charge source and dimensions of the electrode. It decreases as the distance of separation between the charge source and electrode increases. In view of the limited amount of the charge source, the geometric parameters of the electrode and the markers are crucial and affects significantly the performance of the measurement system.

- **Noise:** The magnitude of charge on the markers is relatively small resulting in a weak induced signal on the electrode. Thus, various noises can be superimposed on it, particularly in harsh industry environments, resulting in a contaminated signal. The most common sources of noise are electromagnetic interference and vibration of the mechanical system.

- **Low speed measurement:** The signal-to-noise ratio is generally low at low speeds due to the limited amount of the charge on the markers, making the sensor system not capable of producing valid measurements.

1.3 Aim and Objectives of the Research Programme

A major goal of the instrumentation and control group at the University of Kent is the development of online sensors to monitor the performance of a wide range of rotating machinery as implementation of condition monitoring systems is becoming necessary in order to prevent failure, increase reliability, and decrease maintenance costs.

Over recent years, the instrumentation and control research group has been undertaking substantial research on developing electrostatic sensors for the rotational speed measurement of dielectric rotors. Subsequently, there have been limited attempts to employ electrostatic sensors for the vibration detection of dielectric rotating shafts due to the complexity of the charging/discharging mechanism of the dielectric materials during rotational motion. The developed sensors, operating on electrostatic sensing and processing techniques, have been evaluated on a laboratory-scale test rig. Preliminary results have demonstrated the effectiveness of the technique developed on a variety of dielectric rotors.

It is, however, recognised that metallic shafts and rotors account for a major proportion of mechanical components in rotating machinery. To date, there has been no reported research in the literature on rotational speed and vibration measurement for metallic rotating shafts using electrostatic sensors.

Therefore, the aim of this research is to develop the existing electrostatic sensors to be capable of providing simultaneous online measurements of rotational speed and vibration displacement of metallic rotary shafts. The developed measurement system is expected to be employed as a measuring device in the condition monitoring system of rotating machinery. This proposed research aligns well with the goal of the instrumentation group at the University of Kent.

To achieve this goal, the primary objectives of this research are:

- To reveal the physical principles governing electrostatic sensors in order to develop a detailed characterisation of their operation.

- The design and implementation of a low cost, accurate and robust measurement system for the rotational speed and vibration measurement of metallic shafts, suitable for installation in a wide range of rotating machinery.

- To evaluate the performance of the prototype system and the effectiveness of the measurement algorithms through extensive experiments on purpose-built test rigs.

The research programme comprises several principal areas of investigation:

- A review of the main technical approaches for rotational speed and vibration measurement proposed to date is undertaken for comparison with electrostatic methods. Recent work on electrostatic sensors is summarised in order to highlight progress that has been made in recent years, as well as to identify areas which are still underdeveloped.

- A theoretical analysis of the underlying principles involved regarding electrostatic sensors is undertaken, and a mathematical modelling method is used to investigate the sensing mechanism and the various parameters that affect the measurement.

- Practical considerations involved in the design and implementation of an electrostatic measurement system, including the electronics and signal processing algorithms. The results of practical tests are then used to characterise the sensor performance.

1.4 Thesis Outline

The thesis is organised in six chapters and a brief summary of each chapter is depicted as follows:

- **Chapter 2** provides a comprehensive literature survey concerning the rotational speed and vibration measurement techniques that were developed during recent decades. Measurement methods and techniques based on a variety of physical principles are introduced along with their relative strengths/weaknesses. Separate sections are devoted to sensors using electrostatic sensing technique.

- **Chapter 3** introduces the measurement principles of the rotational speed and vibration of metallic rotors using electrostatic sensors. The sensing mechanism, modelling and characteristics of electrostatic sensors are also presented and discussed. The results of the model are used to guide markers design parameters including dimensions and number.

- **Chapter 4** is a detailed discussion of the measurement system design and implementation including markers, electronics and algorithms. Different possible analogue circuits for signal acquisition are compared, and the digital signal processing unit, is presented, along with the signal processing algorithms.

- **Chapter 5** presents the laboratory-scale tests conducted in the Instrumentation Laboratory at the University of Kent. Extensive tests for rotational speed measurement are undertaken under normal and noisy conditions at different speeds. Comparisons between the single and dual electrostatic sensors were also achieved. Then, experimental tests are conducted on a purpose-built test rig with eccentric shaft to validate the performance of the electrostatic sensor for vibration displacement. The experimental results obtained from all tests are discussed.

- **Chapter 6** draws together and concludes the research findings and their impacts in the field of condition monitoring of rotating machinery. Recommendations for future research and further applications of the developed techniques are proposed.

Chapter 2

Review of Techniques for Rotational Speed and Vibration Measurement

2.1 Introduction

Rotational speed and vibration are key parameters for condition monitoring in a range of industries where rotating machinery is an integral part of the production and manufacturing processes. The performance of such machinery may decrease gradually under harsh working conditions and long operations, so the continuous status monitoring of this equipment is very important for maintaining its good operation and for detecting potential faults at an early stage.

This chapter presents a comprehensive literature review of all existing techniques that can potentially be used for rotational speed and vibration measurement of rotary shafts. The state-of-the-art in the field of study is defined by following the analysis and reviews of all relevant existing techniques and references in the field. In the following sections, an overview of the principles of various available sensing techniques will be illustrated. The benefits and limitations of each technique will also be addressed.

The literature survey is not only useful to acquire necessary background knowledge that might contribute to this work, but it also informs the proposed research strategy and assures its novelty, taking into account the technical challenges and requirements defined in chapter 1.

2.2 Rotational Speed Measurement

Rotational speed monitoring is a critical part of the condition monitoring system for rotating machinery. Moreover, accurate estimation of the rotational speed usually has a high priority in control or regulation processes, as incorrectly estimated values may cause serious disturbances in the operation of machines. Typical examples include fault detection of engines and generators [32], shaft crack detection of nuclear power plant rotating equipment [33], condition monitoring of electric motors and turbines [34] and ignition timing of automotive engines [35].

Over the years, a number of methods have been developed for rotational speed and angular velocity measurement. Traditional mechanical tachometers like centrifugal tachometers have been used primitively to gauge the speed of rotational machinery. Subsequently, a variety of non-contact tachometers based on optical, inductive and magnetic sensing techniques have been developed. Usually, tachometers can be classified into two categories, Analog and Digital. Analog tachometers have been used over the years and are widely used in feedback loops for closely regulating the speeds of drive systems. Digital tachometers are very suitable for precision measurement and monitoring systems [36]-[41].

Shaft encoders, gyroscopes and digital image techniques have also been employed to measure the rotational speed [26]. Yeh et al [42] presented a high-resolution optical shaft encoder to monitor the rotation behaviour of a motor. Lygouras et al [43] presented a solution for processing the pulses from an optical encoder attached to a motor shaft.. Digital image processing techniques have also been used to measure rotation motion. Zhang et al achieved rotational measurement through digital image correlation using a ring template and quadrilateral element [44]. Recently, Wang et al used image similarity evaluation and spectral analysis to compute the rotational speed measurement [45]. Meanwhile, the estimation of instantaneous rotational speed through vibration signal analysis has been studied by many researchers. Bonnardot et al. [46], Combet and Zimroz [47], Urbanek et al. [48], and Lin and Ding [49] applied different algorithms to extract the instantaneous speed fluctuation from vibration signals.

Over recent years, researchers conducted both theoretical and experimental studies on electrostatic sensors for rotational speed measurement. Wang et al [50]-[52], in particular, have successfully employed electrostatic sensors to measure rotational speed based on correlation algorithms.

The following sections presents an overview of the key currents sensors used for rotational speed measurement.

2.2.1 Analogue Tachometers

Analog tachometers have been the first electrical devices used to the measure speed of rotational machineries. The first analogue tachometers were developed by Robinson [36]. Although they are less accurate than other types of tachometers, they are nevertheless still used successfully in many applications.

Analog tachometers are available in different forms:

2.2.1.1 DC Tachometer

The DC tachometer has an output that is approximately proportional to its speed of rotation. Its basic structure is identical to that found in a standard DC generator used for producing power, and is shown in Figure 2.1.

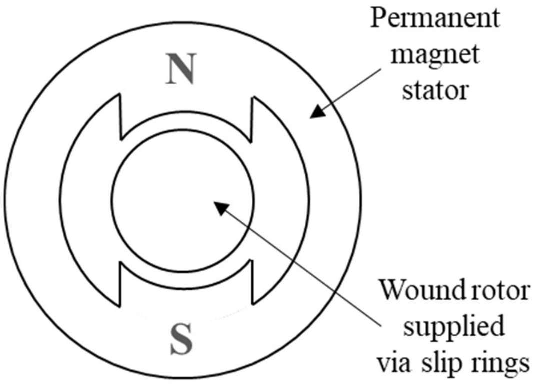

Figure 2.1 DC tachometer [36].

Both permanent-magnet types and separately excited field types are used. However, certain aspects of the design are optimized to improve its accuracy as a speed-measuring instrument. One significant design modification is to reduce the weight of the rotor by constructing the windings on a hollow fiberglass shell. The effect of this is to minimize any loading effect of the instrument on the system being measured. The DC output voltage from the instrument is of a relatively high magnitude, giving a high measurement sensitivity that is typically 5 V per 1000 rpm. The direction of rotation is determined by the polarity of the output voltage. A common range of measurement is 0-6000 rpm. Maximum nonlinearity is usually about 1% of the full-scale reading. One problem with these devices that can cause difficulties under some circumstances is the presence of an AC ripple in the output signal. The magnitude of this can be up to 2% of the output DC level.

2.2.1.2 AC tachometer

The AC tachometer has an output approximately proportional to rotational speed like the DC tachometers. Its mechanical structure takes the form of a two-phase induction motor, with two stator windings and (usually) a drag-cup rotor, as shown in Figure 2.2.

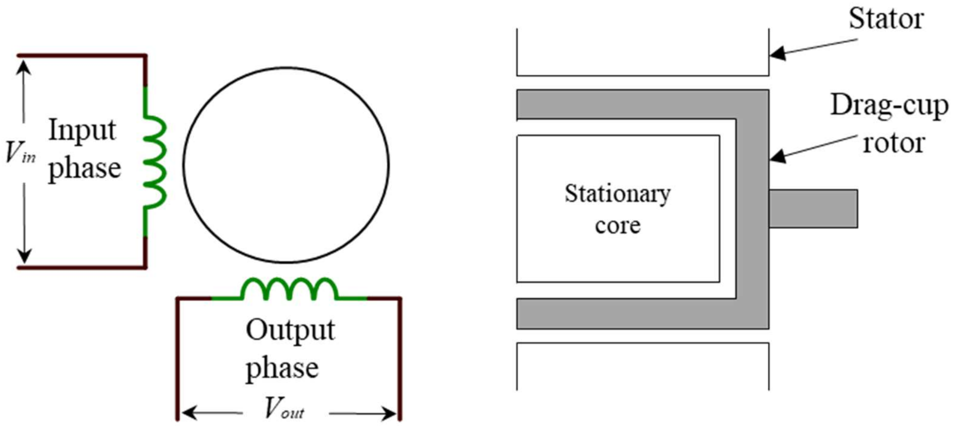

(a) (b)

Figure 2.2 AC tachometer. (a) Layout of windings; (b) sketch of stator and rotor [36].

One of the stator windings is excited with an AC voltage and the measurement signal is taken from the output voltage induced in the second winding. The magnitude of this output voltage is zero when the rotor is stationary, and otherwise is proportional to the angular velocity of the rotor. The direction of rotation is determined by the phase of the output voltage, which switches by 180° as the direction reverses. Therefore, both the phase and magnitude of the output voltage have to be measured. A typical range of measurement is 0 to 4000 rpm, with a relative error of 0.05% of full-scale reading.

Cheaper versions with a squirrel-cage rotor also exist, but measurement error in these devices is typically 0.25%

2.2.2 Digital Tachometers

Digital tachometers are usually non-contact instruments that sense the passage of marker(s) on the surface of a rotating disk or shaft. Measurement resolution is governed by the number of markers around the circumference. Various types of sensor are used, such as optical, inductive and magnetic. As each mark is sensed, a pulse is generated and input to an electronic pulse counter. Usually, velocity is calculated in terms of the pulse count in unit time, which of course only yields information about the mean velocity. If the velocity is changing, instantaneous velocity can be calculated at each instant of time that an output pulse occurs, using the scheme shown in Figure 2.3. In this circuit, the pulses from the transducer, gate the train of pulses from a clock into a counter. Control logic resets the counter and updates the digital output value after receipt of each pulse from the transducer. The measurement resolution of this system is highest when the speed of rotation is low [37]-[41].

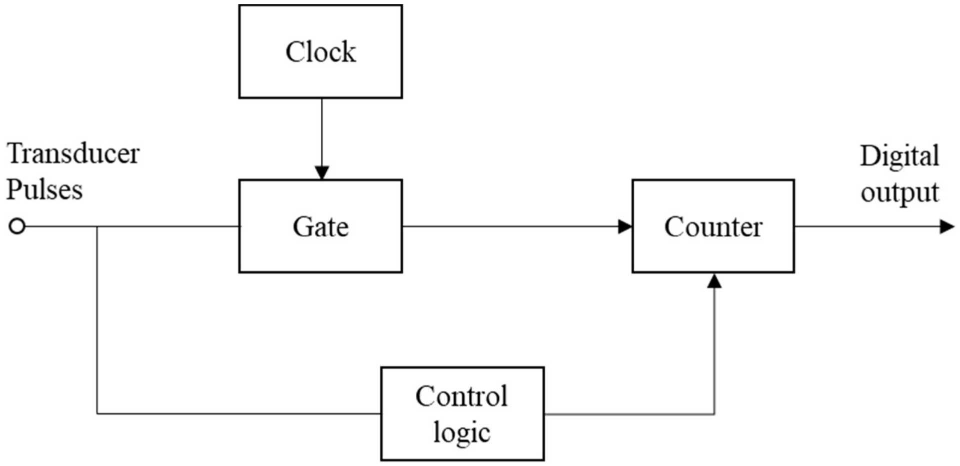

Figure 2.3 Scheme to measure angular speed [37].

2.2.2.1 Optical sensing

Digital tachometers with optical sensors are often known as optical tachometers. Optical encoders operate on a similar physical principle to optical tachometers. Optical pulses can be generated by one of the two alternative photoelectric techniques illustrated in Figure 2.4. In the scheme shown in Figure 2.4(a), the pulses are produced as the windows in a slotted disk pass in sequence between a light source and a detector. The alternative scheme, shown in Figure 2.4(b), has both light source and detector mounted on the same side of a reflective disk that has black sectors painted onto it at regular angular intervals. Light sources are normally either lasers or LEDs, with photodiodes and phototransistors used as detectors. Optical tachometers yield better accuracy than other forms of digital tachometer. However, they are less reliable than other forms because dust and dirt can block light paths.

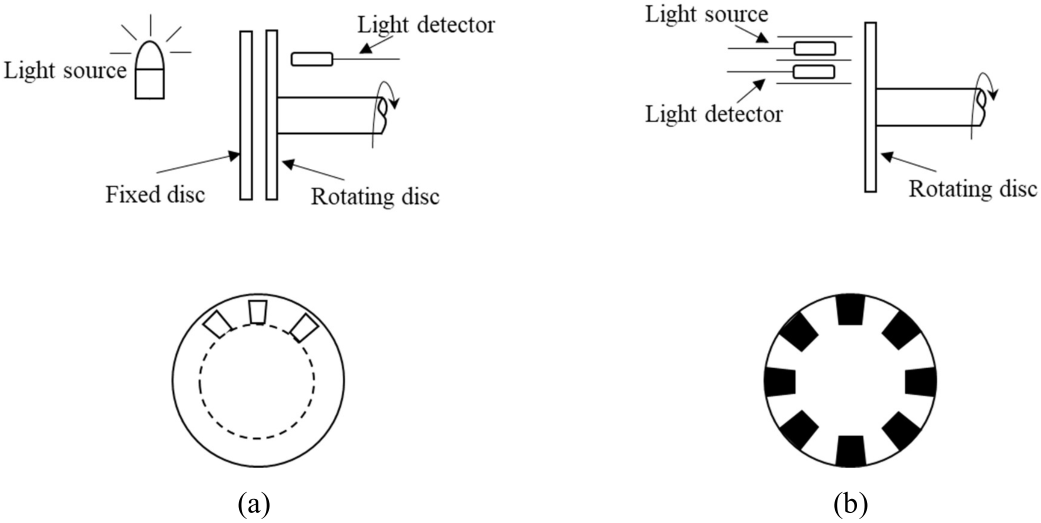

(a) (b)

Figure 2.4 Photoelectric pulse generation techniques: (a) Detail of windows in rotating disk; (b) Detail of disk with alternate black and white sectors [42].

Similarly, non-contact laser tachometers can measure rotational speed from a single pulse per revolution. This pulse is supplied by marking the rotating shaft with a visible reflective tape target. The laser tachometer is equipped with a built-in laser light source providing a laser beam which is aimed at the reflective tape located on the rotating shaft. The pulse from the reflective tape is received back through a single lens reflex optical system and detected by a photocell inside the instrument. The tachometer then computes the rotational speed. Figure 2.5 illustrates the measurement principle of laser tachometers.

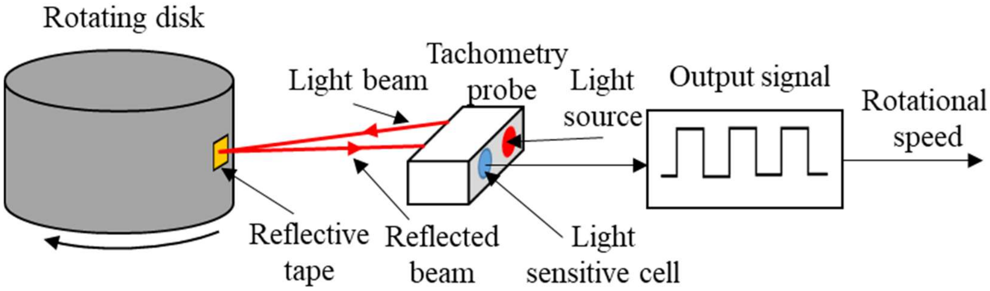

Figure 2.5 Measurement principle of laser tachometer [40].

2.2.2.2 Inductive sensing

Variable reluctance velocity transducers, also known as induction tachometers, are a form of digital tachometer that use inductive sensing. They are widely used in the automotive industry within anti-skid devices, anti-lock braking systems and traction control.

As shown in Figure 2.6, the device has a rotating disk that is constructed from a bonded-fibre material into which soft iron poles are inserted at regular intervals around its periphery. The sensor consists of a permanent magnet with a shaped pole piece, which carries a wound coil. The distance between the pickup and the outer perimeter of the disk is typically 0.5 mm. As the disk rotates, the soft iron inserts on the disk move in turn past the pickup unit. As each iron insert moves toward the pole piece, the reluctance of the magnetic circuit increases and hence the flux in the pole piece also increases. Similarly, the flux in the pole piece decreases as each iron insert moves away from the sensor. The changing magnetic flux inside the pickup coil causes a voltage to be induced in the coil, whose magnitude is proportional to the rate of change of flux. This voltage is positive while the flux is increasing and negative while it is decreasing. Thus, the output is a sequence of positive and negative pulses, whose frequency is proportional to the rotational velocity of the disk. The maximum angular velocity that the instrument can measure is limited to about 10,000 rpm because of the finite width of the induced pulses. As the velocity increases, the distance between the pulses is reduced, and at a certain velocity, the pulses start to overlap. At this point, the pulse counter ceases to be able to distinguish the separate pulses. The optical tachometer has significant advantages in this respect, since the pulse width is much narrower, allowing measurement of higher velocities.

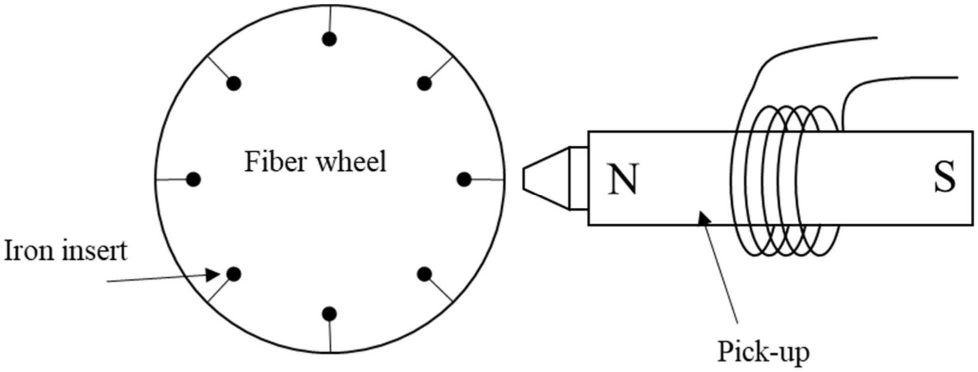

Figure 2.6 Variable reluctance transducer [53].

A simpler and cheaper form of variable reluctance transducer also exists that uses a ferromagnetic gear wheel in place of a fibre disk. The motion of the tip of each gear tooth toward and away from the pickup unit causes a similar variation in the flux pattern to that produced by the iron inserts in the fibre disk. However, the pulses produced by these means are less sharp, and consequently, the maximum angular velocity measurable is lower.

2.2.2.3 Magnetic (Hall-effect) sensing

The rotating element in Hall-effect or magnetostrictive tachometers has a very simple design in the form of a toothed metal gear wheel [53]. The sensor is a solid-state, Hall-effect device that is placed between the gear wheel and a permanent magnet. When an inter-tooth gap on the gear wheel is adjacent to the sensor, the full magnetic field from the magnet passes through it. Later, as a tooth approaches the sensor, the tooth diverts some of the magnetic field, and so the field through the sensor is reduced. This causes the sensor to produce an output voltage that is proportional to the rotational speed of the gear wheel.

2.2.3 Gyroscopes

2.2.3.1 Rate Gyroscope

The rate gyro, illustrated in Figure 2.7, measures the absolute angular velocity of a body, and is widely used for generating stabilizing signals within vehicle navigation systems.

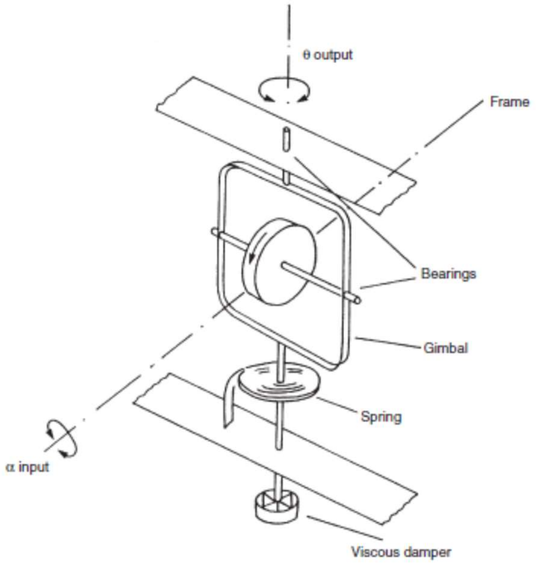

Figure 2.7 Rate gyroscope [54].

The typical measurement resolution given by the instrument is 0.01°/s and rotation rates of up to 50°/s can be measured. The angular velocity, ω, of the body is related to the angular deflection of the gyroscope, ϑ, by

$$\frac{\vartheta}{\omega}(D) = \frac{H_m}{M_i D^2 + \beta_v D_o + K_s} \tag{2.1}$$

where H_m is the angular momentum of the spinning wheel, M_i is the moment of inertia of the system, β_v is the viscous damping coefficient, K_s is the spring constant, and D_o is the D-operator.

2.2.3.2 Fibre-Optic Gyroscope

This type of gyroscope has been recently developed using fibre-optic technology [54]. Incident light from a source is separated by a beam splitter into a pair of beams *a* and *b*, as shown in Figure 2.8. These travel in opposite directions around a fibre-optic coil and emerge from the coil as the beams marked *a'* and *b'*. The beams a' and b' are directed by the beam splitter into an interferometer. Any motion of the coil causes a phase shift between a' and b' which is detected by the interferometer.

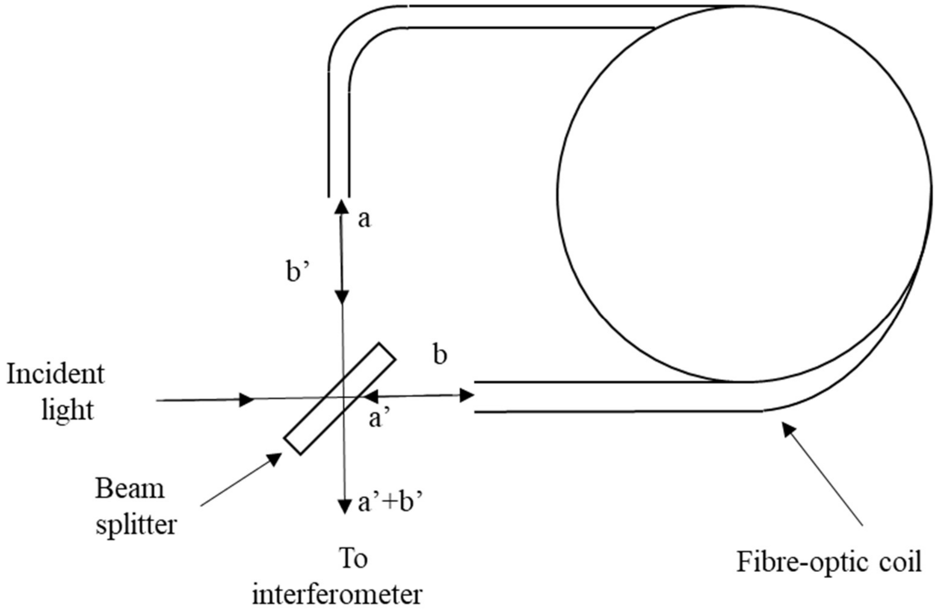

Figure 2.8 Fibre-optic gyroscope [54].

2.2.3.3 MEMS Gyroscope

MEMS gyroscopes are now widely available for measuring rotational velocity [55]. The typical structure of a MEMS gyroscope is shown in Figure 2.9.

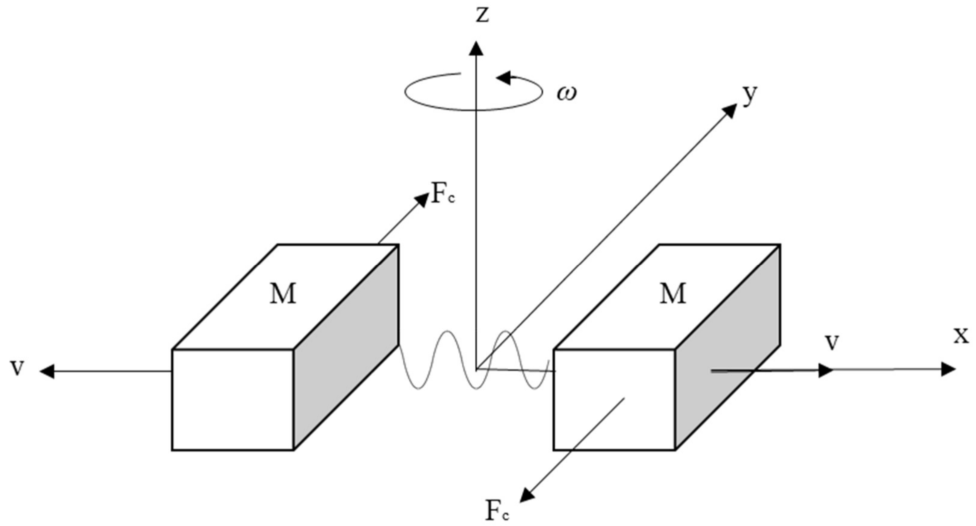

Figure 2.9 Typical structure of a MEMS gyroscope [55].

MEMS gyroscopes operate on a tuning-fork principle, and consists of two equal masses *M* that oscillate and are always moving in opposite directions to each other. When the gyroscope is subjected to an angular velocity *ω*, a Coriolis force *F* is generated on each mass given by

$$F = -2M\omega v \tag{2.2}$$

where v_m is the instantaneous velocity of the masses.

The Coriolis forces on the masses act in opposite directions and cause a lateral displacement of the masses relative to each other. This displacement causes a change in capacitance between the two masses that is proportional to the magnitude of the angular velocity *ω* applied. This change in capacitance is either converted to a digital number in digital MEMS gyroscopes or into an analogue voltage in the case of analogue MEMS gyroscopes.

In common with other types of MEMS devices, MEMS gyroscopes are relatively cheap to produce and provide high performance with low power consumption. They are entirely insensitive to linear motion and only respond to angular motion. Any motion of the device in the x, y, or z direction (as shown in Figure 2.9) causes both masses to move by the same amount in the direction of the motion. Hence, there is no relative displacement between the two masses and so there is no change in capacitance. MEMS gyroscopes are now used in a wide range of applications for measuring rotational velocities.

2.2.4 Electrostatic Sensors

In recent years, substantial effort has been spent on the development of electrostatic sensors in conjunction with correlation signal processing techniques for rotational speed measurement. The electrostatic sensing-based rotational speed measurement technique has advantages of non-contact measurement, low cost and suitability for hostile environments. Since the electrostatic sensors have no direct contact with the shaft, there is no wear problem that adversely affects some of the existing techniques such as mechanical tachometers. Additionally, the electrostatic sensors have no requirement for the fitting of an opaque disc on the shaft, which is essential for photoelectric tachometers and encoders. The presence of dust around the shaft can affect the operation of optical tachometers, but have little impact on the electrostatic sensors. Thus, the structural simplicity, low cost and robustness of the electrostatic sensors make the technique suitable for a wider range of industrial applications.

Wang et al. [51], [52], [56] have conducted extensive research and experimental investigation into rotational speed measurement using electrostatic sensors and correlation signal processing techniques. A variety of electrostatic sensors have been investigated with different electrodes arrangements. A single, double and array of electrodes, which were placed adjacent to the rotating surface, were employed to sense the movement of a dielectric surface through electrostatic induction. The electrodes is interfaced with a signal conditioning circuit which consists of a preamplifier that can amplify the detected charge on the rotor surface to a level that can be digitised in an analogue-to-digital converter. The rotational speed could then be determined through the autocorrelation and cross-correlation of the output signals from the electrodes. Figure 2.10 shows the different sensing arrangements and principles of the rotational measurement system.

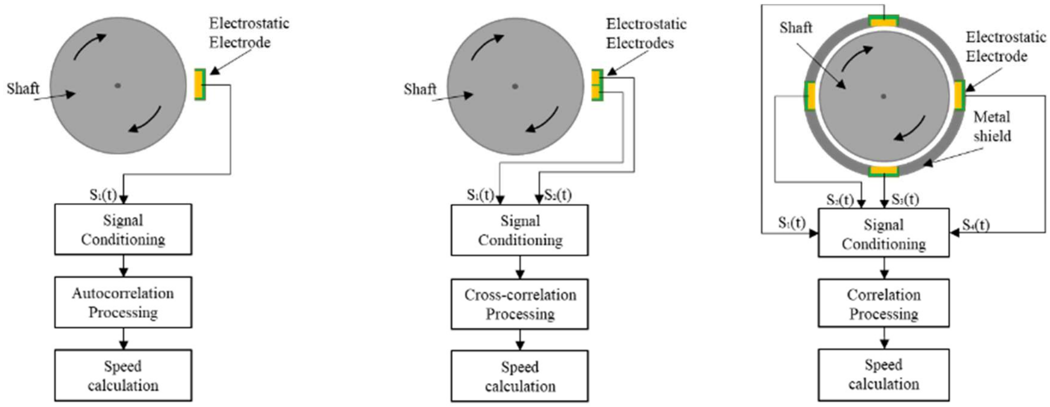

(a) (b) (c)

Figure 2.10 Electrostatic measurement system. (a) Single electrostatic senor. (b) Dual electrostatic sensors. (c) Array of electrostatic sensors.

Experimental results from the measurement systems in Figure 2.10 have shown a maximum error of no greater than ±1.5% over the speed range from 500 rpm to 3000 rpm. Later, the method was developed further by incorporating a data fusion algorithm, capable of producing more accurate measurements with a maximum error within ±0.5% over the range of 200 rpm to 3000 rpm [50].

Much more recently, Li et al [57] proposed a digital approach for using electrostatic sensors for rotational speed measurement to improve the performance of the measurement system. The proposed method is inspired by the photoelectric method and based on the generation of a square wave from an electrostatic sensor in order to obtain the rotational speed via digital methods, thus eliminating the influence of the sampling rate and signal noise, and also simplifying the system complexity.

Although, the aforementioned electrostatic sensing techniques have been well developed and have successfully achieved a rotational speed measurement for dielectric shafts, offering an appealing solution to the condition monitoring, with the virtue of non-contact, low cost, simple structure, and easy installation, they still have several limitations and drawbacks. Output signals are obtained from electrostatic sensors through electrostatic induction of the charge generated on the moving surface of the shaft. However, the level of electrostatic charge due to the air friction with the shaft surface depends on the rotational speed of the shaft. On the other hand, with the generation of electrostatic charge, there is also a phenomenon of electrostatic discharge due to environmental conditions and the material properties of the shaft, which reduces the amount of electrostatic charge generated. When the shaft is rotating continuously, a dynamic balance is reached between the natural discharge and recharge. The induced charge, and hence the output signal from the sensor, depends on the balance of charge resulting from the discharge and recharge phenomena. When the shaft speed is lower than 200 rpm, limited electrostatic charge is generated on the shaft surface and may discharge quickly over one rotation. In this case, it is difficult to obtain valid rotational speed measurements using electrostatic sensors. As a result, the existing sensing system has some major drawbacks and limitations. The existing electrostatic sensors depends primarily on the rotational speed, material and surface condition of the shaft to generate electrostatic charge on its surface. Moreover, the speed measurement is limited to dielectric shafts and is susceptible to environmental conditions, among which the humidity is considered to have a strong impact. At low rotational speed (<200 rpm), the signal-to-noise ratio may deteriorate as the induced charge on the electrode decreases with the discharge effect, making the system invalid for low rotational speed measurement.

2.3 Vibration Measurement

Vibration measurement of rotary shafts plays a significant role in the condition monitoring of rotating machinery [10]. Vibration analysis is used to determine the operating and mechanical condition of equipment. A major advantage is that vibration analysis can identify developing problems before they become too serious and cause unscheduled downtime.

A variety of mechanical defects, such as shaft imbalance, coupling misalignment and bearing deterioration, may give rise to excessive vibrations that cause machine failure. Imbalance is the most common cause of vibrations of rotating machines. In practice, shafts can never be perfectly balanced because of manufacturing errors such as porosity in casting, non-uniform density of material, manufacturing tolerances and gain or loss of material during operation. An unbalanced shaft makes it more susceptible to high amplitude vibration that causes noise and incorrect functionality and thus reduces the life span of the machine [1], [2], [58].

There are three main parameters that are measured to evaluate the vibration characteristics of any dynamic system; displacement, velocity and acceleration. However, each vibration parameter can be converted to the others by derivation or integration process. The displacement are deduced by integrating the velocity and acceleration [59].
There are many types of proximity sensors and they use different methods for sensing. Inductive and capacitive sensors are often used to measure the relative vibration of rotating shafts. Meanwhile, a number of new methods have been proposed for shaft vibration detection. Vyroubal [60] identified the vibration signature using optical sensors through spectral analysis of phase-modulated light pulses. Okabe et al [61] described an ultrasonic sensor based method for shaft vibration detection by measuring the propagation time of the ultrasonic wave from the sensor to the shaft surface. Much more recently, Wang et al [62], [63] employed electrostatic sensors for the vibration detection of rotating machinery.

The basic operational principles of techniques that can be used for shaft vibration measurement will be presented in the following sections.

2.3.1 Inductive Sensors

An inductive sensor is an electronic proximity sensor, which detects metallic objects without physical contact with the target. Inductive sensors are based on electromagnetic induction, use a self-inductance coil or mutual inductance coil to achieve the detection of the electrical signal which is converted from the vibration. The principle structure of a basic inductive sensor is shown in Figure 2.11.

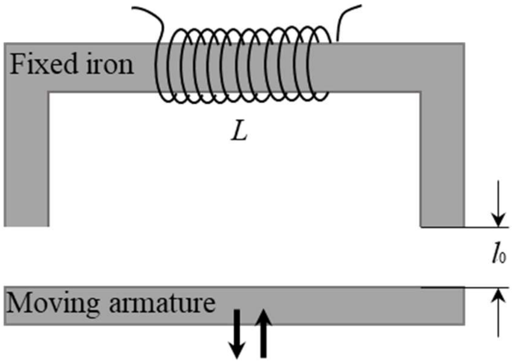

Figure 2.11 Principle structure of inductive sensor [64].

N circles of wire are circled on the fixed Iron. The inductance can be given by

$$L = \frac{N^2 \mu_0 A_0}{2l_0} \tag{2.3}$$

where μ_0, A_0 and l_0 are the magnetic permeability, equivalent cross-sectional area and length of the gap, respectively.

When the vibration of an object causes a change in the area, thickness or length between the fixed Iron and the armature, the inductance changes. By measuring the change of inductance, the vibration measurement can then be achieved.

The prominent features of inductive sensors include simple structure, measurement reliability, high accuracy and output power. The disadvantages are the sensitivity, linearity and measuring range, which makes it unsuitable for the measurement of high-frequency dynamic signals [53], [64].

Eddy-current sensors are a sophisticated version of inductive sensors which are capable of high-resolution measurements of the displacement of any conductive target [65], [66]. Figure 2.12 illustrates the working principle of eddy-current sensors.

The driver creates an alternating current in the sensing coil in the end of the probe. This creates an alternating magnetic field which induces small currents in the target material; these currents are called eddy-currents. The eddy-currents create an opposing magnetic field which resists the field being generated by the probe coil. The interaction of the magnetic fields is dependent on the distance between the probe and the target. As the distance changes, the electronics sense the change in the field interaction and produces a voltage output which is proportional to the change in distance between the probe and target.

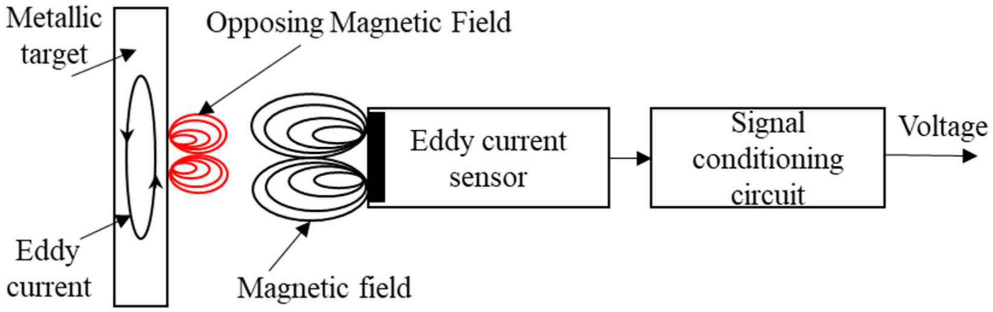

Figure 2.12 Eddy-current sensor working principle [65].

2.3.2 Capacitive Sensors

Capacitive sensors operate by measuring changes in electrical capacitance. Figure 2.13 is the structure diagram of variable-clearance capacitive sensor.

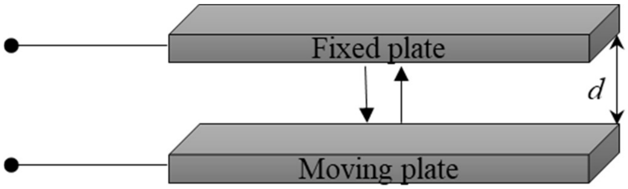

Figure 2.13 Variable-clearance capacitive sensor [66].

When the size of the two parallel plates is much larger than the distance d between them, the capacitance C can be deduced from Gauss's Law. The capacitance C is directly proportional to the surface area A of the objects and the dielectric constant of the material ε_r between them, and inversely proportional to the distance d between them

$$C = \frac{\varepsilon_0 \varepsilon_r A}{d} \tag{2.4}$$

In typical capacitive sensing applications, the probe or sensor is the fixed plate and the moving object (the target) is the other plate. The sizes of the sensor and the target are assumed to be constant, as is the material between them (air). Therefore, any change in capacitance is a result of a change in the distance between the probe and the target.

$$\Delta C = \frac{\varepsilon_0 \varepsilon_r A}{d - \Delta d} - \frac{\varepsilon_0 \varepsilon_r A}{d} = C_0 \frac{\Delta d}{d - \Delta d} \tag{2.5}$$

where, C_0 is the initial capacitance value when the distance is d.

As can be seen from the equation (2.5), the change of capacitance relates to the displacement of the moving plate, and when $\Delta d << d$, we can approximate that ΔC is in a linear relationship with Δd. Therefore, by measuring the changes of capacitance, the vibration displacement can then be measured.

Advantages of the capacitive sensor include high resolution, high precision, short dynamic response time, suitable for online, dynamic measurements and non-contact measurements. The disadvantages include small measuring-range, and its measurement is vulnerable to electrical medium and electromagnetic fields [53]. Now, with the in-depth research of capacitive sensor measurement principle and structure, and the development of new circuit, new materials, new processes, some of its shortages are gradually being overcome. The accuracy and stability of capacitive sensors are increasing and used more widely in non-contact measurement field [67], [68].

2.3.3 Fibre-optic Sensors

According to the principle of fibre-optic sensors, they can be divided into two categories: one category is transmitting light type (or non-functional) sensors and the other is transmitting -sensing type (or functional) sensors [69], [70]. In the transmitting-light type fibre-optic sensors, optical fibre only acts as a light transmission medium, the sensing of the measured signal is achieved by a separate sensitive components. In the transmitting-sensing type fibre-optic sensors, optical fibre is used for sensing the measured signal and transmitting optical signal. The sensor also combines the signal's "sensing" and "transmitting" into one.

In practice, transmitting-sensing type sensors structure is relatively simple and may need fewer coupling devices, but the requirement on optical fibre is higher. It is often required to adopt special optical fibre which is sensitive to the measured signal and that has a good transmission characteristics. Therefore, the non-functional transmitting light type sensors are commonly used in the field of vibration detection, where the basic principle is the use of a separate sensitive component to detect changes of the measured physical quantity, and the light parameter is modulated by sensitive components. Figure 2.14 is a phase-modulated optical fibre vibration sensor schematic diagram.

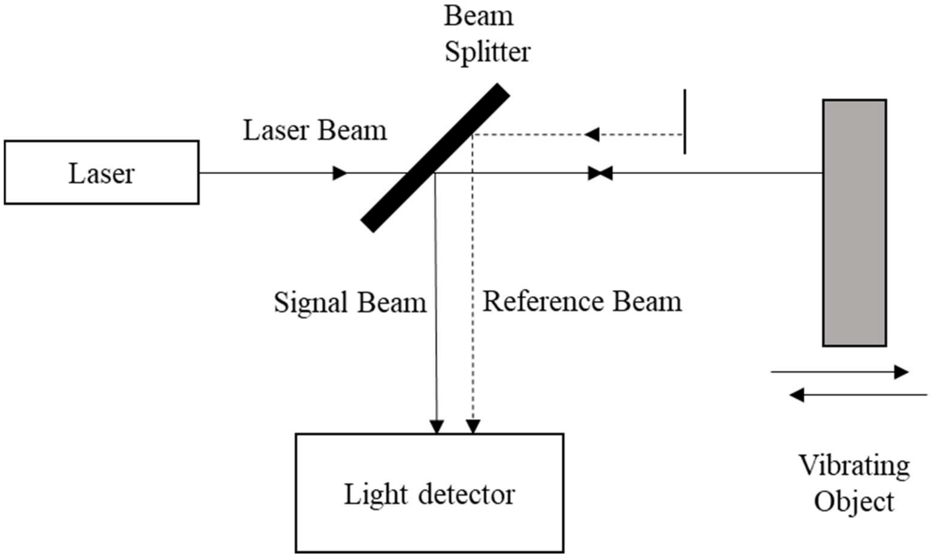

Figure 2.14 Schematic diagram of a phase-modulated fibre-optic vibration sensor [69].

The vibrating object changes the relative phase between the signal beam and reference beam, which results in a phase modulation, and by demodulation, the corresponding vibration amplitude can then be obtained.

The prominent features of the fibre-optic sensor are their ability to be lightweight, very small in size, high sensitivity, fast response, immunity to electromagnetic interference, soft bend and are easy to connect with the computer. The disadvantages include the narrow range of measurement frequency, high cost and unfamiliarity to the end user.

2.3.4 Photoelectric Sensors

Photoelectric sensors detects change in vibration parameters through the change of optical properties. The detector of the photoelectric sensor can then convert this change into electrical signal. Figure 2.15 is principle schematic diagram of the vibration sensor based on laser interferometer principle [71].

Laser beam emitted by the laser source is divided into the reference beam and the measurement beam through the beam splitter. The reference beam is reflected by the flat mirror, and goes through the beam splitter again and received by the optical detector. The measurement beam is focused by the lens and then reflected by the vibrating object.
The reflected beam is frequency-shifted by the motion of the vibrating object due to the Doppler effect. The reflected light with the frequency f_{shift} and the reference beam with frequency f_{ref} are collected and mixed by the optoelectronic receiver. The optoelectronic receiver converts the two beam into one single electrical signal. Finally, the vibration frequency and amplitude can be obtained through digital signal processing.

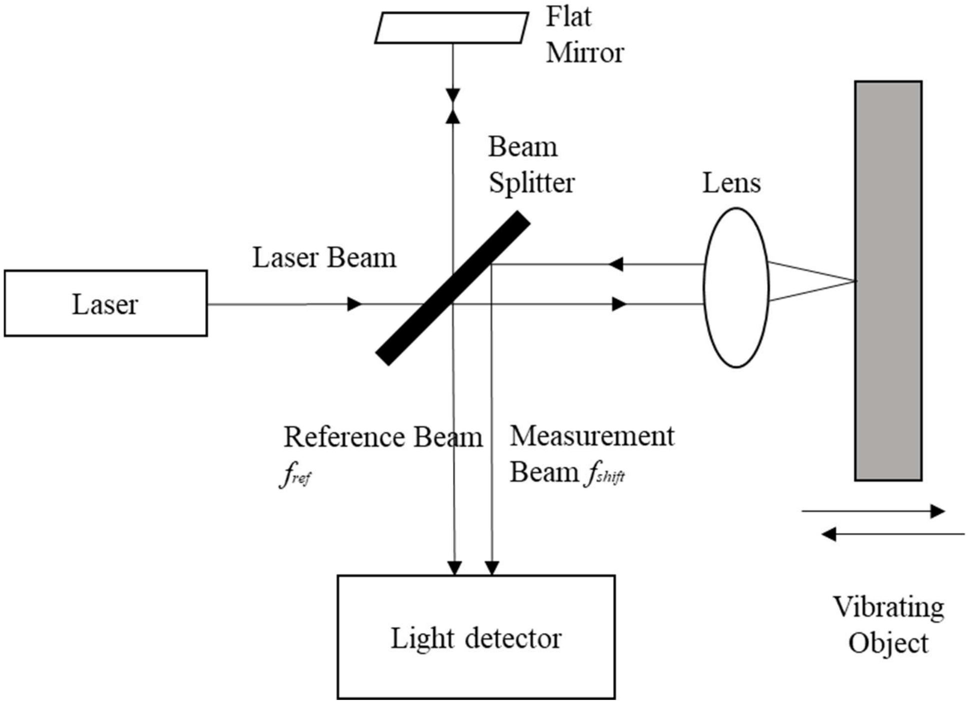

Figure 2.15 Principle schematic diagram of the vibration sensor [71].

Advantages of the photoelectric sensor include high resolution, high precision, fast response and non-contact measurement. The disadvantages include the optoelectronic device characteristics are significantly affected by environmental interferences and the subsequent processing circuit complexity.

2.3.5 Ultrasonic Sensors

In this method, the shaft vibration is detected by measuring the propagation time of the ultrasonic wave from the sensor to the shaft surface [61].

The system uses an ultrasonic sensor attached onto a casing surface as shown in Figure 2.16. The ultrasonic wave is perpendicularly incident from the ultrasonic sensor to the casing and the shaft. When the ultrasonic wave is incident into the casing, it does not only cause multiple reflection between the surface and the bottom of the casing, but also a portion of the ultrasonic wave penetrates through the casing and arrives at the shaft surface. Thus, the analysis of the arrival times of these reflected waves enables the measurement of the location of the shaft each time the ultrasonic wave is sent out. When the reflected waves from the casing bottom and the shaft are separated from each other, the measurement of the shaft vibration can then be quantified.

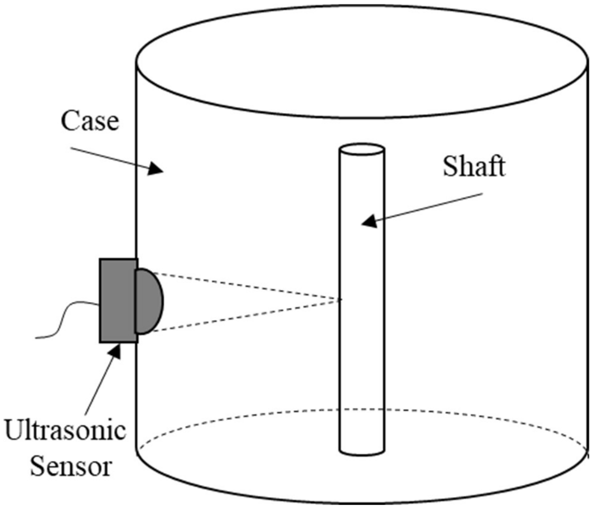

Figure 2.16 Ultrasonic vibration sensor [61].

Advantages of the ultrasonic sensors include non-contact measurement, high accuracy and sensitivity. However, they are susceptible to noise interference.

2.3.6 Electrostatic Sensors

To date, little research has been reported on the use of electrostatic sensors for vibration measurement. There have, however, been attempts to employ electrostatic sensors for the vibration detection of rotating machinery. Wang et al [72] have undertaken research on electrostatic sensors for the vibration detection of rotating machinery. Later, they proposed a method for the radial vibration measurement of a dielectric shaft using electrostatic sensors and Hilbert-Huang Transform [63]. Figure 2.17 shows the basic principle of the radial vibration measurement system using electrostatic sensors.

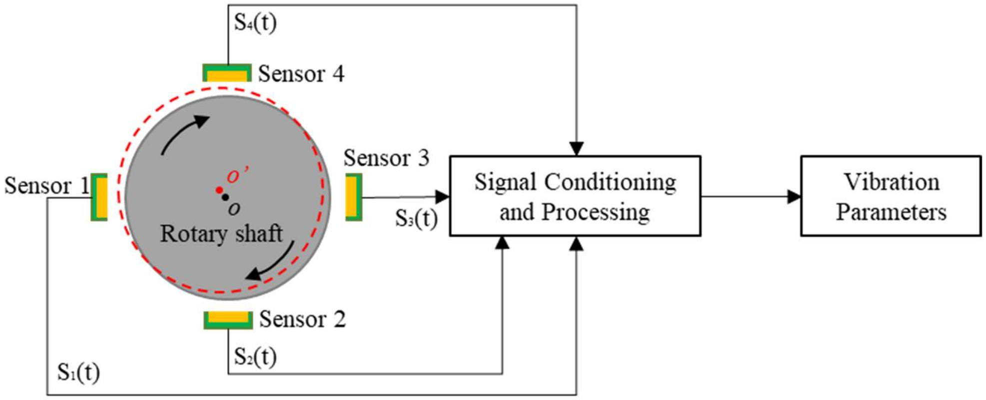

Figure 2.17 Principle of radial vibration measurement using electrostatic sensors.

The signals are generated through electrostatic induction due to the moving charged surface with reference to the electrostatic sensor. The difference between a pair of sensor signals, such as S_1 and S_2, or S_3 and S_4, is able to indicate the drifting motion of the shaft. As shown in Figure 2.17, once the shaft has radial vibration, i.e. the rotating centre changes from *O* to *O'*, sensors 1 and 4 will detect more significant signal amplitude due to the closer distance between the shaft and the electrodes. Meanwhile, sensors *2* and *3* yield lower signal amplitude.

Hilbert-Huang Transform has also been applied to identify and extract the vibration features from the sensor signals. The signals from the electrostatic sensors are conditioned and decomposed into several modes. The vibration frequencies are identified and detected from the Hilbert-Huang spectra.

However, the proposed methods were based on the amplitude of the output signal resulting from electrostatic charge on the surface of a rotating dielectric shaft, assuming that the only factor affecting the amount of induced charge, and hence the signal amplitude, is the distance between the electrode and the shaft. Nevertheless, the electric charge level on the dielectric shaft surface depends significantly on environmental conditions and consequently the signal amplitude varies with environmental factors such as ambient temperature and relative humidity [73]. As a result, these methods cannot be used to achieve an absolute displacement measurement due to the uncertain amount of charge on the shaft surface. Moreover, these methods work only on dielectric shafts and require an array of sensors to be installed around the shaft, making the sensor installation practically difficult.

2.4 Summary

A variety of existing techniques have been investigated for the measurement of rotational speed and vibration of rotary shafts. Sensors for measuring rotational speed, analogue and digital tachometers have first been discussed. Next, Fibre-optic gyroscopes were considered. Finally, the recent development on electrostatic sensors has been presented. Subsequently, the basic operational principles of techniques that can be used for shaft vibration measurement has been presented in the sub-section 2.3.

Although each of the aforementioned techniques has a sound theoretical basis that have been idealised in some respect, all these techniques have their limitations for operations in industrial environments. The mechanical tachometers suffer from the common problems of wear, slippage, low measurement accuracy and a narrow measurement range. Photoelectric tachometers and encoders require fitting on the shaft. The optical sensors may not function well in a hostile environment due to the presence of dust in addition to high capital cost and regular maintenance requirements. Electromagnetic interferences in a hostile environment affect the operation of inductive and magnetic tachometers, and the inductive and capacitive vibration sensors.

Fibre-optic gyroscopes, fibre-optic vibration sensors and imaging-based rotational speed measurement systems are usually unsuitable for wide application in industrial processes due to system complexity and regular maintenance requirements. Additionally, they are prohibitively expensive to implement in routine industrial applications.

Table 2.1 summarizes the advantages and limitations of the main techniques that have been applied to measure the rotational speed and vibration of rotating shafts.

Table 2.1 Comparison of the current measurement techniques.

Sensor Technique	**Measurand**	**Advantages**	**Disadvantages**
Mechanical tachometers	Rotational speed	Low cost	Wear and slippage. Low measurement accuracy. Narrow measurement range.
Optical encoders and digital tachometers	Rotational speed	Good accuracy High resolution Fast response	Requirement for the fitting on the shaft. Contact measurement.
Non-contact Laser tachometer	Rotational speed	Non-contact Good accuracy	Less reliable in dusty environments.
Magnetic (Hall effect)	Rotational speed	Non-contact Good accuracy Immunity to vibration	Vulnerable to external magnetic fields. Only work on metal objects.
Capacitive	Vibration	Non-contact High resolution High precision Fast response time	Small measurement range. Vulnerable to electromagnetic fields.
Ultrasonic	Vibration	Non-contact High accuracy High sensitivity	Susceptibility to noise Interference.

Inductive	Rotational speed/ Vibration	Non-contact Good accuracy High reliability	Limited measurement range. Only work on metal objects. Low sensitivity. Linearity.
Fibre-optic	Rotational speed/ Vibration	Non-contact High accuracy High sensitivity Fast response Immunity to electromagnetic interference	High capital cost. Narrow range of measurement frequency. System complexity. Regular maintenance.
Digital imaging	Rotational speed/ Vibration	Non-contact High accuracy High resolution	Computationally expensive for online measurement. Unsuitable for dusty and harsh environments.
Electrostatic sensors	Rotational speed/ Vibration	Non-contact Low cost Good accuracy Simple structure Easy installation	Require further testing and validation in industrial environments.

The review has indicated that electrostatic sensors are well established and have successfully achieved a rotational speed measurement for dielectric shafts under laboratory conditions. However, there are no reported research in the literature on rotational speed measurement for metallic shafts using electrostatic sensors. Moreover, there has been very limited research on the use of electrostatic sensors to quantify the vibration of rotary shafts. The aim of this research is to develop the existing electrostatic sensors to be capable of providing simultaneous online measurements of rotational speed and vibration displacement of metallic rotary shafts. Thus, the developed measurement system can potentially be employed as a measuring device in the condition monitoring and control of rotating machinery.

Chapter 3

Measurement Principle and Modelling of Electrostatic Sensors

3.1 Introduction

This chapter introduces the measurement principles of the rotational speed and vibration of metallic shafts using electrostatic sensors. Moreover, the sensing mechanism and modelling of electrostatic sensors are also presented and discussed in the following sections.

The sensing system consists mainly of an electrically insulated charged markers fixed on a rotary metallic shaft in conjunction with an insulated electrode placed in the vicinity of the shaft surface. The electric field resulting from the interaction between the inducing charge (charged markers) and the induced charge on the electrode is rather complex. Consequently, the mathematical modelling of the system is established to quantify and analyse the fundamental characteristics of electrostatic sensors for electric charge (point and strip charge) in rotational motion through analytical modelling and numerical simulation.

The established model is principally based on the mathematical model proposed by Wang et al [74]. In the latter model, the target to be measured was a point charge in rotational motion, which can be considered as an infinite element on the charged surface of an insulating shaft. The developed model replaces the point charge by a strip-shaped charge simulating a charged marker fixed on the surface of a metallic shaft.

The effects of physical parameters of the markers on the performance of the measurement system are analysed to obtain the optimal design.

3.2 Measurement Principle

3.2.1 Rotational Speed Measurement

The basic principle of the rotational speed measurement system based on an electrostatic system is shown in Figure 3.1.

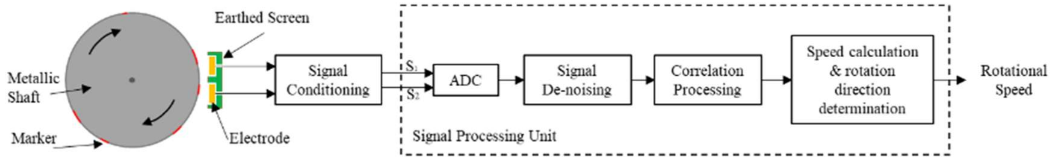

Figure 3.1. Principle of the rotational speed measurement using dual electrostatic sensors.

Figure 3.2 shows a simplified physical model of the electrostatic sensing system for rotational speed measurement. The physical model consists of a metallic shaft, electrically isolated charged markers fixed on the shaft surface, an electrostatic electrode, and associated signal conditioning circuit. Small electrostatically charged markers, made of electret film, are fixed along the circumference of a metallic shaft. The charged marker simulates a strip charge on the shaft surface.

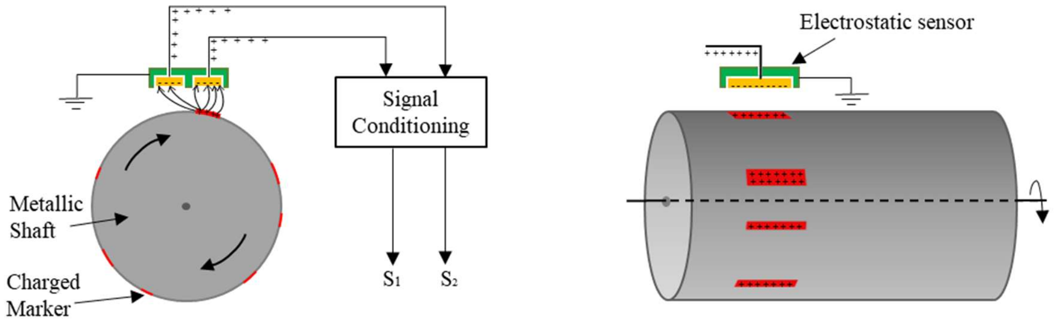

Figure 3.2 A simplified physical model of the sensing system.

If n markers (e.g., n=6) are distributed around the shaft, then the output signal is composed of n pulses corresponding to the n markers, as shown in Figure 3.2. The number and distribution of the markers around the shaft depend primarily on the shaft diameter, angular speed to be measured and the size of the markers. The optimal number has been determined in sub-section (3.5.2) to meet the requirements of the output signal generated by the sensor in order to achieve a reliable rotational speed measurement.

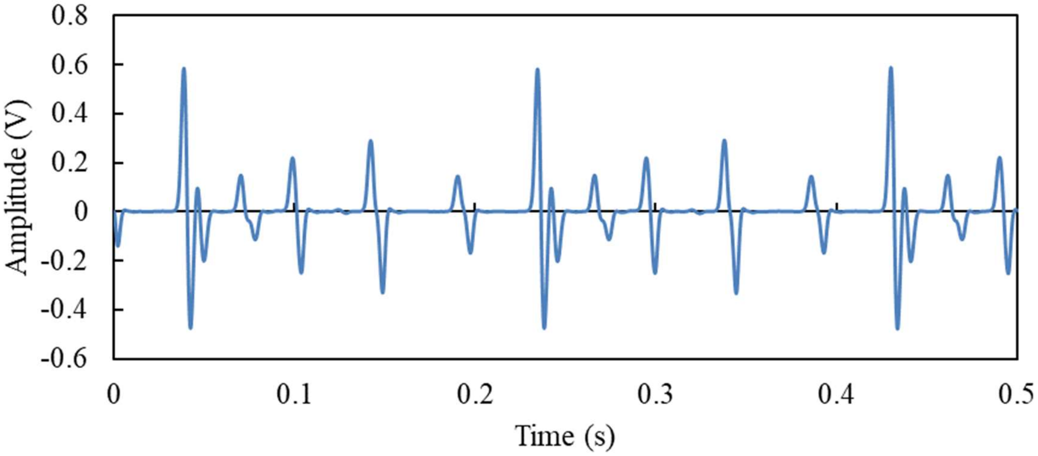

Figure 3.3 Typical signal waveform from the electrostatic sensor (308 rpm).

The electrostatic sensor is placed in the vicinity of the shaft to sense the charged markers on the shaft surface. Electrostatic signal is obtained from the electrostatic sensor through electrostatic induction. A high-performance signal conditioning unit is utilised to condition the extremely weak signals from the sensing point. The data acquisition unit converts the analogue signals to digital forms and transmits the acquired signals to a host computer. Signal processing, including auto-correlation and cross-correlation, and rotational speed calculation are realized in the host computer.

The electrostatic signal is periodic due to the continuous rotational motion of the shaft with reference to the fixed location of the sensor (Figure 3.3). The periodicity of the signal is equal to the period of the rotation motion (T), which is determined from auto-correlation function of the electrostatic signal. A normalised auto-correlation function Ra (m) is defined as

$$Ra(m) = \frac{\sum_{k=1}^{N} S(k)S(k+m)}{\sum_{k=1}^{N} S^2(k)} \tag{3.1}$$

where *S(k) (k = 0, 1, 2, . . ., N)* represents the digitized signal of *S(t)*, *N* is the number of samples in the correlation computation and *m (m = 0, . . ., N)* is the number of delayed points.

Figure 3.4 shows a typical example of the resulting autocorrelation function with the dominant peak marked out on the time axis. The other major peaks in the correlation function (Figure 3.4) are due to the periodic nature of the rotational motion.

The location of the dominate peak (other than the unity at $m = 0$) on the time axis is the period *T*. The amplitude of the dominate peak in the auto-correlation function is the correlation coefficient, which indicates the reliability of the speed measurement through autocorrelation. The rotational speed (S_{rpm}) in Revolutions Per Minute (RPM) is calculated from

$$S_{rpm} = \frac{60}{T} \tag{3.2}$$

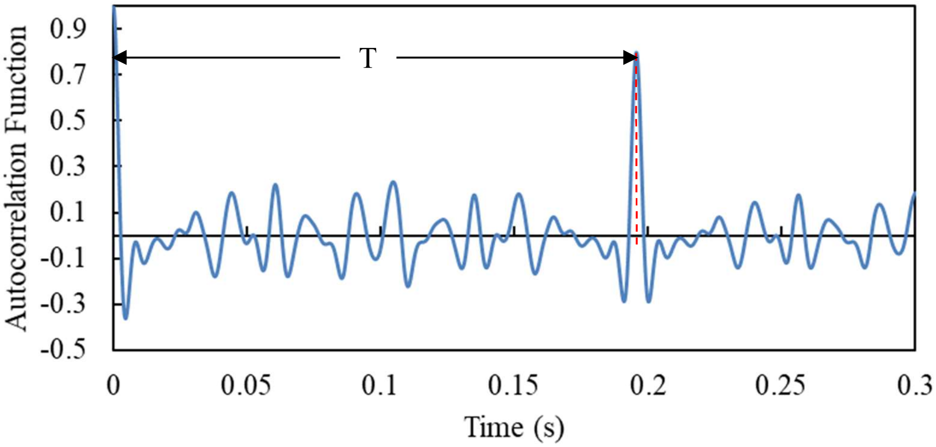

Figure 3.4 Typical autocorrelation function of the electrostatic sensor.

However, the autocorrelation method requires a complete rotation of the shaft before the rotational speed can be calculated. At low rotational speed and for a large shaft diameter, the large period T of the output signal requires a long data size, resulting in low response time in the speed measurement.

In this case, dual electrostatic sensors with a small angular spacing between them can be used to achieve low speed measurements with shorter response time. The two signals $S_1(t)$ and $S_2(t)$, derived from the dual sensors, in Figure 3.5 are very similar to each other apart from the time delay between them. The time delay (τ) between the two electrostatic signals $S_1(t)$ and $S_2(t)$ is equal to the time taken by the shaft passing through the two electrodes and can be determined through cross correlation $Rc(m)$

$$Rc(m) = S_1 * S_2 \tag{3.3}$$

The time corresponding to the dominant peak in the cross-correlation function $Rc(m)$ is the time delay τ (Figure 3.6) and thus the rotational speed (S_{rpm}) is determined from

$$S_{rpm} = \frac{30\varphi}{\pi\tau} \tag{3.4}$$

where φ is the angular spacing in radians between the two sensors.

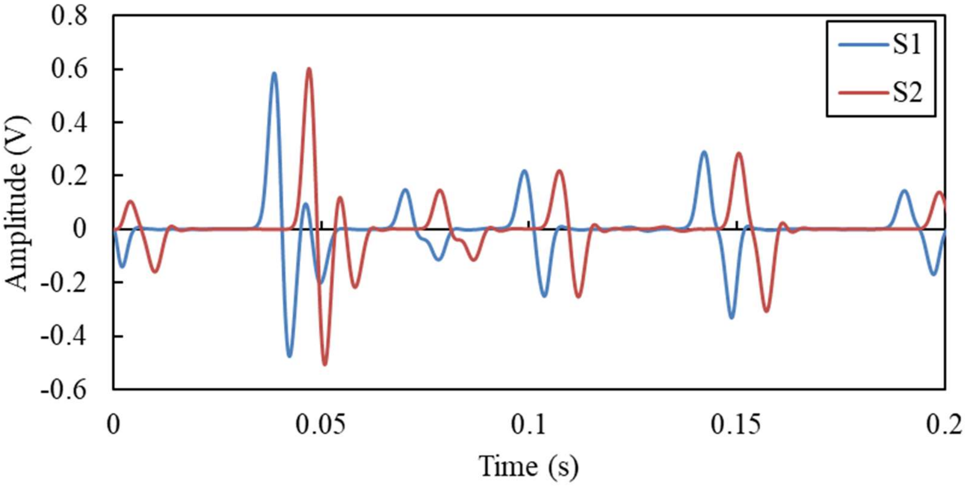

Figure 3.5 Typical signal waveforms from the dual electrostatic sensors (308 rpm).

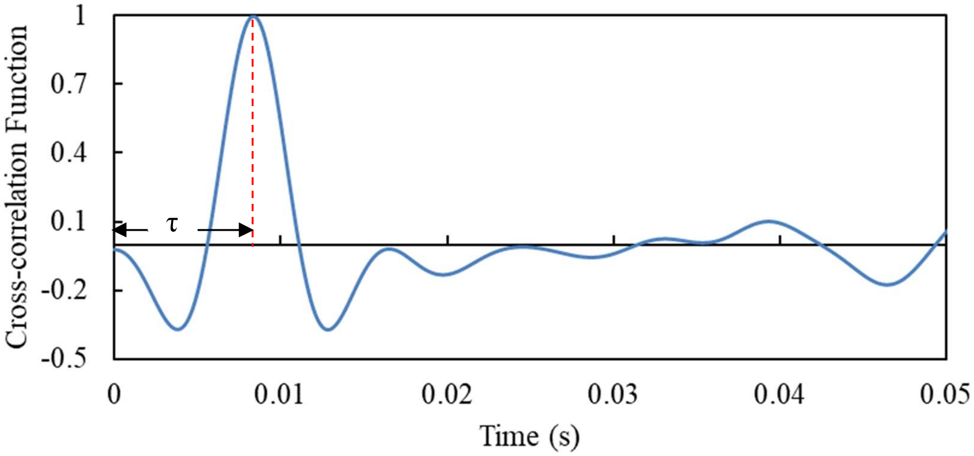

Figure 3.6 Typical cross-correlation function of the electrostatic signals.

The use of cross-correlation method at low speed should be more efficient since a short time is sufficient to achieve the speed measurement. However, when the rotational speed is high, the transit time is too small to be determined accurately and the cross-correlation method has lower sensitivity. In this case, using single sensor is more suitable for high speed measurement in terms of accuracy.

In the proposed system, an electrostatic sensor with double electrodes is used. The sensor can derive three correlation functions including two autocorrelation function, $R_{11}(m)$ and $R_{22}(m)$ of discrete signals $S_1(k)$ and $S_2(k)$ respectively, and a cross-correlation function, $R_{12}(m)$ and $R_{21}(m)$ between the two signals. Therefore, the rotational speed to be measured can be achieved through the autocorrelation method for high speed, while the cross-correlation method can be used to low speed range. A speed threshold between the low and high speed will be determined, based on the system parameters, in the data processing section.

The validity of the correlation method for the rotational speed measurement is based upon the assumption that the electrostatic signal, at a constant rotational speed, is stationary and random. In the cross-correlation method, the signal should be stationary and random during the transit time that the shaft took to move through two electrodes. The higher the randomness of the signal, the better the measurement accuracy. To meet this requirement, the size of the n markers and their distribution around the shaft should be chosen carefully to produce a high random signal over one rotation. A pseudo random code is used in sub-section 4.1.2 to achieve a random distribution of markers around the circumference of the shaft and hence generating a stationary random signal.

3.2.2 Shaft Vibration Measurement

Figure 3.7 shows a simplified physical model of the electrostatic sensing system for displacement measurement. The physical model consists of a metallic shaft, electrically isolated point charges fixed on the shaft surface (e.g. points *M* and *N*), an electrostatic electrode and associated signal conditioning circuit.

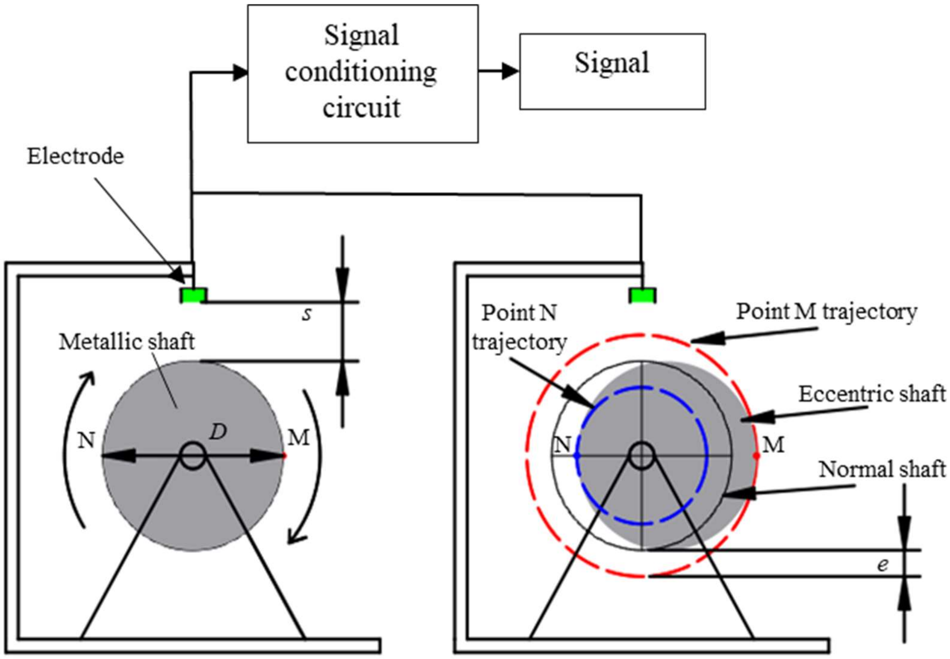

(a) Normal shaft. (b) Eccentric shaft.

Figure 3.7 Physical model of the sensing system.

A small electrostatically charged marker made of electret film is fixed on the metallic shaft. The marker simulates a point charge on the shaft surface. An electrostatic sensor consists of an insulated electrode with a suitable charge detection circuit can detect the charge on the marker and generate an output signal through electrostatic induction.

Previous research [74] shows that the frequency response of the sensor output depends primarily on the circular trajectory diameter *D* of a rotating point charge fixed on the shaft surface (points M or N in Figure 3.7, the distance *s* between the point charge and the electrode, and the angular speed *ω* of the shaft. For a given point charge on the shaft, the rotational motion results in a circular trajectory of the point charge. In the case of a normal shaft, the shortest distance between any rotating point on the shaft and the electrode is constant, as is its trajectory diameter, which is equal to *D*. While each point on an eccentric shaft rotates along a different circular trajectory and results in a variation in the distance *s*. By analysing the frequency response of the output signal, the displacement and hence the imbalance of the shaft can be quantified. When *n* identical markers (e.g. $M_1…M_8$) are fixed around the shaft, the output signal is then composed of *n* pulses corresponding to the *n* markers, as shown in Figure 3.8

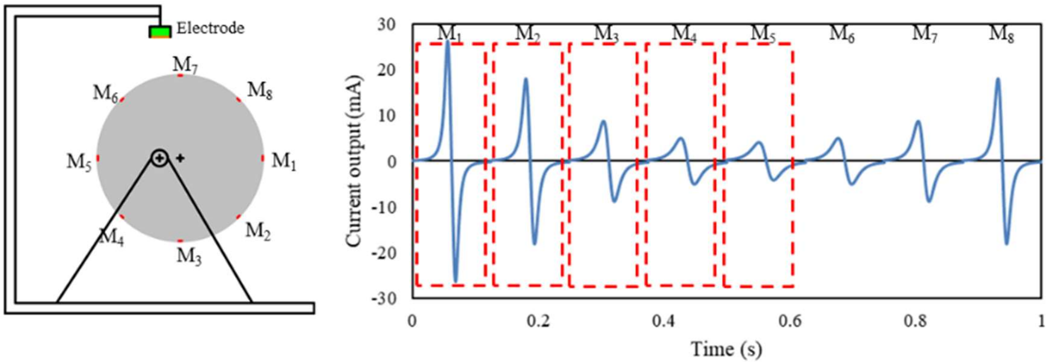

(a) (b)

Figure 3.8 Distribution of markers on the shaft and corresponding output signal results over one rotation (speed=60 rpm). (a) Markers on the shaft. (b) Sensor output signal.

It is worth noting that the markers M_1 and M_5 correspond to the shortest and longest distance from the shaft surface to the electrode, respectively (Points M and N in Figure 3.7).

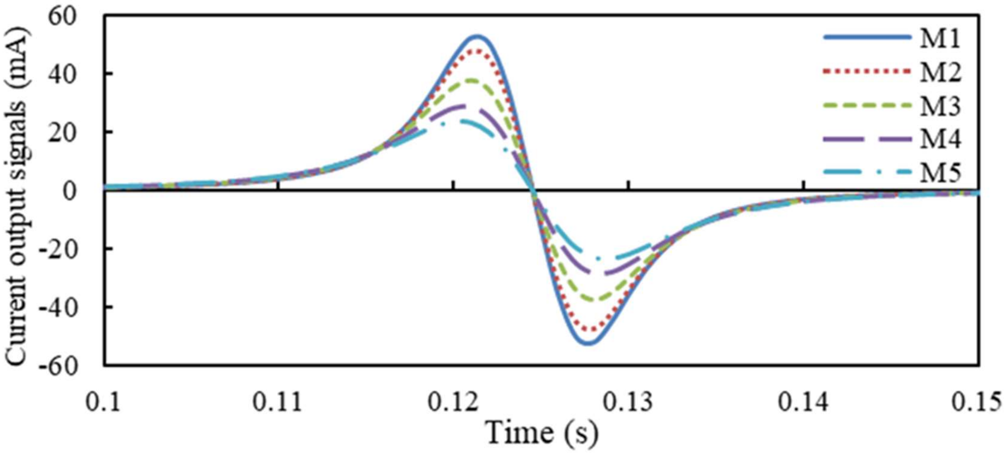

Figure 3.9 Decomposition of the output signal into five single signals.

It can be seen from Figure 3.8 that the distance between M_4 and the centre of rotation is equal to that between M_6 and the centre of rotation. Similar dispositions exist with respect to points M_3-M_7 and M_2-M_8. Consequently, the pulses resulting, respectively, from M_6, M_7-M_8 and M_4, M_3-M_2, are identical. Therefore, it would be sufficient to analyse the first five pulses (M_1-M_5) which are distributed over the semi-circumference of the shaft. The output signal is first decomposed in the time domain into single pulses corresponding to the markers fixed on specific locations around the shaft. The corresponding spectra are plotted in Figure 3.9. However, the decomposition should be performed under the assumption that the pulses resulting from the markers (point charges) do not overlap with each other. Accordingly, the number and arrangement of the markers should be well defined in order to satisfy this condition. The number and arrangement of the markers around the shaft depend primarily on the shaft diameter, angular speed to be measured and the size of the markers. The markers parameters will be determined and defined in the following sections.

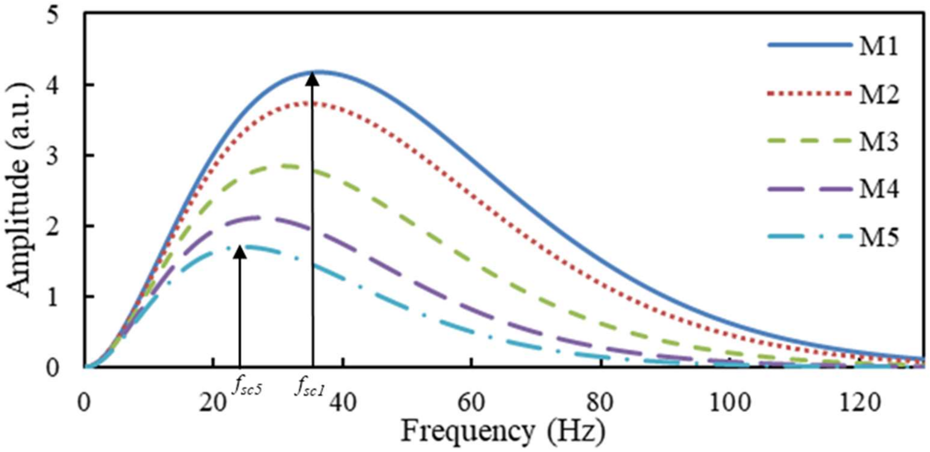

Figure 3.10 Amplitude spectra of the decomposed pulses.

Figure 3.10 shows that, when a point charge on the shaft surface rotates closer to the electrode (e.g. M_1), the frequency at the spectrum crest (f_{sc1}) has a higher value than that of a point charge rotating farther to the electrode. When a point charge rotates is closer to the electrode, the electrode covers a smaller area of the electric field, and the induction occurs for a shorter period and subsequently gives rise to a signal of higher frequency. As a result, the closer the distance between the electrode and the shaft surface, the more the induced charge on the electrode and the higher the frequency.

The magnitude frequency response of the output signals due to different point charges on an eccentric shaft (different displacements), rotating at a constant speed, shows different frequencies at the peak of spectra or the frequency at the spectrum crest (f_{sc}) (Figure 3.10). Therefore, the displacement can be derived from f_{sc}.

3.3 Sensing Mechanism

3.3.1 Principle of Electrostatics

If an isolated point charge of Q_0 coulombs is considered, and if the charge is enclosed in the centre of a spherical Gaussian surface, Gauss' law states that the outward flux of E_f

over any closed surface S_c is equal to the algebraic sum of the charges enclosed divided by ε,

$$\sum Q_0 = \varepsilon \oint_S E_f dS_c \tag{3.5}$$

The flux of electric field E_f from the surface may be deduced by

$$\frac{Q_0}{\varepsilon} = 4\pi r^2 E_f \tag{3.6}$$

where ε is the permittivity and r is the radius of the sphere, or the distance between the particle and the surface. If this Gaussian surface is placed just inside a Faraday cup, then the total charge Q would be induced on the cup surface and hence, measurement of the total charge Q could be made. Consider now a small surface area (A) within the Gaussian surface. The flux terminating on this surface may be approximated by

$$\frac{Q_A}{\varepsilon} \sim AE_f \tag{3.7}$$

where Q_A is the charge induced on the surface.

Q_A will be a fraction of Q_0, and can be written as

$$Q_A \sim \frac{Q_0 A}{r^2} \tag{3.8}$$

The area A is taken as the surface of the electrostatic electrode, and hence its sensitivity to the total charge Q_0 may be deduced by re-arranging the previous equation

$$\frac{Q_A}{Q_0} \sim \frac{A}{r^2} \tag{3.9}$$

It is clearly evident, in theory, that the sensitivity to charge increases with respect to the magnitude of the charge source and dimensions of the electrode. However, it decreases as the distance of separation between the charge source and the electrode increases [75].

3.3.2 Electrostatic Sensing Mechanism

An electrostatic sensing unit is used to sense the induced charge and convert it into measurable signal. The induced charge on the electrode depends on the polarity and magnitude of the source charge.

An electrostatic sensing unit is based upon electrostatic induction phenomenon. This phenomenon is used to enable the electric signal generated by the charge on an insulating surface to be traced and monitored continuously by a measurement system, whose first and principal part is the electrostatic sensing unit.

If a charge source passes in front, or passes the field-of-view of a conducting plate (electrode), electric field lines will terminate on the electrode face. This will induce free electrons to be drawn to or away from the surface of the electrode (depending on the polarity of the charge source) due to electrostatic attraction/repulsion as shown in Figure 3.11(b). Holes will move in the opposite direction. This phenomenon is known as induction [75].

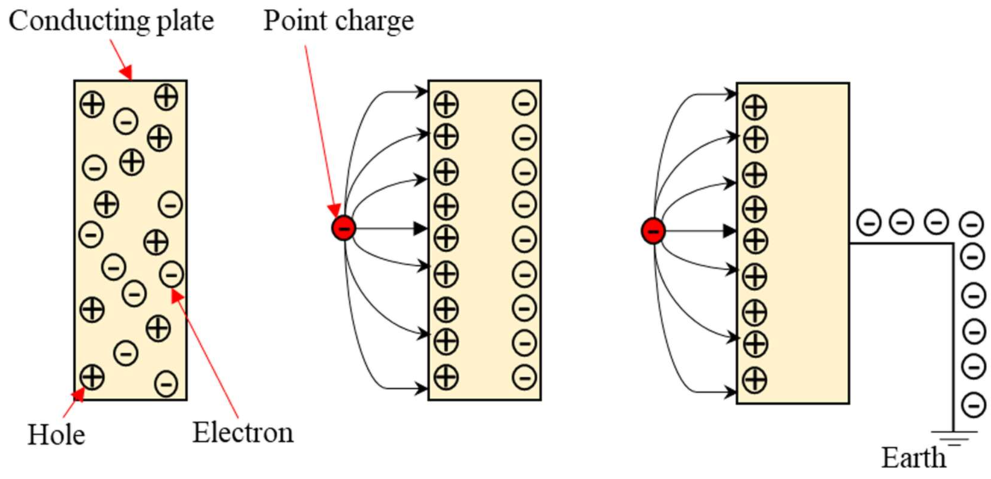

(a) (b) (c)

Figure 3.11 Principle of polarization in an electrostatic sensor. (a) An isolated conducting plate. (b) An isolated plate in the presence of a nearby charge source. (c) Conducting plate connected to earth.

If the electrode is insulated from the earth (Figure 3.11(b)), its potential depends on the amount of charge, the permittivity of, and their locations, relative to the electrode, according to electrostatic principles. The charge due to induction disappears when the charge source moves away from the sensing zone of the electrode.

If the electrode is connected to earth, electrons will flow to or from earth (depending on the polarity of the charge source) to counteract this polarization as shown in Figure 3.11(c).

In an electrostatic system, the electrode is connected to a signal conditioning unit. This signal conditioner will measure the flow of electrons and produce a measurable output.

Figure 3.12 is a schematic diagram showing the process of charge detection in an electrostatic sensing unit as moving charge passes in the vicinity of the sensor's electrode.

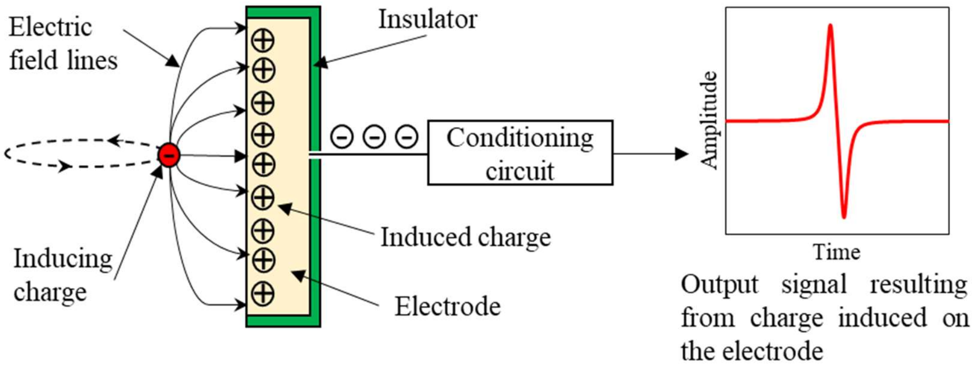

Figure 3.12 Schematic illustration of the electrostatic sensing unit.

3.4 Modelling of the Electrostatic Sensor

In previous research, Wang et al [74] developed simplified physical and mathematical models of a strip-shaped electrostatic sensor for a point charge in rotational motion in the vicinity of an insulated electrode. Using the established model, current output, spatial sensitivity, spatial filtering length and signal bandwidth of the sensor were quantified respectively through analytical modelling and numerical simulation. The purpose of the modelling was to analyse the effects of physical parameters of the sensor on the performance of the measurement system in order to obtain an optimal design of the electrode in terms of dimensions and distance with respect to the shaft surface.

Figure 3.13 shows an overview of the sensing arrangement in the mathematical modelling. The cylinder C_c indicates a metallic shaft with a diameter *D*, on which electrically insulated strip charges and point charge are fixed. A strip-shaped electrode with dimensions *LxW*, made on a small printed circuit board with adequate insulation together with grounding around the electrode, can be regarded as a piece of perfectly conductive metal and is placed at distance *s* from the shaft.

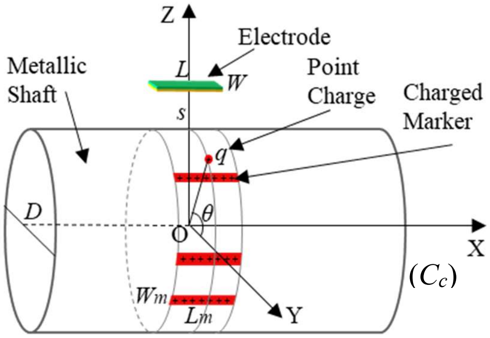

Figure 3.13 Electrostatic sensing arrangement in the mathematical modelling.

To simplify calculations and visualize the distribution of the electric field due to the interaction between a source charge and conducting surface, the method of images together with theories of electrostatics are applied to the mathematical modelling of the electrostatic sensor. The validity of the method of images rests upon a corollary of the uniqueness theorem. That is to say, the method is based on the fact that the tangential component of the electrical field on the surface of a conductor is zero whilst the electric field strength in a region is uniquely defined by its normal component over the surface that confines that region. The mathematical model of a strip electrostatic sensor for rotational speed measurement is shown in figure 3.14.

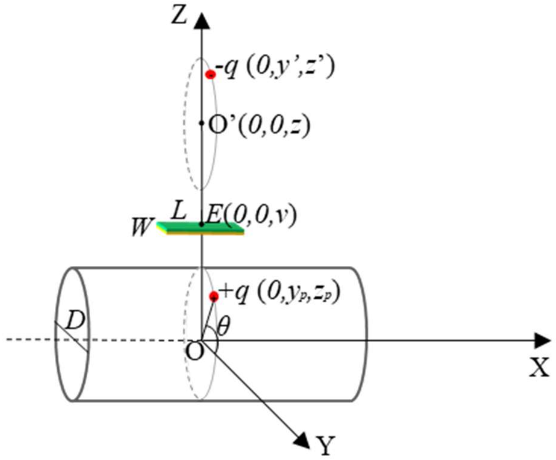

Figure 3.14 Mathematical model of a strip electrostatic sensor.

Assuming that a point charge $+q$ is located at some position (x_p, y_p, z_p) and is fixed on the shaft which is rotating around the X-axis and the geometric dimensions of the strip electrostatic electrode W and L are infinite with zero thickness. Then, according to Coulomb's law and the superposition principle of electrostatic fields, the potential at an arbitrary observation point (x, y, z) is evaluated as

$$V = \frac{1}{4\pi\varepsilon}\left(\frac{q}{\sqrt{(x_p - x)^2 + (y_p - v)^2 + (z_p - z)^2}} + \frac{-q}{\sqrt{(x' - x)^2 + (y' - y)^2 + (z' - z)^2}} \right) \qquad (3.10)$$

where ε is the permittivity of the medium, (x', y', z') denotes the coordinate of the induced charge on the electrode.

$$V = \frac{1}{4\pi\varepsilon}\left(\frac{q}{\sqrt{(x_p - x)^2 + (y_p - y)^2 + (z_p - v)^2}} + \frac{-q}{\sqrt{(x_p - x)^2 + (y_p - y)^2 + (2v - z_p - z)^2}} \right) \qquad (3.11)$$

Charge density σ on the surface of the electrode is given by

$$\sigma = -\varepsilon \frac{\partial V}{\partial z}\bigg|_{z=v} = \frac{-q(v - z_p)}{2\pi[(x_p - x)^2 + (y - y_p)^2 + (v - z_p)^2]^{3/2}} \qquad (3.12)$$

Therefore, the total induced charge Q on the electrode surface is determined from

$$Q = \int_{-L/2}^{L/2} \int_{-W/2}^{W/2} \sigma dydx \tag{3.13}$$

$$Q = \frac{-q}{2\pi} \int_{-L/2}^{L/2} \int_{-W/2}^{W/2} \frac{(v - z_p)}{[(x_p - x)^2 + (y - y_p)^2 + (v - z_p)^2]^{3/2}} dydx \tag{3.14}$$

where $v = 0.5D + S$, $y_p = 0.5D\cos\theta$, $z_p = 0.5D\sin\theta$. θ is the central angle that the point charge passed by. Substituting v, y_p amd z_p into equation (3.14), the total induced charge Q on the electrode becomes

$$Q(\theta, \delta_x) = \frac{-q}{4\pi} \sum_{i=1}^{4} \arctan \left[\frac{(0.5\delta_w + 0.5\beta_i \cos\theta)(0.5\delta_L + (-1)^i \delta_x}{(0.5 + \delta_s - 0.5\sin\theta) \sqrt{\begin{array}{l} (0.5 + \delta_s - 0.5\sin\theta)^2 + \\ (0.5\delta_w + 0.5\beta_i \cos\theta)^2 + \\ (0.5\delta_L + (-1)^i \delta_x)^2 \end{array}}} \right] \tag{3.15}$$

where $\beta_i = \operatorname{sgn}(i - 1.5), \delta_L = \frac{L}{D}, \delta_W = \frac{W}{D}, \delta_s = \frac{s}{D}, \delta_x = \frac{x_p}{D}$,

In this study, the point charge is replaced by a strip charge simulating a strip-shaped charged marker with dimensions $A_m = L_m x W_m$. Accordingly, a mathematical model is derived from the model outlined above.

Assuming that the surface charge density of the marker σ_m is uniform, the strip charge can be considered as the collection of parallel line charges and a line of charge is the collection of point charges distributed along a straight line segment. Therefore, the total charge on the strip marker is $\sigma_m A_m$ and the induced charge on the electrode surface due to the strip charge is the superposition of the induced charge due to all point charges within the strip surface. Hence, the overall induced charge can be obtained by integrating Equation (3.15) over the surface of the strip marker

$$Q(\theta)=\frac{-\sigma_m}{4\pi}\int_{-\theta_m/2}^{\theta_m/2}\int_{-\delta_{L_m}/2}^{\delta_{L_m}/2}\sum_{i=1}^{4}\arctan\left[\frac{(0.5\delta_w+0.5\beta_i\cos(\theta+\alpha)(0.5\delta_L+(-1)^i\delta_x}{(0.5+\delta_s-0.5\sin(\theta+\alpha))\sqrt{\begin{matrix}(0.5+\delta_s-0.5\sin(\theta+\alpha))^2+\\(0.5\delta_w+0.5\beta_i\cos(\theta+\alpha))^2+\\(0.5\delta_L+(-1)^i\delta_x)^2\end{matrix}}}\right]d\delta_x d\alpha \tag{3.16}$$

where θ_m is the central angle corresponding to the width of the marker, $\theta_m=2W_m/D=2\delta_{Wm}$, $\delta_{Lm}=L_m/L$ and σ_m is the surface charge density of the marker.

For a given angular speed ω, $\theta=\omega t$. Equation (3.16) can be rewritten as

$$Q(t)=\frac{-\sigma_m}{4\pi}\int_{-\delta_{W_m}}^{\delta_{W_m}}\int_{-\delta_{L_m}/2}^{\delta_{L_m}/2}\sum_{i=1}^{4}\arctan\left[\frac{(0.5\delta_w+0.5\beta_i\cos(\omega t+\alpha)(0.5\delta_L+(-1)^i\delta_x}{(0.5+\delta_s-0.5\sin(\omega t+\alpha))\sqrt{\begin{matrix}(0.5+\delta_s-0.5\sin(\omega t+\alpha))^2+\\(0.5\delta_w+0.5\beta_i\cos(\omega t+\alpha))^2+\\(0.5\delta_L+(-1)^i\delta_x)^2\end{matrix}}}\right]d\delta_x d\alpha \tag{3.17}$$

3.5 Characteristics of the Electrostatic Sensor

Based on the developed model, the spatial sensitivity, frequency response and the bandwidth of the output signal are analysed. Additionally, the sensing zone of the sensor can also be defined. The parameters of markers can then be optimised with the aid of the modelling results.

3.5.1 Spatial Sensitivity

Sensitivity is one of the most important characteristics which affects the dynamic performance of the sensor. From Equation (3.8), it can be seen that the charge Q induced on the sensor is affected by the location of the strip charge (θ). The spatial sensitivity, $S_s(\theta)$, is defined by [76]

$$S_s(\theta) = \left| \frac{Q(\theta)}{Q_0} \right| \tag{3.18}$$

where $Q(\theta)$ is the induced charge on the sensor surface and Q_0 is the inducing charge on the surface of the marker with area A_m.

Since $Q_0=\sigma A_m$, the spatial sensitivity can be rewritten as

$$S_s(\theta) = \frac{1}{4\pi A} \int_{-\delta_{W_m}}^{\delta_{W_m}} \int_{-\delta_{L_m}/2}^{\delta_{L_m}/2} \sum_{i=1}^{4} \arctan \left[\frac{(0.5\delta_w + 0.5\beta_i \cos(\theta+\alpha)(0.5\delta_L + (-1)^i \delta_x}{(0.5+\delta_s - 0.5\sin(\theta+\alpha)) \sqrt{\begin{array}{l}(0.5+\delta_s - 0.5\sin(\theta+\alpha))^2 + \\ (0.5\delta_w + 0.5\beta_i \cos(\theta+\alpha))^2 + \\ (0.5\delta_L + (-1)^i \delta_x)^2\end{array}}} \right] d\delta_x d\alpha \tag{3.19}$$

From equation (3.19) it can be seen that the spatial sensitivity of the sensor, in a given location θ and for a given dimensions and position of the electrode, is determined by the geometric dimensions of the marker (W_m and L_m). For each of the two parameters, four representative cases are considered in this study: $W_m / W = 0$ (line charge), $L_m / D = 1, 3/2, 2, 4$; and $L_m / D = 0$ (Arc charge), $W_m / W = 1/2, 3/4, 1, 2$.

Substituting $\delta_{Wm} = 0$, $\delta_s = 1/30$, $\delta_W = 1/10$, $\delta_L = 1/3$, $A_m = L_m$ (line charge) to equation (3.19), the effects of the marker length (L_m) on the spatial sensitivity of the sensor are illustrated in Figures 3.15 and 3.16. It is evident that the overall sensitivity decreases with δ_{Lm}, particularly when the length of the marker exceeds the length of the electrode. Suggesting that the farther the distance that the inducing charge is from the centre of the marker, the less the induced charge that is yielded on the electrode. The sensitivity reduces from 30.25% to 29.95% as the δ_{Lm} increases from 0 to 0.5.

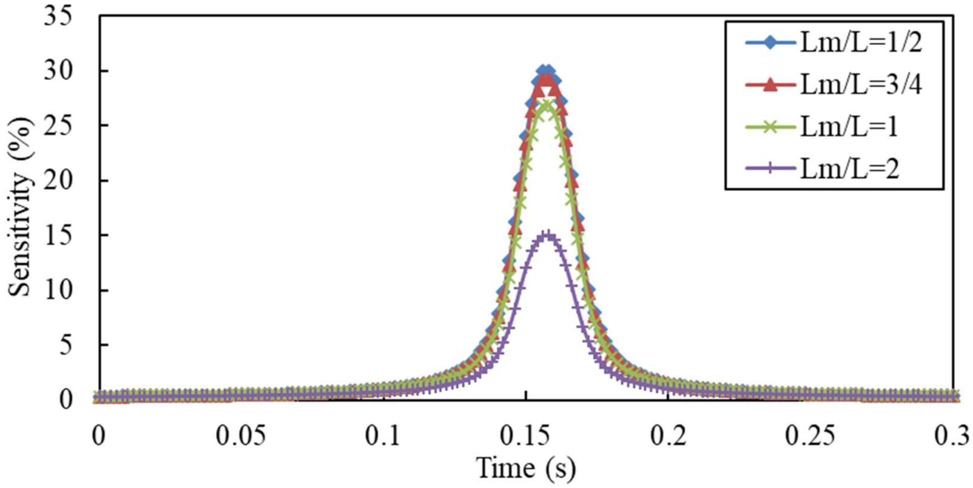

Figure 3.15 Spatial sensitivity for variable marker Length L_m (ω=10 rad/s).

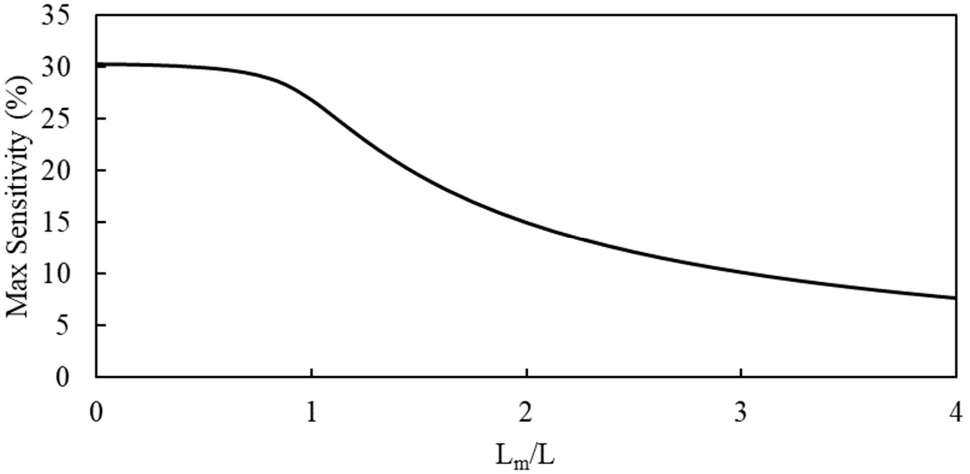

Figure 3.16 Maximum sensitivity for variable marker Length L_m (ω=10 rad/s).

In the case that δ_{Lm}= 0 (Arc charge), $A = \delta_{Wm}$ the effect of the marker width on the spatial sensitivity is obtained and shown in Figure 3.17 and 3.18. As expected, the spatial sensitivity decreases accordingly with the width of the marker δ_{Wm}. Moreover, δ_{Wm} affects the maximum sensitivity more significantly than the length , especially for δ_{Wm}<1, because of the circular curve of the marker cross section, which reduces from 30.25 % to 29% as W_m/W increases from 0 to 0.5.

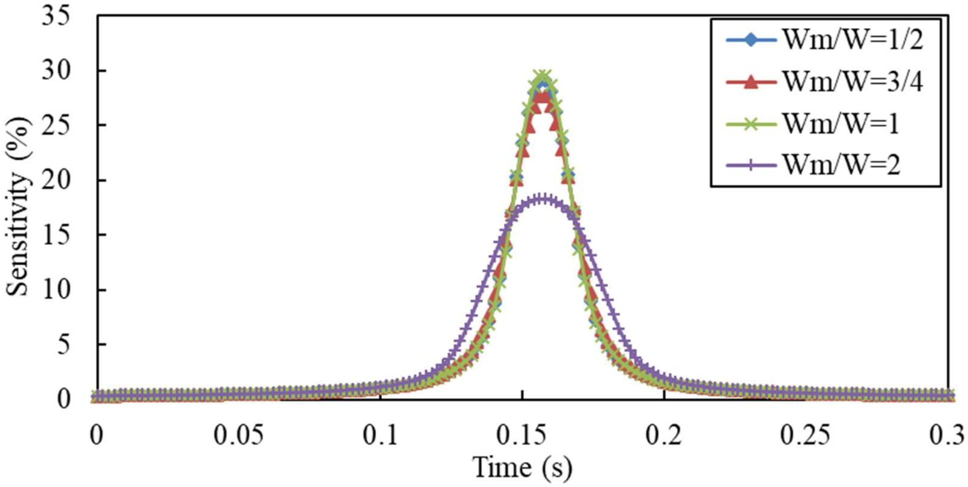

Figure 3.17 Spatial sensitivity for variable marker width W_m (ω=10 rad/s).

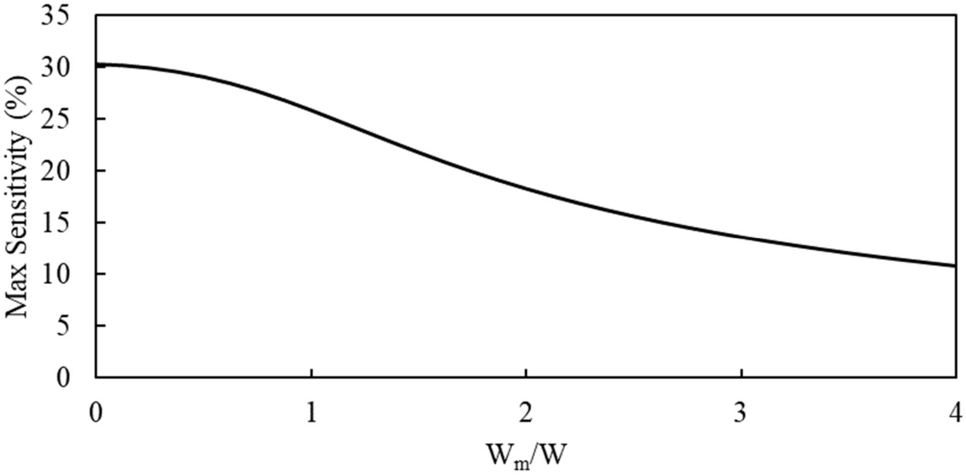

Figure 3.18 Maximum sensitivity for variable marker width W_m (ω=10 rad/s).

3.5.2 Impulse Response

The physical model of the sensing system for rotational speed measurement consists of an insulated strip-shaped electrode connected to a signal conditioning circuit with an input resistance R_i. The actual output voltage signal and the induced charge are related according to the following equation

$$u(t) = R_i \frac{dQ}{dt} \tag{3.20}$$

where *u(t)* is the output voltage and *Ri* is the input resistance of the conditioning circuit. Figures 3.19, 3.20, 3.21 and 3.22 illustrate the output signal and the corresponding power for variable length and width of the marker.

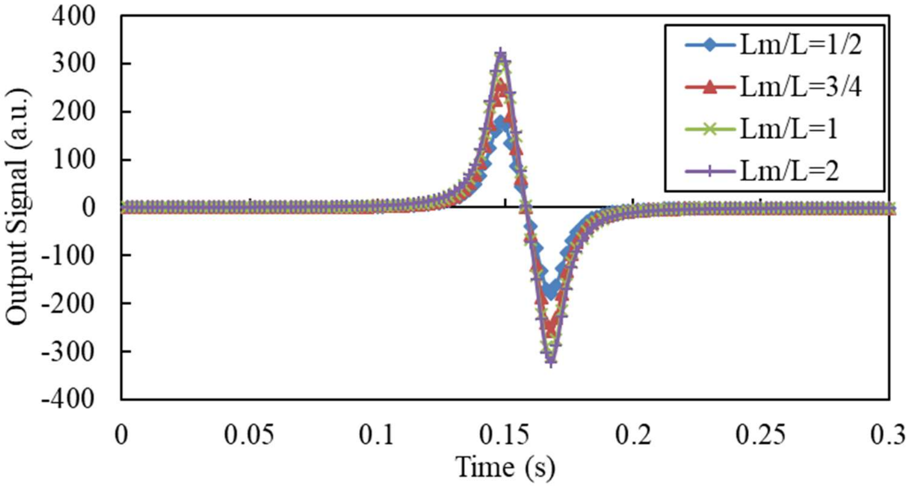

Figure 3.19 Output signal of the sensor for variable marker length L_m/L (ω=10 rad/s).

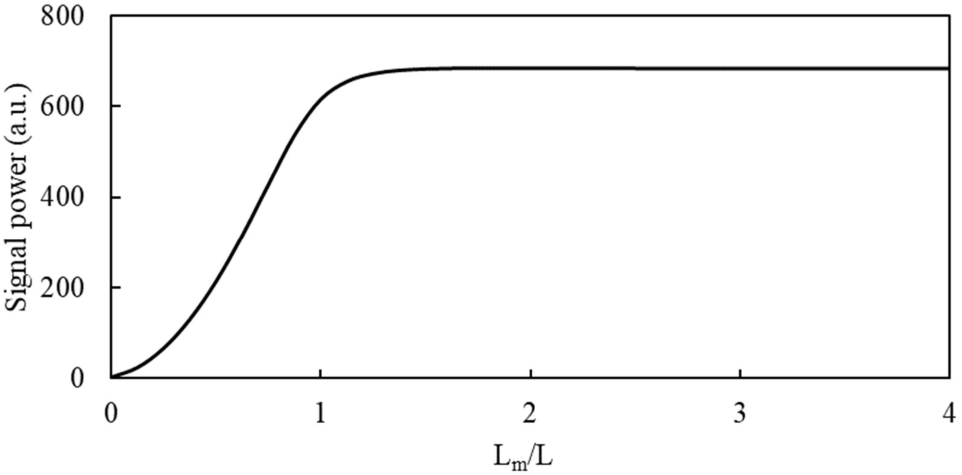

Figure 3.20 Maximum signal power for variable marker length *L_m/L* (ω=10 rad/s).

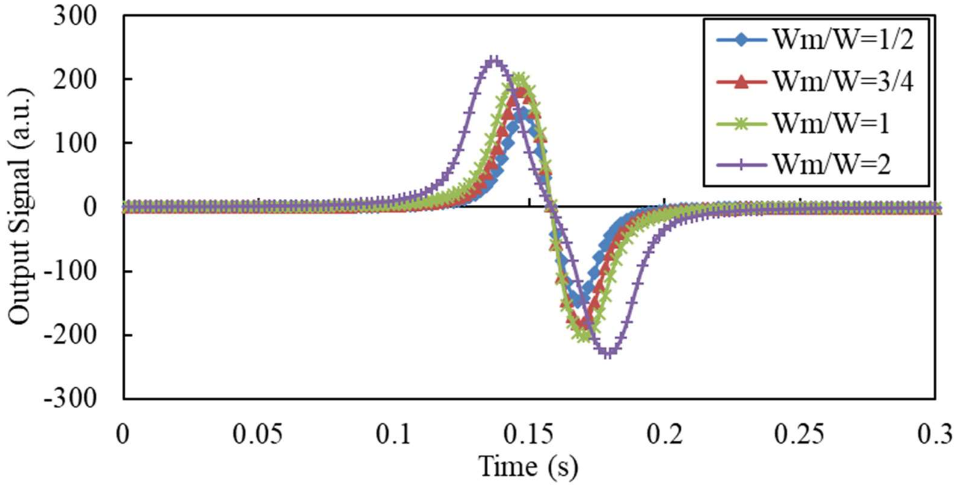

Figure 3.21 Output signal of the sensor for variable marker length *W_m/W* (ω=10 rad/s).

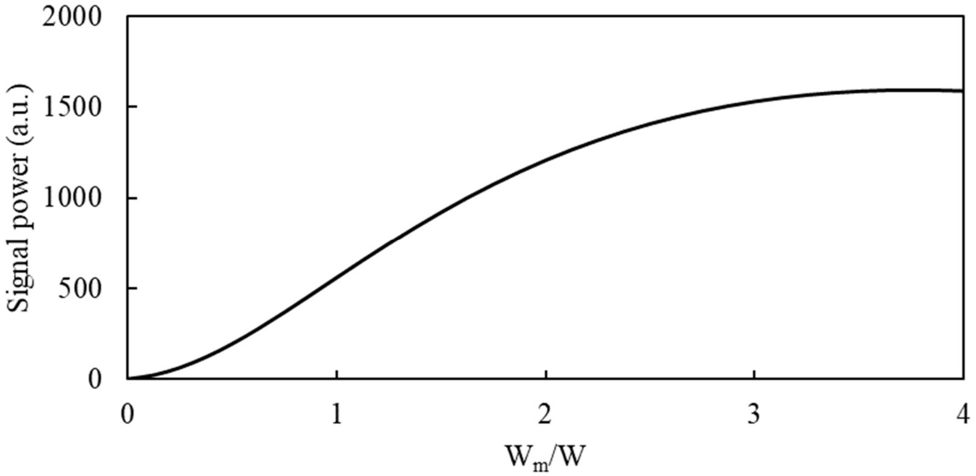

Figure 3.22 Maximum power for variable marker length W_m/W (ω=10 rad/s).

3.5.3 Sensing Zone

'Field of view' is an essential and significant characteristic for electrostatic sensors because the sensor only detects charge in the field of the sensing zone of the electrode. The electrostatic field of view used in Morris's work [77] was defined as the measurable maximum range in space detected by the electrostatic sensor when an inducing charge passes through the sensing zone of the sensor electrode. The part of charge that is out of the range cannot be detected by the electrostatic sensor, thus is the 'blind area' of the sensor. Field of view is an important parameter that characterises the scope of a sensor and is used in this study to determine the maximum number of markers n_{Mmax} that can be fixed on the shaft surface.

Assuming a strip charge with dimensions $L_m x W_m$, fixed on the shaft surface and is passing through an electrode at a constant rotational speed, the corresponding charge induced on the electrode can be illustrated as in Figure (3.23), where a peak starts at p_1 when the level first rises above the baseline and ends at p_2 when the level returns to the baseline level. The duration from p_1 to p_2 is taken as the duration of charge passing the electrode t_p. The electrostatic field of view fv can thus be calculated by the following equation

$$fv = 2D\omega t_p \tag{3.21}$$

where ω the angular speed, D the diameter of the shaft and t_p the duration of charge passing the electrode. The duration t_p can be deduced using

$$t_p = t_{p2} - t_{p1} \tag{3.22}$$

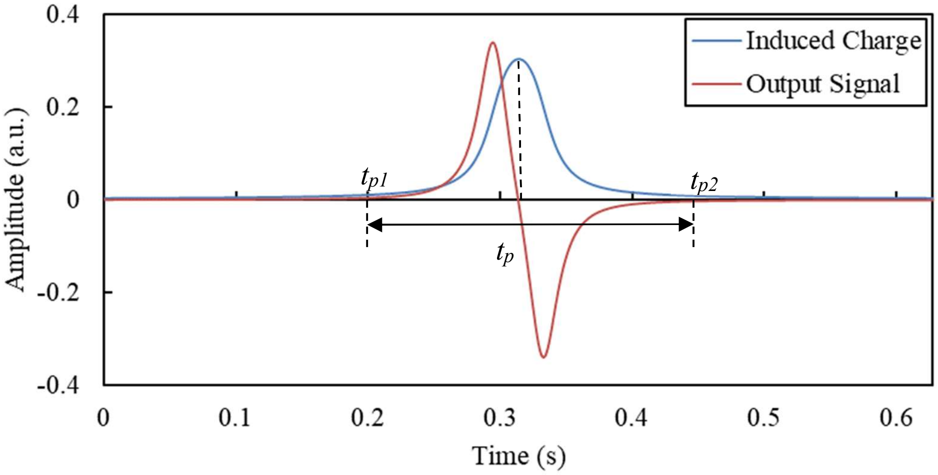

Figure 3.23 A typical induced charge and corresponding output signal within the sensing zone of the electrode.

The proposed measurement methods in this study require that the pulses, by which compose the electrostatic signal is composed, should not overlap, so that the characteristics of each pulse can be easily extracted and used in the signal processing. However, the maximum t_p corresponds to the minimum angular speed ω_{min}. The total duration of the n markers is

$$T = \frac{2\pi}{\omega} = n_{m\max} t_{p\max} \tag{3.23}$$

where n_{mmax} is the maximum number of markers and T the transit time over one rotation of the shaft.

Thus, the maximum number of markers that can fit around the shaft is given by

$$n_{m\max} = \frac{2\pi}{\omega \cdot t_{p\max}} \tag{3.24}$$

3.5.4 Frequency Response

The power spectrum $S_h(f)$ of the output signal $u(t)$, can be determined by the Fourier transform of its autocorrelation function R_{hh}

$$S_h(f) = \int_{-\infty}^{+\infty} R_{hh}(t) e^{-j2\pi f t} dt \tag{3.25}$$

The analytical solution to the Equation (3.25) is very complex, a numerical method is thus used instead to obtain the spectrum and the bandwidth of the signal $u(t)$.

Figures 3.24 and 3.25 show the power spectral density and bandwidth of the output signal for variable width and length of the marker, respectively. It is clear that the electrostatic sensor acts as a low-pass.

The effect of the marker dimensions on the frequency response and bandwidth of the output signal is obtained for δ_{Wm}= 1/2, 3/4, 1, 2, δ_{Lm}= 1/2, 3/4, 1, 2 and ω=10 rad/s.

Figures 3.24, 3.25, 3.26 and 3.27 indicate that a larger and longer marker results in higher power spectrum amplitude. Moreover, the amplitude of the power spectrum increases more rapidly with the length than with the width of the marker. In fact, the length of the marker has no influence on the frequency response and bandwidth of the output signal because the line charge is rotating at the plane, which is perpendicular to the electrode. However, the width of the marker plays a more significant part in the frequency response. The frequency response becomes slower when δ_{Wm} increases and a larger δ_{Wm} yields a narrower bandwidth.

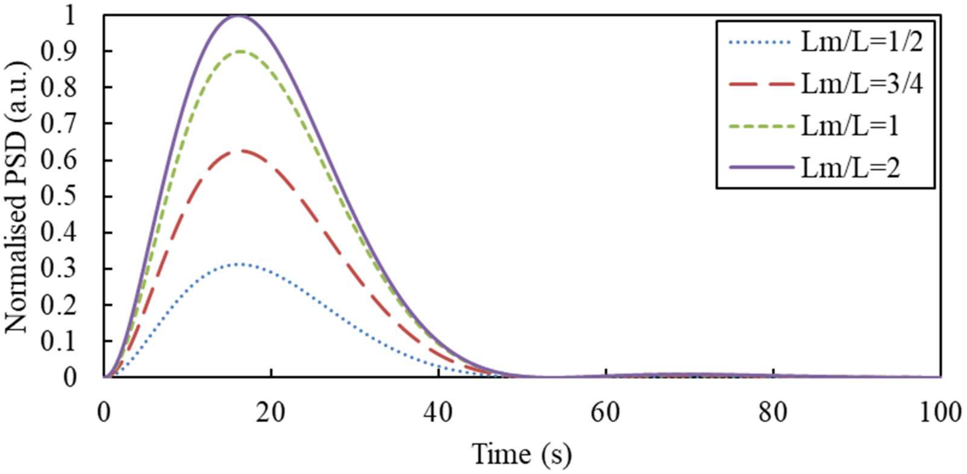

Figure 3.24 Normalised power spectral for variable marker length L_m.

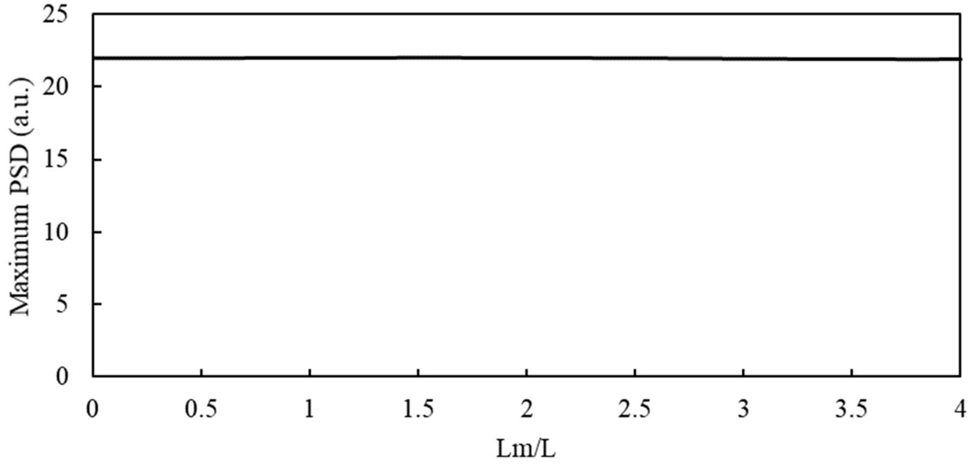

Figure 3.25 Signal bandwidth for variable marker length L_m.

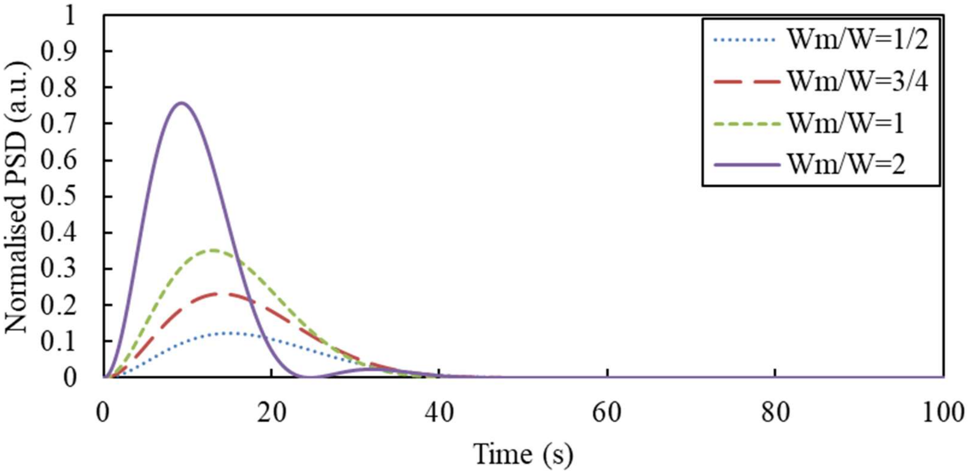

Figure 3.26 Normalised power spectral density for variable marker length W_m.

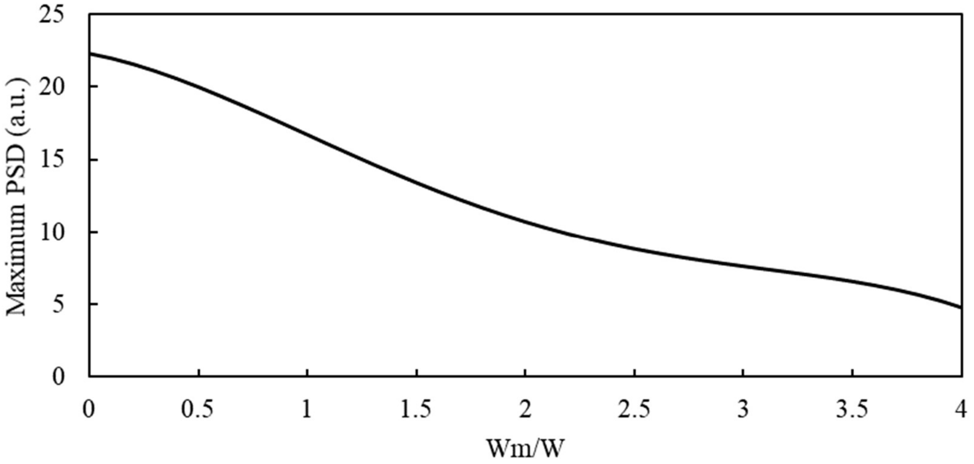

Figure 3.27 Signal bandwidth for variable marker length W_m.

3.6 Optimal Design of Electrodes and Markers

3.6.1 Optimal dimensions of the electrodes

Based on this mathematical model of the strip electrostatic sensors established by Wang et al, the effect of the geometric dimensions of the electrode, on the performance of the sensor was analysed. Through the analysis of the modelling results, the optimal dimensions of the electrostatic sensors have been suggested in terms of higher spatial sensitivity, higher power spectral density and wider bandwidth. The optimal width of the electrode should be in the range of 0.05 to 0.1 of the rotor diameter. The length of the electrode should normally be in the range of 20 mm to 50 mm, depending on the size of the electronic signal conditioning board.

3.6.2 Optimal dimensions of markers

The analysis in sub-section (3.4) suggests that a longer marker yields a higher power spectrum until the length of the marker becomes equal to that of the electrode. When the length of the marker exceeds the length of the electrode, the increase in maximum power spectrum becomes insignificant. On the other hand, the sensitivity is not affected significantly for $\delta_{Lm=1}$. Therefore, the optimal length L_m of the marker would be equal to the length of the electrode.

The width of the marker (W_m) is a crucial parameter that affects both, the sensitivity and the bandwidth. A wider width gives a higher power spectrum but a lower signal bandwidth and lower sensitivity, implying that a trade-off has to be reached in deciding the optimal width of the marker. In consideration of the effects of W_m on the spatial sensitivity, bandwidth and power spectrum of the sensor's output, the optimal width of the marker is suggested to be between 0.4 and 0.6 of the electrode width.

3.7 Displacement of an Unbalanced Shaft

3.7.1 Displacement effect on the frequency response

The effect of the displacement on the frequency response is investigated for a strip shape electrode, using different point charges, with the same magnitude, and rotating along circular trajectories of different diameters (Figure 3.28(a)). Subsequently, different trajectories result in different distances to an electrode (displacement), which is located at a fixed distance from the rotation centre.

Figures 3.28(b) and 3.29(c) show the signal outputs of the electrostatic sensor and the corresponding normalised spectra for two different point charges rotating at ω=12 rad/s, which is equivalent to 115 RPM.

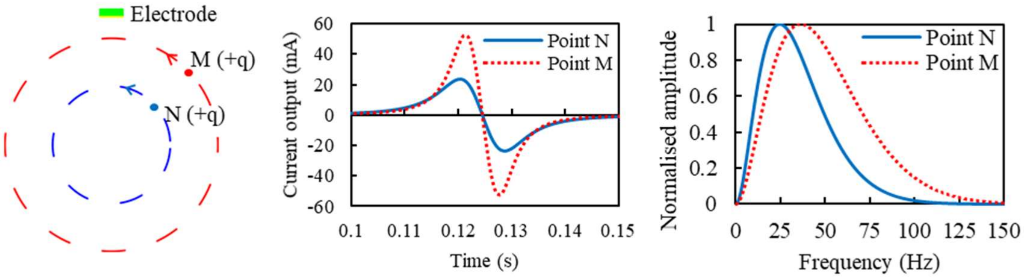

(a) Two point charges (b) Sensor output signals. (c) Spectra of output signals.

Figure 3.28 Sensor's output of two point charges in rotational motion and its corresponding spectra.

3.7.2 Characteristics of an unbalanced shaft

In general, all rotating machines produce some form of vibration which is a function of the machine dynamics such as imbalance, misalignment, bearing deterioration and mechanical looseness. There are three main parameters used to evaluate the vibration characteristics of any dynamic system: displacement, velocity and acceleration. Imbalance is the most common mechanical fault and source of vibration in rotating equipment. Shaft imbalance is a condition in which the centre of mass of the shaft is not coincident with the centre of rotation. A static imbalance is a condition of imbalance where the central principal axis of inertia is displaced in parallel with the axis of rotation, as shown in Figure 3.29 [1], [3], [58].

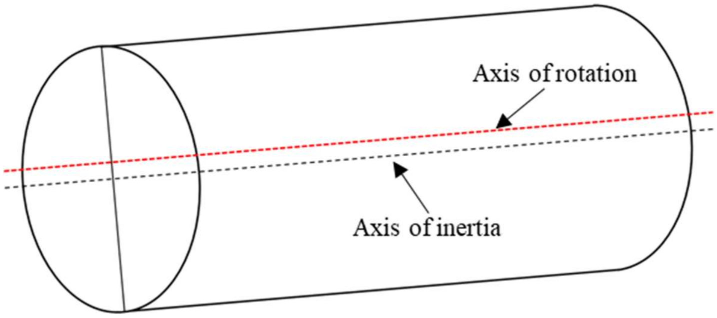

Figure 3.29 Static imbalance of shaft in rotating machines.

This study is concerned with the static imbalance fault which can be determined from the radial vibration of the shaft through instantaneous displacement measurement of the shaft surface with respect to a non-moving reference point.

The vibration due to shaft imbalance can be determined through the displacement measurement of the shaft surface with respect to a fixed position (the sensor). However, it is essential to establish a mathematical model of the shaft displacement. Figure 3.30 shows the geometrical model of an unbalanced shaft in rotational motion when an electrostatic sensor is used. The simulation results from the mathematical model of the shaft displacement will be used in the regression analysis in order to develop an estimated regression equation, which gives the displacement as a function of the frequency at the spectrum crest (f_{sc}). Additionally, the modelling results will be used to evaluate the accuracy of the regression model. The model is established with the following assumptions:

- An electrode is placed on the Y-axis, at distance (R_0+s_0) from the X-axis. The position of the sensor is considered as a fixed reference.
- The circle with diameter $2R_0$ represents a cross section of a metallic shaft.
- The rotation center *O*' of the circle is offset from the geometric center *O* by the distance *e*.
- The rotational motion of the circle about the center *O*' simulates an unbalanced shaft.
- The shaft and hence the circle is rotating at a constant angular speed $\omega = \theta / t$.
- The displacement *s* is the distance between the shaft surface and the sensor.
- The eccentricity *e* with respect to the radius *R* is relatively small ($e << R$).

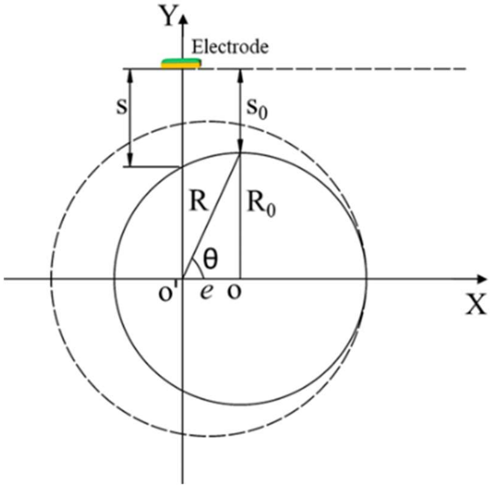

Figure 3.30 An unbalanced shaft.

From Figure 3.30, R_0 is given by

$$R_0^{\ 2} = R^2 + e^2 - 2eR\cos\theta \tag{3.26}$$

Rearranging equation (3.26)

$$R = e\cos\theta + \sqrt{e^{\ 2}\ \cos^2\theta - e^2 + R_0^{\ 2}} \tag{3.27}$$

As the sensor is located at a fixed distance from the X-axis, then

$$R_0 + s_0 = R + s \tag{3.28}$$

By substituting *R* from equation (3.27) to equation (3.28), the shaft displacement with respect to the sensor position can then be determined by

$$s = R_0 + s_0 - e\cos\theta - R_0\sqrt{1 - \frac{e^2}{R_0^{\ 2}}\sin^2\theta} \tag{3.29}$$

As $e << R$, then the displacement *s(θ)* can be approximated by

$$s(\theta) = s_0 - e\cos\theta \tag{3.30}$$

Since $\theta = \omega t$, equation (3.30) can be rewritten as

$$s(t) = s_0 - e\cos\omega t \tag{3.31}$$

where s_0 denotes the distance between the sensor and the normal shaft and *e* the eccentricity of the shaft.

Equation (3.31) implies that the displacement of an unbalanced shaft with respect to a fixed position could be approximated to a sinusoidal waveform, as illustrated in Figure 3.31.

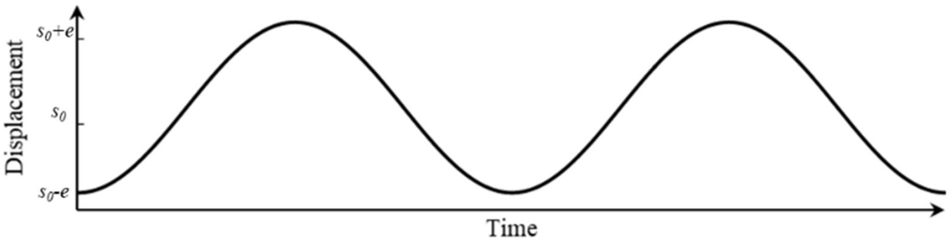

Figure 3.31 Displacement function of an eccentric shaft.

3.7.3 Estimation of the displacement function of an eccentric shaft

Equations (3.17), (3.20) and (3.25) implies that the spectrum of the output signal is a function of ω, s and D. For a rigid shaft supported on rigid bearings, the shaft displacement is independent of the shaft angular speed [58]. Since the bandwidth is proportional to the angular speed, then the frequency at the spectrum crest f_{sc} has a linear relationship with the angular speed. Moreover, the diameter D of each point on the eccentric shaft has a direct relationship with the displacement ($D + s = K$), where K is a constant (Figure 3.24). Thus, the frequency of the spectrum crest f_{sc} can be normalised to the angular speed and can be expressed as a function of the displacement s

$$fsc_{\perp} = \frac{fsc}{\omega} = F(s) \tag{3.32}$$

From equation (3.32), the displacement could be determined analytically as a function of the normalised frequency of the spectrum crest

$$s = F^{-1}(fsc_{\perp}) \tag{3.33}$$

The frequency at the spectrum crest is determined where the spectrum amplitude slope is equal to zero

$$\frac{d(|H_s(f)|)}{df} = 0\text{, at } f = f_{sc} \tag{3.34}$$

However, the analytical solution to equation (3.34) is very complex, a polynomial regression analysis is thus used instead to estimate the relationship between the two variables, the displacement s and f_{sc}.

From Table 3.1, the displacement s can be estimated as

$$s = p_3 \cdot f^3_{sc\perp} + p_2 \cdot f^2_{sc\perp} + p_1 \cdot f_{sc\perp} + p_0 \tag{3.35}$$

where p_0=0.00916; p_1=-0.006206; p_2=0.001786; p_3= -0.0001922; $f_{sc\perp} = \frac{f_{sc}}{\omega}$.

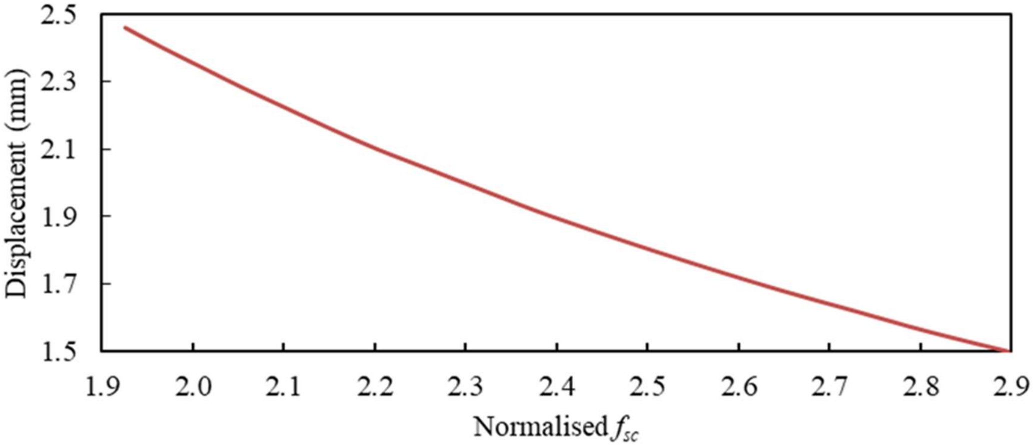

Figure 3.32 Relationship between displacement and normalised f_{sc}.

Table 3.1 $f_{sc\perp}$ at different displacements and diameters.

s (mm)	*D (mm)*	*Θ (rad)*	*fsc⊥*	*Fit std. error*
1.50	60.50	1.57	2.90	-0.16%
1.56	60.44	1.67	2.81	0.05%
1.62	60.38	1.76	2.73	-0.03%
1.68	60.32	1.86	2.65	0.05%
1.74	60.26	1.96	2.58	0.01%
1.80	60.20	2.05	2.51	-0.01%
1.86	60.14	2.15	2.44	0.00%
1.92	60.08	2.25	2.37	0.03%
1.98	60.02	2.34	2.32	-0.11%
2.04	59.96	2.44	2.26	-0.10%
2.10	59.90	2.54	2.20	0.07%
2.16	59.84	2.63	2.15	0.03%
2.22	59.78	2.73	2.10	-0.06%
2.28	59.72	2.83	2.06	-0.03%
2.34	59.66	2.92	2.01	-0.07%
2.40	59.60	3.02	1.97	0.00%
2.46	59.54	3.11	1.93	-0.02%

For an eccentricity of 0.5 mm (δ_e=1/120) and ω =100 rad/s (955 RPM), the displacement fluctuation is 1 mm, resulting in a variation in f_{sc} of 100 Hz (simulated result). Hence, the measurement sensitivity is 0.01 mm/Hz. If the signal is acquired over one second, then the measurement resolution would be 0.01 mm.

Using equation (3.35), displacement values can be estimated for each f_{sc}. It can be seen from Figure 3.33 that the displacement distribution of an eccentric shaft is similar to a sinusoidal distribution function, which agrees with the displacement function of an unbalanced shaft. At a given angular speed ω, the distribution of s can be fitted to a sinusoidal function. Hence, the displacement function can be written as

$$s(t) = A\cos\omega t + B \tag{3.36}$$

where A= -e, which denotes the eccentricity of the shaft and is unknown and B=s_0 which is a constant representing the displacement of a normal shaft.

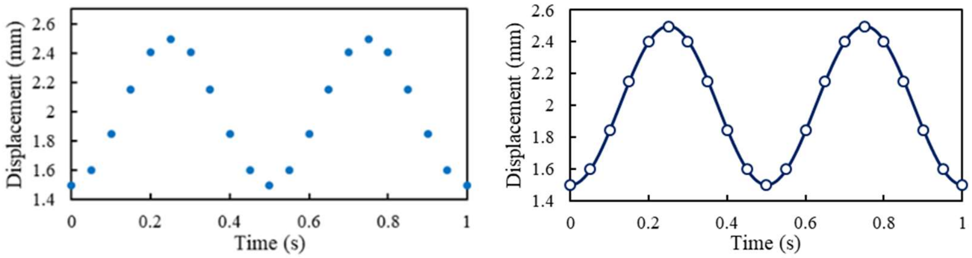

(a) (b)

Figure 3.33 Displacement values and its fitted curve. (a) Displacement values over two rotations. (b) Fitted curve of the displacement distribution.

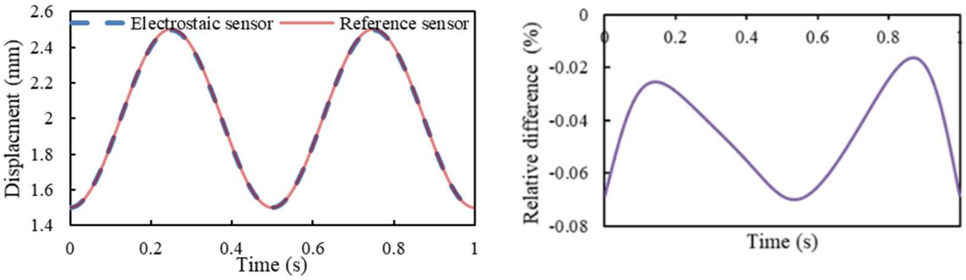

(a) (b)

Figure 3.34 Comparison of the displacement measurement and the relative difference between the electrostatic sensor and the simulated reference. (a) Compasrison of displacement measurments. (b) Relative difference.

Figure 3.34 shows a comparison between the reference simulation results and the modelling results. It is evident that the mathematical modelling results follow closely the reference simulation results, and the small discrepancy is due to the curve fitting errors. As a result, the property of the electrode in the frequency domain, being the frequency at the spectrum crest f_{sc}, has been used to establish a method to measure the instantaneous displacement of the shaft and hence the vibration of an unbalanced shaft is quantified.

3.8 Summary

This chapter has introduced the measurement principles of the rotational speed and vibration of metallic shafts using electrostatic sensors. The mathematical modelling has been established upon the electrostatic sensing mechanism. The established model is based on a strip charge simulating a strip charged marker rotating over the electrode. The strip charge can be considered as the collection of parallel line charges and a line of charge is the collection of point charges distributed along a straight line segment. Based on the developed model, spatial sensitivity, impulse response, sensing zone and frequency of the sensor have been quantified respectively through analytical modelling and numerical simulation. Moreover, the effects of physical parameters of the markers on the performance of the measurement system are analysed to obtain the optimised design of the markers.

Chapter 4

Design and Implementation of the Electrostatic Sensor Based Measurement System

4.1 Introduction

The following chapter presents a description of the electrostatic sensors based measurement system that was used to obtain the results described in chapter 5. The electrostatic sensors based measurement system combines sensing and processing capabilities for online rotational speed and vibration measurement of rotating shafts.

The system operates by acquiring the signal produced by the rotational motion of charges on the shaft surface (charged markers on the shaft) and using analogue and digital processing techniques to yield the rotational speed and vibration measurement of the rotating shaft.

The measurement system can be divided into subsystems to manage signal acquisition, signal conditioning and digital processing requirements.

The functional block diagram for the measurement system is shown in Figure 4.1. The electrode, acting as the sensing elements, generates induced charge or current in response to the rotational motion of the charged markers fixed on the shaft.

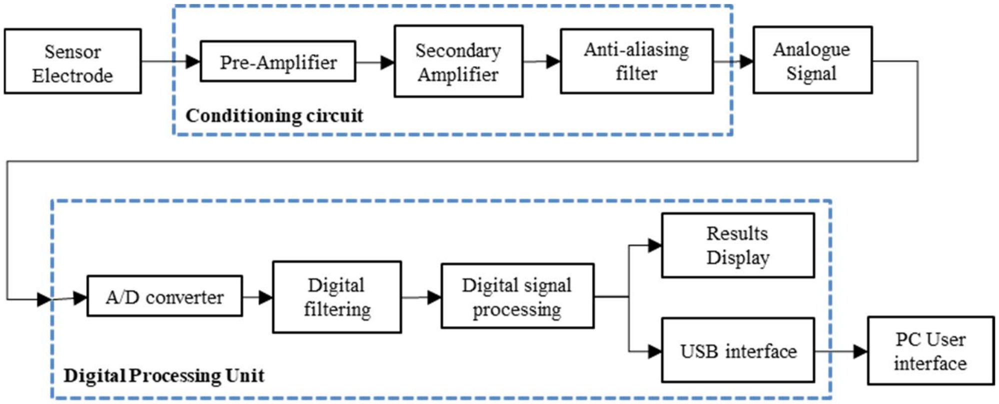

Figure 4.1 Functional block diagram of the measurement system

The signal conditioning circuit converts, amplifies and filters the induced charge or current into proportional voltage signal at a suitable level for A/D conversion. The digital sampling is performed by an embedded system, realized with an on-board microcontroller. The digital signal processing is also performed on-board and the results is displayed on a LCD. The digital signal is also sent to a PC user interface via USB connection to be processed by a bespoke software system which was developed using LabView in order to achieve an on-line measurement. This can provide additional flexibility and wider range of functionalities.

The following sections describe these processes in detail.

4.2 Markers Design

4.2.1 Electret Markers

Electrets are dielectric materials that are in a quasi-permanent electric polarization state (electric charges or dipole polarisation). They are electrostatic dipoles, equivalent to permanent magnets but in electrostatics, which are able to maintain electrostatic charges on their surface through time and can keep an electric field (and a surface voltage V_S) for years due to the charge trapping phenomenon [78]. Electrets are obtained by implanting electric charges into dielectrics. Theoretically, dielectrics do not conduct electricity. Therefore, the implanted charges stay trapped inside. Various electret fabricating processes have been proposed in the state of the art, among which, corona discharge is one of the most widely adopted technologies in both laboratories and industries [79]. Figure 4.2 shows a schematic and a device prototype of the corona charging setup. It consists of a point-grid-plane structure whose point is subjected to a strong electric voltage. This leads to the creation of a plasma, made of ions. These ions are projected onto the surface of the sample to charge, and transfer their charges to the dielectric layer's surface. The grid is used to limit the surface voltage V_S of the electret to a required value. Nevertheless, dielectrics are not perfect insulators and implanted charges can move inside the material or can be compensated by other charges or environmental conditions (dust, humidity), and eventually disappear. Therefore, it is primordial to choose stable electret materials to develop electret-based electrostatic sensors. Nowadays, a focal area of research on electrets concerns the charge stability [79]-[81]. However, Teflon®, Silicon Dioxide (SiO_2) and CYTOP are known as good electrets and are the most used electrets in electret-based energy harvesters [79] and in MEMS devices [82], [83].

In this work, Teflon® FEP is chosen as the electret material for its compatibility with large surface manufacturing, conformability and stability [84]. FEP has very high dielectric strength up to 2.6×10^8 V/m, much higher than the breakdown electric field of the air (3×10^6 V/m). Additionally, metal masking has been used to pattern the electret surface, especially for its simplicity of implementation [85]. A 127µm-thick FEP film glued on an Aluminium electrode and polarized by a Corona triode discharge has been used for the electret. The Corona discharge uses multiple points to polarize a large area. The copper metal mask, cut by laser etching, is placed at the surface of the electret during the charging process and electrically connected to the grid.

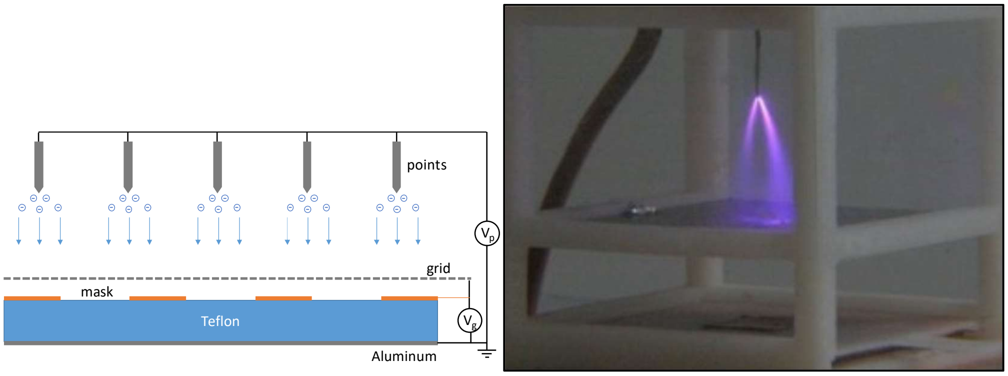

(a) (b)

Figure 4.2 Corona discharge device (a) Schematic and (b) Device prototype (CEA-LETI). Adapted from [79].

The electret is charged during 15 minutes with V_p=-16000V and V_g=-700V, where V_p is the voltage on the points and V_g the voltage on the grid. At the end of the charging process, the electret surface voltage is equal to V_g in the copper masks' holes and to 0 under the metallic parts.

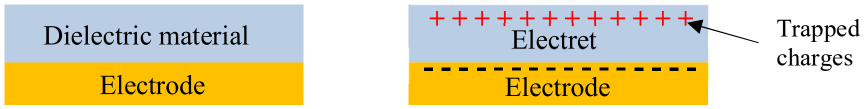

Figure 4.3 An electret film [79].

4.2.2 Generation of a Periodic Random Signal

The electrostatic signal is composed of a series of pulses as shown in chapter 3. Each pulse results from the rotational motion of a charged marker with respect to the electrostatic sensor. However, the pulse waveform and characteristics depend on the dimensions of the marker, for a given sensor arrangement. The width of the marker affects significantly the pulse width and thus the frequency response of the output signal. The length has no effect on the waveform but it affects the amplitude of the pulse.

Each resulting pulse corresponds to a specific marker on the shaft. Consequently, the signal waveform over one rotation of the shaft depends primarily on the distribution and positions of the markers. In order to generate a random signal over one rotation of the shaft, the positions of the markers on the shaft should be randomly distributed. Additionally, the dimensions and more specifically the width of the markers should also be chosen randomly.

To achieve a random distribution of the markers with random sizes, a pseudo-random code was developed in Matlab. The maximum width and the number N_{mmax} of the markers have been determined in sub-section 3.4. The length over which the marker will be distributed is equal to the perimeter of the shaft circumference.

Figure 4.4 is the flowchart of the basic structure for the pseudo-random code that was used to generate random positions and widths of markers.

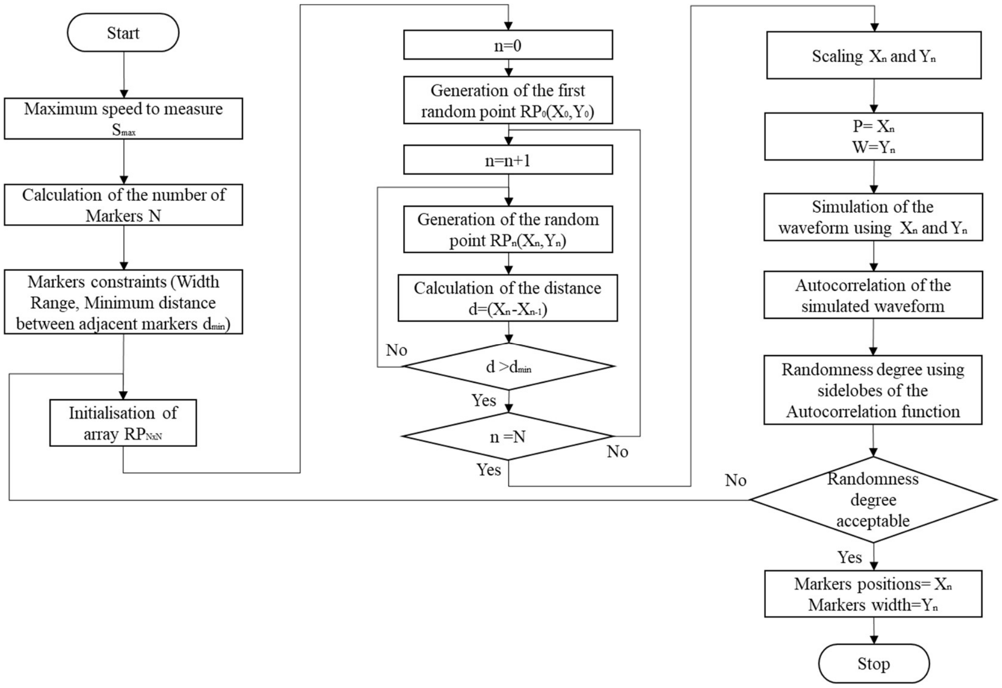

Figure 4.4 Flowchart of the pseudo-random code used to generate random positions and widths of markers.

Figure 4.5 shows a typical example of a random distribution of eight markers over the rotor circumference using the pseudo-random code in Figure 4.4.

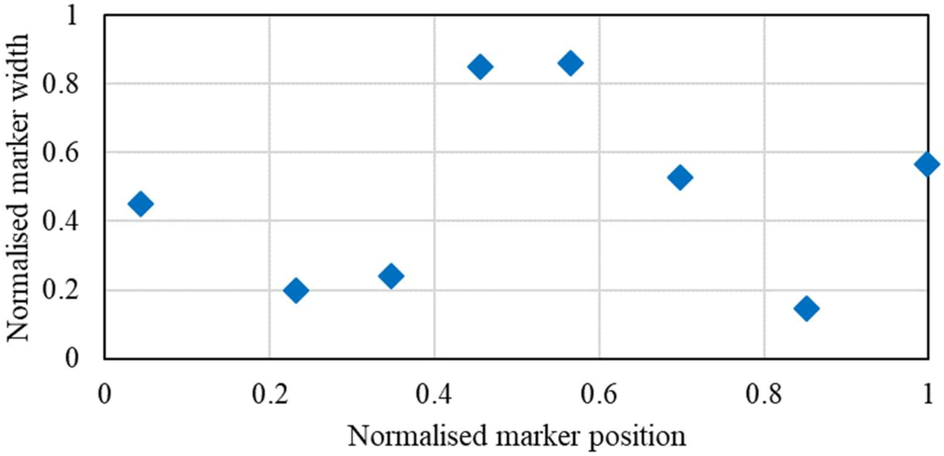

Figure 4.5 Example of pseudo-random distribution of eight markers.

In Figure 4.5 the normalised marker position is the distance of the marker from an origin position on the rotor circumference. The normalised marker width is the width of marker over the maximum width, which is determined in the sub-section 3.5.2. Figure 4.6 is the generated pseudo-random signal resulting from the markers distribution of the Figure 4.5 over one rotation.

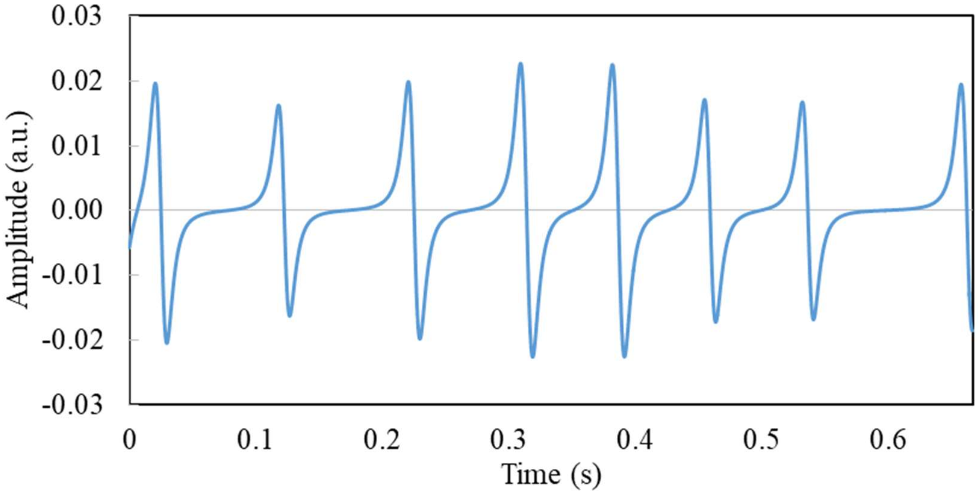

Figure 4.6 Resulting signal from the markers distribution in Figure 4.4 over one rotation (90 rpm).

Figure 4.7 and 4.8 show a typical example of a random periodic signal resulting from the distribution of eight markers and its corresponding autocorrelation function.

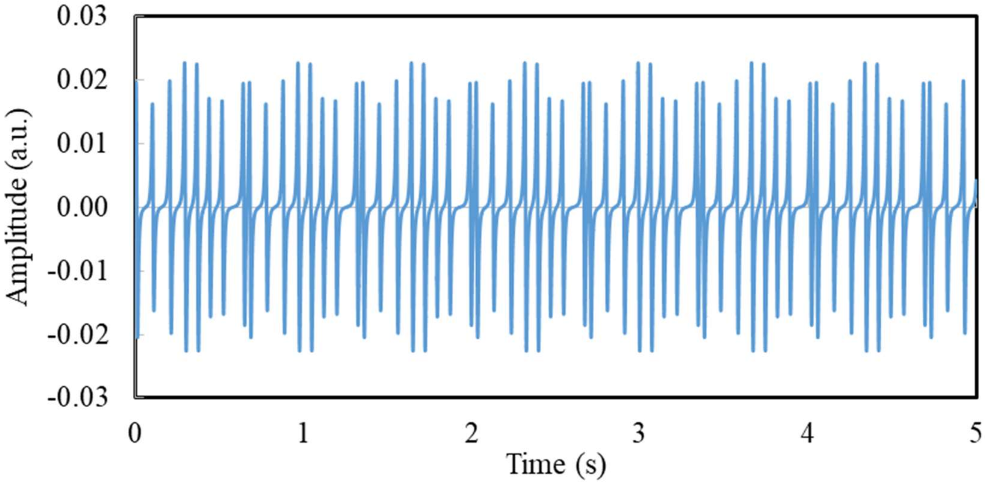

Figure 4.7 A typical example of a random periodic signal.

The autocorrelation function in Figure 4.8 is used to test the randomness of the generated signal. The dominant peak occurs after one complete rotation of the shaft indicating the periodicity of the signal, while the low sidelobes of the autocorrelation with respect to the peak at *t=0* confirms the randomness of the signal within a complete rotation of the shaft.

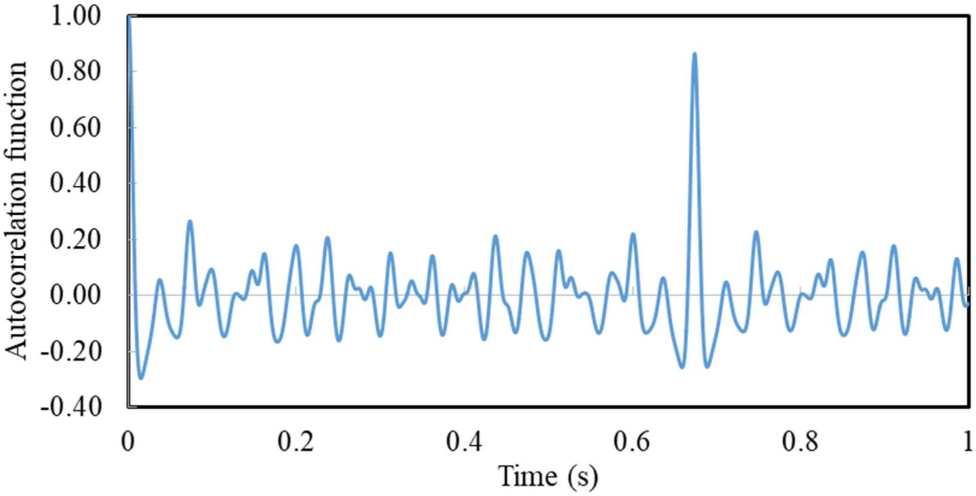

Figure 4.8 Autocorrelation of the generated signal in Figure 4.6 (90 rpm).

4.3 Signal Conditioning Design

4.3.1 Acquisition Methods of Electrostatic Signals

The signal conditioning circuit is designed to detect and measure the electrostatic charge on a rotating shaft surface. However, the signal conditioning circuit is dealing with a random and a small magnitude of charge resulting in a very weak induced current signal on the electrode (of the order of nA). A typical signal conditioning circuit for electrostatic sensor consists mainly of an analogue signal acquisition unit (preamplifier) and a signal amplifier. The acquired signal must be amplified before it can be converted to digital form, ideally to a voltage range large enough to make full use of the available A/D converter resolution. There are several ways how this can be accomplished, which are discussed in the subsequent sections.

4.3.1.1 Voltage amplifier

The most obvious way to amplify the signal is to use a straightforward voltage amplifier. In this case, a high input impedance amplifier is used to detect the voltage induced on the electrode by a nearby charge on the shaft surface. The solution of Poisson's equation

$$\nabla^2\Phi = -\frac{\rho_q}{\varepsilon_0} \tag{4.1}$$

With appropriate boundary conditions governs the voltage, Φ, induced on an electrode due to the presence of free charge, ρ_q, in a dielectric medium and where ε_0 is the permittivity of free space. If the sensor electrode is connected to the input of an amplifier with a very high impedance, then this voltage can be amplified directly to obtain a voltage level appropriate to the A/D converter [86], [87]. There are, however, several factors that must be taken into consideration when using this method.

Firstly, the voltage induced on the electrode is small, and the effective output impedance of the signal source is very high, as any current leaking from the electrode rapidly reduces the voltage induced by a charge. This means that the finite input impedance of a practical amplifier will degrade the signal by leaking away the voltage through the internal impedance of the amplifier. In addition, the various input capacitances must be considered in the electrode output. The effect of these capacitances has been analysed in detail [88], but the calculations require that input capacitances are known in advance. In practice, this is difficult to do accurately and estimates must usually be made, with their associated errors.

4.3.1.2 Charge amplifier

The charge amplifier is a variation of the inverting amplifier with a charge source instead of a voltage source. It is, however, important to note that the charge amplifier does not amplify the charge itself, but instead produce an output voltage proportional to the input charge. In that way, the charge amplifier can be considered as a charge-to-voltage converter. Charge amplifiers can be used in the measurement of induced electrostatic charge on the electrode which can be converted into voltage. Common applications of charge amplifiers include amplification of signals from devices such as piezoelectric sensors and photodiodes, in which the charge output from the device is converted into a voltage. Charge amplifiers are also used in the readout circuitry of CCD imagers and flat-panel X-ray detector arrays [89]. The amplifier is able to convert the very small charge stored within an in-pixel capacitor to a voltage level that can be easily processed.

The basic schematic diagram of the charge amplifier circuit is shown in Figure 4.9. The induced charge signal Q_{in} is the total induced charge on the electrodes, and V_{out} the output of the charge amplifier circuit is a voltage signal.

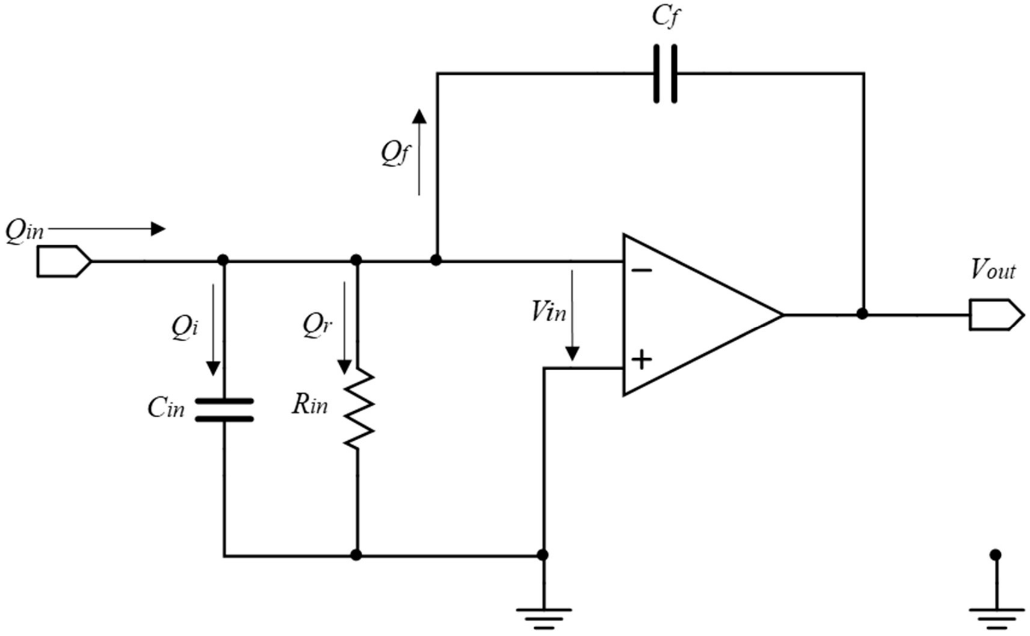

Figure 4.9 Charge amplifier.

In Figure 4.9, C_{in} is the sum of the electrode capacitance and the input capacitance of the operational amplifier. While R_{in} represents the total insulation resistance at the input. V_{in} is the voltage between the two inputs of the op-amp. Assuming that R_{in} is very high, from the Figure 4.9, the amount of the input charge can be described as,

$$Q_{in} = Q_i + Q_f \tag{4.2}$$

And since $Q = VC$, the above equation can be written as,

$$Q_{in} = V_{in} C_{in} - V_f C_f \tag{4.3}$$

If the open-loop gain of the op-amp is large enough, then V_{in} =0 can be obtained. The input charge only charges the feedback capacitor C_f, and the voltage of Capacitor C_f is equal to V_f. Then the output of the charge amplifier V_{out} circuit is

$$V_{out} = V_f \tag{4.4}$$

Combined with Equation (4.3), Equation (4.4) can be written as

$$V_{out} = -\frac{Q_{in}}{C_f} \tag{4.5}$$

Therefore, theoretically the output voltage of the charge amplifier circuit is in direct proportion to the input charge and is inversely proportional to the feedback capacitance, and it has nothing to do with the other elements of the circuit. The high frequency characteristics of the circuit are mainly related to the open-loop frequency response of the Op-amp. Consequently, the upper-frequency limit of the pass band is determined by the open loop bandwidth of the operational amplifier.

However, the ideal circuit shown above is not a practical design for a number of reasons. Practical op-amps have a finite open-loop gain, an input offset voltage and input bias currents. This can cause several issues for the ideal design; most importantly, if V_{in}=0, both the output offset voltage and the input bias current can cause current to pass through the capacitor, causing the output voltage to drift over time until the op-amp saturates. To counter this, a large resistor R_f is inserted in parallel with the feedback capacitor, as shown in Figure 4.9. Subsequently, the feedback resistor R_f bleeds the charge off the capacitor C_f at low frequencies to prevent the amplifier from drifting into saturation. Resistor R_f also provides a DC bias path for the negative input.

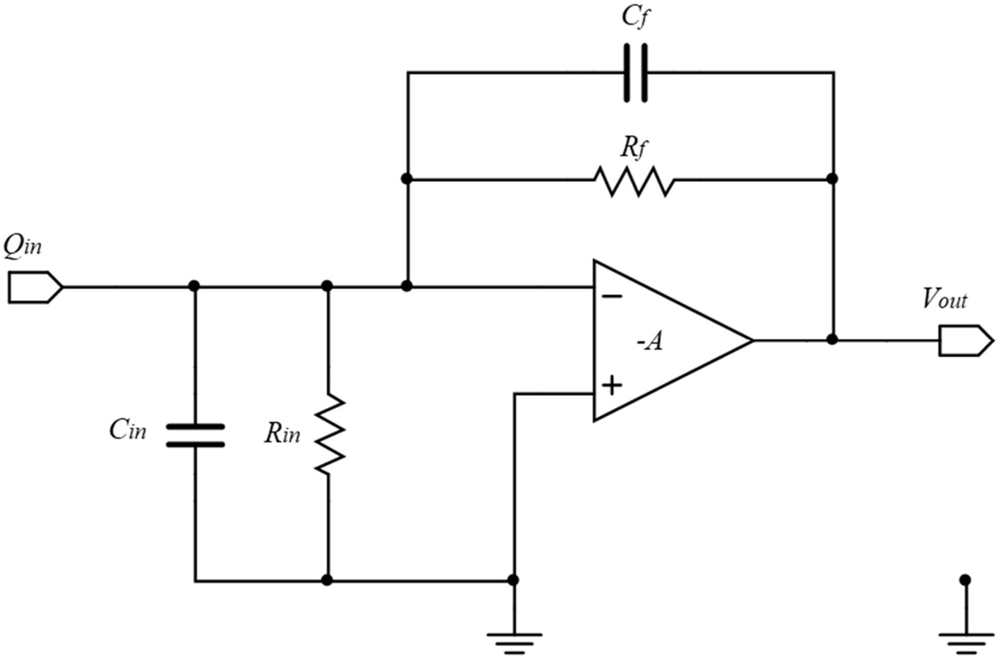

Figure 4.10 Practical circuit of a charge amplifier.

From the equivalent circuit in Figure 4.10, the output voltage V_{out} of the charge amplifier is expressed as

$$V_{out} = -\frac{Q_{in}}{\left(1+\frac{1}{A}\right)\left(C_f + \frac{1}{j\omega R_f}\right) + \frac{1}{A}\left(C_{in} + \frac{1}{j\omega R_{in}}\right)} \tag{4.6}$$

For a very large open-loop gain ($A > 10^6$), Equation (4.6) can be simplified into

$$V_{out} = -\frac{Q_{in}}{C_f + \frac{1}{j\omega R_f}} \tag{4.7}$$

As can be seen from Equation (4.7), the effect of the input capacitance and resistance on the output voltage is negligible. It is also noticeable that the feedback capacitor and resistor form a *RC*-high-pass filter, suggesting that the integrating behaviour at low frequencies is suppressed by R_f. The cut-off frequency of the filter is given by,

$$f_c = \frac{1}{2\pi C_f R_f} \tag{4.8}$$

The feedback resistor does not affect the gain. Thus, the C_f value can be chosen according to the required gain, then R_f value can be identified that creates an appropriate frequency response.

The frequency response of a practical charge amplifier is shown in Figure 4.11.

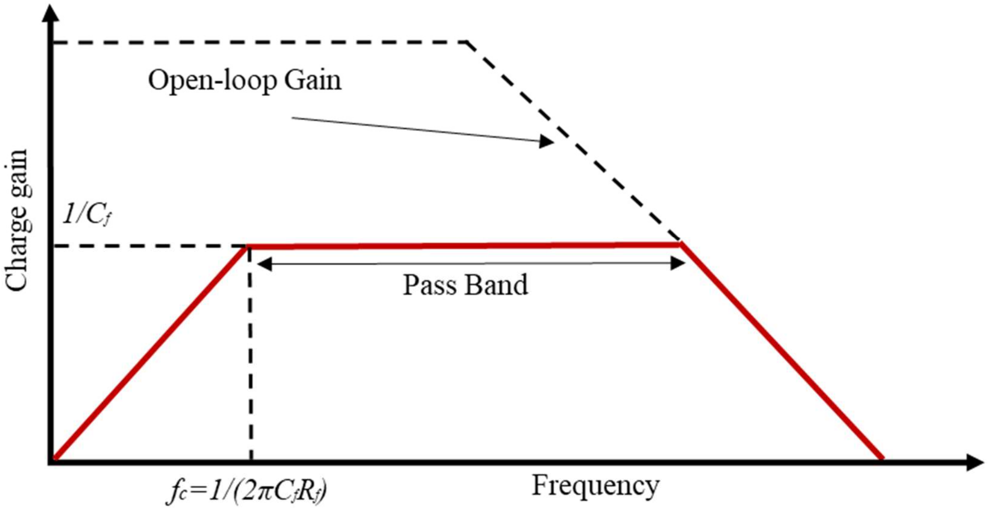

Figure 4.11 Frequency response of a practical charge amplifier.

The gain of the practical amplifier increases from 0 Hz to the low frequency cut-off point, f_C at 20dB/decade as the frequency increases. Beyond f_c, all frequencies are pass band frequencies with a constant gain $1/C_f$. while the upper-limit frequency is determined by the closed loop bandwidth of the op-amp. Therefore, the charge amplifier operates at frequencies greater than the cut-off frequency f_c where actual integration of the input signal is possible. The lower frequency components below f_c are subject to lower gain and distortion as a result of the high pass filtering effect.

In order to improve the low-frequency response, the cut-off frequency should be decreased. This could be achieved by increasing the value of R_f. In this case, the bias current of the amplifier can cause problems with large values of R_f because of the large offset voltages which may occur. The low frequency response can also be extended by increasing C_f but this has the side effect of reducing the gain and worsening the system signal to noise ratio. While the upper cut-off frequency is relatively high, it is limited in practice by the ability of the resistor to discharge the capacitor.

Therefore, there is a trade-off between the gain and the resistor's ability to discharge the capacitor and provide a dc bias-current path for the inverting input terminal.

4.3.1.3 Current-to-Voltage amplifier

The signal induced on the electrode is time-dependent, as it responds to the continually rotating charge on the shaft surface. This change of charge with time, *dq/dt*, can be considered as an input current. To produce an output in the form of a voltage, a current-to-voltage amplifier can be used.

Current-to-voltage converters are among the most used circuits for many different applications. For instance, they are used to characterize solar cells [90], analyse material's electrical properties [91] and in AFM microscopes [92]. The industrial applications comprises the use in transducers, Ethernet connections [93] and fibre-optic communications [94].

Nowadays, the family of current-to-voltage converters is typically called Trans-Impedance Amplifiers (TIA).

Figure 4.12 shows a typical circuit of the current-to-voltage converter. I_{in} is a current source. The capacitance C_{in} is the sum of the source capacitance and the input capacitance of the operational amplifier, while the resistance R_{in} represents the input resistance of the current source and the operational amplifier. A resistor R_f is used in the feedback line connected across an inverting amplifier with an open-loop voltage gain of $(-A)$.

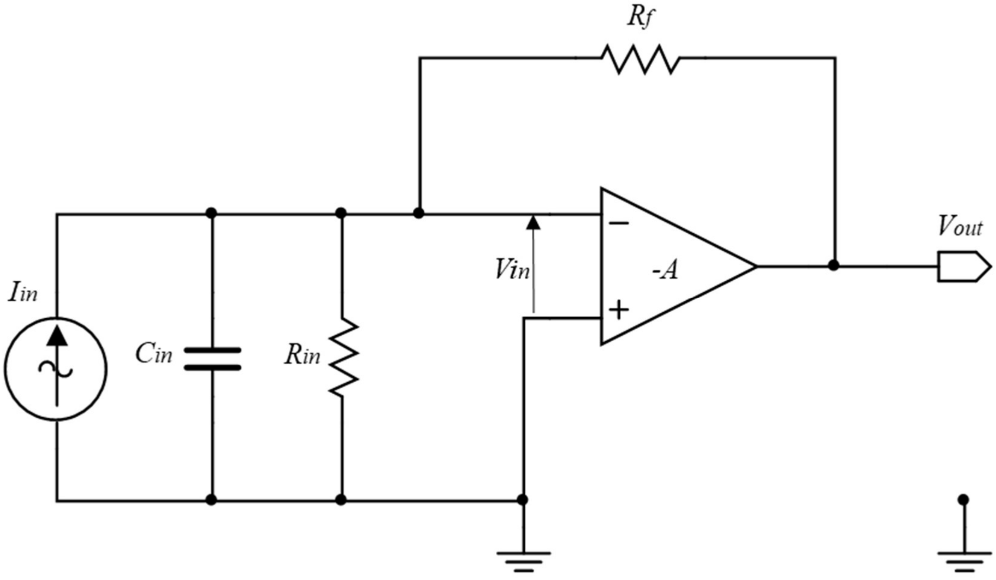

Figure 4.12 Current to voltage converter.

Let Z_{in} represent the parallel impedances of R_{in} and C_{in}. Then, using Kirchhoff's current law,

$$I_{in} = \frac{V_{in}}{Z_{in}} + \frac{V_{in} - V_{out}}{R_f} \tag{4.9}$$

Substituting, $Vin = -\frac{Vout}{A}$ into Equation (4.9), where -A is the open loop gain of the op-amp, gives

$$I_{in} = \frac{\left(-\frac{V_{out}}{A}\right)}{Z_{in}} + \frac{\left(-\frac{V_{out}}{A}\right) - V_{out}}{R_f} \tag{4.10}$$

Solving for V_{out} gives

$$V_{out} = -\frac{AR_f Z_{in} I_{in}}{AZ_{in} + R_f + Z_{in}} \tag{4.11}$$

At low frequency, an op-amp has a very high and approximately constant open-loop gain A. By inspection of (4.11), it is clear that for high values of A,

$$V_{out} = -R_f I_{in} \tag{4.12}$$

Therefore, by using a Trans-Impedance Amplifier, the input impedance at low frequency can be ignored.

However, at high frequency, the input capacitance can no longer be ignored. The input capacitance creates a pole in the frequency domain. To mitigate this effect, a small-value compensating capacitor (C_f in Figure 4.13) can be added in parallel with the feedback resistor to make the circuit stable.

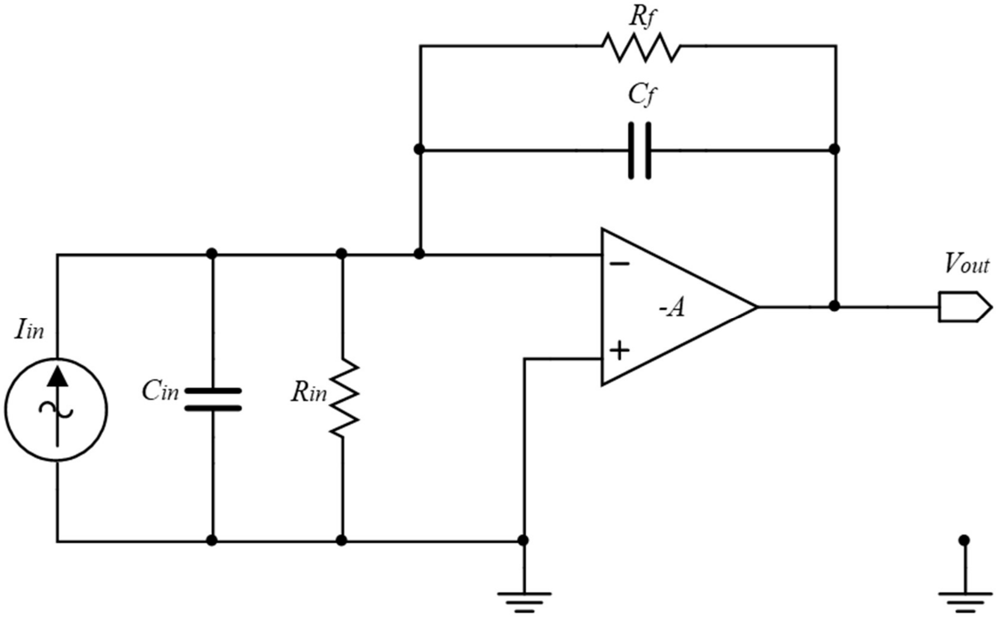

Figure 4.13 Practical circuit of current to voltage converter.

When this feedback capacitor is considered, the output of the amplifier becomes

$$V_{out} = \frac{-i_{in}R_f}{\left(1+\frac{1}{A}\right)\left(1+j\omega C_f R_f\right)+\frac{1}{A}\left(\frac{R_f}{R_{in}}+j\omega C_{in}R_f\right)} \tag{4.13}$$

If A>>>, V_{out} can be approximated to

$$V_{out} = \frac{-i_{in} R_f}{1 + j\omega C_f R_f} \tag{4.14}$$

While adding C_f to compensate the input capacitance and stabilize the circuit, it also introduces a pole in the frequency response of the amplifier at

$$f_c = \frac{1}{2\pi C_f R_f} \tag{4.15}$$

A decrease of C_f, however, will increase the bandwidth of the amplifier, but at the expense of the stability of the system. Therefore, the stability of the current-to-voltage converter is traded off for its bandwidth.

In order to improve the high-frequency response of the practical current to voltage converter, the value of C_f should be cautiously chosen. A compensation capacitor that is too small value may cause the system to exhibit a large overshoot and long ringing, or even self-sustained oscillations at high frequency. With a value too large, the bandwidth of the amplifier will be reduced and the system will respond slowly. In general the capacitor's value is determined empirically to reduce the pole's band-limiting effect.

4.3.2 Induced Signal Properties and Design of the Preamplifier

In general, the magnitude of the total charge induced on the electrode, at the highest sensitivity of the electrode, is in the range of nC. Consequently, the induced current resulting from the rotational motion of the charge is of the order of a few nA.

The A/D converter used to digitise the sensor output signals has an input range of 0 V to 3.3 V. This means that a large amplification is required ($G \sim 10^7$) in order to make full use of the available A/D resolution. Clearly, then, an amplifier is required to convert the sensor's signal into a usable signal.

The bandwidth of the input signal is primarily a function of the rotational frequency and also depends on the geometric parameters of the electrode and rotor. In this study, the rotational speed varies between 30 rpm to 3000 rpm. This means that the frequency of the electrostatic signal collected is around 50 Hz at the highest rotational speed.

Additionally, the mathematical modelling showed that, the electrostatic sensor electrode acts as a low-pass filter, thus suppresses the high frequency components.

In the previous section, different signal acquisition methods were investigated. According to the signal properties and the measurement requirements, the preamplifier topology and parameters can then be defined.

Voltage amplifiers are usually simpler in their design but suffer operational disadvantages when compared to charge and transimpedance amplifiers. There are several factors that must be taken into consideration such the dependency of the input impedance on the output voltage.

The two other methods, being the charge and the current amplifiers, seem to be more suitable for electrostatic sensors. The performance of these two amplifiers will be analysed and compared in order to select the best preamplifier topology for the conditioning circuit of electrostatic sensors.

Both circuits are adequately modelled by an operational amplifier with an *RC* feedback network as shown in Figures 4.9 and 4.12. However, the two circuit have exactly the same layout but they may behave differently depending upon the measurement conditions.

In the case of a TIA, the amplifier behaves as a current-to-voltage converter, however, in other circumstance; the exact same circuit could act as a charge-to-voltage converter (charge amplifier). Hence, it is of crucial to employ the adequate transfer function at the right conditions. Between all the measurement conditions, the frequency of the input signal is, likely, the most important parameter. If the input frequency is below the low pass band filter formed by $C_f R_f$, the circuit behaves as a TIA. However, if the frequency increases, the current gain of the topology decreases with a slope of -20 dB/decade and more importantly, a charge-to-voltage gain appears, the capacitor starts to dominate, as its impedance is very low at high frequency. The signal passes through the capacitor more than the resistor. Consequently, the amplifier begins to amplify charge rather than current as clearly shown in Figure 4.14, this gain is of special importance while measuring the input charge.

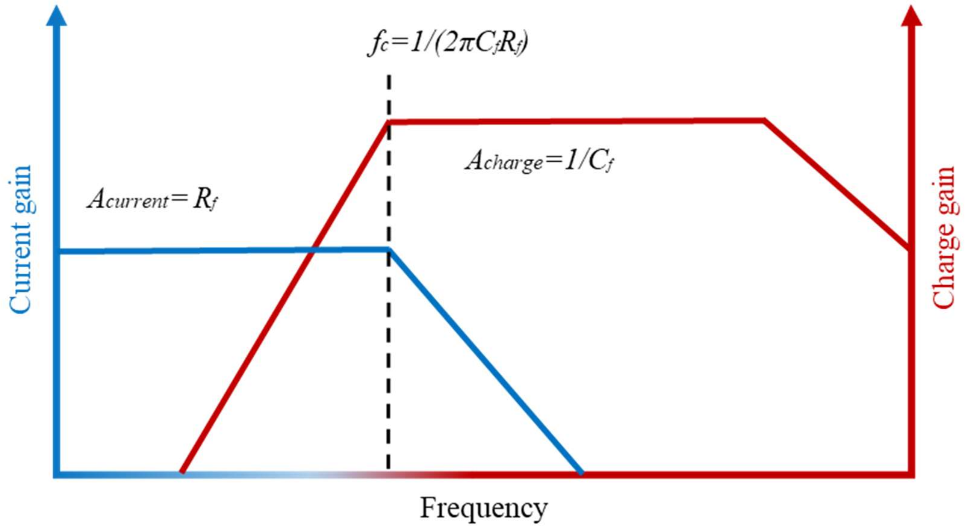

Figure 4.14 Current gain and Charge gain as a function of the frequency.

At low frequencies, the feedback capacitor can be considered as an open circuit, hence, almost no current flows through it. Consequently, if the current is primarily low frequency, the current will circulate through the feedback resistor at a gain R_f. However, the impedance of the feedback capacitor, decreases for higher frequency values. Hence, at higher frequency, some charges may start to flow throughout the capacitor path, as the capacitor impedance could reach the value of the resistor impedance. Consequently, as frequency increases, the amplifier may stop amplifying current and start amplifying charge. Table 4.1 presents a summary of the gains, bandwidth and signals to measure for each amplifier.

Table 4.1 Comparison between TIA and charge amplifiers.

Amplifier topologies			
	Converter type	**Simplified Output**	**Frequency range**
TIA	Current-to-Voltage	$V_{out}= -R_f I_{in}$	$0< f <1/2\pi C_f R_f$
Charge amplifier	Charge-to-Voltage	$V_{out}=-Q_{in}/C_f$	$1/2\pi C_f R_f < f$

Referring to the Figure 4.14 and Table 4.1, it can be concluded that the TIAs are more suitable for low pass signals while the charge amplifiers are more suitable for high pass signals.

4.3.3 Preamplifier Design

Since the induced signal is a low pass signal as shown in the signal analysis in sub-section 4.3.2, a TIA is used to design the preamplifier of the conditioning circuit to convert and amplify the induced signal. The preamplifier circuit is shown in Figure 4.15. In this circuit, the resistor R_f is used in parallel with the capacitor C_f in the feedback line to control the gain and frequency bandwidth. This creates a pole at $\omega=1/C_fR_f$, which rolls off the gain at high frequencies, increasing the stability of the amplifier.
The value of the resistor R_f in the feedback loop determines the gain of the amplification.

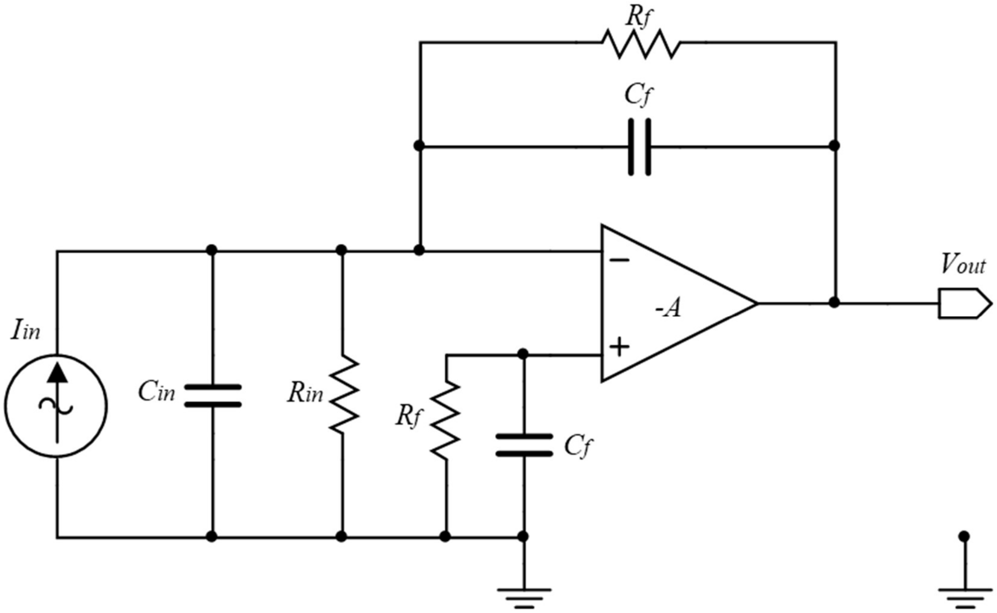

Figure 4.15 Circuit of the preamplifier.

The cut-off frequency of the circuit can be given as

$$f_c = \frac{1}{2\pi C_f R_f} \tag{4.16}$$

The resistor R_f biases the amplifier's gain. The capacitor C_f is open in low frequencies and current passes through R_f. In the frequency higher than f_c the C_f is dominant and efficiently reduces the output gain. The value of both feedback capacitor and feedback resistor can affect the amplifier frequency bandwidth. The resistor R_f is selected in a way that it produces the interested gain for the circuit; so, the bandwidth would be adjusted by selecting the suitable feedback capacitor.

One limitation of using the resistor in the feedback path, especially for large value, is the biasing current. In the amplifier, the flow of the input-bias-current through the feedback resistor creates an output voltage offset. The larger the gain resistor, the greater this effect. To minimise these effects, transimpedance amplifiers are usually designed with FET input Op-amps that have very low input offset voltage and input bias current. In addition, the same value of the resistor and capacitor can be used in the positive input of the Op-amp to prevent any possible offset voltage from amplification.

4.3.4 Voltage amplification stage

The output signal from the current-to-voltage amplifier may still be relatively weak to be sampled by an A/D converter. In addition, the output signal should make full use of the whole range of the A/D converter. Thus, it is suggested an adjustable-gain amplifier to be used as a second stage of amplification. The amplification gain of the first stage should be designed to amplify the highest available level of the induced signal to an interested level. Hereafter, the second amplifier with adjustable gain capability will be applied to amplify the output of the first stage to a level of interest.

The schematic of the amplification stages is shown in Figure 4.16.

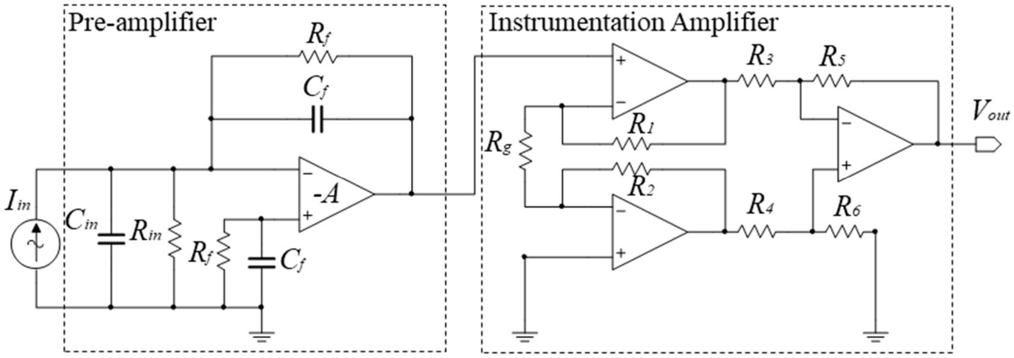

Figure 4.16 Two amplification stages of the conditioning circuit.

In this circuit, an instrumentation amplifier is added to the signal conditioning circuit to able the circuit to be used for a wider range of electrostatic signal detection and amplification. Triple Op-amp topology for instrumentation amplifier, in Figure 4.16 is an integrated circuit with three Op-amp and several resistors. Instrumentation amplifier amplifies the electric potential difference between its two inputs. It has a high common mode rejection, low output offset and high input impedance [95]. The first two integrated Op-amps of the instrumentation amplifier provide voltage gain as a non-inverting amplifier and the last Op-amp is a unity gain amplifier where in its integrated circuit $R_1=R_2$, and $R_3=R_4=R_5=R_6$. The most advantage of the instrumentation amplifier is its gain adjusting design. The gain G_{inst} can be adjusted only with a single external resistor Rg using the following equation

$$G_{inst} = 1 + \frac{2R_1}{R_g} \tag{4.17}$$

As can be seen from Figure 4.16, R_g is a key component in the circuit that controls the input to output impedance ratio, i.e. the magnification of the secondary-amplifier. In this design, a digitally controlled potentiometer (DS1844-100) is used to control the amplitude of the signal.

The total gain G of the signal conditioning circuit would be the multiplication of the gain in two stages, which is

$$G = \left(1 + \frac{2R_1}{R_g}\right) \cdot R_f \tag{4.18}$$

4.3.5 Voltage Reference

The induced signal is a bipolar signal while the A/D converter used for digitisation can only accept positive input voltages i.e., 0-3.3V, so the amplifier output voltage is required to swing about the midpoint of the converter range. Therefore, V_{ref} is used to bias the instrumentation amplifier between 0V and V_{DD} (V_{DD}=3.3V).

The reference voltage is generated using a simple resistive voltage divider network tapped off with the output determined by,

$$V_{ref} = \frac{R_8}{R_7 + R_8} V_{DD} \tag{4.19}$$

The resistors used in the voltage divider are high tolerance resistors (+-0.5%) and are matched during circuit construction. The schematic diagram for the V_{ref} circuit is shown in Figure 4.17. The V_{ref} output has to be as noise free as possible to ensure that it does not create additional noise in the sensor system. Capacitors C_1 and C_2 are used to eliminate power supply (V_{DD}) pick-up noise. An Op-amp is connected in a voltage follower configuration on the output of the voltage divider network. This is used to ensure a stable output voltage and remove any cross-coupling. The use of an Op-amp also allows higher values of resistors to be used in the voltage divider network to reduce power consumption.

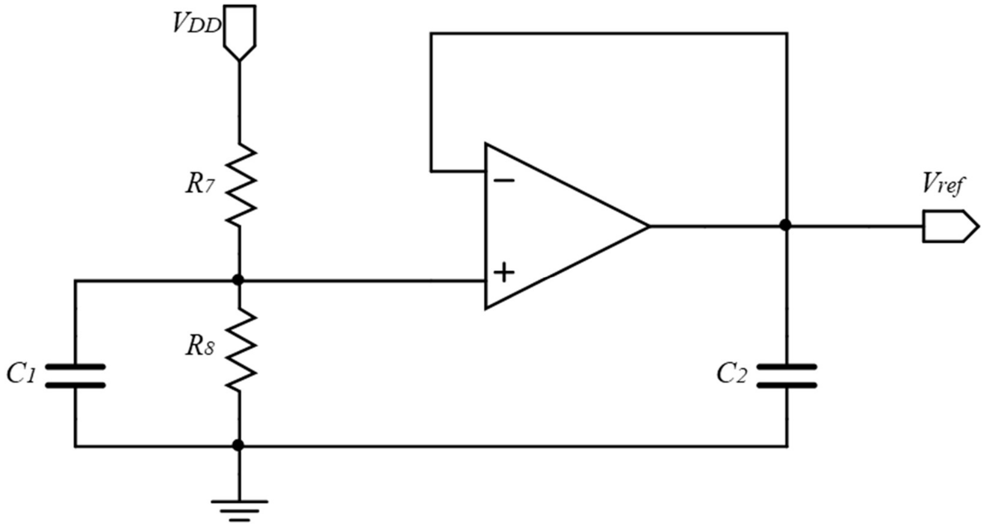

Figure 4.17 Voltage reference circuit.

4.3.6 Anti-Aliasing Filter

In order to conduct an accurate cross-correlation calculation of two digital signals, an essential step is to remove noises from the signals before they are sampled by an A/D converter. A Sallen-Key Butterworth second-order low-pass active filter is adopted to eliminate high-frequency noise in the signal as well as for the purpose of anti-aliasing [96]. Figure 4.18 shows the schematic diagram of the Sallen-Key filter.

As can be seen from Figure 4.18, an operational amplifier is used as a buffer, although the emitter follower is also effective. The transfer function *H(s)* for the filter shown in Figure 4.18 is

$$H(s)=\frac{(2\pi f_c)^2}{s^2+2\pi\frac{f_c}{Q_f}s+(2\pi f_c)^2} \tag{4.20}$$

where the cut-off frequency *fc* and Q_f factor are given by

$$f_c = \frac{1}{2\pi\sqrt{R_9 R_{10} C_3 C_4}} \tag{4.21}$$

$$Q_f = \frac{\sqrt{R_9 R_{10} C_3 C_4}}{C_4 (R_9 + R_{10})} \tag{4.22}$$

The Q_f factor is the key parameter in filter design, which determines the height and width of the peak of the frequency response of the filter. As Q_f increases, the filter will tend to "ring" at a single resonant frequency near the f_c. In order to achieve maximally flat pass band frequency response, the value of Q_f factor is set as 0.707. The transfer function of the filter can be rewritten as follows according to Equations (4.20), (4.21) and (4.22).

$$H(s) = \frac{1}{R_9 R_{10} C_3 C_4 s^2 + C_4 (R_9 + R_{10}) s + 1} \tag{4.23}$$

In order to avoid aliasing, the sampling rate should exceed twice of the cut-off frequency of the low-pass filter.

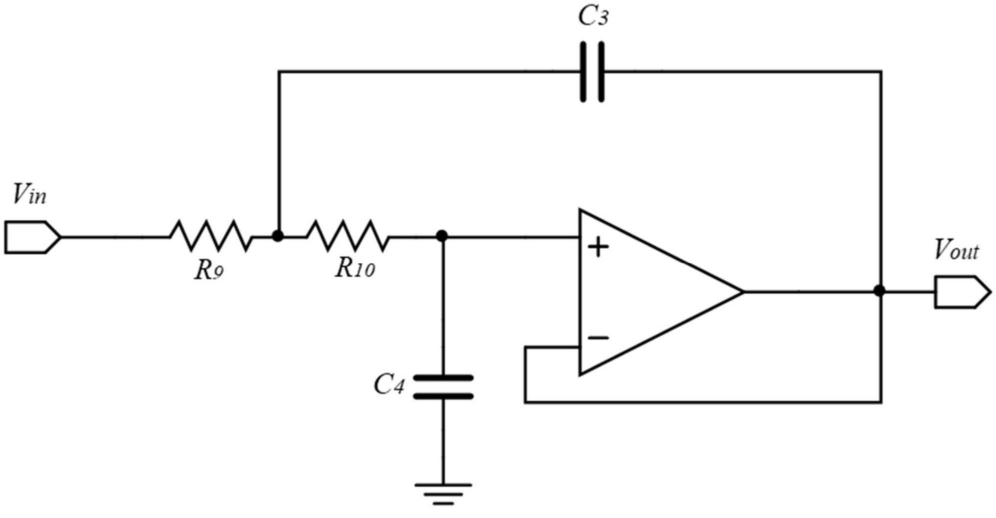

Figure 4.18 Anti-aliasing filter.

4.3.7 Simulation Results

4.3.7.1 Circuit simulation

The signal conditioning circuit is simulated with the Multisim simulator to investigate the circuit for its frequency bandwidth and gain. Figure 4.19 shows the signal conditioning circuit. The parameters of the signal conditioning circuit are optimized in Multisim.

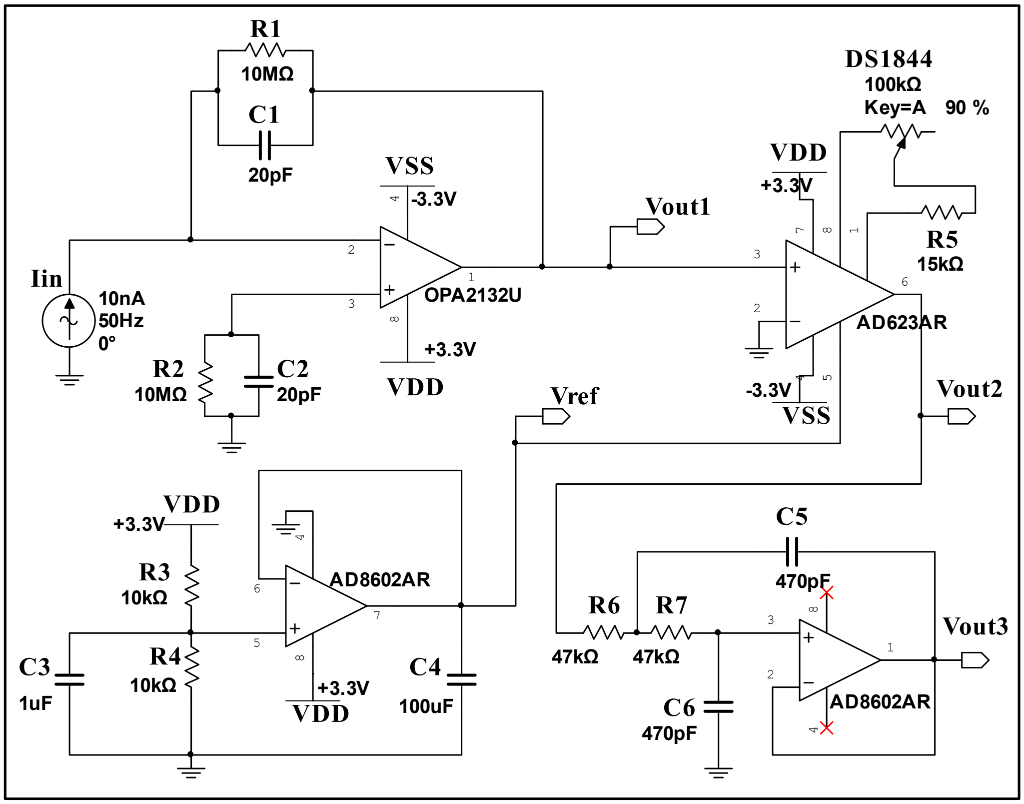

Figure 4.19 Schematic of signal conditioning circuit.

A 10 nA current source with 50 Hz frequency is selected simulating the induced current. A 10 MΩ resistor and a 20 pF capacitor are chosen for feedback resistor R_1 and feedback capacitor C_1. To compensate the effect of bias current the same value component in the feedback loop connected the non-inverting input of the Op-Amp to the ground. As it mentioned, the circuit model of the electrode is a high-output impedance source. To maximise the power transfer between the electrode and the signal conditioning circuit, a high input impedance FET amplifier, OPA2132 [97] is chosen for signal acquisition stage. The OPA2132 amplifier is a low distortion, low noise, FET-input Op-amp.

In the next stage, a high-accuracy instrumentation amplifier AD623 [98] is used as a second and adjustable amplifier. The amplifier has a low offset voltage of maximum 100 µV, and it has a gain equation accuracy of 0.5 %. The gain equation for this amplifier is given as

$$G_{inst} = 1 + \frac{50k\Omega}{R_g} \tag{4.24}$$

To prevent the saturation in the output voltage range, a 250 **Ω** resistor R_5 is used in series with digital potentiometer DS1844. The *Rg* in Equation (4.24) is provided to adjust the output voltage in the level of interest. The gain of the preamplifier is equal to the value of the R_1 (10^7).

From Equation (4.24) and values of *Rg*, the gain of the instrumentation amplifier changes from 1.43 when the digital potentiometer is set in maximum range to 201 when the potentiometer is adjusted to Zero. The total gain range of the proposed signal conditioning circuit can be given by multiplication of these two stages that is an adjustable value from $1.43\text{x}10^7$ to $201\text{x}10^7$.

From Equation (4.16), the frequency bandwidth of the circuit is determined by the feedback resistor R_1 and the feedback capacitor C_1. It is equal to 796 Hz, and it seems to be a suitable bandwidth for electrostatic sensor where the higher frequency of the electrostatic signal is not expected. Additionally, the electrostatic signal is further filtered by a Sallen-Key low-pass filter with a cut-off frequency of 7.2 kHz in order to allow the full range of the signal through without attenuation.

The frequency response of the circuit is provided using an AC analysis in Multisim is shown in Figure 4.20. It verifies the calculated gain and bandwidth of the system when the circuit is adjusted for the maximum gain.

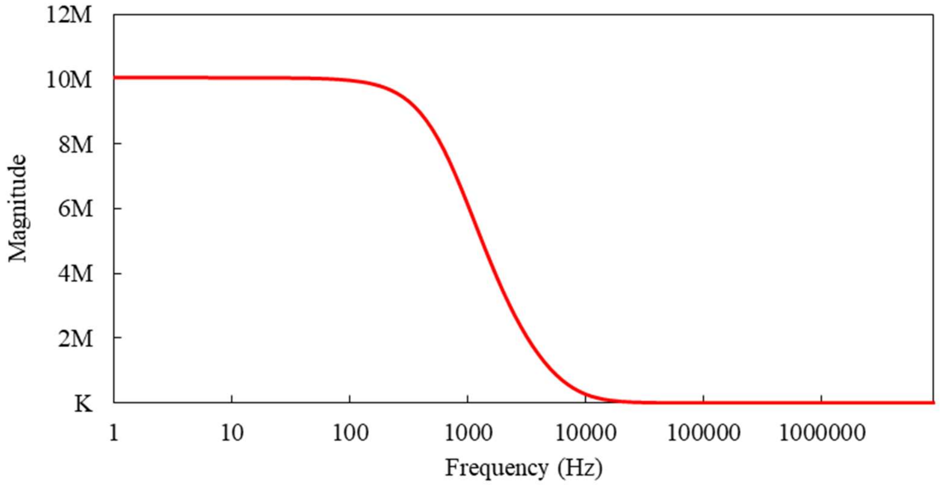

Figure 4.20 Gain characteristics of the signal conditioning circuit.

4.3.7.2 Noise analysis

Noise is an electrical or electromagnetic energy that can damage the main signal. Thermal noise, Shot noise and Flicker noise are three main noises that can be contributed from resistors and semiconductors to the circuit. The noise investigation using the Multisim simulator will give useful information about the noise contribution from each component as well as the filtering design efficiency. To investigate the noise, gain is adjusted to its maximum level where the noise is amplified with the signal to its highest level. The potentiometer is adjusted to zero. Figure 4.20 shows the noise spectrum of the total output noise of the circuit.

The noise spectrum in Figure 4.21 shows a great amplitude reduction on 796 Hz which is equal to the circuit's cut-off frequency. Both Op-amps in the circuit are considered as a low-noise amplifier.

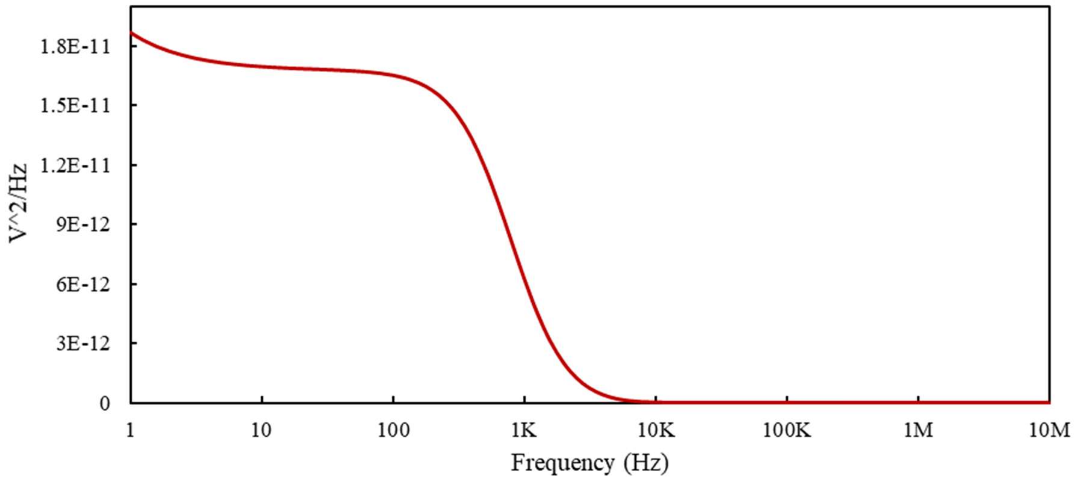

Figure 4.21 Total output noise spectrum.

The electrode of the electrostatic sensor acts as an antenna that can detect any electric fields in its detecting area, including unwanted fields from environmental sources. The sensor amplifies unwanted extrinsic noises along with the main signal which causes the output signal to be contaminated by unwanted extrinsic noise. One of the most extrinsic noise problems can be imposed from a 50 Hz or 60 Hz power line. This kind of noise cannot be easily eliminated using a low-pass filter because its frequency coincides with the range of the desired signal's frequency. In most previous research related to electrostatic sensors an earthed metal screen is proposed to protect the electrode from detection of electric field's sources [99]. However, adding a screen to cover the whole electrode and signal conditioning cannot guarantee the total rejection of the external electrical interference.

4.4 Digital Signal Processing

4.4.1 Signal Analysis and De-noising Approach

4.4.1.1 Signal analysis

The output signal from an electrostatic sensor is a random and low pass signal as shown in Figure 4.22. The signal is also periodic due to the rotational motion. Its bandwidth depends on the geometric properties of the electrode and size of the rotor. The bandwidth is proportional to the rotational speed [74]. Figure 4.22 shows a typical noise- free signal and the corresponding spectrum.

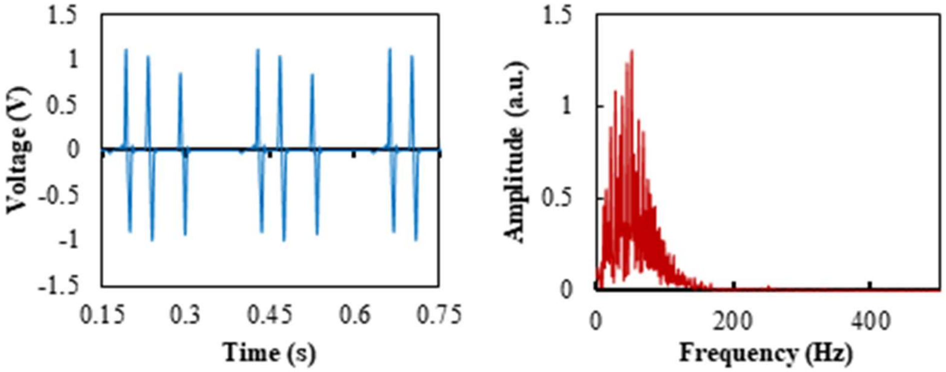

(a) (b)

Figure 4.22 Typical example of a noise-free signal and corresponding frequency spectrum at 200 rpm. (a) Noise-free signal. (b) Power spectrum of signal.

The signal from the electrostatic sensor is usually weak. Thus, various extrinsic and intrinsic noises can be superimposed on it, resulting in a contaminated signal at the output of the conditioning circuit. In some extremely poor conditions, the signal can be partly or totally buried in a strong noise (Figure 4.23). This additive noise significantly degrades the quality of the signal, which can be crucial for signal processing, as a contaminated signal leads to erroneous measurement results.

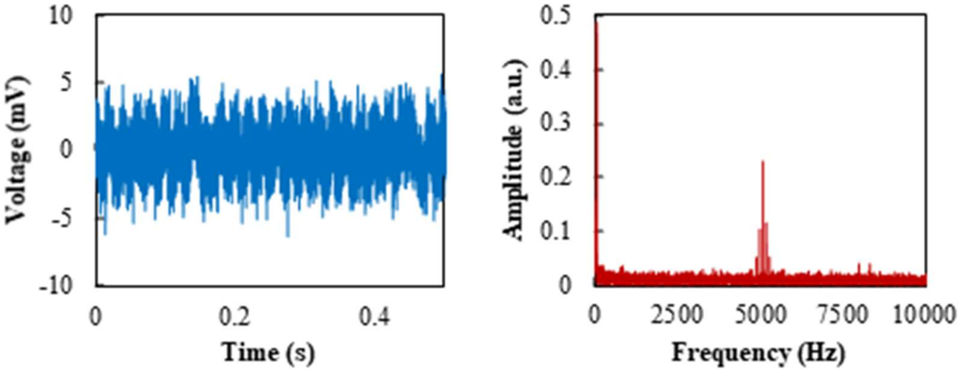

(a) (b)

Figure 4.23 Typical example of a noisy signal and corresponding frequency spectrum. (a) Noisy signal. (b) Power spectrum of the noisy signal.

The types of the source noise that are mixed with the original signal need to be considered when selecting de-noising methods. Generally, the acquired signal is contaminated by different types of noise that can be within or outside the frequency range of the original signal. In some extremely poor conditions, the signal is correlated with noises in which it is buried. The most common sources of noise are the power line interference, vibration of the mechanical system and intrinsic random noise. Power line interference originates primarily from the electromagnetic field of the power lines and the improper grounding of the signal conditioning circuit. The power line noise is centred at 50 Hz or 60 Hz with a bandwidth no more than 1 Hz and is mostly rejected by the earthed metal screen of the sensor [99], [100]. However, adding a screen to cover the electrode and signal conditioning circuit cannot completely reject the external electrical interference. Furthermore, a traditional notch filter cannot be used to remove the residual noise since its frequency component (50 Hz or 60 Hz) may be within the spectrum of the original signal. Thus, a more advanced digital filtering method needs to be employed to suppress this residual noise. The second type of noise that may contaminate the signal is due to the vibration of the mechanical system. Although the adopted method of signal acquisition (current-to-voltage convertor) does not require consideration of the stray capacitance of the electrode in the acquisition circuit, it is still sensitive to the vibration of the sensor and the connecting cable between the sensor and the data acquisition unit. Even tiny displacements of charge in connecting cables due to physical handling can produce current large enough to cause significant noise in the system. The interference frequency of this type of noise is usually composed of the main rotational frequency and its harmonics in addition to high frequency components due to vibration of the connecting cables. Finally, intrinsic noise can be superimposed on the original signal from the signal conditioning circuit. This noise is approximated to white noise which has a continuous frequency spectrum distribution. For that reason, the signal conditioning circuit was designed with extremely low noise using high-performance components. Additionally, a low-pass filter was added to the pre-processing to eliminate the high-frequency noise.

4.4.1.2 Filtering of high frequencies noise

Although the signal conditioner comprises a low-pass filter that helps to remove high-frequency noise, nevertheless, other types of noise, cannot be suppressed by the analogue circuit. To address this problem, a digital filtering algorithm is proposed which combines a cut-off frequency method based on the Fourier transform and a median filter, to remove the high-frequency noise components and also to smooth the signal. A 5th-order IIR Butterworth filter [101] is employed to suppress noise outside the signal bandwidth. Then, a median filter with a window size of 50 is applied to smooth the signal [102]. Figure 4.24 and 4.25 show a typical example of the filtered signals S_{1nf} and S_{2nf} and the corresponding power spectra, respectively. The periodicity of the signals, due to the continuous motion of the shaft, becomes apparent after applying the low-pass filter.

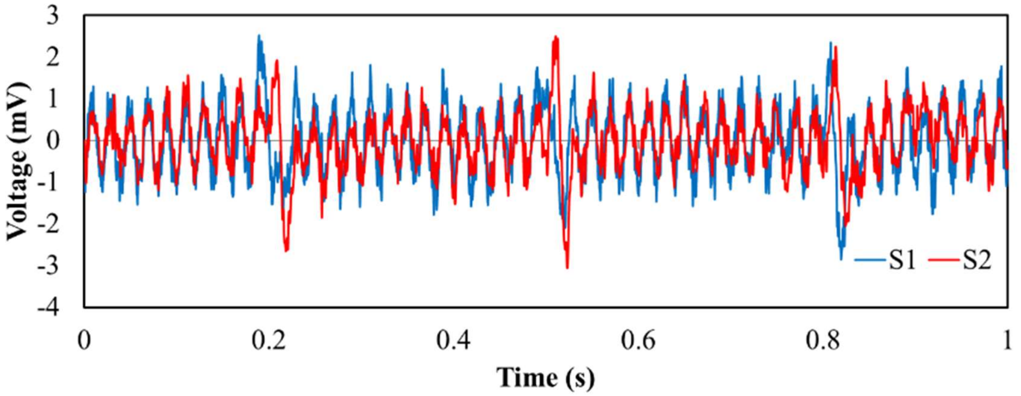

Figure 4.24 Filtered signals S_{1nf} and S_{2nf} from dual electrostatic sensors.

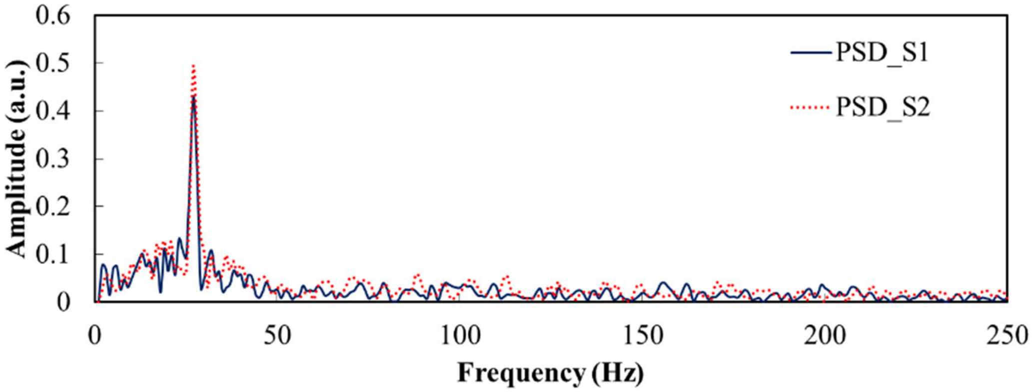

Figure 4.25 Spectra of the filtered signals in Figure 4.24.

Figure 4.26 and 4.27 illustrate the autocorrelation function of the filtered signal S_{1nf} and the cross-correlation function of the two filtered signals S_{1nf} and S_{2nf}. The two correlation functions show that the filtered signals are still buried in strong noise since the dominant peaks, from which the periodicity of the signals is determined, are not clearly defined and stable. Although high-frequency noise has been eliminated using digital low-pass filters, the filtered signals are still contaminated with noises that may be correlated with the original signals and their spectra are within the frequency band of the original signals. Thus, a simple cut-off frequency method is not sufficient to remove such types of noise, making the measurement invalid. Therefore, the filtered signals should be further de-noised using an advanced digital filtering method to remove the frequency components mixed with the desired signal.

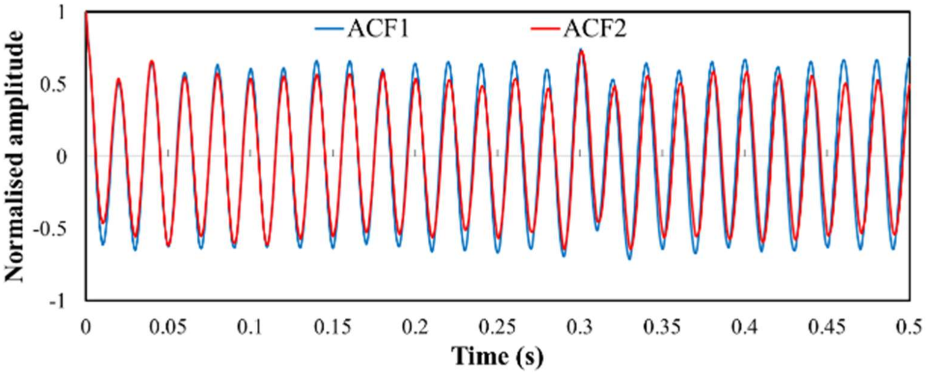

Figure 4.26 Autocorrelation functions of the filtered signal S_{1nf} and S_{2nf}.

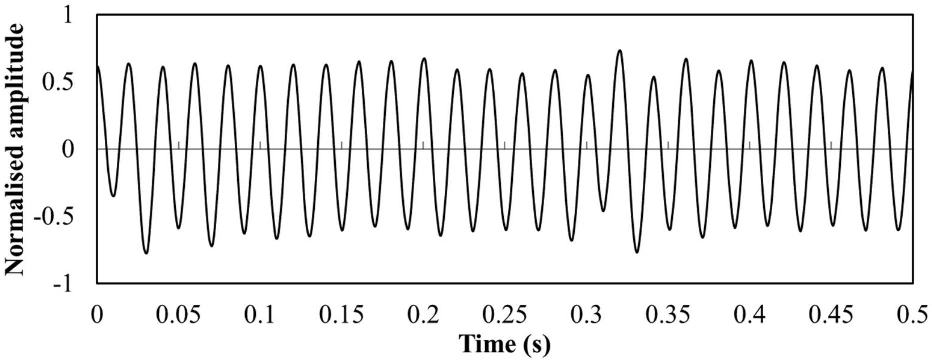

Figure 4.27 Cross-correlation function of the two filtered signals S_{1nf} and S_{2nf}.

4.4.1.3 Filtering of common mode noise

The proposed sensing system for rotational speed measurement is based on dual electrostatic sensors, comprising two electrodes and connected to two independent conditioning circuits [51]. Consequently, the dual sensors derives two signals $S_1(t)$ and $S_2(t)$, similar to each other apart from the time delay between them (Figure 4.24). Since the electrodes and conditioning circuits of the two sensors are almost identical, it can be assumed that they are exposed to common mode noises which they may be correlated with, and their spectra are within the spectrum of the signal. Noises due to power line interference and vibration of the rig can be considered as common mode noise. Thus, employing a method to reduce the common mode noise would suppress most of these noises.

The autocorrelation function (R_{S1S1}) of the noise-free signal $S_1(t)$ and the cross-correlation function (R_{S1S2}) of the noise-free signals, $S_1(t)$ and $S_2(t)$, can be written as

$$R_{S_1S_1}(m) = \sum_{k=1}^{N} S_1(k)S_1(k+m) \tag{4.25}$$

$$R_{S_1S_2}(m) = \sum_{k=1}^{N} S_1(k)S_2(k+m) \tag{4.26}$$

where N is the number of samples in the correlation computation and m ($m = 0, \ldots, N$) is the number of delayed points.

If, however, the two signals ($S_1(t)$) and ($S_2(t)$) are contaminated with a strong common mode periodic noise $n(t)$ with which they are correlated, the autocorrelation function (R_{S1nS1n}) of the noisy signal ($S_{1n}(t)$) and the cross-correlation function (R_{S1nS2n}) of the noisy signals, $S_{1n}(t)$ and $S_{2n}(t)$, become

$$R_{S_{1n}S_{1n}}(m) = \sum_{k=1}^{N} S_{1n}(k)S_{1n}(k+m) \tag{4.27}$$

$$R_{S_{1n}S_{1n}}(m) = \sum_{k=1}^{N} [(S_1(k)+n(k))(S_1(k+m)+n(k+m))] \tag{4.28}$$

$$R_{S_{1n}S_{1n}}(m)=\left\{\begin{array}{l}\sum_{k=1}^{N}S_{1}(k)S_{1}(k+m)+\sum_{k=1}^{N}S_{1}(k)n(k+m)\\+\sum_{k=1}^{N}n(k)S_{1}(k+m)+\sum_{k=1}^{N}n(k)n(k+m)\end{array}\right\} \tag{4.29}$$

$$R_{S_{1n}S_{1n}}(m)=R_{S_{1}S_{1}}(m)+R_{S_{1}n}(m)+R_{nS_{1}}(m)+R_{nn}(m) \tag{4.30}$$

$$R_{S_{1n}S_{2n}}(m)=\sum_{k=1}^{N}S_{1n}(k)S_{2n}(k+m) \tag{4.31}$$

$$R_{S_{1n}S_{2n}}(m)=\sum_{k=1}^{N}((S_{1}(k)+n(k))(S_{2}(k+m)+(n(k+m))) \tag{4.32}$$

$$R_{S_{1n}S_{2n}}(m)=\left\{\begin{array}{l}\sum_{k=1}^{N}S_{1}(k)S_{2}(k+m)+\sum_{k=1}^{N}S_{1}(k)n(k+m)\\+\sum_{k=1}^{N}n(k)S_{2}(k+m)+\sum_{k=1}^{N}n(k)n(k+m)\end{array}\right\} \tag{4.33}$$

$$R_{S_{1n}S_{2n}}(m)=R_{S_{1}S_{2}}(m)+R_{S_{1}n}(m)+R_{nS_{2}}(m)+R_{nn}(m) \tag{4.34}$$

where $S_{1n}(k)$ and $S_{2n}(k)$ are the digitized signals $S_{1n}(t)$ and $S_{2n}(t)$, respectively.

The correlation terms R_{S1n}, R_{nS1}, R_{nS2} and R_{nn} are problematic, in particular when the signal-to-noise ratio is relatively low, as these terms do not tend to zero, because the noise $n(t)$ is periodic and correlates with the original signals ($S_1(t)$ and $S_2(t)$). The effect of the strong noise $n(t)$ can be clearly observed in Figures 4.26 and 4.27 where the peaks of the autocorrelation and cross-correlation functions are completely obscured by the periodic correlation effects caused by the periodic noise in the signals. In this case, the rotational speed measurement is invalid.

To solve this problem, consider the cross-correlation function between S_{1n} and (S_{1n}-S_{2n})

$$R_{S_{1n}(S_{1n}-S_{2n})}=R_{(S_{1}+n)(S_{1}-S_{2})}=R_{S_{1}S_{1}}-R_{S_{1}S_{2}}+R_{nS_{1}}-R_{nS_{2}} \tag{4.35}$$

and the cross-correlation function between S_{2n} and (S_{1n}-S_{2n})

$$R_{S_{2n}(S_{1n}-S_{2n})} = R_{(S_2+n)(S_1-S_2)} = R_{S_2S_1} - R_{S_2S_2} + R_{nS_1} - R_{nS_2} \tag{4.36}$$

Then, subtracting Equation (4.36) from Equation (4.35)

$$R_{\mathrm{mod}} = R_{S_1S_1} + R_{S_2S_2} - R_{S_1S_2} - R_{S_2S_1} \tag{4.37}$$

where R_{mod} is the modified correlation function of the two noisy signals S_{1n} and S_{2n}.

Equation (4.37) shows that the modified correlation function R_{mod} is composed only by the autocorrelation and cross-correlation functions of the noise-free signals (S_1) and (S_2). Figure 4.28 illustrates the modified correlation function. It is worth noting that the peaks of R_{S1S1} and R_{S2S2} are located at the same time lag, i.e. the period of the periodic noises (T). Additionally, the peaks of the cross-correlation R_{S1S2} and R_{S2S1} are inverted in Equation (4.37) and are located at the time lags τ and (T- τ), respectively (Figure 4.28). T and τ denote the period of the two signals and the time delay between them, respectively. As a result, the modified correlation function of the noisy signals has significantly removed the effects due to the periodic noises and the correlation peaks become more apparent, enabling the determination of the rotational speed.

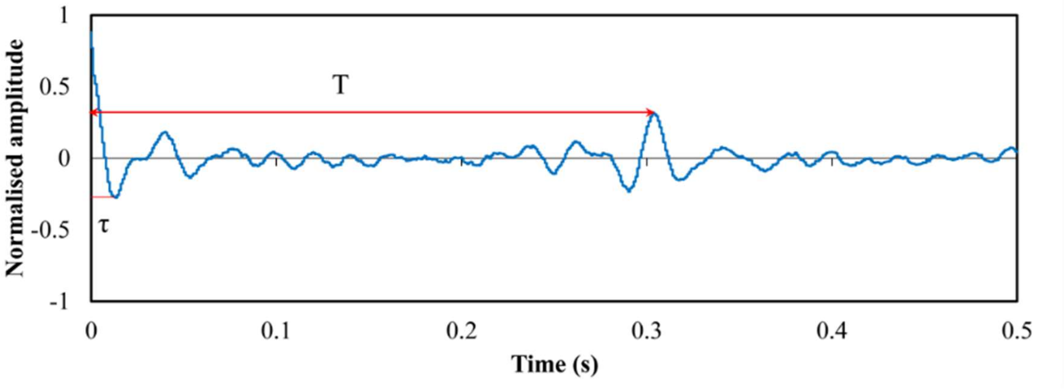

Figure 4.28 Modified correlation function of the two filtered signals S_{1nf} and S_{2nf}.

It is worth noting that the height of the correlation peaks is affected by the level of the white noise superimposed on the original signal.

4.4.2 Parameters Analysis of the measurement System

In a correlation speed measurement system, sampling frequency and data length are two critical parameters which affect the measurement system performance in terms of accuracy, response time and range of measurement. The sampling frequency is strongly related to the frequency characteristic of the signal and the accuracy of the measurement. On the other hand, the data length should satisfy the minimum requirement for the correlation calculation and together with the sampling frequency, the measurement range and the dynamic response time can then be determined. Therefore, the analysis of these two parameters is essential to select the optimal values in order to meet the application requirements.

Under ideal conditions, the average rotational speed of the shaft, as detailed in the measurement principle, is equal to

$$S_{rpm} = \frac{60}{T} = \frac{30\phi}{\pi\tau_0} \tag{4.38}$$

where φ is the angular spacing between the two electrodes, T and τ_0 are the transit times of the first dominated peaks in the autocorrelation and cross-correlation functions, respectively.

Equation (4.38) implies that the angular spacing φ between the two sensors and the transit time (T or τ_0) are the two significant factors influencing the measurement of the speed. Among them, the transit time is the most important factor. However, the accuracy of the transit time depends primarily on the sampling frequency of the analogue signal and the data length in the correlation processing. While, the error due to φ can be adjusted through calibration.

Previous research [74] demonstrated that the bandwidth B of the electrostatic signal in rotational motion can be expressed by

$$B = \frac{\pi K \cdot S_{\max}}{60 \arctan(2w/(2s+D))} \tag{4.39}$$

where S_{max} is the maximum rotational speed of the shaft, W is the width of the electrode, D is the diameter of the shaft, s is the distance between the electrode and the shaft and K is a constant. The simulation results has shown that K is in the range from 0.85 to 0.95. According to the sampling theorem, the sampling frequency must be greater than twice the maximum frequency of the signal

$$f_{s_1} \geq 2BW \tag{4.40}$$

In a digital processing system, values in discrete time are sampled to calculate the correlation function. The transit time is deduced from the maximum value of the correlation function. However, the real transit time may not locate at the discrete points of the correlation function, which can lead to an error in transit time determination and hence in the speed measurement. Supposing the sampling period is Δt, if the peak of the correlation function locates between $n\Delta t$ and $(n+1)\Delta t$, then the maximum error from the peak position is $\pm \frac{1}{2}\Delta t$, so the relative error of the transit time, is

$$\frac{\Delta\tau}{\tau} = \pm\frac{\frac{1}{2}\Delta t}{n\Delta t} = \pm\frac{1}{2n} \tag{4.41}$$

For a given rotational speed, the transit time $\tau = n\Delta t$ is fixed. If the sampling frequency becomes higher, the sampling period will be smaller, so n will become larger. According to Equation (4.41), the relative error of the transit time will be reduced by using a large number of n.

If the sampling period Δt is fixed, the largest relative error occurs at the time of the smallest transit time, which happens at the maximum measuring speed, since the transit time is inversely proportional to the rotational speed as indicated in Equation (4.38). Therefore, the minimum required sampling rate can also be determined from the maximum rotational speed that the system can measure and the maximum acceptable tolerance of the measurement.

Assuming that the relative error of the transit time should not exceed the tolerance $\pm\delta$

$$\frac{\Delta\tau}{\tau_{S_{\max}}}=\frac{1}{2n_{S_{\max}}}\leq\pm\delta \tag{4.42}$$

where $\tau_{S\max}$ and $n_{S\max}$ are the transit time and the number of the sampling period with respect to the maximum speed.

By employing the autocorrelation method, the transit time $T=n_1\Delta t$. Using Equation (4.38) and Equation (4.42), the maximum relative error E_r in % is

$$E_{r1}(\%)=\frac{\Delta t\cdot S_{\max}}{120}\cdot 100\leq\pm\delta\% \tag{4.43}$$

In the case of cross-correlation method, the transit time $\tau_0=n_2\Delta t$. The maximum relative error in % is

$$E_{r2}(\%)=\frac{2\pi}{\phi}\cdot\frac{\Delta t\cdot S_{\max}}{120}\cdot 100\leq\pm\delta\% \tag{4.44}$$

Considering the tolerance condition in Equation (4.44), the transit time derived from autocorrelation, the sampling period can be written as

$$\Delta t\leq\frac{\phi}{2\pi}\frac{120\delta}{S_{\max}} \tag{4.45}$$

Thus, the sampling frequency f_{s2} should be

$$f_{s2}\geq\frac{S_{\max}}{120\delta} \tag{4.46}$$

Similarly, using the cross-correlation method, sampling frequency is

$$f_{s3}\geq\frac{2\pi S_{\max}}{120\phi\delta} \tag{4.47}$$

As a result, the selection of sampling frequency should take the above three conditions into account and choose the maximum between fs_1 and fs_2 for the autocorrelation method and the maximum between fs_2 and fs_3 for the cross-correlation method.

For an electrode width W=3mm, D=60mm and d=2mm, the maximum signal bandwidth B is $0.5S_{max}$. Consequently, the first criterion of the sampling frequency would be

$$f_{s_1} \geq S_{max} \tag{4.48}$$

For φ =0.22 rad, δ =1% and for S_{max}=3000 rpm, then $fs_1 \geq$ 3000 Hz, $fs_2 \geq$ 2500 Hz and fs_3 $\geq$71363 Hz.

It is evident that the cross-correlation method require a much higher sampling rate than the autocorrelation ($2\pi/\varphi$ times) in order to achieve the same measurement accuracy.

For a given sampling rate f_s and considering the accuracy tolerance δ, the maximum speed from autocorrelation and cross-correlation methods are determined by

$$S_{1\max} = 120\delta f_s \tag{4.49}$$

$$S_{2\max} = \frac{\phi}{2\pi} 120\delta f_s \tag{4.50}$$

where S_{1max} and S_{2max} are the maximum speed obtained from autocorrelation and cross-correlation methods, respectively. δ and f_s are the relative error tolerance of the transit time and the sampling frequency.

Figure 4.29 illustrates the relative error tolerance as a function of rotational speed in autocorrelation and cross-correlation methods. For φ =0.22 rad, f_s=50 KHz and a relative error of 0.5%, S_{1max}=30000 rpm and S_{2max}=1420 rpm.

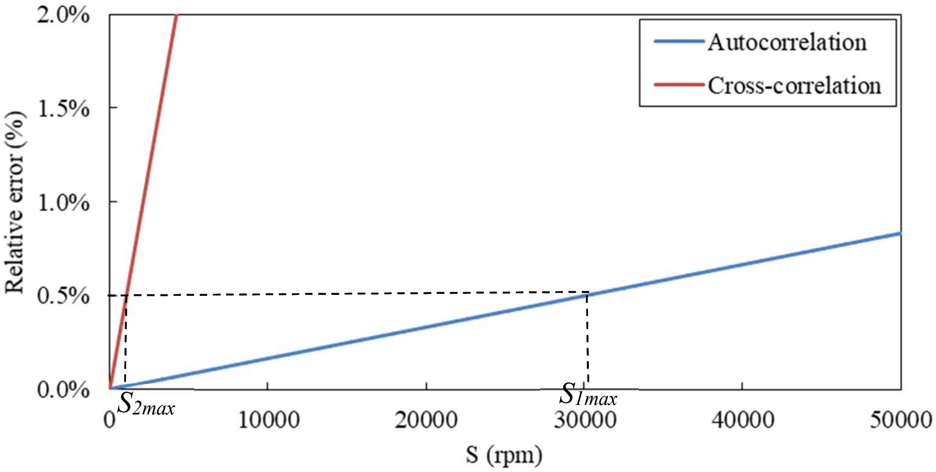

Figure 4.29 Relative error of the transit time measurement for a variable speed.

After the sampling frequency was analysed, some principles on the selection of data length will be presented.

It is suggested that the data length of the correlation function should be at least 10 times the number of points corresponding to the maximum transit time which occurs at the minimum speed. Therefore, the data length *N* should be

$$N \geq 10N_{\max} \tag{4.51}$$

where N_{max} corresponds to the number of points at maximum transit time.

It is evident that the longer the data length is, the more accurate the correlation result should be. However, the increase in the data length will decrease the dynamic response of the system and will also require high-level hardware performance to calculate the correlation function.

Using the autocorrelation method, the number of points required to determine the minimum speed is

$$N_1 \geq 10n_{\max} = 10 \cdot \frac{60f_s}{S_{\min}} = \frac{600f_s}{S_{\min}} \tag{4.52}$$

Similarly, in the cross-correlation method

$$N_2 \geq \frac{\phi}{2\pi}\frac{600 f_s}{S_{\min}} \tag{4.53}$$

For a fixed acquisition time N/f_s, the minimum speed that can be achieved from autocorrelation and cross-correlation methods are determined by

$$S_{1\min} = \frac{600 f_s}{N} \tag{4.54}$$

$$S_{2\min} = \frac{\phi}{2\pi}\frac{600 f_s}{N} \tag{4.55}$$

where S_{1min} and S_{2min} are the minimum speed from autocorrelation and cross-correlation, respectively.

Figure 4.30 Shows the relationship between the acquisition time $T_A = N/f_s$ and the rotational speed for φ=0.22.

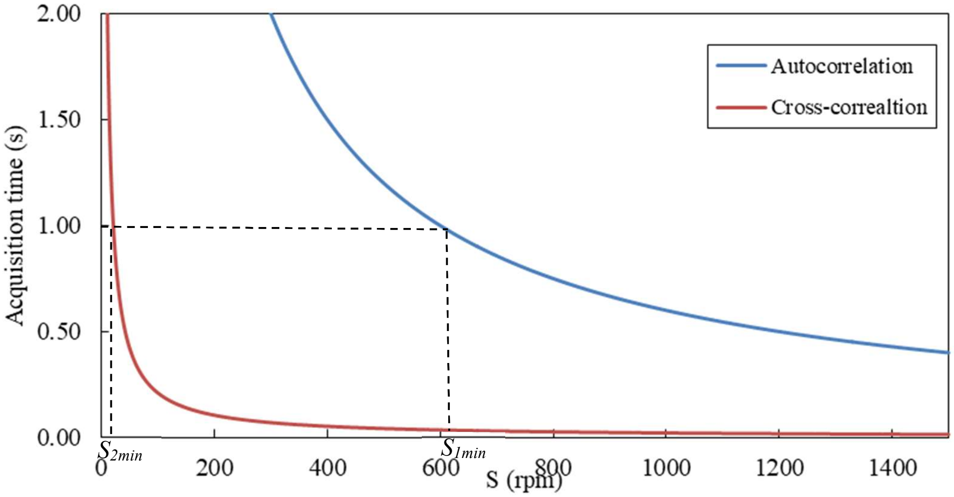

Figure 4.30 Data acquisition time as a function of the rotational speed.

For an acquisition time N/f_s=1s, $S_{1\min}$=600 rpm and S_{2min}=21 rpm.

In conclusion, in order to cover a wider range of measurement with a predefined measurement tolerance and dynamic response time, both methods, autocorrelation and cross-correlation, should be employed and incorporated in the measurement algorithm. For low rotational speed, the cross-correlation method is valid for the range [S_{2min}, S_{1min}] while the autocorrelation method is more suitable for the range [S_{1min}, S_{1max}]. It is worth noting that S_{1min} is the threshold speed that can be used in the measurement algorithm for the selection of the calculation method.

4.4.3 Measurement Algorithm

The flowchart of the key signal processing stages is shown in Figure 4.31. After the digitization of the two electrostatic signals, at the preset sampling frequency and data length, they are fed into the digital processing system. At first, the signal de-noising is employed to improve the S/N ratio. Then, the speed threshold S_{rpmth} is calculated using Equation (4.54). Through correlation, two rotational speed values can be calculated using the autocorrelation and cross-correlation methods. The speed S_{rpm2} derived from the cross-correlation is compared to the threshold speed. If S_{rpm2} is greater than the threshold, then the rotational speed is equal to S_{rpm2}, otherwise, it is equal to S_{rpm1}.

The vibration measurement requires only one signal, e.g. first signal. The selected signal is first decomposed into *n* pulses, corresponding to *n* markers located on the shaft surface using the zero-crossing of the selected signal. Then, the amplitude spectra of the *n* pulses are obtained. The frequencies at the spectra crests f_{cs} can be determined from the peaks of the spectra which are then normalised to the angular speed. Using Equation (3.30), the displacement function and thus the vibration displacement amplitude of the shaft can then be obtained.

Finally, the measurement results, rotational speed and shaft displacement, are then displayed and also sent to the user interface.

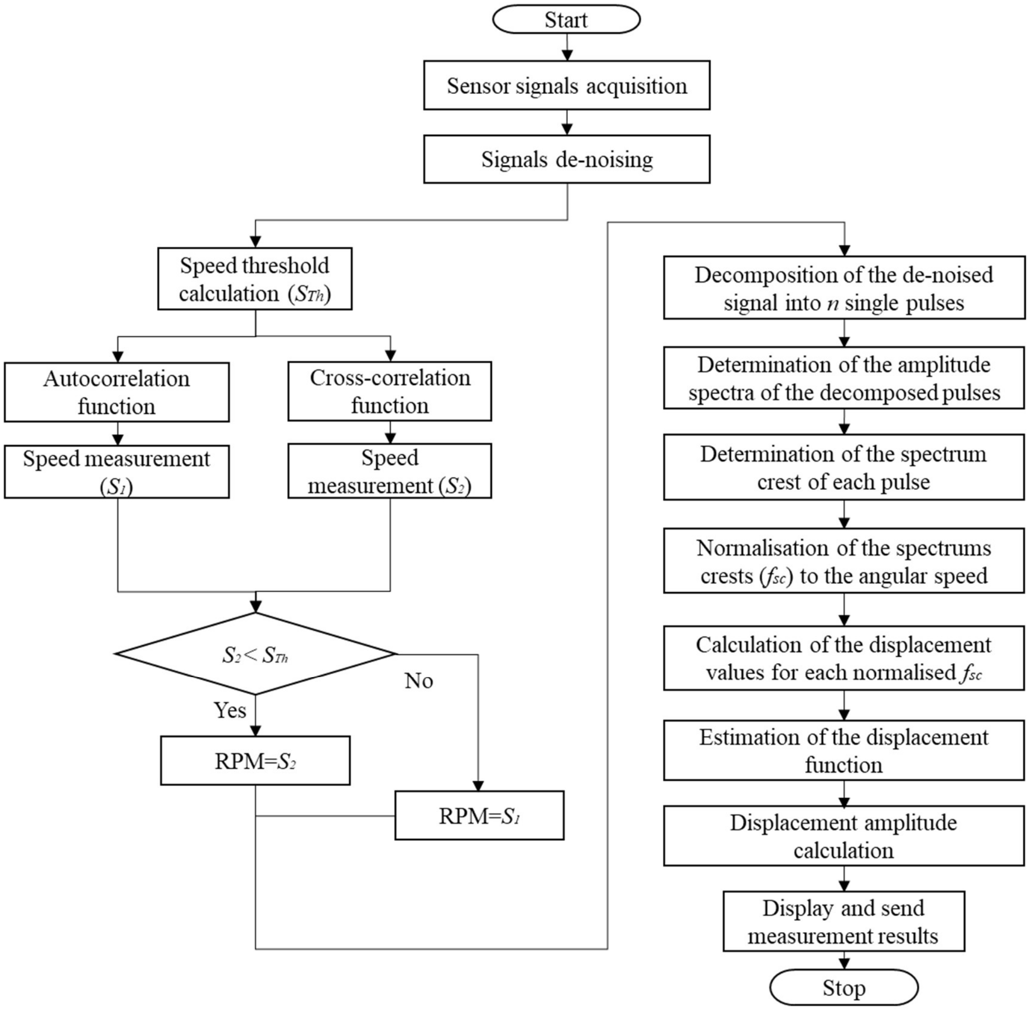

Figure 4.31 Flowchart of the digital signal processing.

4.5 Summary

This chapter details the hardware and software design of the electrostatic sensors based measurement system for online rotational speed and vibration measurement of rotating shafts. By considering the characteristics and properties of the induced signal, the appropriate acquisition method was chosen and the preamplifier design was optimised. The use of a transimpedance amplifier as preamplifier enables a better low-frequency response of the system and hence an accurate measurement of low rotational speed. A de-noising method and an improved correlation technique are applied to improve the performance and enhance the robustness of the measurement system. The digital processing unit design takes full account of the measurement requirements in terms of accuracy, response time and range of measurement. In the aspect of software design, the bespoke program was thoroughly optimised in order to ensure its implementation efficiency.

Chapter 5

Experimental Results and Discussion

5.1 Introduction

This chapter details the experimental validation of the electrostatic measurement system for both rotational speed and vibration measurement of rotary metallic shafts. Tests were conducted on small scale test rigs in the Instrumentation Laboratory at the University of Kent.

The developed measurement system was firstly evaluated for rotational speed measurement and tests were undertaken under normal and noisy conditions at different speeds. Comparisons between the single and dual electrostatic sensors were also achieved. Then, experimental tests were conducted on a purpose-built test rig with eccentric shaft to validate the performance of the electrostatic sensor for vibration displacement.

Typical test results, which were selected from a significant amount of data, were presented in this chapter. Measurement results that were processed, recorded and analysed in the tests include rotational speed, vibration displacement, signal amplitude and correlation coefficient of the electrostatic signal.

5.2 Rotational Speed Measurement

5.2.1 Normal Environment

5.2.1.1 Experimental Conditions

Experimental tests were conducted on a purpose-built test rig as shown in Figure 5.1 to validate the performance of the electrostatic sensor for rotational speed measurement against a reference laser tachometer. The rotational speed of the motor is adjustable through the motor controller. The shaft is made of steel with a diameter of 60 mm and supported by two roller bearings. In order to obtain an independent reference speed to evaluate the measurement system, a commercial laser based tachometer (Monarch Instruments, PLT200) was used to obtain reference speed of the shaft. The operation manual of the tachometer states that the best achievable accuracy is ±0.01%.

As shown in Figure 5.1, eight charged markers, each being made from 20x2 mm^2 electret material film, were distributed and fixed along the circumference of the shaft as suggested in sub-section 4.2.2. The lengthwise direction of which is parallel to the axial direction of shaft. Electrets are dielectrics that have a quasi-permanent electrostatic charge. The electret markers were fabricated through a typical micro fabrication process using Teflon FEP films (Fluorinated Ethylene Propylene). The FEP film with a thickness of 127μm was charged with the use of a point-to-plane corona discharge. After charging, the surface potential of the FEP electret film reaches -560 V.

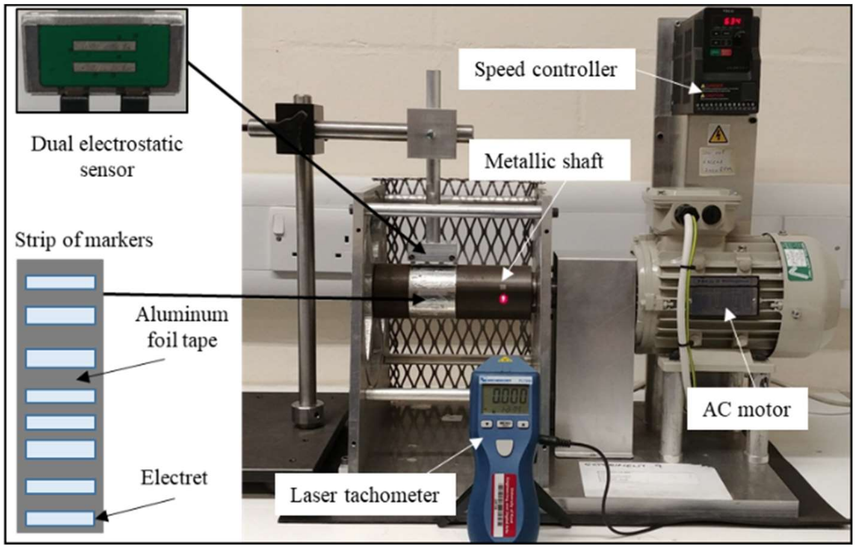

Figure 5.1 Test rig for the rotational speed measurement.

Dual electrostatic sensors, which consisted of an upstream and a downstream sensors, was placed above the central axis of the shaft and 2 mm away from the shaft surface.

The measurement system consisted of dual electrostatic sensors, the signal conditioning unit and the digital processing unit as detailed in chapter 4. In this experiment, the upstream sensor of the dual sensors was used as a single sensor.

The electrostatic sensor was designed and fabricated based on a double-sided printed circuit board (PCB). The electrodes are 3-mm wide tin-plated copper strips embedded in the bottom layer of the PCB. The area around the electrodes is filled with earthed copper to minimise the influence of external electromagnetic interferences. On the top layer of the PCB are the signal conditioning circuits connected to each electrode. The current signals from the electrode are first converted into a proportional voltage signals using an I-V converter. To maximize the power transfer between the electrodes and the signal conditioning circuits, FET amplifiers are chosen for I-V conversion. Then the bipolar signals are further amplified and level shifted using a high-accuracy instrumentation amplifier to match the input range of a single-supply A/D converter. The instrumentation amplifier also provides an adjustable gain for the circuit using a digital potentiometer. Finally, Sallen-Key low-pass filters are used to remove high frequency noise from the sensor outputs and provide anti-aliasing in the A/D conversion. The sensor is shielded with an earthed metal screen to reject external electromagnetic interferences. Figures 5.2 and 5.3 shows the block diagram of the signal conditioning circuit and the design of the electrostatic sensors, respectively.

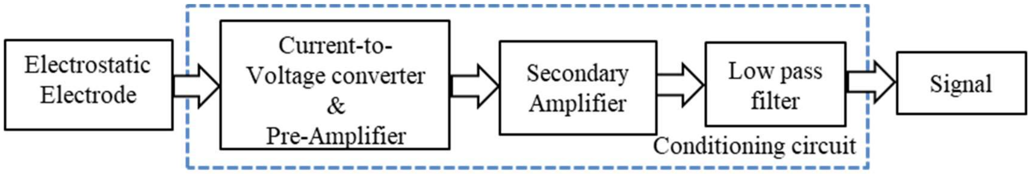

Figure 5.2 Block diagram of the signal conditioning circuit.

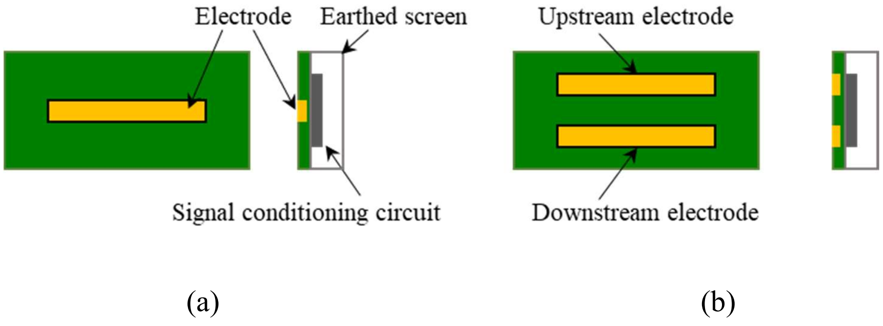

Figure 5.3 Design and construction of the electrostatic sensors. (a) Single electrostatic sensor. (b) Dual electrostatic sensors.

The digital processing unit consists of two parts, one is the acquisition module NI USB-6341 with 16-bit ADC from National Instrument and another is a correlation signal processing system based on LabVIEW, which uses the measurement algorithm presented in sub-section 4.4.3 to calculate the rotational speed.

According to the analysis in sub-section 4.4.2, the parameters of the measurement, sampling frequency and data length, system should be set according to the measuring range of the speed, the response time and the acceptable measurement tolerance. In this study, the measurement system is evaluated for the rotational speed range from S_{min} = 21 rpm to S_{max} = 3000 rpm. The relative error tolerance of the transit time and the data acquisition time set to be $\delta\% = \pm 2\%$, T_a=1s, assuming that the processing time is relatively small with respect the acquisition time. Although the relative error tolerance of the transit time was set at ±2%, the relative error was further reduced by applying an interpolation method in the calculation.

Based on the analysis in sub-section 4.4.2, a sampling frequency of 50 kHz with an acquisition time of 1s should be sufficient to satisfy the measurement requirements.

All the tests were conducted in normal conditions where the noise caused by the test rig vibration and the external electromagnetic interference were insignificant. The environmental conditions of the laboratory were controlled by an air conditioning with an ambient temperature of 22 °C and relative humidity of 49%.

5.2.1.2 Results and Discussions

5.2.1.2.1 Sensor Signals

A typical electrostatic signal waveforms $S_1(t)$ (upstream signal) and $S_2(t)$ (downstream signal) from the dual sensors at a shaft speed of 400 rpm are shown in Figures 5.5 and 5.6. Due to the nature of the rotational motion, the resulting signals are periodic. Figures 5.7 and 5.8 depict the autocorrelation function of $S_1(t)$ and the cross correlation function between $S_1(t)$ and $S_2(t)$. The period (T) of the signals, determined from the location of the dominant peak in the autocorrelation function, is used to calculate the speed. The abscissa value corresponding to the peak in Figure 5.7 is the transit time τ, which equals to the time taken by the shaft moving over the two sensors.

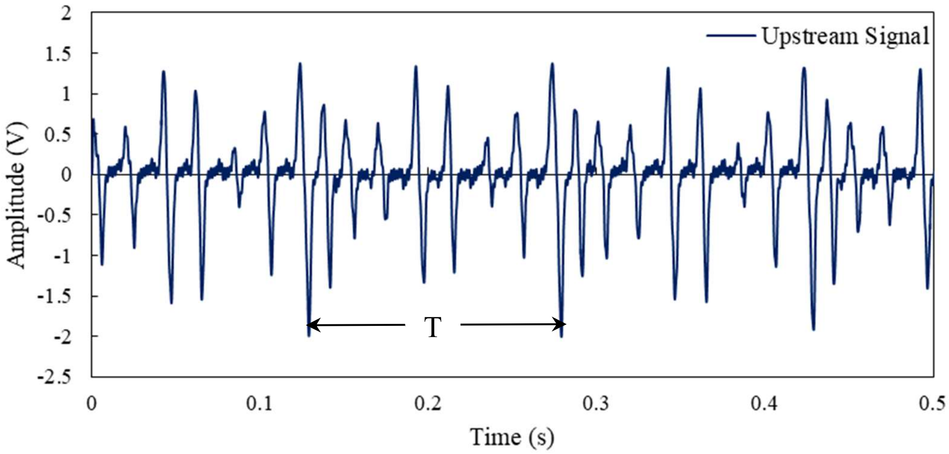

Figure 5.4 Typical signal waveform from the upstream sensor.

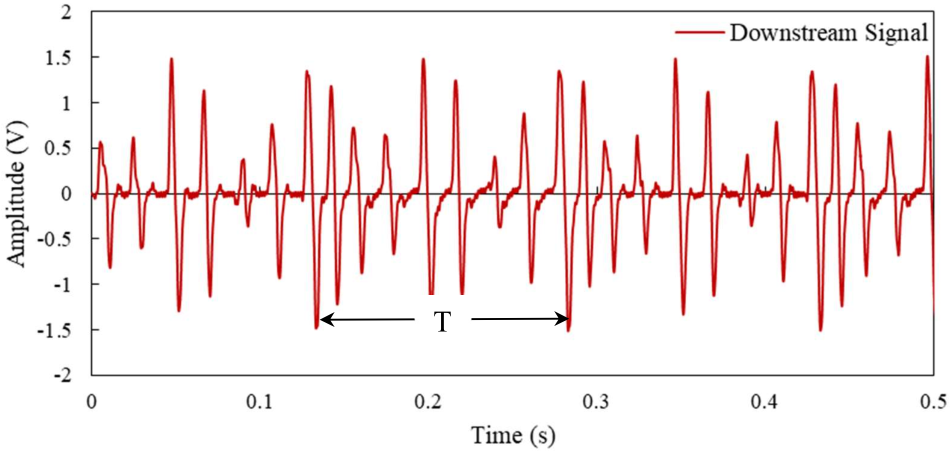

Figure 5.5 Typical signal waveform from the downstream sensor.

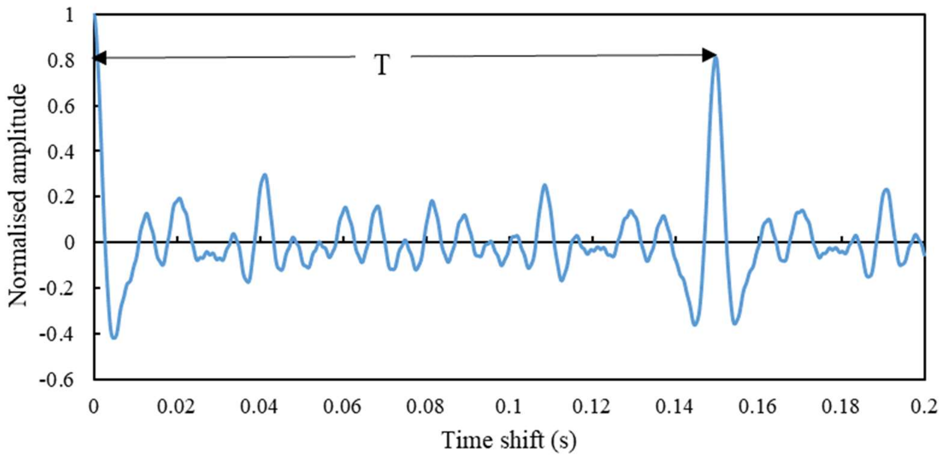

Figure 5.6 Autocorrelation function of the upstream signal.

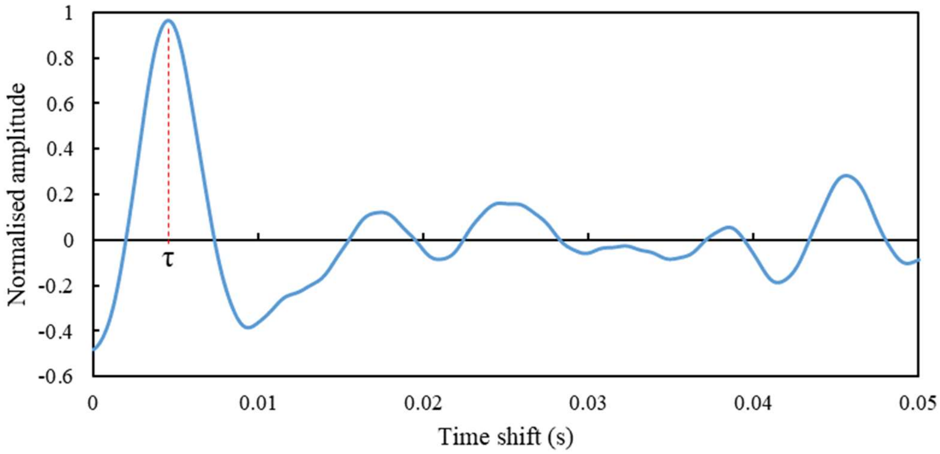

Figure 5.7 Cross-correlation function between upstream and downstream signals.

5.2.1.2.2 Signal Amplitude

A minimum strength of the electrostatic signal has to be maintained to achieve a valid measurement of the rotational speed using electrostatic sensors. The charged markers (Electrets) can guarantee a minimum charge magnitude enabling the electrostatic sensors to generate an electrical signal at relatively low speed. During the rotational motion of the shaft, additional charge is generated and accumulated on the surface of the markers due to its friction with the air (triboelectric effect). The resulting charge on the markers further enhances the signal-to-noise ratio, leading to a valid measurement at lower speed. In this experiment, the magnitude of the permanent charge of electrets were assumed to be stable during the rotational motion. However, the signal amplitude depends also on several factors, including environmental conditions, markers material type, markers surface conditions, rotor size and rotational speed. For a given markers and rotor size, the ambient temperature and relative humidity were set within a narrow range while the effects of operating speed on the signal amplitude is investigated.

In this study the root mean square (RMS) amplitude of an electrostatic signal is used to quantify the signal strength. Figure 5.8 presents the strength of the signal from the electrostatic sensor. It can be obviously observed from Figure 5.8 that the signal strength increases with the rotational speed due to the increased electrostatic charge on the rotating markers surface. The rms signal strength is about 0.16 V at the lowest speed (120 rpm) and reaches 1.26 V at 3000 rpm, for the signal conditioning unit used.

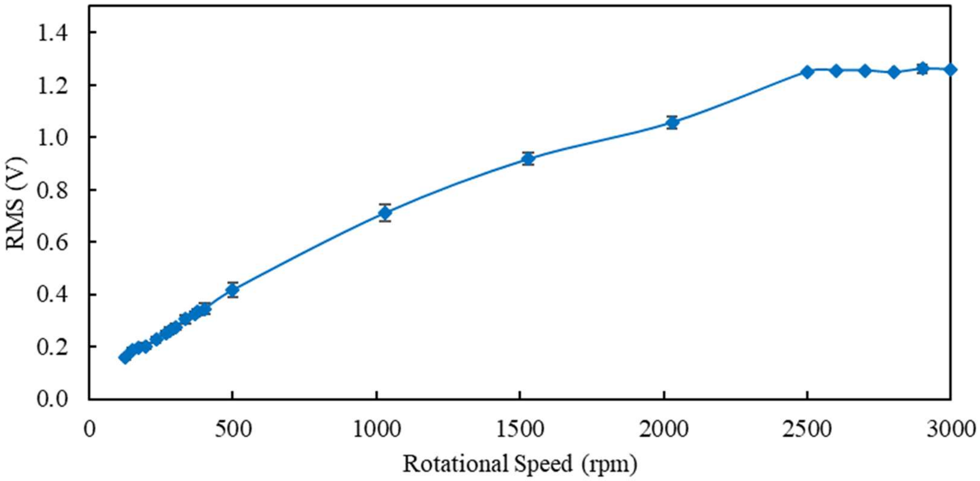

Figure 5.8 Signal amplitude from the single sensor.

It is worth noting that the signal strength saturates above the speed of 2500 rpm, which can be explained by the fact that at this speed the charge density is limited by the breakdown electric field of the air. Consequently, the dynamic balance reached between the natural discharge and recharge becomes constant.

5.2.1.2.3 Correlation Coefficients

Correlation coefficient normally represents the similarity between two signals as those in the dual sensors. In the case of the single sensor, the correlation coefficient represents the degree of repetitiveness or periodicity of the sensor signal due to the rotational motion.

As shown in Figure 5.19, the correlation coefficient obtained from the dual and single sensors tend to increase with the shaft speed due to more electrostatic charge accumulated on the markers surface and hence more stability of the electrostatic signals. However, Figure 5.10 indicate that the correlation coefficients of the dual sensors are consistently higher than that for the single sensor.

In the dual sensors, the short spacing between the sensors gives rise to a higher similarity between the two signals resulting in higher correlation coefficients. The cross-correlation coefficients obtained from the dual sensors, as shown in Figure 5.10, are consistently above 0.6. For the single sensor, the autocorrelation coefficients, especially at a speed of below 175 rpm, are below 0.5. This is attributed to the fact that the resulting electrostatic field and hence the output signal is not stable at low speed, due to the instability of electrostatic charge on the markers surface. As the speed increases, especially above 500 rpm, the resulting electrostatic field is relatively stable and hence the correlation coefficients, for both sensors, are considerably higher.

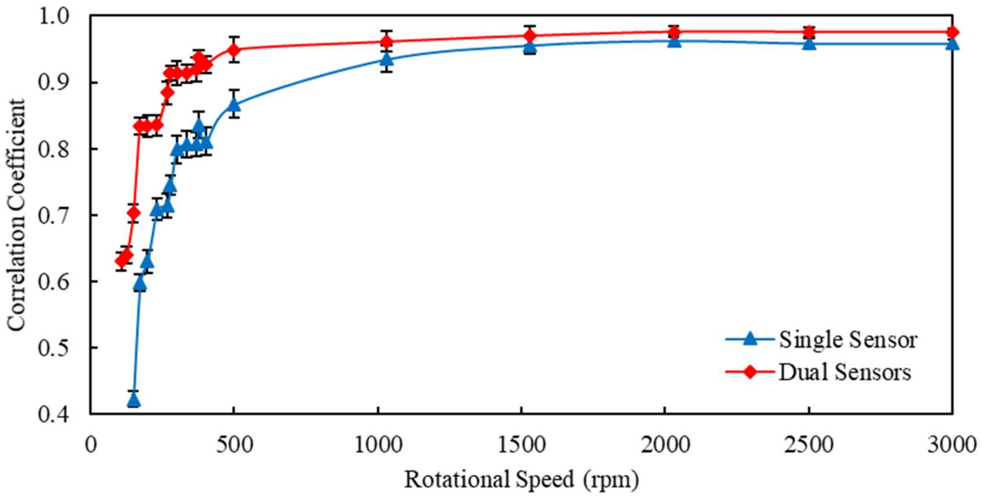

Figure 5.9 Correlation coefficients from the single and dual sensors.

5.2.1.2.4 Accuracy

The accuracy of the measurement system depends mainly on the electrostatic signals quality and their sampling frequency. When the rotor speed is very low, the level of charge on the markers surface is low, leading to a weakened signal and low correlation coefficients as shown in Figure 5.9. In this case, it is usually difficult to obtain valid rotational speed measurements. The effect of the sampling rate on the accuracy of the measurement, which is related to the accuracy of the transit time, was detailed in chapter 4.

In order to assess the accuracy of the measurement systems, the speed of the rotor was adjusted from 0 to 3000 rpm through the motor controller. Figure 5.10 and 5.11 shows a direct comparison between the measured speed from the single sensor and dual sensors, and the reference speed under identical conditions. The measured rotational speeds are average values of 20 measurements.

During the experiments with the single sensor, it was found difficult to obtain valid speed measurements when the reference speed was just below 150 rpm due to the low signal-to-noise ratio and low correlation coefficient, while the short spacing between the two sensors resulted in good similarity between the two signals, making the dual sensors system capable of producing valid measurements at a lower speed (down to 100 rpm). Although the rotational speed can be measured at low speed through the dual sensors, the measurement accuracy is less than that obtained from the single sensor.

From Figures 5.10 and 5.11, it can also be observed that the measured speed from the single sensor is much closer to the reference speed than that from the dual sensors.

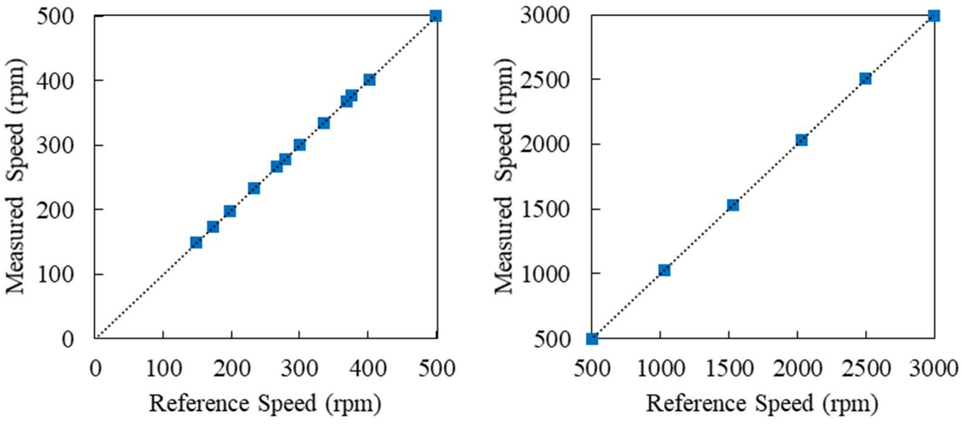

(a) (b)

Figure 5.10 Comparison between the measured speed and the reference speed for single sensor. (a) Lower speed conditions. (b) Higher speed conditions.

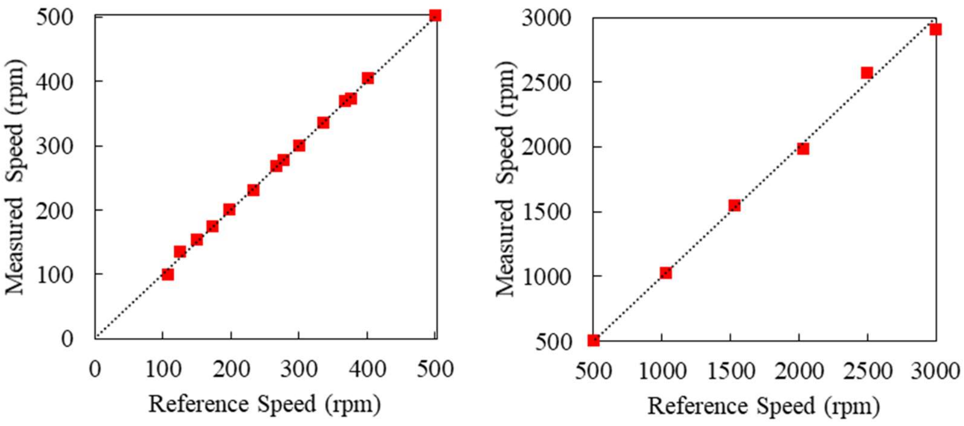

(a) (b)

Figure 5.11 Comparison between the measured speed and the reference speed for dual sensors. (a) Lower speed conditions. (b). Higher speed conditions.

Figure 5.12 and 5.13 shows the relative error of the measured rotational speed from the single sensor. The relative error from the single sensor was within ±0.2% when the rotational speed ranging from 100 rpm to 500 rpm and within ±0.23% from 500 rpm to

3000 rpm. For the dual sensors, the relative error were within ±7.6% over the speed range of 150 rpm to 500 rpm and within ±2.9% over the range of 500 rom to 3000 rpm.

For a given sampling rate, the relative error increases with the speed, as shown in sub-section 4.4.2. However, the relative errors of the measured speed from both sensors, as shown in Figures 5.12 and 5.13, demonstrated that the measurement accuracy at lower speed is not as high as expected from the analysis in sub-section 4.42. In fact, for the speed below of 500 rpm, the error due to the signal quality is much more significant than that due to the accuracy of the transit time. Hence, the measurement value, for both sensors, is less accurate when the speed decreases since less electrostatic charge is induced on the sensor resulting in lower signal quality. When the speed is greater than 500 rpm, the signal quality is more consistent with higher correlation coefficients as shown in Figure 5.9. In this case, the relative error is predominantly due to the error in the transit time measurement. The accuracy of the rotational speed decreases with the speed as the correlation peaks move towards the vertical axis of the correlation functions. This outcome agrees with the analysis in sub-section 4.4.2. However, a higher sampling rate is required to achieve a higher measurement accuracy under high speed conditions.

On the other hand, the relative errors from dual sensors are consistently larger than those from the single sensor as shown in Figures 5.13 and 5.14, because the spacing between the two electrodes yields a short time delay between the two signals compared to the transit time in the autocorrelation. Therefore, the accuracy in the transit time measurement from dual sensors, for a given sampling rate, is always lower than that from the single sensor and the cross-correlation method has lower sensitivity than the autocorrelation method.

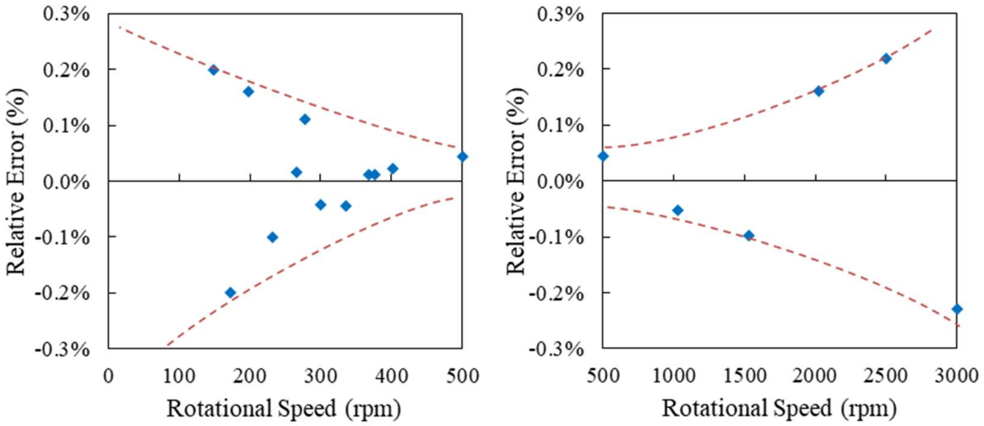

(a) (b)

Figure 5.12 Relative error of the measured rotational speed from the single sensor.

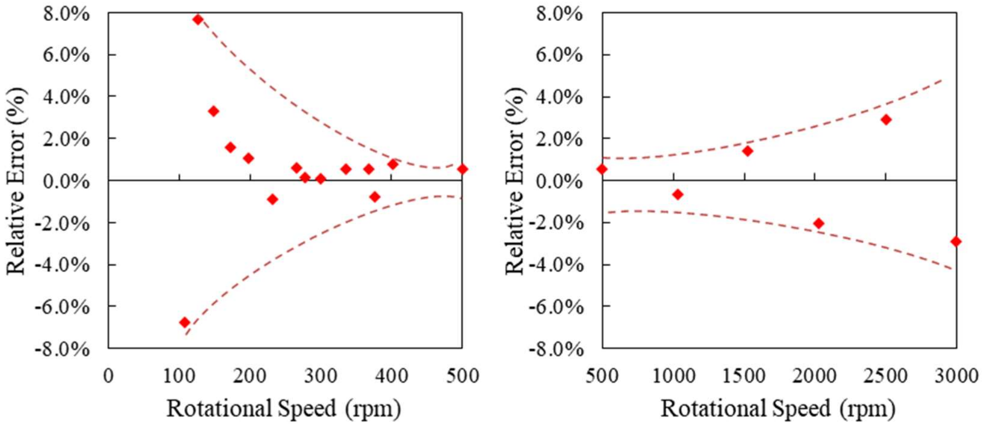

(a) (b)

Figure 5.13 Relative error of the measured rotational speed from the dual sensors.

5.2.1.2.5 Repeatability

Repeatability is an important parameter in the performance evaluation of a measurement system. In this study, normalised standard deviation is used to assess the repeatability r of the measurement system, which is defined as

$$r = \frac{STD}{\overline{RPM}} \times 100\% \tag{5.1}$$

where STD and $\overline{RPM}$ are the standard deviation and average value of the measured speed, respectively.

The reason to normalise the absolute standard deviation (STD) to the average value (RPM) is to achieve a percentage-wise representation of the repeatability, regardless of the magnitude of the measurand. A total of 20 measurements under the same conditions were processed in each repeatability test. It can be observed from Figure 5.14 that the normalised standard deviation is not greater than 2% for the dual sensors and 0.25% for the single sensor for the speed range from 500 rpm to 300 rpm.

However, Figure 5.15 indicate that the repeatability of the single sensor is consistently higher than that of the dual sensors. The short time delay between the two signals results in an instability of the correlation peak in the cross-correlation function.

As the rotational speed increases, the repeatability improves because of the increased charge on the rotating markers surface leading to a more stable correlation peak.

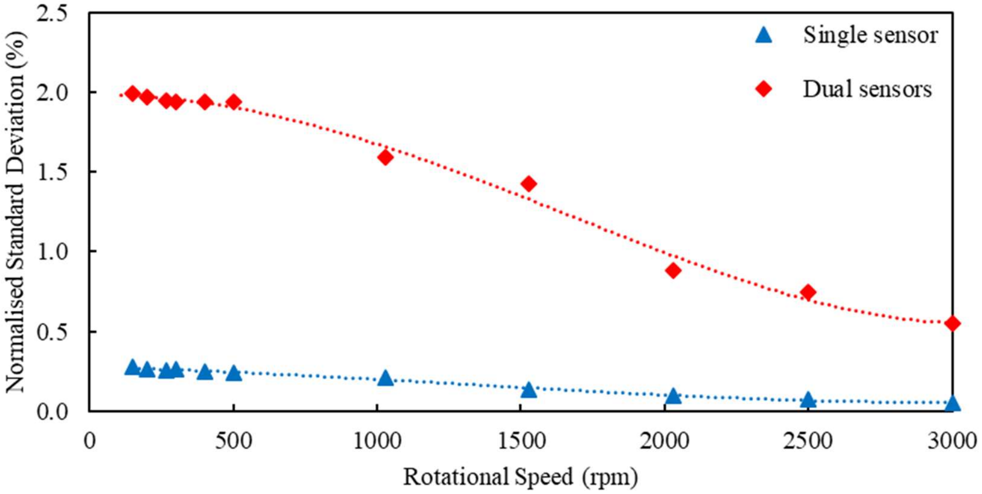

Figure 5.14 Normalised standard deviation of the measured speed for the single and dual sensors.

5.2.2 Electrically Noisy Environment

5.2.2.1 Experimental Conditions

The signal from an electrostatic sensor is usually vulnerable and susceptible to contamination in a hostile environment. The acquired original signal may be contaminated by different types of noise, particularly the common mode noise. The low signal-to-noise ratio, especially at low speed, makes the measurement difficult and sometimes invalid as seen in the sub-section 5.2.1.2.

A technique for removing the effect of common mode noise on cross correlation measurement was demonstrated in sub-section 4.4.1.3. Experimental tests in electrically noisy environments were conducted.

Experimental tests were conducted on two purpose-built test rigs as shown in Figure 5.15 to establish the efficacy of the technique. The measurement system was based on dual sensors. The sensor output signals are sampled at a frequency of 50 kHz using a high-performance data acquisition unit (NI USB-6351) with 16-bit ADC [104] and processed on a host computer. All the tests were conducted under ambient temperature of 23°C ~ 24°C and relative humidity of 57% ~ 65%.

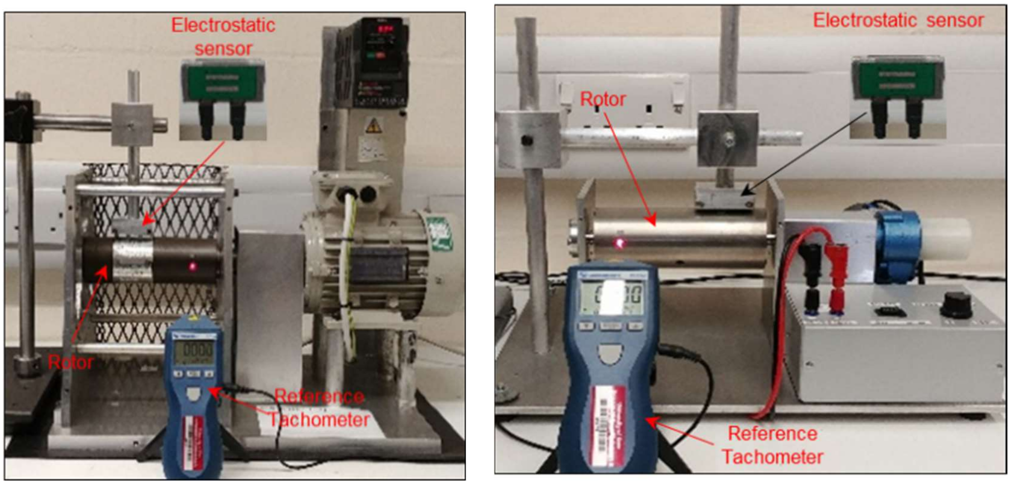

(a) (b)

Figure 5.15 Test Rig. (a) Test rig for 300-3000 rpm. (b) Test rig for 0-300 rpm.

5.2.2.2 Results and Discussion

The speed measurement using the proposed method and conventional method are plotted in Figures 5.16 and 5.17. Each measured speed is the average of 20 instantaneous measurements.

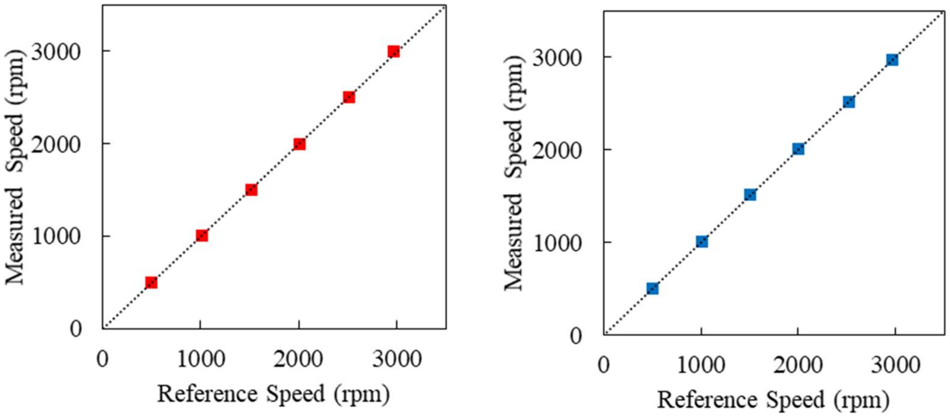

(a) (b)

Figure 5.16 Comparison of measured speeds up to 3000 rpm. (a) Conventional correlation method. (b) Modified correlation method.

It can be seen that the two methods can achieve the rotational speed measurements over the range between 500 rpm and 3000 rpm. However, the proposed method outperforms the conventional one in terms of accuracy as shown in Figure 5.19. The relative error using the modified correlation method was within ±0.1% and with a repeatability of <0.05%.

A second series of experiments was conducted for the speed range from 40 rpm to 300 rpm. Figure 5.18 shows that the lower end range of the conventional method is 160 rpm whereas the proposed method can achieve valid measurements down to 40 rpm with a relative error within ± 0.2 % and a maximum repeatability of 0.7% (Figure 5.18).

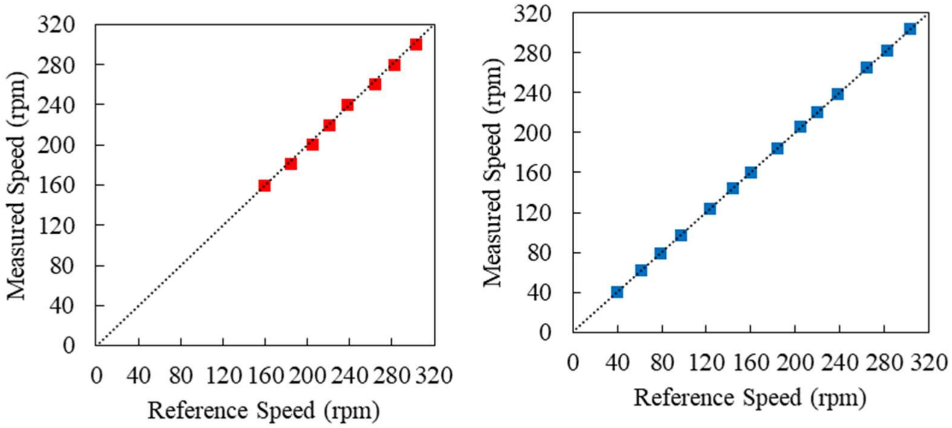

(a) (b)

Figure 5.17 Comparison of measured speeds up to 300 rpm. (a) Conventional correlation method. (b) Modified correlation method.

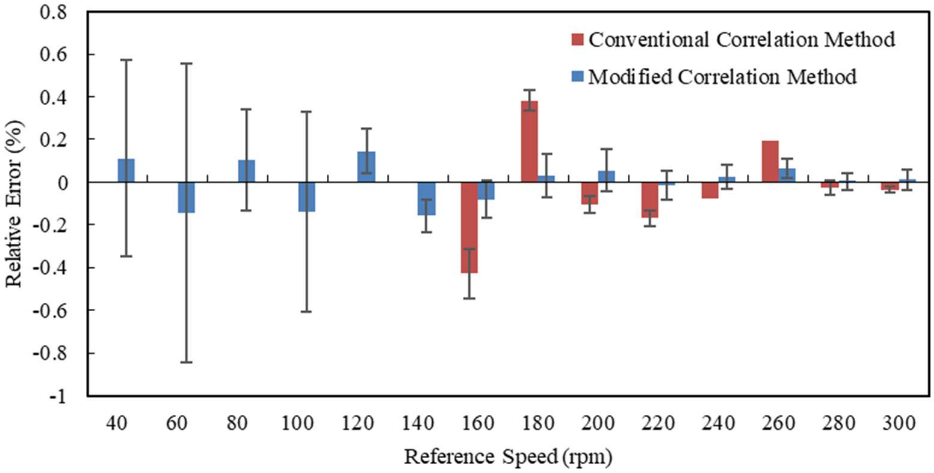

Figure 5.18 Relative error of the measured speed for low speed range.

5.3 Shaft Vibration Measurement

5.4.1 Experimental Conditions

Experimental tests were conducted on the same test rig used in the rotational speed experiments. An eccentric metallic shaft with a diameter of 60 mm and an eccentricity of 0.5 mm from the rotation axis was tested. A single electrostatic sensor (Figure 5.19) was placed 2 mm away from the shaft surface. To simulate eight point charges on the rotor surface, eight charged markers, each being made from 20x3 mm^2 electret material film, were fixed evenly along the circumference of the eccentric shaft. Two of them were located at the shortest and longest distance with respect to the centre of rotation. The electret markers were fabricated using Teflon FEP films with a thickness of 127µm and a surface potential of -560 V.

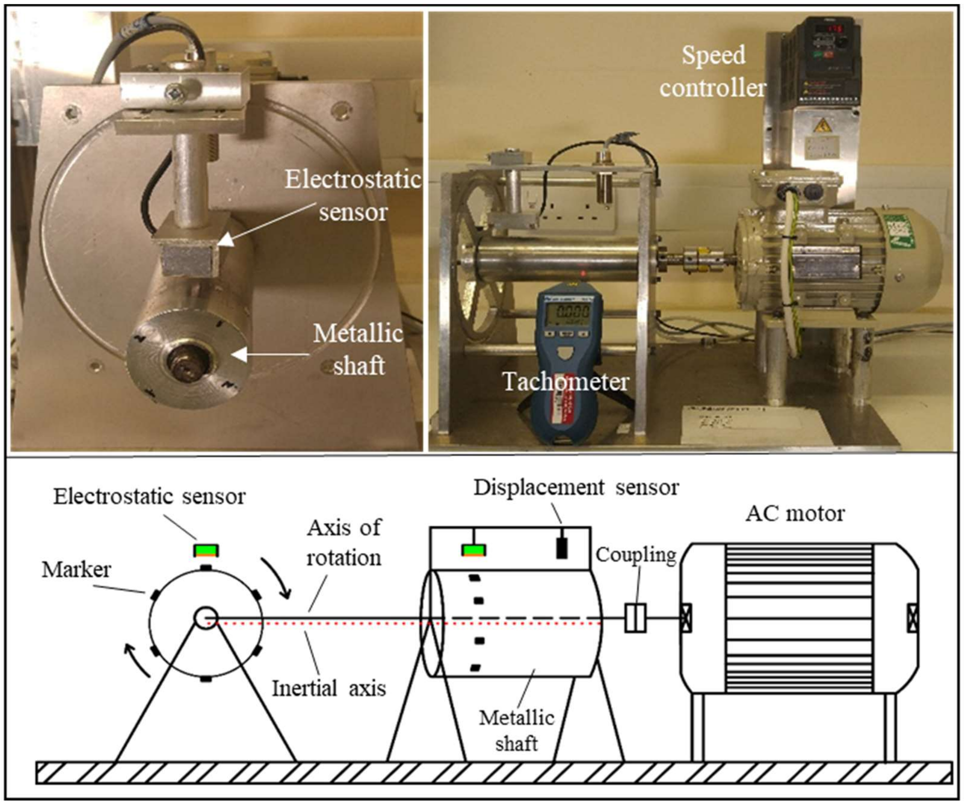

Figure 5.19 Test rig for the shaft vibration measurement.

The electrostatic sensor used in this experiment was a single sensor system (Figure 5.20). The electrode is a 4-mm wide tin-plated copper strip embedded in the bottom layer of the PCB. The signal conditioning unit and the digital processing unit were similar to those used in the rotational speed experiment. The output sensor signal was sampled at a frequency of 50 kHz with an acquisition time of 1s using a data acquisition device (National Instruments, model USB-6341) and processed on a host computer. A bespoke software system was developed using LabView in order to achieve on-line displacement measurement.

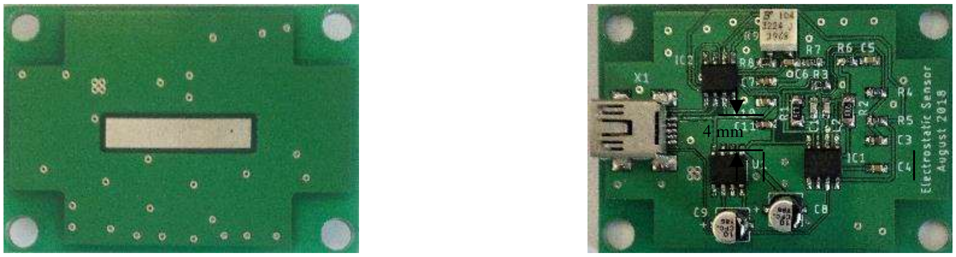

(a) (b)

Figure 5.20 Electrostatic sensor and signal conditioning circuit.

The output of the sensor, resulting from the induced charge on the electrode, is derived and measured. Then, the frequency response of the output signal is obtained. A displacement sensor of eddy current type (Model LD701-2/5, OMEGA) was used as a reference instrument to obtain the relative distance between sensor and the shaft surface. All the tests were conducted in a laboratory with air conditioning (ambient temperature of 26 °C and relative humidity of 42%).

5.3.1 Results and Discussion

Figure 5.21 shows the output signal from the electrostatic sensor for one period which is the time of the shaft over one rotation.

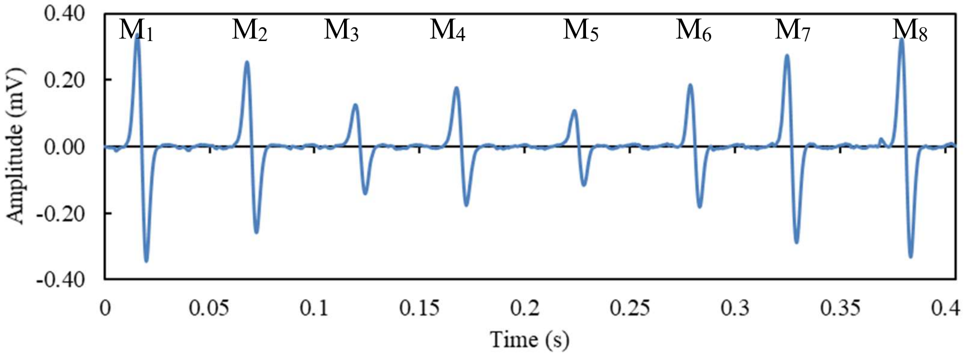

Figure 5.21 Output signal from the electrostatic sensor.

For each period, the signal is composed by a series of eight pulses resulting from the eight markers on the shaft. It is clear that the amplitude of the signal from the eccentric shaft fluctuates due to the variations in the distance between the shaft and the sensor over one rotation.

Following the measurement methodology in sub-section 3.6.2, the signal in Figure 5.19 is first decomposed in the time domain into eight single signals corresponding to the eight point charges on the shaft. Then, frequency analysis of each single signal is performed in order to extract the frequency at the spectrum crest f_{sc}. Figure 5.22(a) presents the f_{sc} values of the eight signals for an eccentric shaft (e = 0.5 mm) at 148 rpm. Using the regression analysis in sub-section 3.6.2, displacement values can be estimated for each f_{sc}. It can be observed from Figure 5.22(b) that the displacement distribution of an eccentric shaft can fit a sinusoidal function, which agrees with the simulation results in the sub-section 3.6.

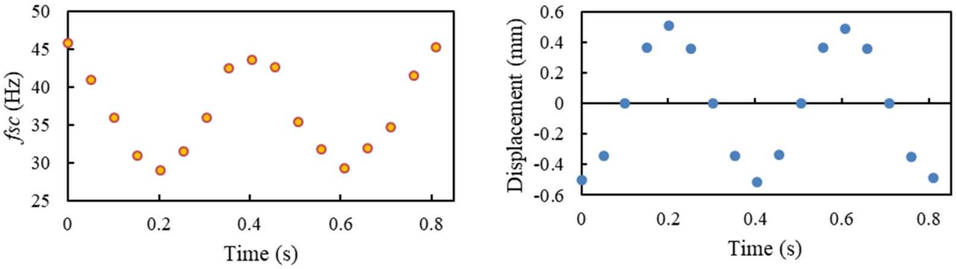

(a) (b)

Figure 5.22 f_{sc} and estimated dispalecement (a) f_{sc} over two rotations. (b) Estimated displacement values.

Figure 5.23(a) presents a direct comparison of the displacement (AC component) of eight points on the eccentric shaft between the electrostatic sensor and the reference sensor (eddy current sensor). The shaft has an eccentricity of 0.5 mm, and is rotating at 148 RPM. All the measured displacements are the average of 20 values with a maximum standard deviation of 4.5 %. It is evident that the measured displacements is pretty close to the reference. Figure 5.23(b) presents that the relative error of the measured displacement which is within ±4.2%.

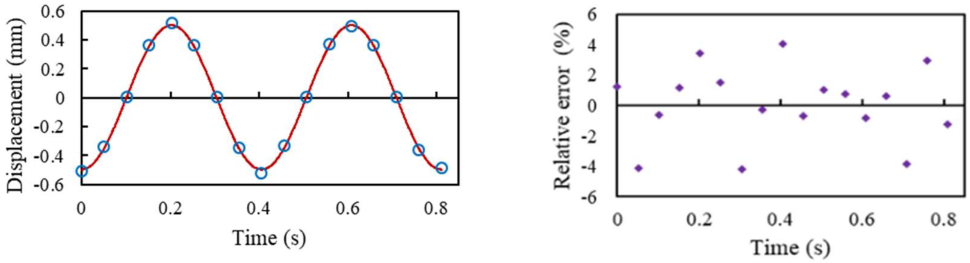

(a) (b)

Figure 5.23 Comparison of the displacement values with the reference sensor output (a). Displacement values (b) Relative error.

Figure 5.24(a) shows the comparison between the reference and the electrostatic sensor results using a sinusoidal curve fitting. The displacement measurement from the electrostatic sensor in Figure 5.24(a) shows a peak-to-peak displacement of about 1 mm, independent from the rotational speed. The root mean square error (RMSE) between the two displacement curves resulting from the reference sensor and the electrostatic sensor is within 0.77%.

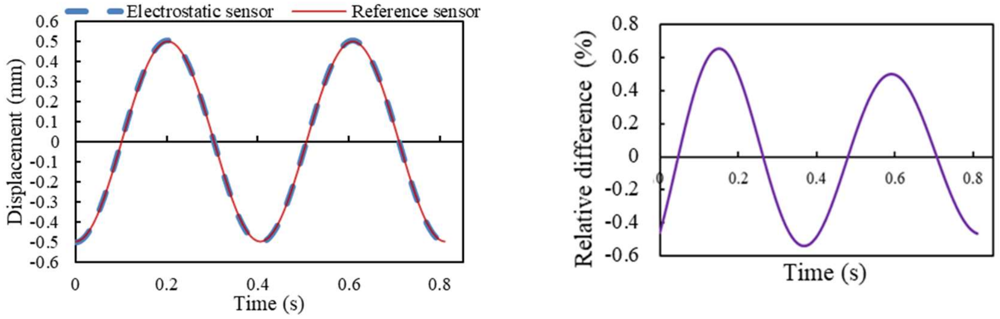

(a) (b)

Figure 5.24 Comparison of the displacement curve from the electrostatic and the reference sensors. (a) Displacement measurement (b) Relative difference.

Figure 5.24(b) shows that the maximum relative error is within ± 0.6% compared to ±4.2% of the discrete displacement values (Figure 5.23(b)). This result suggests that applying sinusoidal curve fitting to the discrete displacement values with a known frequency (angular speed) has reduced the relative error. It can also be observed from 5.24(b) that the relative error in the displacement measurement increases when the displacement decreases. The capability of the system to measure smallest displacement values (and hence higher measurement resolution) can be achieved by improving the data acquisition parameters (e.g. sampling frequency, ADC resolution etc.).

5.4 Summary

A range of experiments have been carried out on a laboratory-scale test rigs to validate the proposed measurement methods and evaluate the effectiveness of the developed measurement systems. The detailed descriptions of the laboratory-scale test rigs along with the experimental conditions have been given.

The rotational speed measurement methods have been verified through analysing the output signals from the electrostatic sensors. Meanwhile, experimental investigations into the use of single and dual electrostatic sensors in conjunction with electret markers for the rotational speed measurement of metallic shafts have been conducted on an experimental setup. Both sensors have produced accurate results under higher speed conditions due to increased charge on the markers. Results presented have demonstrated that the measurement system using a single electrostatic sensor yielded a maximum error of ±0.23% over the speed range of 500 rpm to 3000 rpm, while the use of dual electrostatic sensors yielded a maximum error of ±2.9%. The dual sensors system is more suitable for low speed measurement when the single sensor system does not function well under such conditions due to the less evident periodicity of the signal from a single electrode. It was found that is difficult to obtain rotational speed measurement through autocorrelation when the shaft is rotating below 150 rpm. The maximum error from the signal sensor and the dual sensors were within ±0.2% and ±7.6%, respectively, over the speed below of 500 rpm. The relative error of the dual sensors system in comparison with the single sensor has been found to be relatively over the whole speed range due to the short time delay in the cross-correlation method.

Subsequently, the measurement system was further evaluated in an electrically noisy environment. The improved correlation technique has been shown to improve the performance and enhance the robustness of the rotational speed measurement system. The modified correlation method has proven to be effective in a replicated hostile environment where the original signals are contaminated with correlated strong common-mode periodic noises. This technique is suitable for any correlation-based measurement where there is strong periodic noise. The lab-scale experimental results have demonstrated that the measurement error is within ±0.2% over the speed range from 40 rpm to 3000 rpm with a repeatability of <0.7%. Additionally, the lower end of the measurement range has been extended from 160 rpm to 40 rpm. The advantages of this technique over the conventional method are more demonstrable when the signal-to-noise ratio is very low where the peak in the conventional correlation function is not apparent and stable.

As a result, for a given sampling rate, dual sensors outperform the single sensor in terms of response time and lower end measurement range while the single sensor ensures better accuracy.

Finally, the electrostatic sensing sensors were evaluated for the vibration displacement of metallic shafts. The frequency response properties of an electrostatic sensor have been used to detect and quantify an unbalanced shaft through displacement measurement. Experimental results have demonstrated that electrostatic sensors can be used to measure the displacement of an eccentric shaft. Hence, the vibration of an unbalanced shaft can be quantified. Results obtained have demonstrated that the measurement system performs well with a maximum error no greater than ±0.6% under all test conditions.

In summary, the obtained experimental results have proven that the proposed measurement system with dedicated algorithms is capable of achieving simultaneous measurements of rotational speed and displacement vibration of metallic rotary shafts.

The results presented in this chapter have demonstrated the potential of using the proposed measurement system in condition monitoring systems.

Chapter 6

Conclusions and Recommendations for Future Work

6.1 Research Contributions

The research work presented in this thesis is concerned with the development of an electrostatic measurement system for the rotational speed and vibration measurement of metallic rotating shafts.

The work conducted in the course of this research has advanced progress in many areas of rotational speed and vibration measurement using electrostatic sensors that have unresolved challenges associated with them. In particular, electrostatic sensors have been studied using mathematical modelling, implemented in a low cost measurement system design and shown to perform well under industrial operating conditions, obviating many of the difficulties characteristic of other measurement systems.

A prototype system, including a sensing element, a signal conditioning unit and a digital signal processing unit with dedicated algorithms, has been implemented and experimentally proven effective for the online rotational speed and vibration displacement measurement. The prototype system was extensively evaluated on laboratory-scale test rigs. Test results obtained have demonstrated that the developed system performs well under laboratory operating conditions.

In this chapter, the conclusions that have been drawn from the research programme are summarised and the recommendations for future work are highlighted.

6.2 Conclusions from this Research

6.2.1 Modelling of Electrostatic Sensors

A mathematical model of an electrostatic sensing system based on an insulated electrode and strip-shaped charged markers in rotational motion was established. Based on the developed model, the spatial sensitivity, frequency response and the bandwidth of the output signal were analysed. Moreover, the sensing zone of the sensor was also defined. The effects of the geometric parameters of the markers on the performance of the measurement system and subsequent optimisation of the markers dimensions and number were achieved. For a given sized rotor, the following key parameters are recommended in consideration of modelling results:

- A wider marker yields a higher power spectrum but a narrower signal bandwidth. Thus the optimised width is suggested to be between 0.4 and 0.6 of the electrode width to keep wide signal bandwidth and relatively high power spectrum simultaneously.

- A longer marker yields a higher power spectrum but it has no effect on the signal bandwidth. However, when the length of the marker exceeds that of the electrode, the increase in maximum power spectrum becomes insignificant. Therefore, the optimal length of the marker would be equal to the length of the electrode.

- The measurement method requires that the signal pulses should not overlap, so that the characteristics of each pulse can be easily extracted and used in the signal processing. Accordingly, the maximum number of markers that can fit around the shaft is $2\pi/(\omega_{min}t_{pmax})$, where t_{pmax} is the maximum duration of the pulse and ω_{min} is the minimum angular speed.

6.2.2 Signal Conditioning Circuits and Signal Processing Algorithms

The sensor electronics and processing algorithms developed for the rotational speed and vibration test rigs operate as intended. By considering the characteristics and properties of the induced signal, the appropriate preamplifier design was chosen. The use of a transimpedance amplifier as preamplifier enables a better low-frequency response of the system and hence an accurate measurement of low rotational speed. To maximize the power transfer between the electrodes and the signal conditioning circuits, FET amplifiers was chosen for I-V conversion. Then the bipolar signals were further amplified and level-shifted using a high-accuracy instrumentation amplifier to match the input range of a single-supply A/D converter. The instrumentation amplifier allows to adjust the gain of the circuit through a digital potentiometer. Finally, Sallen-Key low-pass filters were used to remove high frequency noise from the sensor outputs and provide anti-aliasing in the A/D conversion. The sensor was shielded with an earthed metal screen to reject external electromagnetic interferences.

A de-noising method and an improved correlation technique were developed and applied to improve the performance and enhance the robustness of the measurement system. The digital processing unit design takes full account of the measurement requirements in terms of accuracy, response time and range of measurement. In the aspect of software design, the bespoke program was thoroughly optimised in order to ensure its implementation efficiency.

6.2.3 Experimental Evaluations

Experimental results presented in Chapter 5 have indicated that the developed technique is capable of giving accurate and repeatable online measurement of rotational speed and vibration measurement. This has been verified by continuous tests under laboratory conditions. The measurement parameters that have been determined using the developed system include rms signal level, frequency at the spectrum crest, transit time and correlation coefficient.

Results obtained from both single and dual electrostatic sensors in conjunction with electret markers for the rotational speed measurement have a similar trend and suggest that accurate results under higher speed conditions are due to increased charge on the markers. It also has been found in this research that the rms signal level depends primarily on the amount of permanent charge on the markers, the rotational speed and the environmental conditions. As rotational speed reduces, in particular below 500 rpm, the electrostatic charge level decreases, and the correlation peak becomes lower and less stable. The cross-correlation coefficients obtained from the dual sensors were consistently above 0.6, while the autocorrelation coefficients obtained from the single sensor, especially at speeds below 175 rpm, were below 0.5.

It was found difficult to obtain rotational speed measurement below 150 rpm through single sensors, due to the low signal-to-noise ratio and low correlation coefficient, while the short spacing between the two sensors resulted in good similarity between the two signals, making the dual sensors system capable of producing valid measurements at lower speed, down to 100 rpm.

Results presented in Chapter 5 have demonstrated that the measurement system using a single electrostatic sensor yielded a maximum error of ±0.23% over the speed range of 500 rpm to 3000 rpm, while the use of dual electrostatic sensors yielded a maximum error of ±2.9% over the same range. The maximum error from the signal sensor and the dual sensors were within ±0.2% and ±7.6%, respectively, over the speed below 500 rpm. Moreover, the relative error of the dual sensors system in comparison with the single sensor has been found to be relatively higher over the whole speed range due to the short time delay in the cross-correlation method. The repeatability of the measurement system has been found to be better than 2% for the dual sensors and 0.25% for the single sensor over the speed range of 500 rpm to 3000 rpm. The measurement system was further evaluated in an electrically noisy environment where the original signals are contaminated with correlated strong common-mode periodic noises. The lab-scale experimental results have demonstrated that the measurement error is within ±0.2% over the speed range from 40 rpm to 3000 rpm with a repeatability of <0.7%. Additionally, the lower end of the measurement range has been extended from 160 rpm to 40 rpm.

As a result, for a given sampling rate, dual sensors outperform the single sensor in terms of response time and lower end measurement range while the single sensor ensures better accuracy.

Finally, the performance of the electrostatic sensing sensors were assessed for the vibration displacement of metallic shafts. The frequency response properties of an electrostatic sensor have been used to detect and quantify an unbalanced shaft through displacement measurement. Experimental results have demonstrated that the measurement system performs well with a maximum error no greater than ±0.6% under all test conditions.

In summary, the obtained experimental results have proven that the proposed sensing system and the computational algorithms are capable of achieving simultaneous measurements of rotational speed and vibration displacement of metallic rotary shafts.

6.3 Recommendations for Future Research

The research work presented in this thesis has demonstrated the viability and potential of electrostatic sensors in the condition monitoring of rotating machinery. There are, however, a number of areas that need further research and improvements in the near future. The key areas are identified and stated as follows:

6.3.1 Industrial-Scale Trials

The prototype measurement system should be assessed in real industrial environments under variations in ambient temperature, relative humidity, mechanical vibration and electromagnetic noise. Investigations into the operability and effectiveness of the prototype system on industrial-scale rotating shafts, such as wind turbines, should be undertaken. The simulation and laboratory-scale results can then be compared with those from an industrial-scale. However, further upgrade and modification of the measurement system may be required according to the application. The system installation must be redesigned to fit the sensor unit to the mechanical structure of the rotating shaft. Also, a more secure communication strategy should be considered to ensure stable data interaction between the sensors and host computer.

A technique for removing the effect of common mode noise on cross-correlation measurement have been demonstrated in sub-section 4.4.1.3. Although the likelihood of external periodic noise has been considered in this technique, the extent of real world noise on the sensors has not been established. The experiment in sub-section 5.2.2, using added periodic noise from strong power line interference, provides an illustration of the method, but the effect of magnitude and frequency spectrums of real industrial noise are not clear. Additional tests in electrically noisy industrial environments would establish the efficacy of the technique.

Industrial-scale tests should also investigate the effect of environmental factors on the performance of the electrostatic sensors. As indicated earlier, the strength of the output signal depends on a variety of environmental conditions, among which humidity and temperature are considered to have a strong impact. The environmental conditions may affect the permanent charge stability of the electret markers and also the accumulated charge due to the triboelectric effect between the electret surface and the air. The effect of environmental factors on the strength of the electrostatic signal can be quantified by the root-mean-square (rms) magnitude of the electrostatic signal.

In order to ensure the operability of the sensor in a harsh environment, the signal conditioning circuit with programmable gain can be employed to convert the induced charge into a voltage signal at a suitable level for subsequent A/D conversion.

6.3.2 Further Study of Data Processing Techniques

The accuracy of the whole measuring system depends strongly on the measurement algorithms, on the assumption that other important parameters of the sensing element (electrode), analogue part (conditioning circuit) and the digital part (size of the A/D converters, sampling frequency and number of samples) of the system are carefully determined and fixed.

The proposed measurement algorithms were based on the detection of the correlation peak for rotational speed measurement. Therefore, it is worthwhile to conduct an in-depth investigation of peak detection algorithms to further improve the measurement certainty and accuracy. Wavelet analysis is one of the powerful tools to deal with noise of both stationary and non-stationary signals. Unlike the traditional frequency domain method, such as Fourier transform, wavelet analysis can extract signal features in both time and frequency domains. Wavelet multi-scale decomposition method can be used to separate the noise and signal at different scales, and improve the signal to noise ratio in different scales. Moreover, the time delay can also be determined from the rising edges of peaks in the correlation function using the wavelet transforms.

Finally, the application of data fusion techniques could be investigated to optimise and integrate the rotational speed measurements from the autocorrelation and correlation methods so that the robustness and reliability of the measurement system are improved even under harsh conditions.

6.3.3 Dynamic Imbalance Detection

Imbalance is the most common mechanical fault and source of vibration in rotating equipment. The vibration caused by an unbalanced shaft may destroy critical parts of the rotating machine, such as bearings, seals, and couplings. Shaft imbalance is a condition in which the centre of mass of the shaft is not coincident with the centre of rotation. Unbalanced shaft fault can be classified into three categories:

- ***Static imbalance:*** Shaft rotational axis and the principal axis of inertia are parallel.
- ***Couple imbalance:*** The principal inertia axis is not parallel with the axis of rotation.
- ***Dynamic imbalance:*** A combination of static and couple imbalances.

Although dynamic imbalance is the most common problem in rotating machines, this research has only addressed the static imbalance fault through the instantaneous displacement measurement between the shaft surface and the electrostatic sensor. However, the proposed measurement method can be developed in future work to detect and quantify the two other types of imbalance, i.e. the couple and dynamic imbalance.

6.3.4 Integrated Condition Monitoring System

Another potential research area is to integrate electrostatic sensors into a condition monitoring system for the monitoring of rotating machinery. Rotating machinery covers a broad range of important dynamic and manufacturing systems. Condition monitoring and fault diagnosis of such systems is of particular importance in several industries. It is known that the most popular methods of rotating machine condition monitoring utilize rotational speed and vibration signal analysis. By using an appropriate signal processing method, it is possible to detect faults and identify deviation of the operating parameters of these machines from normal values.

It is envisaged that the development of the system, in particular the vibration measurement, will lead to a robust instrumentation system for control and diagnosis of industrial rotating machinery.

References

[1] R. B. Randall, "State of the art in monitoring rotating machinery-part 1," *Sound and Vibration,* vol. 38, *(3),* pp. 14-21, 2004.

[2] A. Heng *et al*, "Rotating machinery prognostics: State of the art, challenges and opportunities," *Mechanical Systems and Signal Processing,* vol. 23, *(3),* pp. 724-739, 2009.

[3] A. Muszynska, "Vibrational diagnostics of rotating machinery malfunctions," *International Journal of Rotating Machinery,* vol. 1, *(3-4),* pp. 237-266, 1995.

[4] B. Lu *et al*, "A review of recent advances in wind turbine condition monitoring and fault diagnosis," in *2009 IEEE Power Electronics and Machines in Wind Applications,* Lincoln, NE, USA*,* 24-26 June, 2009.

[5] W. Yang *et al*, "Cost-effective condition monitoring for wind turbines," *IEEE Trans. Ind. Electron.,* vol. 57, *(1),* pp. 263-271, 2009.

[6] E. Wiggelinkhuizen *et al*, "Assessment of condition monitoring techniques for offshore wind farms," *Journal of Solar Energy Engineering,* vol. 130, *(3),* pp. 031004, 2008.

[7] L. Wang and R. X. Gao, *Condition Monitoring and Control for Intelligent Manufacturing.*London, UK: Springer-Verlag. 2006.

[8] A. H. Tsang, "Condition-based maintenance: tools and decision making," *Journal of Quality in Maintenance Engineering,* vol. 1, *(3),* pp. 3-17, 1995.

[9] D. Clifton and L. Tarassenko, "Condition monitoring of gas-turbine engines," *Transfer Report, Department of Engineering Science, University of Oxford,* 2006.

[10] P. Tavner, "Review of condition monitoring of rotating electrical machines," *IET Electric Power Applications,* vol. 2, *(4),* pp. 215-247, 2008.

[11] F. P. G. Márquez *et al*, "Condition monitoring of wind turbines: Techniques and methods," *Renewable Energy,* vol. 46, *(1)*, pp. 169-178, 2012.

[12] D. Mba, R. Bannister and G. Findlay, "Condition monitoring of low-speed rotating machinery using stress waves Part 1," *Proc. Inst. Mech. Eng. Part E J. Process Mech. Eng.,* vol. 213, *(3),* pp. 153-170, 1999.

[13] D. Brown and J. Jorgensen, "Machine Condition Monitoring Using Vibration Analysis," *Application Note.* Copenhagen, Denmark: *Bruel & Kjaer,* 1987.

[14] K. Elbhbah and J. K. Sinha, "Vibration-based condition monitoring of rotating machines using a machine composite spectrum," *Journal of Sound and Vibration,* vol. 332, *(11),* pp. 2831-2845, 2013.

[15] R. B. Randall, *Vibration-Based Condition Monitoring: Industrial, Aerospace and Automotive Applications.* New Jersey, USA: *John Wiley & Sons, 2011.*

[16] R. Yan and R. X. Gao, "Hilbert–Huang transform-based vibration signal analysis for machine health monitoring," *IEEE Transactions on Instrumentation and Measurement,* vol. 55, *(6),* pp. 2320-2329, 2006.

[17] S. Bagavathiappan *et al*, "Infrared thermography for condition monitoring–A review," *Infrared Phys. Technol.,* vol. 60, *(1)*, pp. 35-55, 2013.

[18] P. Guo, D. Infield and X. Yang, "Wind turbine generator condition-monitoring using temperature trend analysis," *IEEE Transactions on Sustainable Energy,* vol. 3, *(1),* pp. 124-133, 2011.

[19] R. R. Schoen *et al*, "An unsupervised, on-line system for induction motor fault detection using stator current monitoring," *IEEE Trans. Ind. Appl.,* vol. 31, *(6),* pp. 1280-1286, 1995.

[20] Y. Yonghui *et al*, "An integrated on-line oil analysis method for condition monitoring," *Measurement Science and Technology,* vol. 14, *(11),* pp. 1973, 2003.

[21] A. Prabhakaran and C. Jagga, "Condition monitoring of steam turbine-generator through contamination analysis of used lubricating oil," *Tribol. Int.,* vol. 32, *(3),* pp. 145-152, 1999.

[22] X. Zhu, C. Zhong and J. Zhe, "Lubricating oil conditioning sensors for online machine health monitoring–a review," *Tribol. Int.,* vol. 109, pp. 473-484, 2017.

[23] D. Mba and R. B. Rao, "Development of Acoustic Emission Technology for Condition Monitoring and Diagnosis of Rotating Machines; Bearings, Pumps, Gearboxes, Engines and Rotating Structures." London , UK: *Sage Publ.,* 2006.

[24] X. Li, "A brief review: acoustic emission method for tool wear monitoring during turning," *Int. J. Mach. Tools Manuf.,* vol. 42, *(2),* pp. 157-165, 2002.

[25] Y. Li *et al*, "The measurement of instantaneous angular speed," *Mechanical Systems and Signal Processing,* vol. 19, *(4),* pp. 786-805, 2005.

[26] P. R. Belanger, "Estimation of angular velocity and acceleration from shaft encoder measurements," in *Proceedings 1992 IEEE International Conference on Robotics and Automation,* Nice, France, 12-14 May, 1992.

[27] R. Ambienta, "Vibration Measurement A,*" Copenhagen, Denmark: Bruel & Kjaer* ,2000.

[28] Y. Yan *et al*, "Velocity measurement of pneumatically conveyed solids using electrodynamic sensors," *Measurement Science and Technology,* vol. 6, *(5),* pp. 515, 1995.

[29] J. Ma and Y. Yan, "Design and evaluation of electrostatic sensors for the measurement of velocity of pneumatically conveyed solids," *Flow Meas. Instrum.,* vol. 11, *(3),* pp. 195-204, 2000.

[30] J. Shao *et al*, "Velocity measurement of pneumatically conveyed particles using intrusive electrostatic sensors," *IEEE Transactions on Instrumentation and Measurement,* vol. 59, *(5),* pp. 1477-1484, 2010.

[31] X. Qian and Y. Yan, "Flow measurement of biomass and blended biomass fuels in pneumatic conveying pipelines using electrostatic sensor-arrays," *IEEE Transactions on Instrumentation and Measurement,* vol. 61, *(5),* pp. 1343-1352, 2012.

[32] J. YANG *et al*, "Fault detection in a diesel engine by analysing the instantaneous angular speed," *Mechanical Systems and Signal Processing,* vol. 15, *(3),* pp. 549-564, 2001.

[33] M. S. Lebold *et al*, "Using torsional vibration analysis as a synergistic method for crack detection in rotating equipment," *2004 IEEE Aerospace Conference Proceedings (IEEE Cat. no. 04TH8720),* vol. 6, pp. 3517-3527 Vol.6, 2004.

[34] AB Sasi *et al*, "The exploitation of instantaneous angular speed for condition monitoring of electric motors," in *14th International Conference on Condition Monitoring and Diagnostic Engineering Management (COMADEM 2001),* Manchester, UK, pp. 1-8, 4-6 September 2001.

[35] J. Binder, "New generation of automotive sensors to fulfil the requirements of fuel economy and emission control," *Sensors and Actuators A: Physical,* vol. 31, *(1),* pp. 60-67, 1992.

[36] C. E. Robinson, "Analog Tachometers," *IEEE Transactions on Industry and General Applications,* vol. IGA-2, *(2),* pp. 144-146, 1966.

[37] R. Bonert, "Design of a high performance digital tachometer with a microcontroller," *IEEE Transactions on Instrumentation and Measurement,* vol. 38, *(6),* pp. 1104-1108, 1989.

[38] A. Segovia *et al*, "Stroboscopic microcontroller-based tachometer," *Rev. Sci. Instrum.,* vol. 70, *(3),* pp. 1875-1879, 1999.

[39] R. C. Kavanagh, "Improved digital tachometer with reduced sensitivity to sensor nonideality," *IEEE Transactions on Industrial Electronics,* vol. 47, *(4),* pp. 890-897, 2000.

[40] S. Y. Yurish and N. V. Kirianaki, "Design of high performance digital tachometers and tachometric systems based on the method of the depended count," in *The Experience of Designing and Application of CAD Systems in Microelectronics, 2003. CADSM 2003. Proceedings of the 7th International Conference.* Slavske, Ukraine, 22-22 Feb. 2003.

[41] R. Myers *et al*, "Magnetoelectric laminate composite based tachometer for harsh environment applications," *Appl. Phys. Lett.,* vol. 91, *(12),* 2007.

[42] W. Yeh *et al*, "High resolution optical shaft encoder for motor speed control based on an optical disk pick-up," *Rev. Sci. Instrum.,* vol. 69, *(8),* pp. 3068-3071, 1998.

[43] J. N. Lygouras *et al*, "High-performance position detection and velocity adaptive measurement for closed-loop position control," *IEEE Transactions on Instrumentation and Measurement,* vol. 47, *(4),* pp. 978-985, 1998.

[44] X. Zhang *et al*, "Digital image correlation using ring template and quadrilateral element for large rotation measurement," *Optics and Lasers in Engineering,* vol. 50, *(7),* pp. 922-928, 2012.

[45] T. Wang *et al*, "Rotational Speed Measurement Through Image Similarity Evaluation and Spectral Analysis," *IEEE Access,* vol. 6, pp. 46718-46730, 2018.

[46] F. Bonnardot *et al*, "Use of the acceleration signal of a gearbox in order to perform angular resampling (with limited speed fluctuation)," *Mechanical Systems and Signal Processing,* vol. 19, *(4),* pp. 766-785, 2005.

[47] F. Combet and R. Zimroz, "A new method for the estimation of the instantaneous speed relative fluctuation in a vibration signal based on the short time scale transform," *Mechanical Systems and Signal Processing,* vol. 23, *(4),* pp. 1382-1397, 2009.

[48] J. Urbanek *et al*, "A two-step procedure for estimation of instantaneous rotational speed with large fluctuations," *Mechanical Systems and Signal Processing,* vol. 38, *(1),* pp. 96-102, 2013.

[49] H. Lin and K. Ding, "A new method for measuring engine rotational speed based on the vibration and discrete spectrum correction technique," *Measurement,* vol. 46, *(7),* pp. 2056-2064, 2013.

[50] L. Wang, *et al*, "Enhancing the performance of a rotational speed measurement system through data fusion," in *IOP Journal of Physics: Conf. Series (IMEKO 2018),* Belfast, UK*,* 3- 6 September 2018.

[51] L. Wang *et al*, "Rotational Speed Measurement Using Single and Dual Electrostatic Sensors," *IEEE Sensors Journal,* vol. 15, *(3),* pp. 1784-1793, 2015.

[52] L. Wang *et al*, "Rotational Speed Measurement Through Electrostatic Sensing and Correlation Signal Processing," *IEEE Transactions on Instrumentation and Measurement,* vol. 63, *(5),* pp. 1190-1199, 2014.

[53] W. Y. Du, "Resistive, Capacitive, Inductive, and Magnetic Sensor Technologies*," New York, USA: CRC Press,* 2014.

[54] H. C. Lefevre, "*The Fiber-Optic Gyroscope,"*, London, UK, *Artech House,* 2014.

[55] D. Piyabongkarn *et al*, "The development of a MEMS gyroscope for absolute angle measurement," *IEEE Trans. Control Syst. Technol.,* vol. 13, *(2),* pp. 185-195, 2005.

[56] L. Wang *et al*, "Comparison of single and double electrostatic sensors for rotational speed measurement," *Sensors and Actuators A: Physical*, vol. 266, p.p 46-55, 2017.

[57] L. Li *et al*, "Digital Approach to Rotational Speed Measurement Using an Electrostatic Sensor," *Sensors,* vol. 19, *(11),* 2019.

[58] M. MacCamhaoil, "Static and dynamic balancing of rigid rotors," Copenhagen, Denmark: Bruel & Kjaer, 2016.

[59] C. M. Harris and A. G. Piersol, "Harris' Shock and Vibration Handbook," New York, USA: McGraw-Hill Education, 2009

[60] D. Vyroubal, "Optical method for instant estimate of vibration signature based on spectrum analysis of phase-modulated light pulses," *IEEE Transactions on Instrumentation and Measurement,* vol. 53, *(1),* pp. 181-185, 2004.

[61] S. Okabe and S. Tanaka, "Measurement of shaft vibration using ultrasonic sensor," *SICE 2003 Annual Conference (IEEE Cat. no. 03TH8734),* Fukui, Japan, vol. 2, 4-6 Aug., 2003, pp. 1155-1158.

[62] L. Wang *et al*, "Intelligent condition monitoring of rotating machinery through electrostatic sensing and signal analysis," in *2013 IEEE International Conference on Smart Instrumentation, Measurement and Applications (ICSIMA),* Kuala Lumpur, Malaysia, Nov. 2013, pp. 1–4.

[63] L. Wang *et al*, "Radial vibration measurement of rotary shafts through electrostatic sensing and Hilbert-Huang Transform," *2016 IEEE International Instrumentation and Measurement Technology Conference Proceedings,* Taipei, Taiwan, May 2016, pp. 1–5.

[64] S. Fericean and R. Droxler, "New noncontacting inductive analog proximity and inductive linear displacement sensors for industrial automation," *IEEE Sensors Journal,* vol. 7, *(11),* pp. 1538-1545, 2007.

[65] M. R. Nabavi and S. N. Nihtianov, "Design Strategies for Eddy-Current Displacement Sensor Systems: Review and Recommendations," *IEEE Sensors Journal,* vol. 12, *(12),* pp. 3346-3355, 2012.

[66] B. George, Z. Tan and S. Nihtianov, "Advances in Capacitive, Eddy Current, and Magnetic Displacement Sensors and Corresponding Interfaces," *IEEE Transactions on Industrial Electronics,* vol. 64, *(12),* pp. 9595-9607, 2017.

[67] M. Kim *et al*, "A new capacitive displacement sensor with high accuracy and long-range," *Sensors and Actuators A: Physical,* vol. 130, pp. 135-141, 2006.

[68] S. Avramov-Zamurovic and R. D. Lee, "A high-stability capacitance sensor system and its evaluation," *IEEE Transactions on Instrumentation and Measurement,* vol. 58, *(4),* pp. 955-961, 2008.

[69] Y. R. García, J. M. Corres and J. Goicoechea, "Vibration Detection Using Optical Fiber Sensors," *Journal of Sensors,* vol. 2010, *(1)*, 2010.

[70] Q. Yaobin *et al*, "Study on the high frequency vibration measurement by using optical fiber sensing," *2017 16th International Conference on Optical Communications and Networks (ICOCN),* Wuzhen, China*,* 7-10 August, 2017, pp. 1-3.

[71] H. A. Deferrari, R. A. Darby and F. A. Andrews, "Vibrational Displacement and Mode-Shape Measurement by a Laser Interferometer," *J. Acoust. Soc. Am.,* vol. 42, *(5),* pp. 982-990, 1967.

[73] Y. Hu *et al*, "Online Continuous Measurement of the Operating Deflection Shape of Power Transmission Belts Through Electrostatic Charge Sensing," *IEEE Transactions on Instrumentation and Measurement,* vol. 66, *(3),* pp. 492-501, 2017.

[74] L. Wang and Y. Yan, "Mathematical modelling and experimental validation of electrostatic sensors for rotational speed measurement," *Meas. Sci. Technol.,* vol. 25, *(11),* pp. 115101, 2014.

[75] C. I. Calle, "Electrostatics principles," in *Electrostatic Phenomena on Planetary Surfaces*, Bristol, UK: IOP publ. 2017.

[76] Y. Yan *et al*, "Velocity measurement of pneumatically conveyed solids using electrodynamic sensors," *Measurement Science and Technology,* vol. 6, *(5),* pp. 515-537, 1995.

[77] S. Morris, "Real-Time Electrostatic Charge Monitoring of the Wear Surfaces and Debris Generated by Sliding Bearing Steel Contacts." University of Southampton, UK, 2003.

[78] G. M. Sessler, "Physical principles of electrets," in *Electrets*, New York, USA: Springer-Verlag,1980.

[79] S. Boisseau, G. Despesse and B. A. Seddik, "Electrostatic conversion for vibration energy harvesting," in *Small-Scale Energy Harvesting*, M. Lallart, Ed. Rijeka, Croatia: InTech, 2012, ch. 5.

[80] Q. Chen, "PTFE electret negative charge stability after RF plasma treatment," *J. Phys. D,* vol. 35, *(22),* pp. 2939-2944, 2002.

[81] Y. Sakane *et al*, "The development of a high-performance perfluorinated polymer electret and its application to micro power generation," *J Micromech Microengineering,* vol. 18, *(10),* pp. 104011, 2008.

[82] P. Günther, "SiO2 electrets for electric-field generation in sensors and actuators," *Sensors and Actuators A: Physical,* vol. 32, *(1),* pp. 357-360, 1992.

[83] Y. Suzuki, "Recent progress in MEMS electret generator for energy harvesting," *IEEJ Trans Elec Electron Eng,* vol. 6, *(2),* pp. 101-111, 2011.

[84] G. M. Sessler, "Electrets," New York, USA: Springer-Verlag,1987.

[85] K. Tao *et al*, "A three-dimensional electret-based micro power generator for low-level ambient vibrational energy harvesting," *J Micromech Microengineering,* vol. 24, *(6),* pp. 065022, 2014.

[86] J. B. Gajewski, "Non-contact electrostatic flow probes for measuring the flow rate and charge in the two-phase gas–solids flows," *Chemical Engineering Science,* vol. 61, *(7),* pp. 2262-2270, 2006.

[87] J. B. Gajewski, "Mathematical model of non-contact measurements of charges while moving," *Journal of Electrostatics,* vol. 15, *(1),* pp. 81-92, 1984.

[88] J. B. Gajewski, "Measuring probes, head, and system for the non-contact, electrostatic measurements of the two-phase flow parameters in pneumatic transport of solids," *Journal of Electrostatics,* vol. 32, *(3),* pp. 297-303, 1994.

[89] S. O. Kasap and J. Rowlands, "Direct-conversion flat-panel X-ray image detectors," *IEE Proceedings-Circuits, Devices and Systems,* vol. 149, *(2),* pp. 85-96, 2002.

[90] C. Alippi and C. Galperti, "An Adaptive System for Optimal Solar Energy Harvesting in Wireless Sensor Network Nodes," *IEEE Transactions on Circuits and Systems I: Regular Papers,* vol. 55, *(6),* pp. 1742-1750, 2008.

[91] J. McGrath *et al*, "Analysis of parasitic protozoa at the single-cell level using microfluidic impedance cytometry," *Scientific Reports,* vol. 7, *(1),* pp. 2601, 2017.

[92] T. Fujii *et al*, "Micropattern measurement with an atomic force microscope," *Journal of Vacuum Science & Technology B: Microelectronics and Nanometer Structures Processing, Measurement, and Phenomena,* vol. 9, *(2),* pp. 666-669, 1991.

[93] C. H. Fields *et al*, "110 GHz transimpedance amplifier in InP-HBT technology for 100 Gbit ethernet," *IEEE Microwave and Wireless Components Letters,* vol. 20, *(8),* pp. 465-467, 2010.

[94] S. Salhi *et al*, "Design of high speed transimpedance amplifier for optical communication systems," *2017 Seminar on Detection Systems Architectures and Technologies (DAT),* Algiers, Algeria, pp. 1-5, *20-22 Feb.*, 2017.

[95] D. F. Bowers, "Instrumentation Amplifiers," *Wiley Encyclopedia of Electrical and Electronics Engineering,* 1999.

[96] J. Karki, "Active low-pass filter design," *Texas Instruments Application Report,* 2000.

[97] O. OPA132 and F. OPA4132–High-Speed, "Input Operational Amplifiers: Datasheet," *Texas Instruments Inc,* 1995.

[98] A. Devices, "AD623: Single-Supply, Rail-to-Rail, Low Cost Instrumentation Amplifier," Analog Devices AD623 Datasheet, vol. 8, 1997.

[99] J. B. Gajewski, "Electrostatic flow probe and measuring system calibration for solids mass flow rate measurement," *J. Electrostatics,* vol. 45, *(4),* pp. 255-264, 1999.

[100] C. Xu *et al*, "Sensing characteristics of electrostatic inductive sensor for flow parameters measurement of pneumatically conveyed particles," *J. Electrostatics,* vol. 65, *(9),* pp. 582-592, 2007.

[101] I. W. Selesnick and C. S. Burrus, "Generalized digital Butterworth filter design," *IEEE Transactions on Signal Processing,* vol. 46, *(6),* pp. 1688-1694, 1998.

[102] N. Gallagher and G. Wise, "A theoretical analysis of the properties of median filters," *IEEE Transactions on Acoustics, Speech, and Signal Processing,* vol. 29, *(6),* pp. 1136-1141, 1981.

Appendix A

Electronic Circuits and PCB schematics

This section shows the schematics of the single electrostatic sensor used in the tests. The electronic circuit of the dual sensors consists of two identical single sensor circuits.

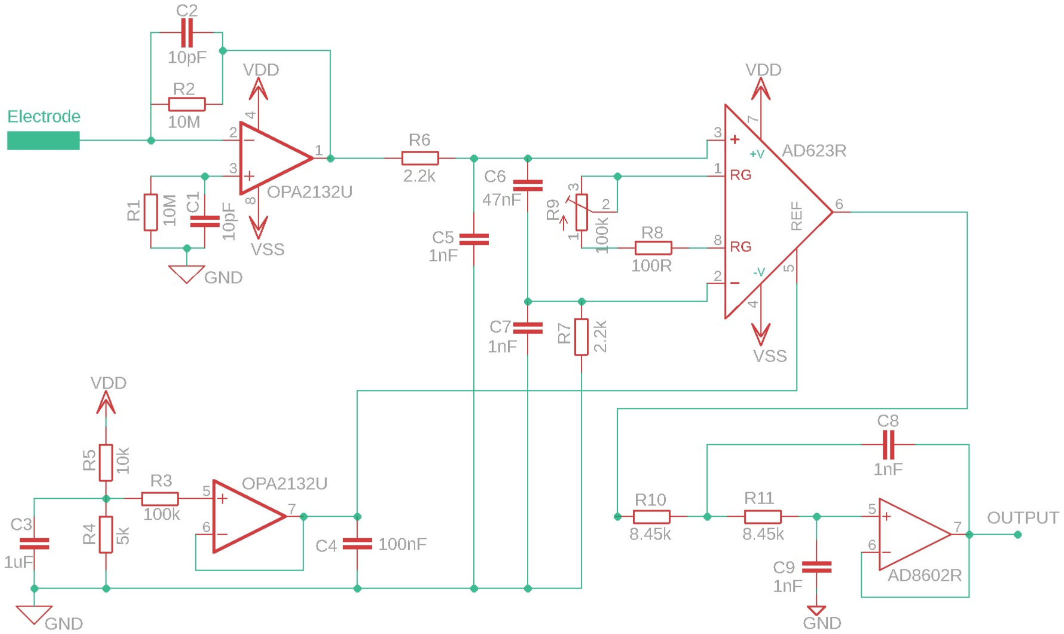

Figure A.6.1 Schematic of the signal condition circuit.

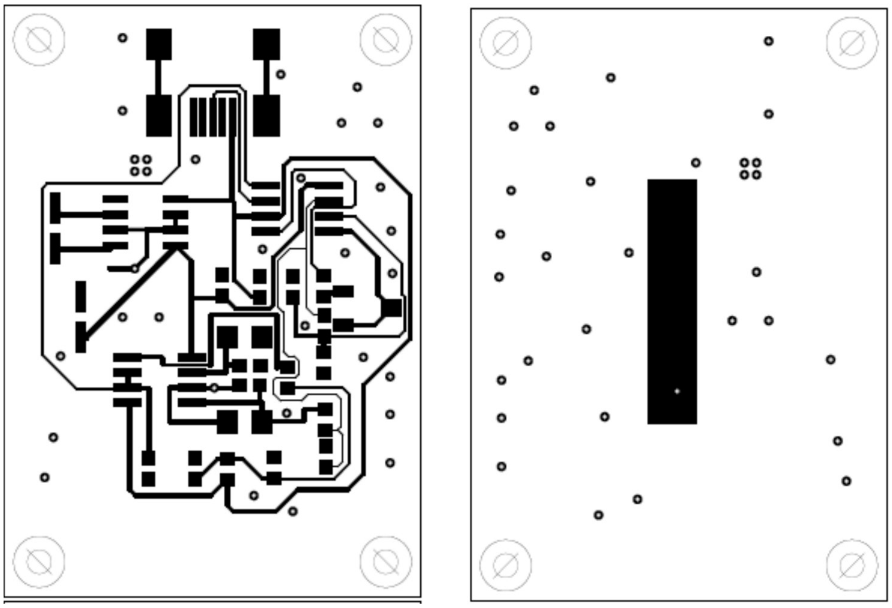

(a) (b)

Figure A.6.2 Signal conditioning PCB layout. (a) Top layer. (b) Bottom layer (2:1).

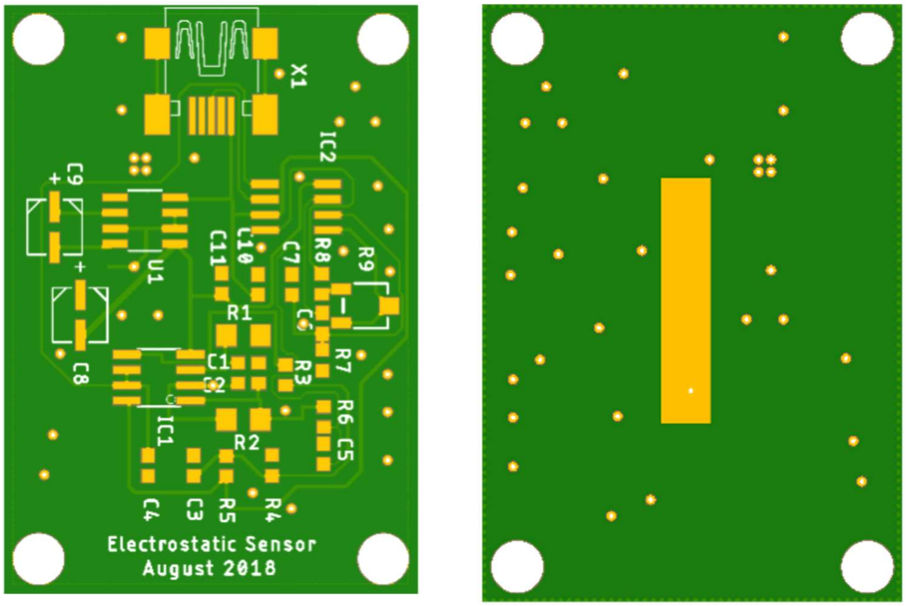

(a) (b)

Figure A.6.3 PCB preview. (a) Top preview. (b) Bottom preview.

Appendix B

Matlab Code

The following is an example of the sensor model simulation code written for Matlab software, and used to calculate the charge induced onto a sensor electrode and the sensor's characteristics by a given rotating strip charge with dimensions (L_mxW_m) at a distance s from the electrode.

```
% The below code calculates the sensor’s characteristics for variable
width of electrode. The same code can be used for variable length with
slight modifications.

clear all;
close all;
clc;

syms x t S h w Q y d wm

w=10;   %Angular speed in rad
D=0.06; %Diameter of the shaft in mm
s=D/30; %Distance between the electrode and the shaft
z=0;    %Position of the marker along the lengthwise axis of the shaft
L=D/3;  %Length of the electrode
W=D/10; %Width of the electrode
pii=pi;
fs=1000;%Sampling frequency

% Sensitivity equation from the mathematical model

Ss1=(1/(4*pi))*(atan((((0.5*L-z)*(0.5*W-0.5*D*cos(w*t+wm)))/((0.5*D+s-
0.5*D*sin(w*t+wm))*sqrt((((0.5*W-0.5*D*cos(w*t+wm))^2)+(0.5*D+s-
0.5*D*sin(w*t+wm))^2+(0.5*L-z)^2))))));

Ss2=(1/(4*pi))*(atan((((0.5*L+z)*(0.5*W-0.5*D*cos(w*t+wm)))/((0.5*D+s-
0.5*D*sin(w*t+wm))*sqrt((((0.5*W-0.5*D*cos(w*t+wm))^2)+(0.5*D+s-
0.5*D*sin(w*t+wm))^2+(0.5*L+z)^2))))));

Ss3=(1/(4*pi))*(atan((((0.5*L-z)*(0.5*W+0.5*D*cos(w*t+wm)))/((0.5*D+s-
0.5*D*sin(w*t+wm))*sqrt((((0.5*W+0.5*D*cos(w*t+wm))^2)+(0.5*D+s-
0.5*D*sin(w*t+wm))^2+(0.5*L-z)^2))))));

Ss4=(1/(4*pi))*(atan((((0.5*L+z)*(0.5*W+0.5*D*cos(w*t+wm)))/((0.5*D+s-
0.5*D*sin(w*t+wm))*sqrt((((0.5*W+0.5*D*cos(w*t+wm))^2)+(0.5*D+s-
0.5*D*sin(w*t+wm))^2+(0.5*L+z)^2))))));

Ss=Ss1+Ss2+Ss3+Ss4;

n=0;
for WM=-2*2*W/(D):2*4*W/((D)*64):2*2*W/(D);%64 point charges
```

```
    n=n+1;
    Wm=WM*D/2;
    dWm(n)=Wm/W;

      i=0;
      for  t1=0:1/fs:pi/w;
           i=i+1;
           k(i)=t1;
           Sen(n,i)=double(subs(Ss,[t wm],[t1 WM]));
      end
end

n1=(n+1)/2;
B=zeros(n1,length(k));
B(1,:)=Sen(n1,:);
j=0;
for j=2:n1;
    B(j,:)=B(j-1,:)+Sen(n1+1-j,:)+Sen(n1-1+j,:);
    j=j+1;
end

wid(1)=1;
for a=2:n1
 wid(a)=wid(a-1)+2;
end
B1=bsxfun(@rdivide,B*100,wid.');

width(1)=0;
for a=2:n1
 width(a)=dWm(n1+a-1)-dWm(n1-a+1);
end

Smax=max(B1(:,:).');
Is=diff(B.')*fs;

% Bandwidth of the output signal

g=0;
for u=1:n1;
    g=g+1;
bw(g) = powerbw(Is(:,g),fs);
end

% Power spectrum density of the output current

[Psd,F] = periodogram(Is,hanning(length(Is)),100*length(Is),fs);
maxpsd=max(Psd(:,:));
maxpsd1=max(Psd(:));
PsdN=Psd/maxpsd1;

% Calculation of the total sensitivity

Sens(1,:)=B1(5,:);
Sens(2,:)=B1(7,:);
Sens(3,:)=B1(4,:);
Sens(4,:)=B1(17,:);
Sensitivity=Sens.';
```

```
% Calculation of the induced current

IS=Is.';
Output(1,:)=IS(5,:);
Output(2,:)=IS(7,:);
Output(3,:)=IS(9,:);
Output(4,:)=IS(17,:);

% Calculation of the PSD

psdN=PsdN.';
PSD(1,:)=psdN(5,:);
PSD(2,:)=psdN(7,:);
PSD(3,:)=psdN(9,:);
PSD(4,:)=psdN(17,:);
PSDn=PSD.';

% Presentation of the results

figure
subplot(3,2,1)
plot(k(1:end),Sensitivity)
axis([-inf inf -inf inf])
title('Sensitivity (%)')
legend('Wm/W=1/2','Wm/W=3/4','Wm/W=1','Wm/W=2')
xlabel('Time(s)')
ylabel('Sensitivity (%)')

subplot(3,2,3)
plot(k(2:end),Output)
axis([-inf inf -inf inf])
title('Output signal')
legend('Wm/W=1/2','Wm/W=3/4','Wm/W=1','Wm/W=2')
xlabel('Time(s)')
ylabel('Output Current (a.u.)')

subplot(3,2,5)
plot(F,PSDn)
axis([0 40 -inf inf])
title('Normalised Power Spectral Density')
legend('Wm/W=1/2','Wm/W=3/4','Wm/W=1','Wm/W=2')
xlabel('Time(s)')
ylabel('Normalised PSD')

subplot(3,2,2)
plot(width,Smax)
axis([0 4 -inf inf])
title('Maximum Sensitivity for variable Wm/W')
xlabel('Wm/W')
ylabel('Max Sensitivity (%)')

subplot(3,2,4)
plot(width,maxpsd)
title('Maximum Power Spectral Density for variable Wm/W')
xlabel('Wm/W')
ylabel('Max PSD (a.u.)')
```

```
subplot(3,2,6)
xq = 0:0.1:4;
p = polyfit(width,bw,4);
f1 = polyval(p,xq);
plot(xq,f1);
title('Bandwidth for variable Wm/W')
xlabel('Wm/W')
ylabel('Bandwidth')
```

Publications from This Work

The following publications were produced during the course of the work leading to the preparation of this thesis.

Articles published in journals

1. K. Reda and Y. Yan, “An Improved Method for the Processing of Signals Contaminated With Strong Common-Mode Periodic Noise in Correlation Velocity Measurement,” IEEE Sensors Letters, Vol. 3, No. 7, pp. 7001404, July 2019.
2. K. Reda and Y. Yan, “Vibration Measurement of an Unbalanced Metallic Shaft Using Electrostatic Sensors”, IEEE Transactions on Instrumentation & Measurement, Vol. 68, No. 5, PP. 1467-1476, 2018.
3. L. Wang, Y. Yan and K. Reda, “Comparison of single and double electrostatic sensors for rotational speed measurement,” Sensors and Actuators, Vol. 266, No. 15, pp. 46–55, 2017.

Articles in conference proceedings

1. L. Wang, Y. Yan and K. Reda, “Enhancing the performance of a rotational speed measurement system through data fusion,” Journal of Physics: Conference Series, Vol. 1065, No. 7, pp. 1-4, August 2018.
2. K. Reda and Y. Yan, “Online continuous detection of an unbalanced metallic shaft using electrostatic sensors,” in proc. of IEEE Instrumentation and Measurement Technology Conference (I2MTC), pp. 2073-2078, Houston, USA, 14-17 May 2018.
3. K. Reda, Y. Yan and L. Wang, “A comparative study of different shaped electrostatic sensors for rotational speed measurement,” in proc. of IEEE SENSORS, pp. 819-821, Glasgow, Scotland, 29 Oct-1 Nov 2017.

IEEE
Sensors Letters VOL. 3, NO. 7, JULY 2019

IEEE Sensors Council

An Improved Method for the Processing of Signals Contaminated With Strong Common-Mode Periodic Noise in Correlation Velocity Measurement

Kamel Reda* and Yong Yan**

School of Engineering and Digital Arts, University of Kent, Canterbury CT2 7NT, U.K.
**Member, IEEE*
***Fellow, IEEE*

Manuscript received May 10, 2019; revised June 7, 2019; accepted June 20, 2019. Date of publication June 28, 2019; date of current version July 15, 2019.

Abstract—Electrostatic sensors have been successfully used for the velocity measurement of pneumatically conveyed particles and the rotational speed measurement. However, the signal from an electrostatic sensor is usually vulnerable and susceptible to contamination in a hostile environment. The acquired original signal may be contaminated by different types of noise that can be within or outside the frequency range of the signal. This article presents a novel correlation signal processing method to minimize the impact of noise in the signal through a denoising process and, hence, improve the performance of correlation-based measurements in general. The method is applied to the rotational speed measurement based on electrostatic sensors in particular. The denoising process is an essential task in digital signal processing to improve the signal-to-noise ratio before implementing the measurement algorithm. A hybrid denoising method is proposed to combine a cutoff frequency method to remove the noise components outside the signal bandwidth and a median filter to smooth the signal. Subsequently, the signal is denoised in the time domain by employing an advanced digital filtering method based on correlation techniques to suppress the noise frequency components mixed with the original signal. The rotational speed measurement system with the proposed technique has proven to be effective in denoising signals that are buried in noise with which they are correlated. Moreover, the technique is capable of producing more accurate and repeatable measurements with a wider measurement range than the existing system. Experimental results suggest that the relative error of the improved system is mostly within ±0.1% over the speed range of 300–3000 r/min and within ±0.2% over the speed range of 40–300 r/min.

Index Terms—Sensor signal processing, buried signal, correlation measurement, denoising, electrostatic sensors, rotational speed.

I. INTRODUCTION

Correlation techniques have been applied extensively and successfully in multiphase flow measurement over the past two decades [1]–[3]. In recent years extensive research and experimental investigations have been conducted on the use of electrostatic sensors in conjunction with correlation signal processing techniques for rotational speed measurement [4]–[6]. Experimental results have shown a maximum error of no greater than ±1.5% over the speed range from 500 to 3000 r/min. Much more recently, the method has been developed further by incorporating a data fusion algorithm, capable of producing more accurate measurements with a maximum error within ±0.5% over the range of 200 to 3000 r/min [7]. Although the proposed electrostatic sensing technique has successfully achieved a rotational measurement for rotary shafts, it has some limitations that will be dealt with in this article. The existing electrostatic sensors depend primarily on the rotational speed, material properties, and surface conditions of the shaft [4]. Consequently, the speed measurement is susceptible to environmental conditions, among which humidity, vibration, and electromagnetic interferences are considered to be the main factors. In a hostile environment and at low rotational speed (<200 r/min), the signal-to-noise ratio may deteriorate as the induced electrostatic charge on the electrode decreases with the discharge effect and in the presence of strong noises, making the system ineffective for low rotational speed measurement. This article is based on the previous work and concentrates on the improvement of the performance of the measurement system. The proposed system aims at providing more accurate and repeatable measurements over a wider range of rotational speeds. To tackle the aforementioned challenge, additional signal processing strategies are implemented to improve the performance of the measurement system. The proposed technique uses dual electrostatic sensors coupled with an improved signal processing algorithm to enhance the signal-to-noise ratio and to widen the measurement range. The basic principle and the detailed structure of the rotational speed measurement system based on dual electrostatic sensors have been reported previously [5]. The rotational speed is derived from the period (T) of the sensor output signals or from the time delay (τ) between them. Moreover, both (T) and (τ) can be determined from the autocorrelation and cross correlation of the output signals, respectively. A series of experiments was conducted on purpose-built test rigs to evaluate the performance of the improved system in terms of accuracy, repeatability, rangeability, and robustness.

II. SIGNAL ANALYSIS AND DENOISING APPROACH

A. Signal Analysis

The output signal from an electrostatic sensor is a random and low-pass signal as shown in Fig. 1. The signal is also periodic due to the rotational motion. Its bandwidth depends on the geometric properties of the electrode and size of the rotor [8]. The bandwidth is proportional to the rotational speed [8]. Fig. 1 shows a typical noise-free signal and the corresponding spectrum.

The signal from the electrostatic sensor is usually weak. Thus, various extrinsic and intrinsic noises can be superimposed on it, resulting in a contaminated signal at the output of the conditioning circuit. In some extremely poor conditions, the signal can be partly or totally

Corresponding author: Yong Yan (y.yan@kent.ac.uk).
Associate Editor: F. Costa.
Digital Object Identifier 10.1109/LSENS.2019.2925665

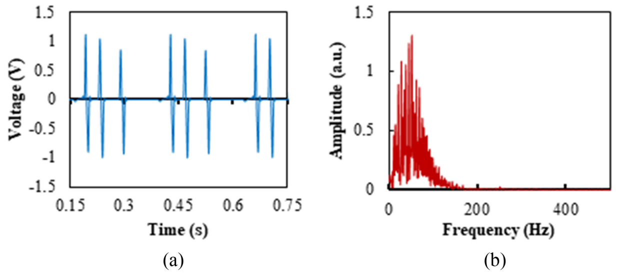

Fig. 1. Typical example of a noise-free signal and corresponding frequency spectrum at 200 r/min. (a) Noise-free signal. (b) Power spectrum of signal.

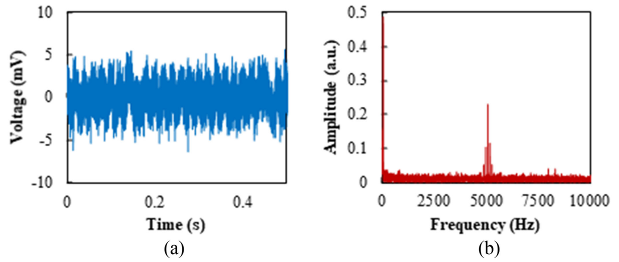

Fig. 2. Typical example of a noisy signal and corresponding frequency spectrum. (a) Noisy signal. (b) Power spectrum of the noisy signal.

buried in a strong noise (see Fig. 2). This additive noise significantly degrades the quality of the signal, which can be crucial for signal processing, as a contaminated signal leads to erroneous measurement results.

The types of the source noise that are mixed with the original signal need to be considered when selecting denoising methods. Generally, the acquired signal is contaminated by different types of noise that can be within or outside the frequency range of the original signal. In some extremely poor conditions, the signal is correlated with noises in which it is buried. The most common sources of noise are the power line interference, vibration of the mechanical system, and intrinsic random noise. Power line interference originates primarily from the electromagnetic field of the power lines and the improper grounding of the signal conditioning circuit. The power line noise is centered at 50 or 60 Hz with a bandwidth no more than 1 Hz and is mostly rejected by the earthed metal screen of the sensor [9], [10]. However, adding a screen to cover the electrode and signal conditioning circuit cannot completely reject the external electrical interference. Furthermore, a traditional notch filter cannot be used to remove the residual noise since its frequency component (50 or 60 Hz) may be within the spectrum of the original signal. Thus, a more advanced digital filtering method needs to be employed to suppress this residual noise. The second type of noise that may contaminate the signal is due to the vibration of the mechanical system. Although the adopted method of signal acquisition (current-to-voltage convertor) does not require consideration of the stray capacitance of the electrode in the acquisition circuit, it is still sensitive to the vibration of the sensor and the connecting cable between the sensor and the data acquisition unit. Even tiny displacements of charge in connecting cables due to physical handling can produce current large enough to cause significant noise in the system. The interference frequency of this type of noise is usually composed of the main rotational frequency and its harmonics in addition to high-frequency components due to vibration of the connecting cables. Finally, intrinsic noise can be superimposed on the original signal from the signal conditioning circuit. This noise is approximated to white noise which has a continuous frequency spectrum distribution. For that reason, the signal conditioning circuit was designed with extremely low noise using high-performance components

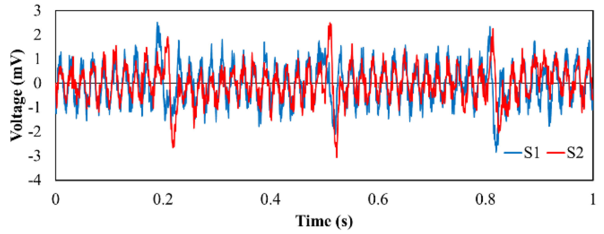

Fig. 3. Filtered signals S_{1nf} and S_{2nf} from a dual electrostatic sensor.

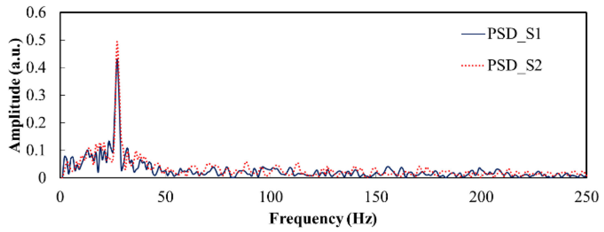

Fig. 4. Spectra of the filtered signals in Fig. 3.

[11]. Additionally, a low-pass filter was added to the preprocessing to eliminate the high-frequency noise.

B. Filtering of High-Frequency Noise

Although the signal conditioner comprises a low-pass filter that helps to remove high-frequency noise, nevertheless, other types of noise cannot be suppressed by the analogue circuit. To address this problem, a digital filtering algorithm is proposed which combines a cutoff frequency method based on the Fourier transform and a median filter, to remove the high-frequency noise components and also to smooth the signal. A fifth-order IIR Butterworth filter is employed to suppress noise outside the signal bandwidth. Then, a median filter with a window size of 50 is applied to smooth the signal. Figs. 3 and 4 show a typical example of the filtered signals S_{1nf} and S_{2nf} and the corresponding power spectra, respectively. The periodicity of the signals, due to the continuous motion of the shaft, becomes apparent after applying the low-pass filter.

Figs. 5 and 6 illustrate the autocorrelation function of the filtered signal S_{1nf} and the cross-correlation function of the two filtered signals S_{1nf} and S_{2nf}. The two correlation functions show that the filtered signals are still buried in strong noise since the dominant peaks, from which the periodicity of the signals is determined, are not clearly defined and stable. Although high-frequency noise has been eliminated using digital low-pass filters, the filtered signals are still contaminated with noises that may be correlated with the original signals, and their spectra are within the frequency band of the original signals. Thus, a simple cutoff frequency method is not sufficient to remove such types of noise, making the measurement invalid. Therefore, the filtered signals should be further denoised using an advanced digital filtering method to remove the frequency components mixed with the desired signal.

C. Filtering of Common Mode Noise

The proposed sensing system for rotational speed measurement is based on a dual electrostatic sensor, comprising two electrodes and connected to two independent conditioning circuits [5]. Consequently, the dual sensor derives two signals $S_1(t)$ and $S_2(t)$, similar to each other apart from the time delay between them (see Fig. 3). Since the electrodes and conditioning circuits of the two sensors are almost identical, it can be assumed that they are exposed to common mode noises which they may be correlated with, and their spectra are within the spectrum of the signal. Noises due to power line interference and vibration of the rig can be considered as common mode noise.

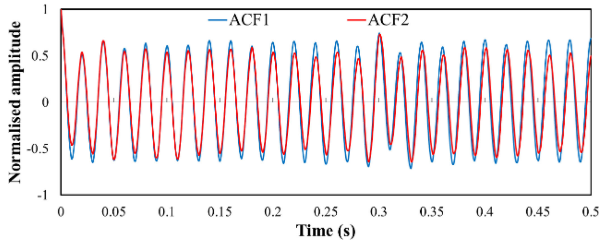

Fig. 5. Autocorrelation functions of the filtered signal S_{1nf} and S_{2nf}.

Thus, employing a method to reduce the common mode noise would suppress most of these noises.

The autocorrelation function ($R_{S_1S_1}$) of the noise-free signal $S_1(t)$ and the cross-correlation function ($R_{S_1S_2}$) of the noise-free signals $S_1(t)$ and $S_2(t)$ can be written as follows:

$$R_{S_1S_1}(m) = \sum_{k=1}^{N} S_1(k)S_1(k+m) \tag{1}$$

$$R_{S_1S_2}(m) = \sum_{k=1}^{N} S_1(k)S_2(k+m) \tag{2}$$

where N is the number of samples in the correlation computation, and m ($m = 0, \ldots, N$) is the number of delayed points.

If, however, the two signals ($S_1(t)$) and ($S_2(t)$) are contaminated with a strong common mode periodic noise $n(t)$ with which they are correlated, the autocorrelation function ($R_{S_{1n}S_{1n}}$) of the noisy signal ($S_{1n}(t)$) and the cross-correlation function ($R_{S_{1n}S_{2n}}$) of the noisy signals $S_{1n}(t)$ and $S_{2n}(t)$, become

$$R_{S_{1n}S_{1n}}(m) = \sum_{k=1}^{N} S_{1n}(k)S_{1n}(k+m) \tag{3}$$

$$R_{S_{1n}S_{1n}}(m) = \sum_{k=1}^{N} [(S_1(k)+n(k))(S_1(k+m)+n(k+m))] \tag{4}$$

$$R_{S_{1n}S_{1n}}(m) = \sum_{k=1}^{N} S_1(k)S_1(k+m) + \sum_{k=1}^{N} S_1(k)n(k+m) + \sum_{k=1}^{N} n(k)S_1(k+m) + \sum_{k=1}^{N} n(k)n(k+m) \tag{5}$$

$$R_{S_{1n}S_{1n}}(m) = R_{S_1S_1}(m) + R_{S_1n}(m) + R_{nS_1}(m) + R_{nn}(m) \tag{6}$$

$$R_{S_{1n}S_{2n}}(m) = \sum_{k=1}^{N} S_{1n}(k)S_{2n}(k+m) \tag{7}$$

$$R_{S_{1n}S_{2n}}(m) = \sum_{k=1}^{N} ((S_1(k)+n(k))(S_2(k+m)+(n(k+m))) \tag{8}$$

$$= \sum_{k=1}^{N} S_1(k)S_2(k+m) + \sum_{k=1}^{N} S_1(k)n(k+m) + \sum_{k=1}^{N} n(k)S_2(k+m) + \sum_{k=1}^{N} n(k)n(k+m) \tag{9}$$

$$R_{S_{1n}S_{2n}}(m) = R_{S_1S_2}(m) + R_{S_1n}(m) + R_{nS_2}(m) + R_{nn}(m) \tag{10}$$

where $S_{1n}(k)$ and $S_{2n}(k)$ are the digitized signals $S_{1n}(t)$ and $S_{2n}(t)$, respectively.

The correlation terms $R_{S_{1n}}$, R_{nS_1}, R_{nS_2}, and R_{nn} are problematic, in particular, when the signal-to-noise ratio is relatively low, as these terms do not tend to zero, because the noise $n(t)$ is periodic and correlates with the original signals ($S_1(t)$ and $S_2(t)$). The effect of the strong noise $n(t)$ can be clearly observed in Figs. 5 and 6 where the peaks of the autocorrelation and cross-correlation functions are completely obscured by the periodic correlation effects caused by the periodic noise in the signals. In this case, the rotational speed measurement is invalid.

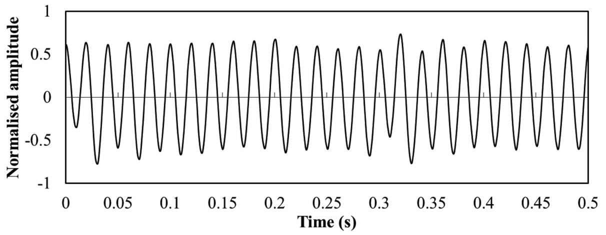

Fig. 6. Cross-correlation function of the two filtered signals S_{1nf} and S_{2nf}.

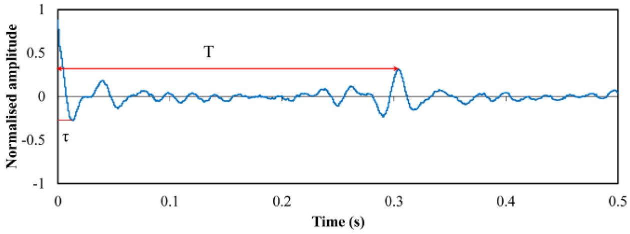

Fig. 7. Modified correlation function of the two filtered signals S_{1nf} and S_{2nf}.

To solve this problem, consider the cross-correlation function between S_{1n} and ($S_{1n} - S_{2n}$)

$$R_{S_{1n}(S_{1n}-S_{2n})} = R_{(S_1+n)(S_1-S_2)} = R_{S_1S_1} - R_{S_1S_2} + R_{nS_1} - R_{nS_2} \tag{11}$$

and the cross-correlation function between S_{2n} and ($S_{1n} - S_{2n}$)

$$R_{S_{2n}(S_{1n}-S_{2n})} = R_{(S_2+n)(S_1-S_2)} = R_{S_2S_1} - R_{S_2S_2} + R_{nS_1} - R_{nS_2}. \tag{12}$$

Then, subtracting (12) from (11)

$$R_{\mathrm{mod}} = R_{S_1S_1} + R_{S_2S_2} - R_{S_1S_2} - R_{S_2S_1} \tag{13}$$

where R_{mod} is the modified correlation function of the two noisy signals S_{1n} and S_{2n}.

Equation (13) shows that the modified correlation function R_{mod} is composed only by the autocorrelation and cross-correlation functions of the noise-free signals (S_1) and (S_2). Fig. 7 illustrates the modified correlation function. It is worth noting that the peaks of $R_{S_1S_1}$ and $R_{S_2S_2}$ are located at the same time lag, i.e., the period of the periodic noises (T). Additionally, the peaks of the cross correlation $R_{S_1S_2}$ and $R_{S_2S_1}$ are inverted in (13) and are located at the time lags τ and (T-τ), respectively (see Fig. 7). T and τ denote the period of the two signals and the time delay between them, respectively. As a result, the modified correlation function of the noisy signals has significantly removed the effects due to the periodic noises and the correlation peaks become more apparent, enabling the determination of the rotational speed.

It is worth noting that the height of the correlation peaks is affected by the level of the white noise superimposed on the original signal.

III. EXPERIMENTAL VALIDATION

Experimental tests were conducted on two purpose-built test rigs [11] as shown in Fig. 8 to validate the performance of the improved measurement system against an optical tachometer as a reference meter. The sensor output signals are sampled at a frequency of 50 kHz using a high-performance data acquisition unit (NI USB-6351) with

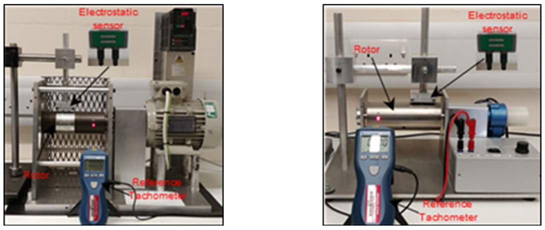

(a) (b)

Fig. 8. Test rig. (a) Test rig for 300–3000 r/min. (b) Test rig for 0–300 r/min.

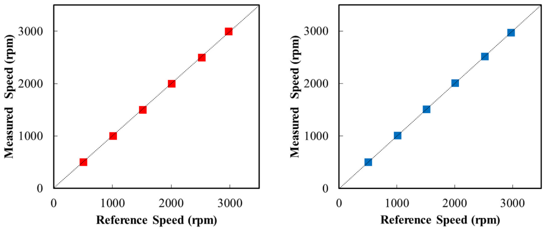

(a) (b)

Fig. 9. Comparison of measured speeds up to 3000 r/min. (a) Conventional correlation method. (b) Modified correlation method.

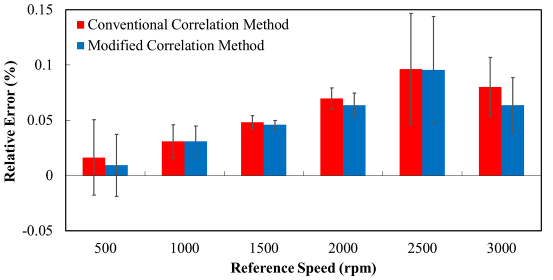

Fig. 10. Relative error of the measured rotational speed.

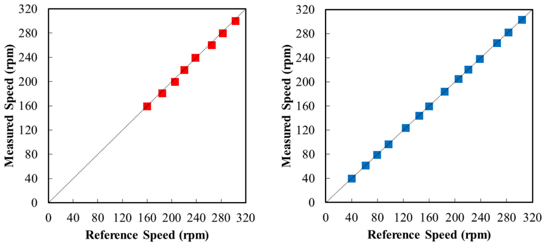

(a) (b)

Fig. 11. Comparison of measured speeds up to 300 r/min. (a) Conventional correlation method. (b) Modified correlation method.

16-b ADC and processed on a host computer through an optimized code using LabView [5], [11]. The speed measurement using the proposed method and conventional method are plotted in Fig. 9. Each measured speed is the average of 20 instantaneous measurements.

It can be seen that the two methods can achieve the rotational speed measurements over the range between 500 and 3000 r/min. However, the proposed method outperforms the conventional one in terms of accuracy as shown in Fig. 10. The relative error using the modified correlation method is within ±0.1% and with a repeatability of $<0.05\%$, compared with $<0.33\%$ in the data fusion method [7].

A second series of experiments was conducted for the speed range from 40 to 300 r/min. Fig. 11 shows that the lower end range of the conventional method is 160 r/min, whereas the proposed method can achieve valid measurements down to 40 r/min with a relative error within ±0.2% and a maximum repeatability of 0.7% (see Fig. 12).

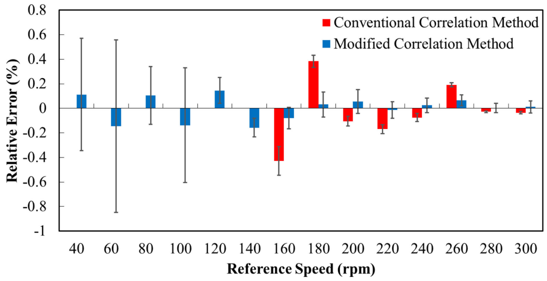

Fig. 12. Relative error of the measured speed for low speed range.

IV. CONCLUSION

A denoising method for signals used in correlation measurement systems has been proposed and evaluated. The improved correlation technique has been shown to improve the performance and enhance the robustness of the rotational speed measurement system. The modified correlation method has proven to be effective in a replicated hostile environment where the original signals are contaminated with correlated strong common-mode periodic noises. This technique is suitable for any correlation-based measurement where there is strong periodic noise. The lab-scale experimental results have demonstrated that the measurement error is within ±0.2% over the speed range from 40 to 3000 r/min with a repeatability of $<0.7\%$. Additionally, the lower end of the measurement range has been extended from 160 to 40 r/min. The advantages of this technique over the conventional method are more demonstrable when the signal-to-noise ratio is very low and where the peak in the conventional correlation function is not apparent and stable. Field trials should be conducted in the near future to assess the effectiveness of the improved system under practical conditions.

REFERENCES

[1] Y. Liu, Y. Zhang, Z. Cao, and L. Xu, "An adaptive algorithm for cross-correlation velocity measurement," in *Proc. 8th IEEE Int. Symp. Instrum. Control Technol.*, London, U.K., Jul. 2012, pp. 96–100.

[2] J. Gajewski, "Accuracy of cross correlation velocity measurements in two-phase gas–solid flows," *Flow Meas. Instrum.*, vol. 30, pp. 133–137, 2013.

[3] Z. Cui, H. Wang, W. Yin, and W. Yang, "Flow velocity measurement by cross-correlation with tailored modulation," in *Proc. IEEE Int. Instrum. Meas. Technol. Conf.*, May 2015, pp. 1906–1909.

[4] L. Wang, Y. Yan, Y. Hu, and X. Qian, "Rotational speed measurement through electrostatic sensing and correlation signal processing," *IEEE Trans. Instrum. Meas.*, vol. 63, no. 5, pp. 1190–1199, May 2014.

[5] L. Wang, Y. Yan, Y. Hu, and X. Qian, "Rotational speed measurement using single and dual electrostatic sensors," *IEEE Sensors J.*, vol. 15, no. 3, pp. 1784–1793, Mar. 2015.

[6] L. Li *et al.*, "Use of double correlation techniques for the improvement of rotation speed measurement based on electrostatic sensors," *Meas. Sci. Technol.*, vol. 27, 2016, Art. no. 025004.

[7] L. Wang, Y. Yan, and K. Reda, "Enhancing the performance of a rotational speed measurement system through data fusion," in *Proc. IOP J. Phys., Conf. Ser.*, Sep. 2018, vol. 1065, pp. 1–1.

[8] L. Wang and Y. Yan, "Mathematical modelling and experimental validation of electrostatic sensors for rotational speed measurement," *Meas. Sci. Technol.*, vol. 25, no. 11, 2014, Art. no. 115101.

[9] J. Gajewski, "Non-intrusive solids charge and mass flow measurements with an electrostatic flow probe," *J. Electrostatics*, vol. 46, no. 4, pp. 271–284, 1999.

[10] C. Xu *et al.*, "Sensing characteristics of electrostatic inductive sensor for flow parameters measurement of pneumatically conveyed particles," *J. Electrostatics*, vol. 65, no. 9, pp. 582–592, 2007.

[11] K. Reda and Y. Yan, "Vibration measurement of an unbalanced metallic shaft using electrostatic sensors," *IEEE Trans. Instrum. Meas.*, vol. 68, no. 5, pp. 1467–1476, May 2019.

Vibration Measurement of an Unbalanced Metallic Shaft Using Electrostatic Sensors

Kamel Reda and Yong Yan, *Fellow, IEEE*

***Abstract*— Vibration measurement of a rotary shaft is essential for the diagnosis and prognosis of industrial rotating machinery. However, the imbalance of a shaft, as quantified through vibration displacement, is the most common cause of machine vibration. The objective of this paper is to develop a novel technique through electrostatic sensing for the online, continuous and noncontact displacement measurement of a rotary shaft due to imbalance faults. A mathematical model is established to extract useful information about the shaft displacement vibration from the simulated signal in the frequency domain. Experimental tests were conducted on a purpose-built test rig to measure the displacement vibration of the shaft. An eccentric shaft was tested with the output signal from the electrostatic sensor analyzed. The effectiveness of the proposed method is verified through computer simulation and experimental tests. Results obtained indicate that the measurement system yields a relative error of within ±0.6% in the displacement measurement.**

***Index Terms*— Displacement, electrostatic sensors, fault detection, imbalance, rotating machinery, vibration.**

I. INTRODUCTION

VIBRATION measurement of rotary shafts plays a significant part in the condition monitoring of rotating machinery. A variety of mechanical defects, such as shaft imbalance, coupling misalignment, and bearing deterioration, may give rise to excessive vibrations that cause machine failure. Imbalance is the most common cause of vibrations of rotating machines. In practice, shafts can never be perfectly balanced because of manufacturing errors such as porosity in casting, nonuniform density of material, manufacturing tolerances, and gain or loss of material during operation. An unbalanced shaft makes it more susceptible to high-amplitude vibrations that cause noise and incorrect functionality and thus reduces the lifespan of the machine.

There is a range of techniques available for shaft vibration detection through the measurement of displacement, velocity, or acceleration [1]–[4]. However, in certain cases where the mass of the machine casing is much greater than that of the shaft or rotor, conventional contact type sensors such as accelerometers and velocity transducers may not be suitable for detecting the vibration of the shaft [3]. Noncontact type sensors are desirable in such cases. Several types of proximity sensors based on eddy current, ultrasonic, capacitive, or inductive principles are often used to measure the relative vibration of a rotating shaft [5], [6]. Recently, a number of new methods have been proposed for shaft vibration detection. Tong *et al.* [7] designed a reflective intensity-modulated noncontact optical fiber sensing system to detect the radial vibration of high-speed rotating machinery. Vyroubal [8] identified the vibration signature using optical sensors through spectral analysis of phase-modulated light pulses. Okabe and Tanaka [9] described an ultrasonic sensor-based method for shaft vibration detection by measuring the propagation time of the ultrasonic wave from the sensor to the shaft surface. Sophisticated optical sensors can be designed to operate in a harsh environment and can perform noncontact displacement measurement with high sensitivity and resolution. However, such devices are prohibitively expensive for routine industrial applications. Much more recently, Wang *et al.* [10] employed electrostatic sensors for the vibration detection of rotating machinery. Later, they proposed a method for the radial vibration measurement of a shaft using electrostatic sensors and Hilbert–Huang transform [11]. However, both methods were based on the amplitude of the output signal resulting from electrostatic charge on the surface of a rotating dielectric shaft, assuming that the only factor affecting the amount of induced charge, and hence, the signal amplitude is the distance between the electrode and the shaft. Nevertheless, the electric charge level on the dielectric shaft surface depends significantly on environmental conditions and consequently the signal amplitude varies with environmental factors such as ambient temperature and relative humidity [12], [13]. As a result, these methods cannot be used to achieve an absolute displacement measurement due to the uncertain amount of charge on the shaft surface. Moreover, these methods work only on dielectric shafts and require an array of sensors to be installed around the shaft, making the sensor installation practically difficult.

This paper presents a novel technique to measure the vibration caused by an unbalanced shaft by applying a magnitude-independent method in the frequency domain with the use of electrostatic sensors. The proposed method is based on the frequency properties of the sensor signal, rather than its amplitude to quantify the shaft displacement. This method and, hence, the measurements are independent of the level of the accumulated charge on the shaft surface, which makes

Manuscript received July 23, 2018; revised October 4, 2018; accepted November 11, 2018. This work was supported by the University of Kent. The Associate Editor coordinating the review process was Subhas Mukhopadhyay. *(Corresponding author: Yong Yan.)*

The authors are with the School of Engineering and Digital Arts, University of Kent, Canterbury CT2 7NT, U.K. (e-mail: kr314@kent.ac.uk; y.yan@kent.ac.uk).

Color versions of one or more of the figures in this paper are available online at http://ieeexplore.ieee.org.

Digital Object Identifier 10.1109/TIM.2018.2882900

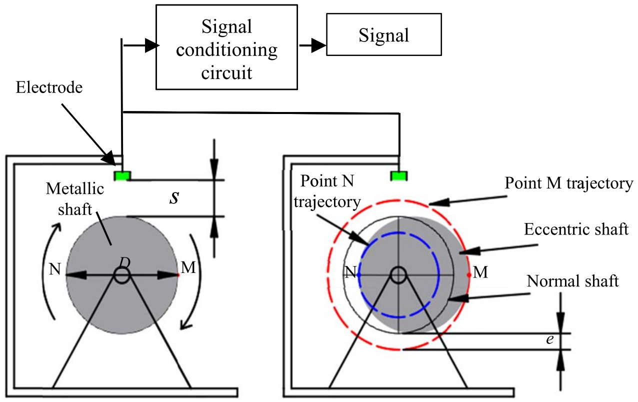

(a) (b)

Fig. 1. Physical model of the sensing system. (a) Normal shaft. (b) Eccentric shaft.

the measurement system more stable and reliable in harsh industrial environments. In addition, the proposed technique can work on metallic shafts and uses only a single electrostatic sensor. The shaft imbalance detection method along with preliminary experimental results was presented at the 2018 International Instrumentation and Measurement Technology Conference [14]. This paper presents in detail the principle of the vibration displacement measurement of an unbalanced shaft along with experimental results. Mathematical modeling of the sensing system is also established to study the frequency response characteristics of an eccentric metallic shaft.

II. MEASUREMENT PRINCIPLE

Fig. 1 shows a simplified physical model of the electrostatic sensing system for displacement measurement. The physical model consists of a metallic shaft, electrically isolated point charges fixed on the shaft surface (e.g., points M and N), an electrostatic electrode, and associated signal conditioning circuit.

A small electrostatically charged marker made of electret film with an area of 4 mm^2 is fixed on the metallic shaft. The marker simulates a point charge on the shaft surface. An electrostatic sensor consists of an insulated electrode with a suitable charge detection circuit can detect the charge on the marker and generate an output signal through electrostatic induction. Wang and Yan [15] show that the frequency response of the sensor output depends primarily on the circular trajectory diameter D of a rotating point charge fixed on the shaft surface (points M or N in Fig. 1), the distance s between the point charge and the electrode, and the angular speed of the shaft. For a given point charge on the shaft, the rotational motion results in a circular trajectory of the point charge. In the case of a normal shaft, the shortest distance between any rotating point on the shaft and the electrode is constant, as is its trajectory diameter, which is equal to D. While each point on an eccentric shaft rotates along a different circular trajectory and results in a variation in the distance s. By analyzing the frequency response of the output signal, the displacement and, hence, the imbalance of the shaft can be quantified. When n identical markers (e.g., $M_1, \ldots, M_8$) are fixed around the shaft, the output signal is then composed of n pulses corresponding to the n markers, as shown in Fig. 2.

It is worth noticing that the markers M_1 and M_5 correspond to the shortest and longest distance from the shaft surface to the electrode, respectively (points M and N in Fig. 1).

It can be seen from Fig. 2 that the distance between M_4 and the center of rotation is equal to that between M_6 and the center of rotation. Similar dispositions exist with respect to points M_3–M_7 and M_2–M_8. Consequently, the pulses resulting, respectively, from M_6, M_7–M_8, and M_4, M_3–M_2 are identical. Therefore, it would be sufficient to analyze the first five pulses (M_1–M_5) which are distributed over the semicircumference of the shaft. The output signal is first decomposed in the time domain into single pulses corresponding to the markers fixed on specific locations around the shaft. The corresponding spectra are plotted in Fig. 4. However, the decomposition should be performed under the assumption that the pulses resulting from the markers (point charges) do not overlap with each other. Accordingly, the number and arrangement of the markers should be well defined in order to satisfy this condition. The number and arrangement of the markers around the shaft depend primarily on the shaft diameter, angular speed to be measured and the size of the markers.

Fig. 4 shows that, when a point charge on the shaft surface rotates closer to the electrode (e.g., M_1), the frequency at the spectrum crest (f_{sc1}) has a higher value than that of a point charge rotating farther to the electrode. When a point charge rotates closer to the electrode, the electrode covers a smaller area of the electric field, and the induction occurs for a shorter period and subsequently gives rise to a signal of higher frequency. As a result, the closer the distance between the electrode and the shaft surface, the more the induced charge on the electrode and the higher the frequency.

The magnitude frequency response of the decomposed output signals (Fig. 3) due to different point charges on an eccentric shaft (different displacements), rotating at a constant speed, shows different frequencies at the peak of spectra or the frequency at the spectrum crest (f_{sc}) (Fig. 4). Therefore, the displacement can be derived from f_{sc}.

III. MATHEMATICAL MODELING OF THE SENSOR

A. Mathematical Model of the Sensor

A mathematical model of the electrostatic sensing system for the rotational motion of an electrostatic point charge should be established in order to study the sensing characteristics of the sensor. From the developed model, we can derive an analytical relationship between the displacement s and the characteristics of the sensor in the frequency domain. Fig. 5 shows an overview of the sensing arrangement in the mathematical modeling. The circle C in Fig. 5 indicates a cross section of a metallic shaft with a diameter D, on which an electrically insulated point charge is fixed. The rotational motion of the point charge at angular speed ω creates, in effect, an impulse input to the sensing system. A strip-type electrode with dimensions L × W, made on a small printed circuit board (PCB) with adequate insulation together with grounding around the electrode, can be regarded as a piece of perfectly conductive metal and is placed at distance s from the shaft.

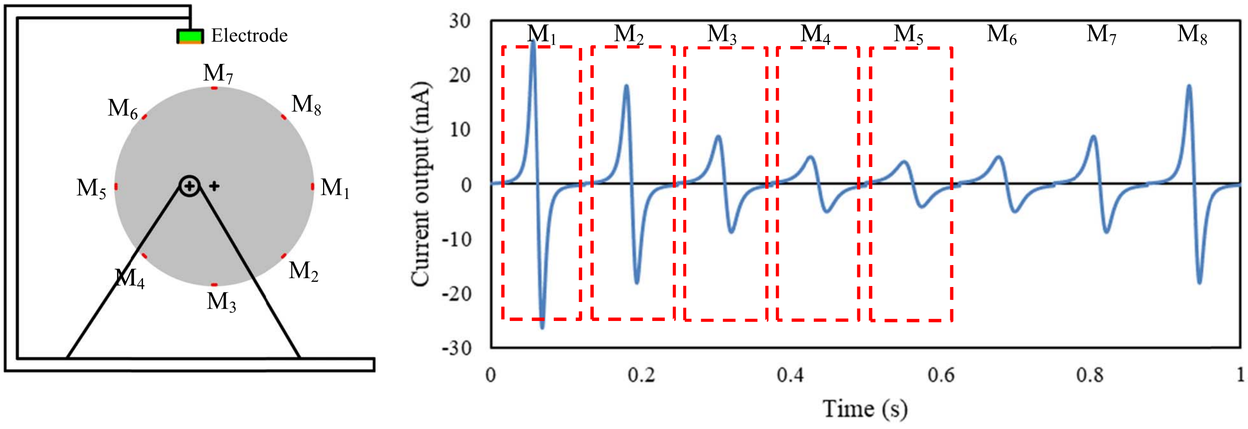

(a) (b)

Fig. 2. Distribution of markers on the shaft and corresponding output signal results over one revolution (speed = 60 r/min). (a) Markers on the shaft. (b) Sensor output signal.

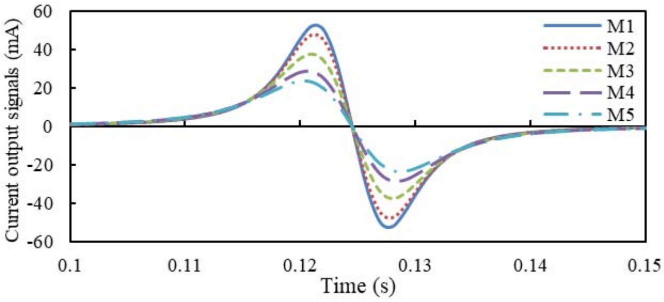

Fig. 3. Decomposition of the output signal into five single pulses.

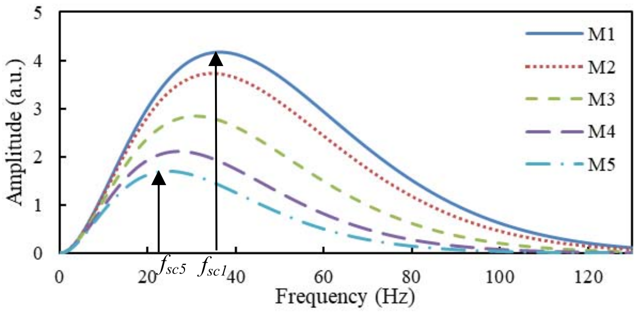

Fig. 4. Amplitude spectra of the decomposed pulses.

Based on Gauss's law, the total induced charge Q on the surface of the electrode due to the rotating charge q on the shaft is given by [15]

$$Q(t) = \frac{-q}{2\pi}\int_{-\frac{W}{2}}^{+\frac{W}{2}}\int_{-\frac{L}{2}}^{+\frac{L}{2}} \times \frac{0.5D+s-0.5D\sin\omega t}{((z-0.5D\cos\omega t)^2+(0.5D+s-0.5D\sin\omega t)^2+x^2)^{\frac{3}{2}}} \times dx\,dz. \tag{1}$$

Then, expression (2), shown at the bottom of this page, is obtained. Taking D as the basic dimensional unit in the sensing system and W, L, and s can all be normalized with reference to D, the total charge $Q(t)$ is obtained in (3), shown at the bottom of this page, where $\beta_i = \mathrm{sgn}(i-1.5), \delta_L = (L/D), \delta_W = (W/D), \delta_s = (d/D)$.

If the electrode is connected to a signal conditioning circuit, as shown in Fig. 6, that converts the induced charge into an induced current, then the actual current output $I_s(t)$ of the sensor is thus,

$$I_s(t) = \frac{dQ(t)}{dt}. \tag{4}$$

B. Impulse and Frequency Response of the Sensor

A point charge approaching toward the electrode along a circular trajectory from infinity is equivalent to an impulse

---

$$Q(t) = \frac{-q}{2\pi}\sum_{i=1}^{2}\arctan\left[\frac{0.5L(0.5W+0.5D\beta_i\cos\omega t)}{(0.5D+s-0.5D\sin\omega t)\sqrt{\begin{array}{l}(0.5D+s-0.5D\sin\omega t)^2\\+(0.5W+0.5D\beta_i\cos\omega t)^2+(0.5L)^2\end{array}}}\right] \tag{2}$$

$$Q(t) = \frac{-q}{2\pi}\sum_{i=1}^{2}\arctan\left[\frac{0.5\delta_L(0.5\delta_w+0.5\beta_i\cos\omega t)}{(0.5+\delta_s-0.5\sin\omega t)\sqrt{\begin{array}{l}(0.5+\delta_s-0.5\sin\omega t)^2\\+(0.5\delta_w+0.5\beta_i\cos\omega t)^2+(0.5\delta_L)^2\end{array}}}\right] \tag{3}$$

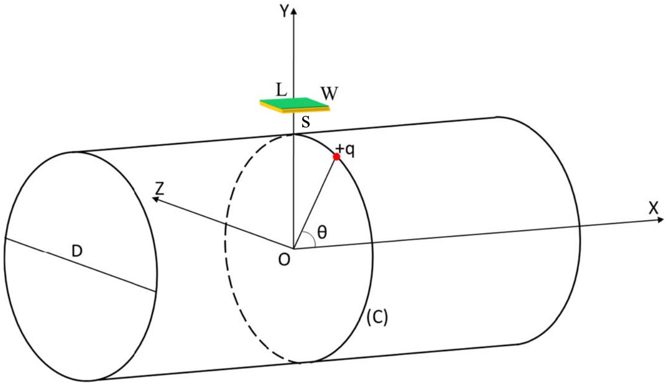

Fig. 5. Electrostatic sensing arrangement in the mathematical modeling.

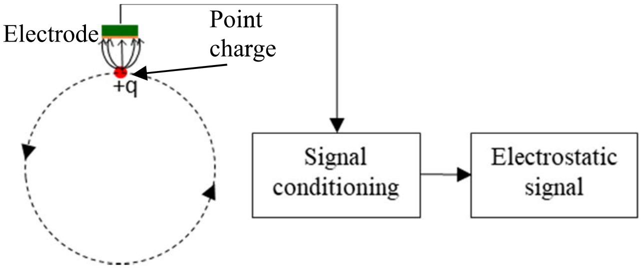

Fig. 6. Simplified model of the sensing system.

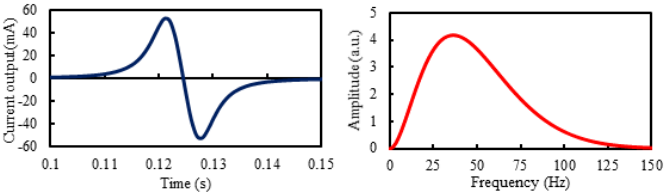

(a) (b)

Fig. 7. Typical example of the sensor output and corresponding frequency spectrum. (a) Sensor output signal. (b) Spectrum of output signal.

input with amplitude q [i.e., $q\delta(t)$] to the sensing system, thus the impulse response $h_s(t)$ of the system [Fig. 7(a)] is given by

$$h_s(t) = \frac{dQ(t)}{q dt}. \tag{5}$$

The frequency response of the sensing system [Fig. 7(b)] can be determined from the Fourier transform of the impulse response $h_s(t)$

$$H_s(f) = \int_{-\infty}^{+\infty} h_s(t) e^{-j2\pi f t} dt. \tag{6}$$

By substituting $h_s(t)$ in (5) into (6), the amplitude of the frequency spectrum can be written as

$$|H_s(f)| = F(\omega, D, s). \tag{7}$$

Equation (7) implies that the amplitude of the spectrum is a function of the angular speed ω, the diameter of the shaft D, and the distance s between the shaft surface and the electrode.

C. Displacement Effect on the Frequency Response

The effect of the displacement on the frequency response is investigated for a strip-shape electrode [16], using different point charges, with the same magnitude, and rotating along circular trajectories of different diameters [Fig. 8(a)]. Subsequently, different trajectories result in different distances to an electrode (displacement), which is located at a fixed distance from the rotation center.

Fig. 8(b) and (c) shows the signal outputs of the electrostatic sensor and the corresponding normalized spectra for two different point charges rotating at $\omega = 12$ rad/s, which is equivalent to 115 r/min.

Fig. 8(c) illustrates the output signals in the frequency domain, indicating the effect of the displacement on the frequency characteristics of the sensor. It can be noted that a shorter distance between the electrode and the circular trajectory of the point charge results in a more induced charge on the electrode and hence higher signal amplitude [Fig. 8(b)]. Moreover, a shorter distance yields a wider bandwidth and a higher frequency at the maximum amplitude [Fig. 8(c)], suggesting that the point charge being within the sensing region of the electrode for a shorter period of time at a constant angular speed.

D. Characteristics of an Unbalanced Shaft

1) Vibration of an Unbalanced Shaft: In general, all rotating machines produce some form of vibration is a function of the machine dynamics such as imbalance, misalignment, bearing deterioration, and mechanical looseness [17]. There are three main parameters used to evaluate the vibration characteristics of any dynamic system: displacement, velocity, and acceleration [18], [19]. Imbalance is the most common mechanical fault and source of vibration in rotating equipment. Shaft imbalance is a condition in which the center of mass of the shaft is not coincident with the center of rotation. A static imbalance is a condition of imbalance where the central principal axis of inertia is displaced in parallel with the axis of rotation, as shown in Fig. 9.

This paper is concerned with the static imbalance fault that can be determined from the radial vibration of the shaft through instantaneous displacement measurement of the shaft surface with respect to a nonmoving reference point.

2) Modeling of the Displacement Due to Static Imbalance of a Shaft: The vibration due to shaft imbalance can be determined through the displacement measurement of the shaft surface with respect to a fixed position (the sensor). However, it is essential to establish a mathematical model of the shaft displacement. Fig. 10 shows the geometrical model of an unbalanced shaft in rotational motion when an electrostatic sensor is used. The simulation results from the mathematical model of the shaft displacement will be used in the regression analysis in order to develop an estimated regression equation, which gives the displacement as a function of the frequency at the spectrum crest (f_{sc}). In addition, the modeling results will be used to evaluate the accuracy of the regression model. The model is established with the following assumptions.

1) An electrode is placed on the y-axis, at distance (R_0+s_0) from the x-axis. The position of the sensor is considered as a fixed reference.
2) The circle with diameter $2R_0$ represents a cross section of a metallic shaft.

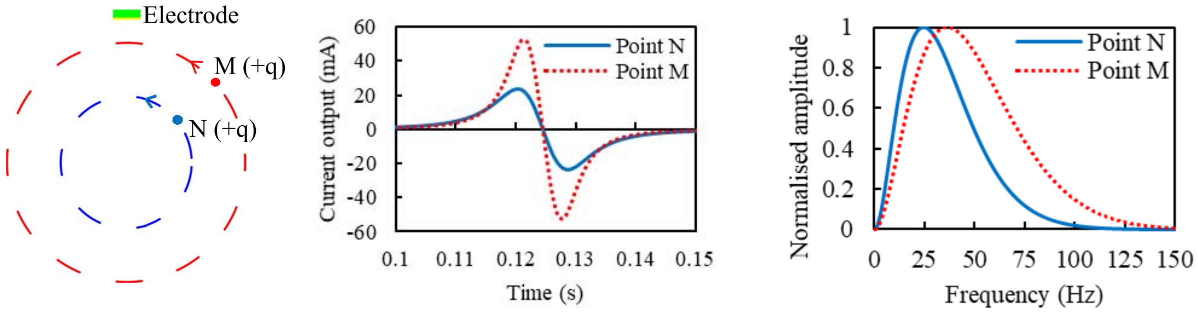

(a) (b) (c)

Fig. 8. Sensor's output of two point charges in rotational motion and its corresponding spectra. (a) Two point charges. (b) Sensor output signals. (c) Spectra of output signals in rotational motion.

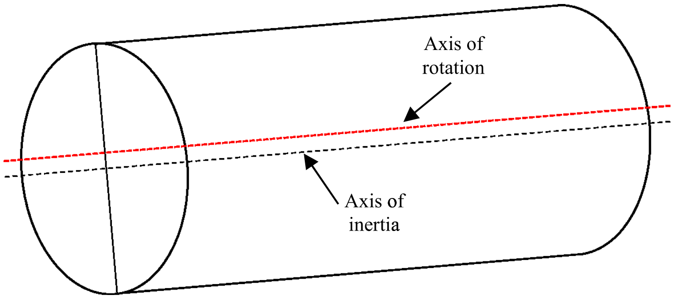

Fig. 9. Static imbalance of shaft in rotating machines.

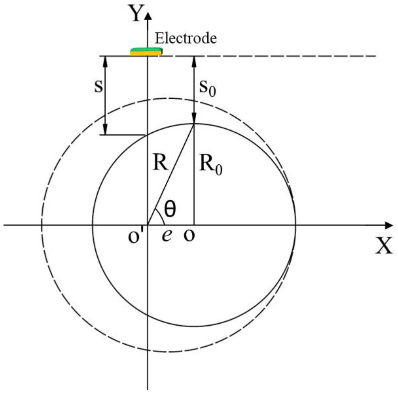

Fig. 10. Unbalanced shaft.

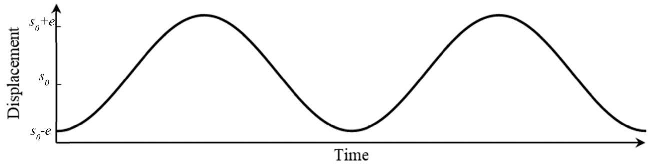

Fig. 11. Displacement function of an eccentric shaft.

3) The rotation center O' of the circle is offset from the geometric center O by the distance e.
4) The rotational motion of the circle about the center O' simulates an unbalanced shaft.
5) The shaft and, hence, the circle are rotating at a constant angular speed $\omega = \theta/t$.
6) The displacement s is the distance between the shaft surface and the sensor.

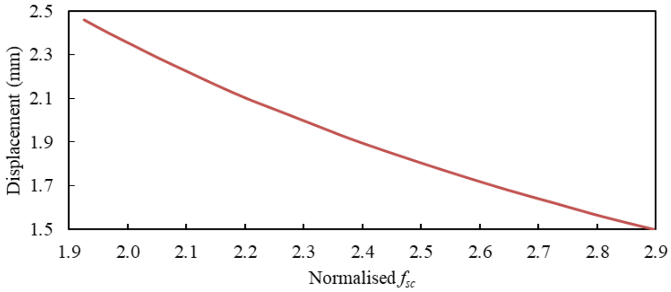

Fig. 12. Relationship between displacement and normalized f_{sc}.

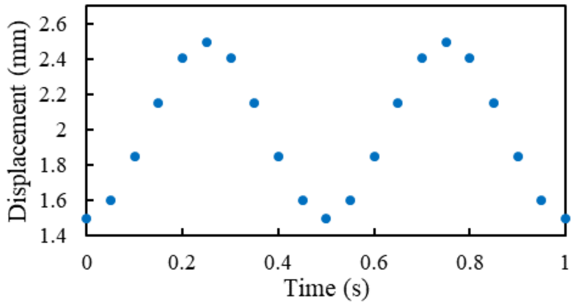

Fig. 13. Displacement values over two revolutions.

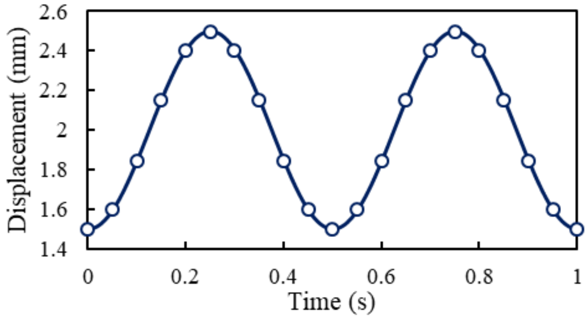

Fig. 14. Fit curve of the displacement distribution.

7) The eccentricity e with respect to the radius R is relatively small ($e \ll R$).

From Fig. 10, R_0 is given by

$$R_0^2 = R^2 + e^2 - 2eR\cos\theta. \tag{8}$$

Rearranging (8)

$$R = e\cos\theta + \sqrt{e^2\cos^2\theta - e^2 + R_0^2}. \tag{9}$$

TABLE I

$f_{sc\perp}$ AT DIFFERENT DISPLACEMENTS AND DIAMETERS

s (mm)	*D (mm)*	*Θ (rad)*	$f_{sc\perp}$	Fit std. error
1.50	60.50	1.57	2.90	-0.16%
1.56	60.44	1.67	2.81	0.05%
1.62	60.38	1.76	2.73	-0.03%
1.68	60.32	1.86	2.65	0.05%
1.74	60.26	1.96	2.58	0.01%
1.80	60.20	2.05	2.51	-0.01%
1.86	60.14	2.15	2.44	0.00%
1.92	60.08	2.25	2.37	0.03%
1.98	60.02	2.34	2.32	-0.11%
2.04	59.96	2.44	2.26	-0.10%
2.10	59.90	2.54	2.20	0.07%
2.16	59.84	2.63	2.15	0.03%
2.22	59.78	2.73	2.10	-0.06%
2.28	59.72	2.83	2.06	-0.03%
2.34	59.66	2.92	2.01	-0.07%
2.40	59.60	3.02	1.97	0.00%
2.46	59.54	3.11	1.93	-0.02%

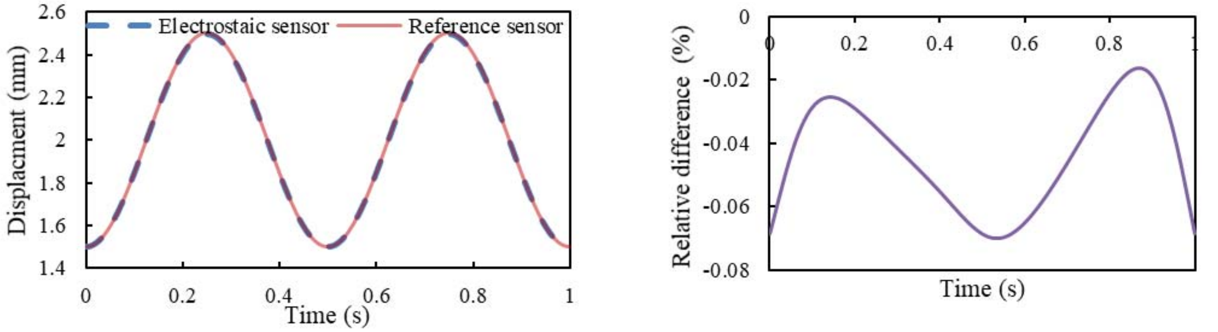

(a) (b)

Fig. 15. Comparison of the displacement measurement and the relative difference between the electrostatic sensor and the simulated reference. (a) Comparison of displacement measurements. (b) Relative difference.

As the sensor is located at a fixed distance from the x-axis, then

$$R_0 + s_0 = R + s. \tag{10}$$

By substituting R from (9) to (10), the shaft displacement with respect to the sensor position can then be determined by

$$s = R_0 + s_0 - e\cos\theta - R_0\sqrt{1 - \frac{e^2}{R_0^2}\sin^2\theta}. \tag{11}$$

As $e \ll R$, then the displacement can be approximated by

$$d(\theta) = s_0 - e\cos\theta. \tag{12}$$

Since $\theta = \omega t$, (12) can be rewritten as

$$s(t) = s_0 - e\cos\omega t \tag{13}$$

where S_0 denotes the distance between the sensor and the normal shaft and e denotes the eccentricity of the shaft.

Equation (13) implies that the displacement of an unbalanced shaft with respect to a fixed position could be approximated to a sinusoidal waveform, as illustrated in Fig. 11.

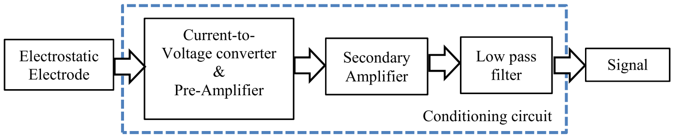

Fig. 16. Block diagram of the signal conditioning circuit.

E. Estimation of the Displacement Function of an Eccentric Shaft

Equation (7) defines the spectrum of the output signal as a function of ω, s, and D. For a rigid shaft supported on rigid bearings, the shaft displacement is independent of the shaft angular speed [3]. Wang and Yan [15] demonstrate that the bandwidth is proportional to the angular speed. Subsequently, the frequency at the spectrum crest f_{sc} has a linear relationship with the angular speed. Moreover, the diameter D of each point on the eccentric shaft has a direct relationship with the displacement ($D + s = K$), where K is a constant (Fig. 1). Thus, the frequency of the spectrum crest f_{sc} can be normalized to the angular speed and can be expressed as a function of the displacement s

$$fsc_{\perp} = \frac{fsc}{\omega} = F(s). \tag{14}$$

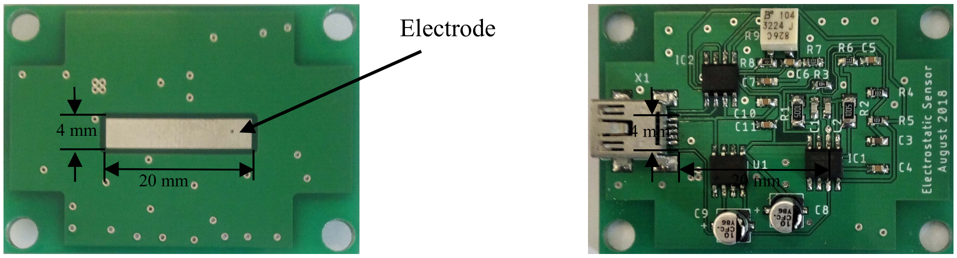

(a) (b)

Fig. 17. Electrostatic sensor and signal conditioning circuit. (a) Electrode layer. (b) Components layer.

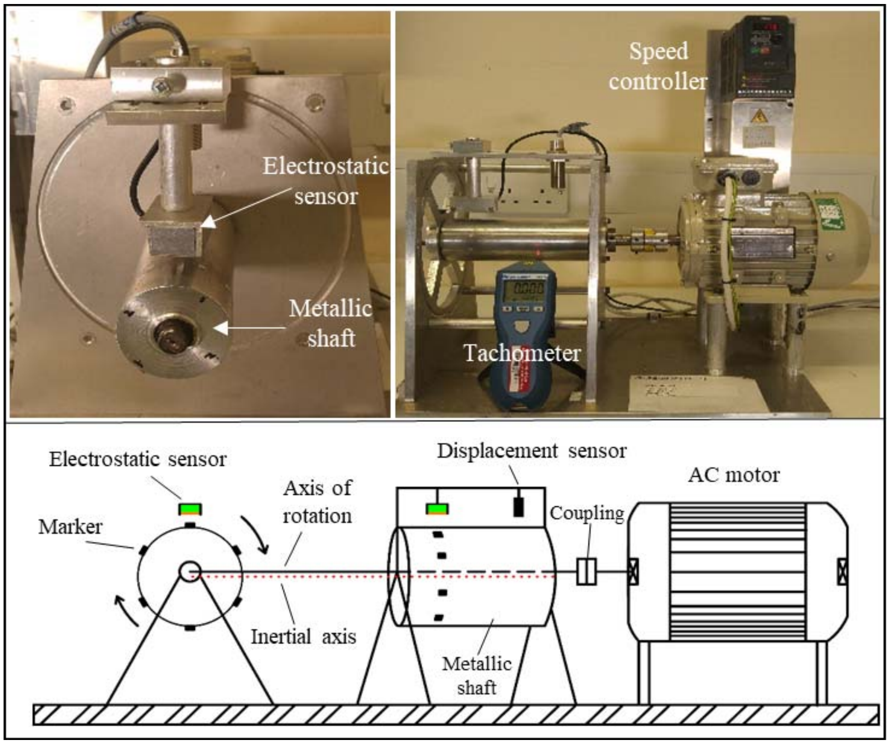

Fig. 18. Test rig.

From (14), the displacement could be determined analytically as a function of the normalized frequency of the spectrum crest

$$s = F^{-1}(f\mathrm{sc}_{\perp}). \tag{15}$$

The frequency at the spectrum crest is determined where the spectrum amplitude slope is equal to zero

$$\frac{d(|H_s(f)|)}{df} = 0, \quad \text{at } f = f_{\mathrm{sc}}. \tag{16}$$

However, the analytical solution to (16) is very complex, a polynomial regression analysis is thus used instead to estimate the relationship between the two variables, the displacement s and the normalized f_{sc} (Fig. 12).

From Table I, the displacement s can be estimated as

$$\mathrm{s} = p_3 \cdot f_{\mathrm{sc}\perp}^3 + p_2 \cdot f_{\mathrm{sc}\perp}^2 + p_1 \cdot f_{\mathrm{sc}\perp} + p_0 \tag{17}$$

where $p_0 = 0.00916$, $p_1 = -0.006206$, $p_2 = 0.001786$, $p_3 = -0.0001922$, and $f_{sc\perp} = (f_{sc}/\omega)$.

For an eccentricity of 0.5 mm (δ_e = 1/120) and ω = 100 rad/s (955 r/min), the displacement fluctuation is 1 mm, resulting in a variation in f_{sc} of 100 Hz (simulated result). Hence, the measurement sensitivity is 0.01 mm/Hz. If the signal is acquired over 1 s, then the measurement resolution would be 0.01 mm.

Using (17), displacement values can be estimated for each f_{sc}. It can be seen from Fig. 13 that the displacement distribution of an eccentric shaft is similar to a sinusoidal distribution function, which agrees with the displacement function of an unbalanced shaft. At a given angular speed ω, the distribution of s can be fit to a sinusoidal function as shown in Fig. 14. Hence, the displacement function can be written as

$$s(t) = A\cos\omega t + B \tag{18}$$

where $A = -e$, which denotes the eccentricity of the shaft and is unknown and $B = s_0$ which is a constant representing the displacement of a normal shaft.

Fig. 15 shows a comparison between the reference simulation results and the modeling results. It is evident that the mathematical modeling results follow closely the reference

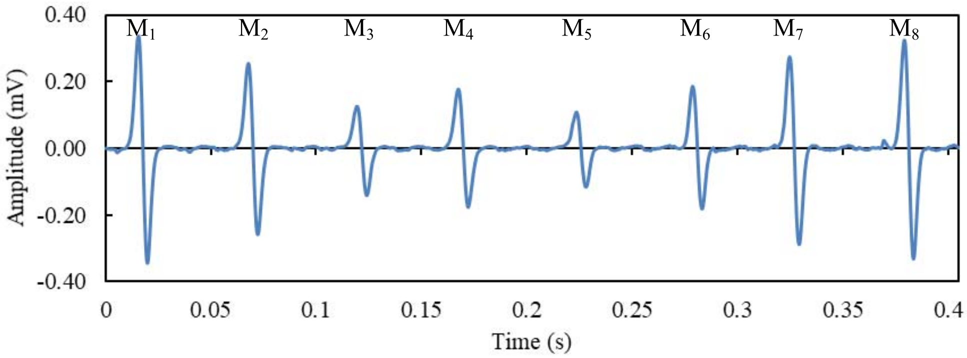

Fig. 19. Output signal from the electrostatic sensor.

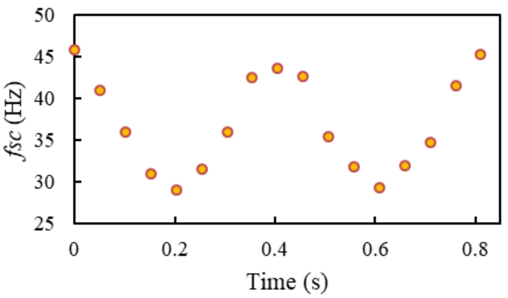

Fig. 20. f_{sc} over two revolutions.

simulation results, and the small discrepancy is due to the curve fitting errors.

As a result, the property of the electrode in the frequency domain, being the frequency at the spectrum crest f_{sc}, has been used to establish a method to measure the instantaneous displacement of the shaft and, hence, the vibration of an unbalanced shaft is quantified.

IV. EXPERIMENTAL RESULTS AND DISCUSSION

A. Experimental Setup

The electrostatic sensor was designed and fabricated based on a double-sided PCB. As shown in Fig. 17, the electrode is a 4-mm-wide tin-plated copper strip embedded in the bottom layer of the PCB. The area around the electrode is filled with earthed copper to minimize the influence of external electromagnetic interferences. On the top layer of the PCB is the signal conditioning circuit. The current signal from the electrode is first converted into a proportional voltage signal using an I–V converter. To maximize the power transfer between the electrode and the signal conditioning circuit, a FET amplifier is chosen for I–V conversion. Then, the bipolar signal is further amplified and level shifted using a high-accuracy instrumentation amplifier to match the input range of a single-supply A/D converter. The instrumentation amplifier also provides an adjustable gain for the circuit using a potentiometer. Finally, a Sallen–Key low-pass filter is used to remove high-frequency noise from the sensor output and provide antialiasing in the A/D conversion. The sensor is shielded with an earthed metal screen to reject external electromagnetic interferences. Fig. 16 shows the block diagram of the signal conditioning circuit. The output sensor signal was sampled at a frequency of 50 kHz using a data acquisition device (National Instruments, model USB-6341) and processed on a host computer. A bespoke software system was developed using LabView in order to achieve an online displacement measurement.

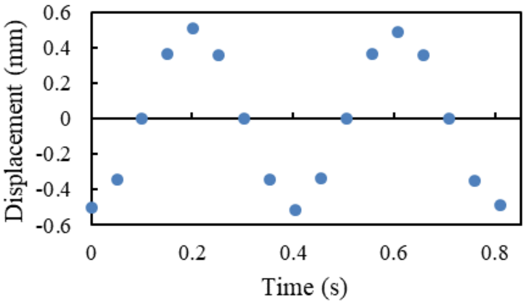

Fig. 21. Estimated displacement values.

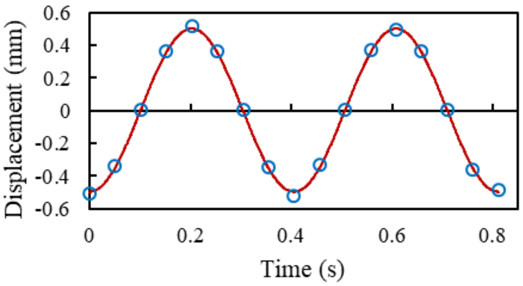

Fig. 22. Comparison between the displacement values and the reference sensor output.

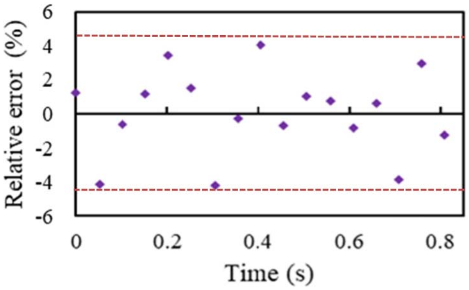

Fig. 23. Relative error of the displacement measurement.

Experimental tests were conducted on a purpose-built test rig as shown in Fig. 18 to validate the performance of the electrostatic sensor for vibration displacement measurement

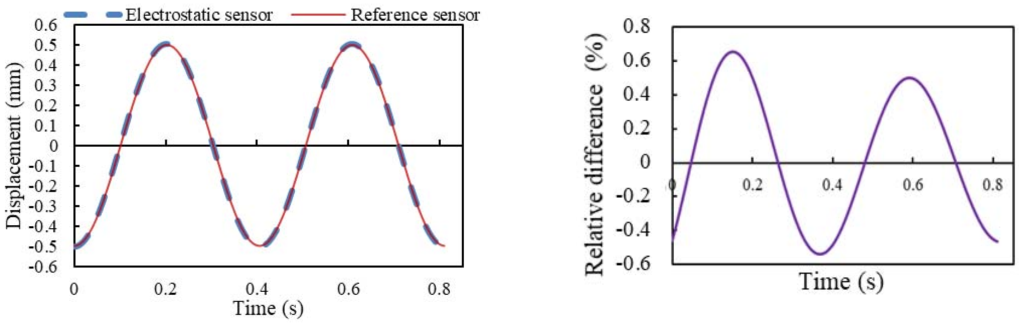

(a) (b)

Fig. 24. Comparison of the displacement curve from the electrostatic and the reference sensors. (a) Displacement measurement. (b) Relative difference.

against a reference displacement sensor. The rotational speed of the motor is adjustable through the motor controller. A commercial laser-based tachometer (Monarch Instruments, PLT200) was used to obtain reference speed of the shaft. An eccentric metallic shaft with a diameter of 60 mm and an eccentricity of 0.5 mm from the rotation axis was tested. An electrostatic sensor (Fig. 17) was placed 2 mm away from the shaft surface. To simulate eight point charges on the rotor surface, eight charged markers, each being made from 2×2 mm^2 electret material film, were fixed evenly along the circumference of the eccentric shaft. Two of them were located at the shortest and longest distance with respect to the center of rotation. Electrets are dielectrics that have a quasi-permanent electrostatic charge. The electret markers were fabricated through a typical microfabrication process using Teflon fluorinated ethylene propylene (FEP) films. The FEP film with a thickness of 127 μm was charged with the use of a point-to-plane corona discharge. After charging, the surface potential of the FEP electret film reaches −560 V [20], [21]. The output of the sensor, resulting from the induced charge on the electrode, is derived and measured. Then, the frequency response of the output signal is obtained. A displacement sensor of eddy current type (Model LD701-2/5, OMEGA) was used as a reference instrument to obtain the relative distance between sensor and the shaft surface. All the tests were conducted in a laboratory with air conditioning (ambient temperature of 22 °C and relative humidity of 49%).

B. Results and Discussion

A minimum strength of the electrostatic signals has to be maintained to achieve a valid measurement of the displacement using electrostatic sensors. The root mean square (rms) amplitude of an electrostatic signal is used to quantify the signal strength. Wang and Yan [15] show that if the electrode is moved away from the shaft surface, the effect of electrostatic induction on the electrode is reduced, leading to a weakened signal. In this experiment, the electrostatic sensor was placed 2 mm away from the shaft surface, the rms signal strength is about 77.25 mV for the signal conditioning unit used. In addition, the rejection of extrinsic noise due to a near power line (50 Hz) is efficient since an earthed metal screen is used to prevent the interference of electromagnetic fields. However, further investigation is required when applying this technique in an industrial environment with various sources of electromagnetic interference. Fig. 19 shows the output signal from the electrostatic sensor for one period which is the time of the shaft over one revolution.

For each period, the signal is composed by a series of eight pulses resulting from the eight markers on the shaft. It is clear that the amplitude of the signal from the eccentric shaft fluctuates due to the variations in the distance between the shaft and the sensor over one revolution.

Following the measurement methodology in Section III, the signal in Fig. 19 is first decomposed in the time domain into eight single pulses corresponding to the eight point charges on the shaft. Then, frequency analysis of each single pulses is performed in order to extract the frequency at the spectrum crest f_{sc}. Fig. 20 shows the f_{sc} values of the eight pulses for an eccentric shaft ($e = 0.5$ mm) at 148 r/min. Using the regression analysis in Section III, displacement values can be estimated for each f_{sc}. It can be observed from Fig. 21 that the displacement distribution of an eccentric shaft can fit a sinusoidal function, which agrees with the simulation results in Section III.

Fig. 22 shows a direct comparison of the displacement (ac component) of eight points on the eccentric shaft between the electrostatic sensor and the reference sensor (eddy current sensor). The shaft has an eccentricity of 0.5 mm and is rotating at 148 r/min. All the measured displacements in Fig. 20 are the average of 20 values with a maximum standard deviation of 4.5%. It is evident that the measured displacements are pretty close to the reference. Fig. 23 shows that the relative error of the measured displacement is within ±4.2%.

Fig. 24 shows the comparison between the reference and the electrostatic sensor results using a sinusoidal curve fitting. The displacement measurement from the electrostatic sensor in Fig. 24 shows a peak-to-peak displacement of about 1 mm, independent of the rotational speed. The rms error between the two displacement curves resulting from the reference sensor and the electrostatic sensor is within 0.77%.

Fig. 24(b) shows that the maximum relative error is within ±0.6% compared to ±4.2% of the discrete displacement values (Fig. 23). This result suggests that applying sinusoidal curve fitting to the discrete displacement values with a known frequency (angular speed) has reduced the relative error. It can also be observed from Fig. 24(b) that the relative error in the displacement measurement increases when the displacement decreases. The capability of the system to measure the smallest displacement values (and hence higher measurement resolution) can be achieved by improving the data acquisition parameters (e.g., sampling frequency, analog-to-digital converter resolution, and so on).

V. CONCLUSION

The frequency response properties of an electrostatic sensor have been used to detect and quantify an unbalanced shaft through displacement measurement. Experimental results have demonstrated that electrostatic sensors can be used to measure the displacement of an eccentric shaft. Hence, the vibration of an unbalanced shaft can be quantified. Results obtained have demonstrated that the measurement system performs well with a maximum error no greater than ±0.6% under all test conditions. Further research is required to investigate the effect of the markers size and dimensions on the accuracy and repeatability of the measurement. Moreover, the measurement resolution is expected to improve by optimizing the data acquisition parameters. Although this method has focused on the detection of static imbalance, it can be developed to detect and quantify the two other types of imbalance, i.e., the couple and dynamic imbalance.

ACKNOWLEDGMENT

The authors would like to thank the Atomic Energy and Alternative Energies Commission for providing the electret materials in this paper.

REFERENCES

[1] J. Z. Szabó, "Vibration diagnostic test for effect of unbalance," in *Proc. IEEE 16th Int. Conf. Intell. Eng. Syst. (INES)*, Lisbon, Portugal, Jun. 2012, pp. 81–85.

[2] W. Qiao and X. Gong, "Imbalance fault detection of direct-drive wind turbines using generator current signals," *IEEE Trans. Energy Convers.*, vol. 27, no. 2, pp. 468–476, Jun. 2012.

[3] M. L. Adams, *Rotating Machinery Vibration: From Analysis to Troubleshooting*. Boca Raton, FL, USA: CRC Press, 2010.

[4] R. B. Randall, "State of the art in monitoring rotating machinery—Part 1," *Sound Vib.*, vol. 38, no. 3, pp. 14–21, 2004.

[5] H. Chaurasiya, "Recent trends of measurement and development of vibration sensors," *Int. J. Comput. Sci. Iss.*, vol. 9, no. 4, pp. 353–358, 2012.

[6] R. Atashkhooei, J.-C. Urresty, S. Royo, J.-R. Riba, and L. Romeral, "Runout tracking in electric motors using self-mixing interferometry," *IEEE/ASME Trans. Mechatronics*, vol. 19, no. 1, pp. 184–190, Feb. 2014.

[7] Q. Tong, H. Ma, L. Liu, X. Zhang, and G. Li, "Key technology study on radial vibraition system of high-speed rotating machinery," *Chin. J. Sci. Instrum.*, vol. 5, no. 32, pp. 1026–1032, 2011.

[8] D. Vyroubal, "Optical method for instant estimate of vibration signature based on spectrum analysis of phase-modulated light pulses," *IEEE Trans. Instrum. Meas.*, vol. 53, no. 1, pp. 181–185, Feb. 2004.

[9] S. Okabe and S. Tanaka, "Measurement of shaft vibration using ultrasonic sensor," in *Proc. SICE Annu. Conf.*, Fukui, Japan, Aug. 2003, pp. 1155–1158.

[10] L. Wang, Y. Yan, Y. Hu, and X. Qian, "Intelligent condition monitoring of rotating machinery through electrostatic sensing and signal analysis," in *Proc. IEEE Int. Conf. Smart Instrum., Meas. Appl. (ICSIMA)*, Kuala Lumpur, Malaysia, Nov. 2013, pp. 1–4.

[11] L. Wang, Y. Yan, Y. Hu, and X. Qian, "Radial vibration measurement of rotary shafts through electrostatic sensing and Hilbert–Huang transform," in *Proc. IEEE Int. Instrum. Meas. Technol. Conf.*, Taipei, Taiwan, May 2016, pp. 1–5.

[12] J. Lowell and A. Brown, "Contact electrification of chemically modified surfaces," *J. Electrostat.*, vol. 21, no. 1, pp. 69–79, 1988.

[13] W. D. Greason, "Investigation of a test methodology for triboelectrification," *J. Electrostat.*, vol. 49, pp. 245–256, Aug. 2000.

[14] K. Reda and Y. Yan, "Online continuous detection of an unbalanced metallic shaft using electrostatic sensors," in *Proc. IEEE Int. Instrum. Meas. Technol. Conf. (I2MTC)*, Houston, TX, USA, May 2018, pp. 1–6.

[15] L. Wang and Y. Yan, "Mathematical modelling and experimental validation of electrostatic sensors for rotational speed measurement," *Meas. Sci. Technol.*, vol. 25, no. 11, p. 115101, 2014.

[16] K. Reda, Y. Yan, and L. Wang, "A comparative study of different shaped electrostatic sensors for rotational speed measurement," in *Proc. IEEE SENSORS*, Glasgow, U.K., Oct./Nov. 2017, pp. 1–3.

[17] J. T. Broch, *Mechanical Vibration and Shock Measurements*. Copenhagen, Denmark: Brüel & Kjær, 1984.

[18] M. MacCamhaoil, *Static and Dynamic Balancing of Rigid Rotors*. Copenhagen, Denmark: Brüel & Kjær, 1984.

[19] F. Fahy and D. Thompson, *Fundamentals of Sound and Vibration*. Boca Raton, FL, USA: CRC Press, 2016.

[20] S. Boisseau, G. Despesse, and A. Sylvestre, "Optimization of an electret-based energy harvester," *Smart Mater. Struct.*, vol. 19, no. 7, p. 075015, 2010.

[21] S. Boisseau, G. Despesse, and B. A. Seddik, "Electrostatic conversion for vibration energy harvesting," in *Small-Scale Energy Harvesting*, M. Lallart, Ed. Rijeka, Croatia: InTech, 2012, ch. 5.

Kamel Reda received the B.Eng. degree in electronics and the M.Eng. degree in instrumentation and sensors from CNAM University, Paris, France, in 2001 and 2014, respectively, and the MBA degree from University Paris 1 Panthéon-Sorbonne, Paris, in 2004. He is currently pursuing the Ph.D. degree in instrumentation and sensors with the University of Kent, Canterbury, U.K.

His current research interests include rotational speed and vibration measurement through electrostatic sensing and digital signal processing.

Yong Yan (M'04–SM'04–F'11) received the B.Eng. and M.Sc. degrees in instrumentation and control engineering from Tsinghua University, Beijing, China, in 1985 and 1988, respectively, and the Ph.D. degree in flow measurement and instrumentation from the University of Teesside, Middlesbrough, U.K., in 1992.

In 1988, he joined Tsinghua University, as an Assistant Lecturer. In 1989, he joined the University of Teesside, as a Research Assistant in 1989. From 1993 to 1996, he was a Lecturer with the University of Teesside. From 1996 to 2004, he was a Senior Lecturer, a Reader, and a Professor with the University of Greenwich, London, U.K. He is currently a Professor of electronic instrumentation, with the Head of Instrumentation and Control Research Group, University of Kent, Canterbury, U.K., and the Director of innovation with the School of Engineering and Digital Arts, University of Kent. His current research interests include multiphase flow measurement, combustion instrumentation, and intelligent measurement and condition monitoring.

Sensors and Actuators A 266 (2017) 46–55

Contents lists available at ScienceDirect

Sensors and Actuators A: Physical

journal homepage: www.elsevier.com/locate/sna

Comparison of single and double electrostatic sensors for rotational speed measurement

Lijuan Wang[a,b], Yong Yan[b,*], Kamel Reda[b]

[a] School of Control and Computer Engineering, North China Electric Power University, Beijing 102206, PR China
[b] School of Engineering and Digital Arts, University of Kent, Canterbury, Kent CT2 7NT, UK

ARTICLE INFO

Article history:
Received 23 March 2017
Received in revised form 7 June 2017
Accepted 8 September 2017
Available online 9 September 2017

Keywords:
Rotational speed measurement
Electrostatic sensor
Correlation signal processing
Performance assessment
Surface roughness

ABSTRACT

Accurate and reliable measurement of rotational speed is crucial in many industrial processes. Recent research provides an alternative approach to rotational speed measurement of dielectric rotors through electrostatic sensing and signal processing. This paper aims to explore the electrostatic phenomenon of rotational machineries, design considerations of the spacing between double electrostatic sensors and effect of dielectric rotors on the performance of the rotational speed measurement systems based on single and double electrostatic sensors. Through a series of experimental tests with rotors of different material types, including polytetrafluoroethylene (PTFE), polyvinyl chloride (PVC) and Nylon, different surface roughness (Ra 3.2 and Ra 6.3) and difference diameters (60 mm and 120 mm), the accuracy and reliability of the two measurement systems are assessed and compared. Experimental results suggest that more electrostatic charge is generated on the PTFE rotors with a larger diameter and coarser surface and hence better performance of the measurement systems. The single-sensor system yields a relative error of within ±1% while the double-sensor system produces an error within ±1.5% over the speed range of 500–3000 rpm for all tested rotors. However, the single-sensor system outperforms the double-sensor system at high rotational speeds (>2000 rpm) with a relative error less than ±0.05%.

1. Introduction

Accurate and reliable measurement of rotational speed for rotating devices and machineries is desirable in many industries. Rotational speed is an important parameter to identify operating status, make fault diagnosis and establish an effective maintenance strategy in order to reduce downtime of an industrial process. Traditional contact-type measurement devices such as centrifugal tachometers, timing tachometers and electric-dynamic tachometers suffer from the common problems of wear, slippage and low measurement accuracy. Hence, a variety of non-contact measurement systems based on optical, electromagnetic and digital imaging techniques have been developed [1–3]. In recent years, instantaneous rotational speed has been estimated through vibration signal analysis by many researchers [4,5]. However, photoelectric tachometers require the fitting of external illumination sources, encoders on the shaft or refection marks on the rotor surface [6]. This kind of tachometer is difficult to use in hostile environments. Stroboscopic tachometers work well under low and stable speed conditions [6]. Magnetic inductive tachometers are limited to the measurement of metallic rotors and are susceptible to electromagnetic interference [6]. Imaging based systems suffer from similar drawbacks as the photoelectric types in addition to high cost and structural complexity [3].

Electrostatic sensor arrays in conjunction with correlation signal processing algorithms have been deployed to measure rotational speed with high accuracy and good repeatability [7]. However, the mechanical structure required for the installation of the electrostatic sensor arrays is impractical to be fitted on large rotors in many cases. To solve this problem, the measurement system using a single or double electrostatic sensors has been proposed [8,9]. Although basic electrostatic properties of some dielectric materials are well known, the effects of the material type and surface roughness of the rotor on the performance of single- and double-sensor systems are still not clear. In the present research new contributions are made in the respects of theoretical analysis and experimental investigations. Firstly, the electrostatic phenomenon of rotational machineries and design considerations of the spacing between the double sensors are discussed in detail. Secondly, comparative assessments between the single- and double-sensor systems are conducted. In addition, a high-performance data acquisition device is applied to improve the accuracy of the measurement systems. A commercial laser based tachometer with an accuracy of ±0.01% is utilized to provide reference measurements.

---

[*] Corresponding author.
E-mail address: y.yan@kent.ac.uk (Y. Yan).

http://dx.doi.org/10.1016/j.sna.2017.09.014

Finally, three dielectric materials, including polytetrafluoroethylene (PTFE), polyvinyl chloride (PVC) and Nylon, with two kinds of surface roughness (Ra 3.2 and Ra 6.3), are tested over a speed range of 500–3000 rpm. The performance of the two measurement systems is assessed and compared.

2. Measurement principle and system design

2.1. Electrostatic phenomenon of rotational machineries

Certain materials are potential to become electrically charged after fricative contact with a different material due to triboelectric effect. There are several factors affecting the polarity and magnitude of the charge generated on the rotor surface, such as material type and surface roughness of the rotor, temperature and humidity of the environment. Work function represents the capability of a material to hold onto its free electrons [10]. In general, the material with greater work function is easier to appropriate electrons from materials with lower work functions and less likely to give up its free electrons when contacting with other materials. Meanwhile, the material with weaker work function is more likely to acquire positive charges by losing or giving up some of its free electrons. Consequently, dielectric materials have higher work functions and are hence to be electrically charged when rubbed with air which has a lower work function. Electrostatic charge is generated and accumulated on the dielectric rotor surface during the continuous process of contact, friction and separation between the rotor surface and air. Moreover, the level of electrostatic charge generated on the rotor surface is normally determined by many factors, such as physical properties (material type, size and surface roughness) of the rotor, rotational speed and ambient conditions (humidity and temperature).

With the generation of electrostatic charge, there is also a phenomenon of electrostatic discharge, which reduces the amount of electrostatic charge generated. The remaining electrostatic charge [11] on the rotor surface is determined by

$$Q = Q_0 e^{-\frac{t}{\tau}} = Q_0 e^{-\frac{t}{\varepsilon_0 \varepsilon_r \rho}} \tag{1}$$

where Q_0 and Q are respectively the initial and final levels of electrostatic charge generated on an object and τ is the relaxation time of the object, which is derived from the permittivity of free space ε_0, the relative permittivity ε_r and the resistivity ρ of the object. Eq. (1) indicates that electrostatic discharge depends on the permittivity and resistivity of the material. The larger permittivity and resistivity, the longer relaxation time of electrostatic discharge and hence more electrostatic charge maintained on its surface.

2.2. Measurement principle

The structure of electrostatic sensors based the rotational speed measurement system is shown in Fig. 1. The single or double electrostatic sensors are placed in the vicinity of the rotor to sense the charge on the rotor surface. Electrostatic signals are obtained from the electrostatic sensors through electrostatic induction due to the charge generated on the moving surface of the rotor. A high-performance signal conditioning unit is utilized to condition the extremely weak signals from the sensing point. The data acquisition unit converts the analog signals to digital forms and transmits the acquired signals to a host computer. Signal processing, including auto-correlation and cross-correlation, and rotational speed calculation are realized in the host computer.

In the case of single electrostatic sensor based system, the electrostatic signal $S(t)$ is periodic due to the continuous rotational motion of the rotor with reference to the fixed location of the sensor. The periodicity of the signal is equal to the period of the rotation motion (T), which is determined from auto-correlation function of the electrostatic signal. A normalized auto-correlation function $R_a(m)$ is defined as:

$$R_a(m) = \frac{\sum_{k=1}^{N} S(k)S(k+m)}{\sum_{k=1}^{N} S^2(k)} \tag{2}$$

where $S(k)$ ($k = 0, 1, 2, \ldots, N$) represents the digitized signal $S(t)$, N is the number of samples in the correlation computation and m ($m = 0, \ldots, N$) is the number of delayed points.

The location of the dominate peak (other than the unity at $m = 0$) on the time axis is the period T. The amplitude of the dominate peak in the auto-correlation function is the correlation coefficient, which indicates the reliability of the speed measurement through auto-correlation. The rotational speed (n) in Revolutions Per Minute (RPM) is calculated from

$$n = \frac{60}{T} \tag{3}$$

In the case of the double electrostatic sensors based system, the time delay (τ) between the two electrostatic signals $S_1(t)$ and $S_2(t)$ is equal to the time of the rotor travelling from upstream to downstream sensors and is determined through cross-correlation function $R_c(m)$:

$$R_c(m) = \frac{\sum_{k=1}^{N} S_1(k)S_2(k+m)}{\sqrt{\sum_{k=1}^{N} S_1^2(k)}\sqrt{\sum_{k=1}^{N} S_2^2(k)}} \tag{4}$$

The time corresponding to the dominant peak in the cross-correlation function $R'(m)$ is the time delay τ and thus the rotational speed (n) is determined from

$$n = \frac{30\alpha}{\pi\tau} \tag{5}$$

where α is the angular spacing in radians between the two sensors.

2.3. Sensor design

The mathematical modelling and optimal design of the single electrostatic sensor have been reported in a previous paper [12]. As suggested, the optimal width of the electrode is between 0.05 and 0.1 times of the diameter of the rotor; the length of the electrode is normally in the range of 20 mm to 50 mm in view of the practically suitable physical dimensions of the printed circuit board. The diameter of the rotors used in this study is 60 mm or 120 mm, so the width of the electrode is set to 3 mm and the length is 20 mm

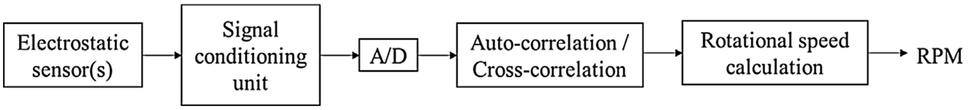

Fig. 1. Structure of electrostatic sensors based rotational speed measurement system.

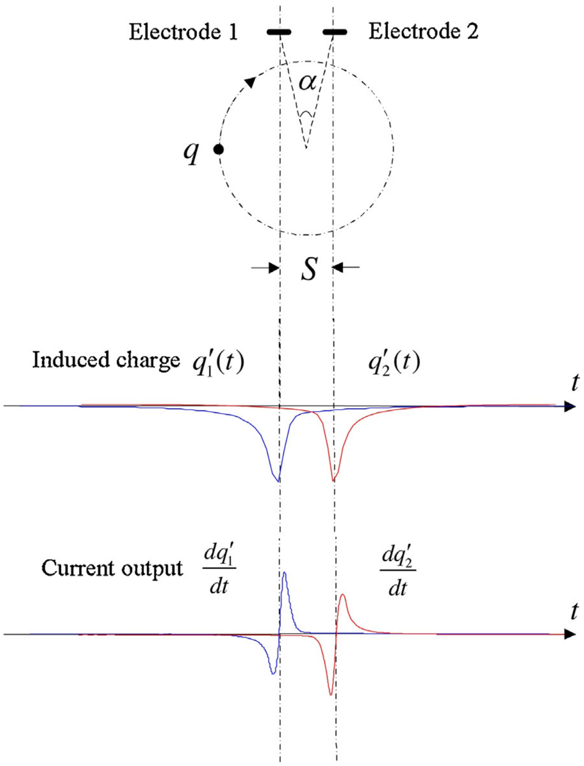

Fig. 2. A typical example of the induced charge on the double electrodes and corresponding sensor output.

(See Fig. 3 (a)). The strip electrode is made of copper and embedded in a small piece of printed circuit board (PCB). The size of the PCB is designed as 42 mm × 20 mm. The charge detection and pre-amplifier circuits are mounted on the other side of the PCB. In order to avoid external electromagnetic interference, the whole circuits are enclosed by an earthed screen.

As for the design of the double electrostatic sensors, the spacing between the two electrodes is another important parameter, which mainly affects the similarity between the two signals and hence the accuracy and reliability of the rotational speed measurement system. In general, the spacing between the two electrodes should be narrow enough to keep higher signal similarity. Meanwhile, it is more accurate to fit a correlogram at the minimum transit time under the condition of highest speed. However, if the two electrodes are mounted extremely close to each other the electrical field interaction between them would become significant, resulting in reduced signal similarity and increased statistical error in the speed measurement. A mathematical model regarding to a point charge passing over the two electrodes is established and the resulting output of the double sensors is shown in Fig. 2. Due to the interaction between the two electrodes and associated insulators and the inherent asymmetry of the construction of the PCB, the two signals are not identical, but one of them is a flipped version of the other with respect to both polarity and time. Consequently, the spacing between the two electrodes should be set ranging from 2 or 4 times of the width of the electrode. So the spacing used in this study is 7 mm (See Fig. 3(b)). In consideration of the sensor design and construction, the material and thickness of the coating between and outside the two electrodes should be made as identically as possible.

3. Experimental results and discussion

3.1. Test conditions

Experimental tests were conducted on a purpose-build test rig, as shown in Fig. 4. The test rotor is driven by a three-phase asynchronous motor via a coupling. The rotor is able to provide the rotational speed ranging from 0 to 3000 rpm by adjusting the motor controller. The electrostatic sensor is placed 2 mm away from the

(a) Structure of a single electrostatic sensor (b) Structure of double electrostatic sensors

Fig. 3. Design and construction of the electrostatic sensors.

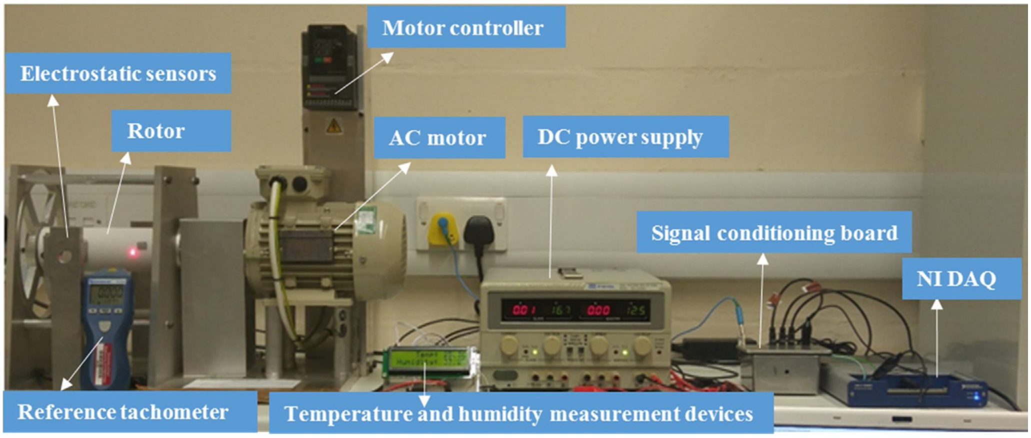

Fig. 4. Rotational speed measurement system.

Table 1
Test programme.

Electrostatic sensor	Rotor			
	Material type	Surface roughness	Rotor diameter (mm)	Rotational speed (rpm)
Single/Double	PTFE	Ra = 3.2, 6.3	D = 60	n: 0–3000
		Ra = 6.3	D = 120	
	PVC	Ra = 3.2, 6.3	D = 60	
		Ra = 6.3	D = 120	
	Nylon	Ra = 3.2, 6.3	D = 60	
		Ra = 6.3	D = 120	

rotor surface. The sensor outputs are sampled at a frequency of 10 kHz using a data acquisition unit (National Instruments, Data Acquisition Device USB-6351), which is sufficient to generate satisfactory measurements for the single-sensor and double-sensor systems. The signals are then transmitted to a host computer and processed through auto-correlation and cross-correlation. In order to evaluate the performance of the two measurement systems, the measured rotational speeds are compared with the reference speed acquired from a commercial laser based tachometer [13] (Monarch Instruments, PLT200). The best achievable accuracy of the commercial tachometer is ±0.01%, as stated in the operation manual. During the experimental tests the ambient temperature and relative humidity were measured to be from 20 °C to 24 °C and between 28% and 35%, respectively.

A series of experiments were conducted on the test rig under different test conditions which are summarized in Table 1. In order to investigate the effect of material type on the performance of the single or double electrostatic sensors based rotational speed measurement systems, test rotors are made of three common dielectric materials (PTFE, PVC and Nylon). The surface roughness of each rotor is set to Ra 3.2 and Ra 6.3, respectively, where Ra (roughness average) is the most commonly used one-dimensional roughness parameter (i.e., arithmetic mean deviation of the surface profile) in the manufacturing industry [14]. The higher the value of Ra, the coarser the surface texture. The rotors with a diameter of 60 mm have surface roughness of Ra 3.2 and Ra 6.3, respectively whilst the larger rotor (120 mm diameter) has a surface roughness of Ra 6.3. The surface roughness was achieved using a computerized numerical control (CNC) machine with a lathe tool and verified with a set of surface roughness comparators (reference plates). The axial length of the rotors is set to 152 mm.

3.2. Material characteristics

The likely electrostatic charging trend of common materials is shown in Fig. 5 under certain conditions [15]. A material on the right-hand side of the series will always charge positively when brought into contact with a material on the left (i.e. the latter will charge negatively). This is because a material on the right side of the series has a lower work function than those on the left and thus tends to lose electrons and accumulate positive charge. In general, materials with higher work functions tend to appropriate electrons from materials with lower work functions. According to the physical characteristics of PTFE, PVC and Nylon outlined in Table 2 [16–20], PVC and PTFE with higher work functions are easier to charge negatively when they rub with the air with a lower work function. Disagreements between the charging series (Fig. 5) and the work functions (Table 2) are noted and commented by other researchers [16].

Table 2
Physical characteristics of different material [10,16–19].

Material	Work function (eV)	Permittivity	Resistivity (Ωm)
PTFE	4.26	2.10	10^{16}
PVC	4.85	3.18	10^{16}
Nylon	4.08	3.50	10^{12}

Surface roughness is one of the important factors affecting the level and the distribution of the electrostatic charge generated through friction. It is typically considered to be the high-frequency and short-wavelength component of a surface. The rough surface usually have higher friction coefficients than smooth surface. In addition, the peaks on the surface may have substantial charge that generates a large electric field in a very small area resulting in corona discharge or the breaking down of the air molecules [18].

3.3. Sensor signals

A typical signal waveform from the single electrostatic sensor and resulting auto-correlation function are plotted in Fig. 6(a) and (b). When the rotor is rotating continuously, electrostatic charge is generated on its surface and a dynamic balance is reached between the natural discharge and recharge. The period (T) of the signal, determined from the location of the dominant peak in the auto-correlation function is shown in Fig. 6(b). The signal waveforms from the double electrostatic sensors and resulting cross-correlation function are plotted in Fig. 7(a) and (b). The two signals are similar but there is a time delay between them. The time delay (τ) is determined from the location of the first dominant peak in the cross-correlation function.

3.4. Signal amplitude

Apart from environmental factors (ambient temperature and relative humidity), the amplitude of electrostatic signal also depends on operating conditions, such as material type, surface

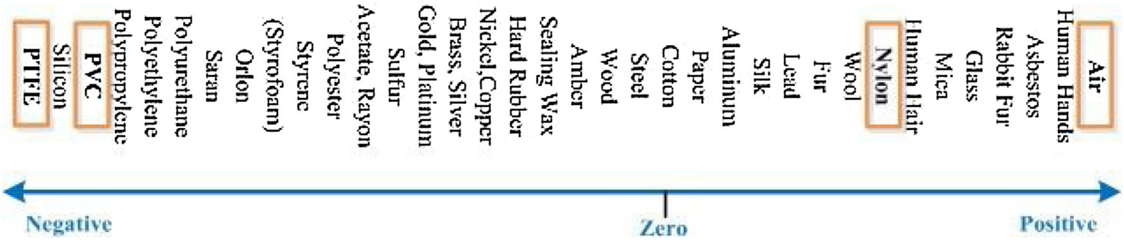

Fig. 5. Triboelectric series [13].

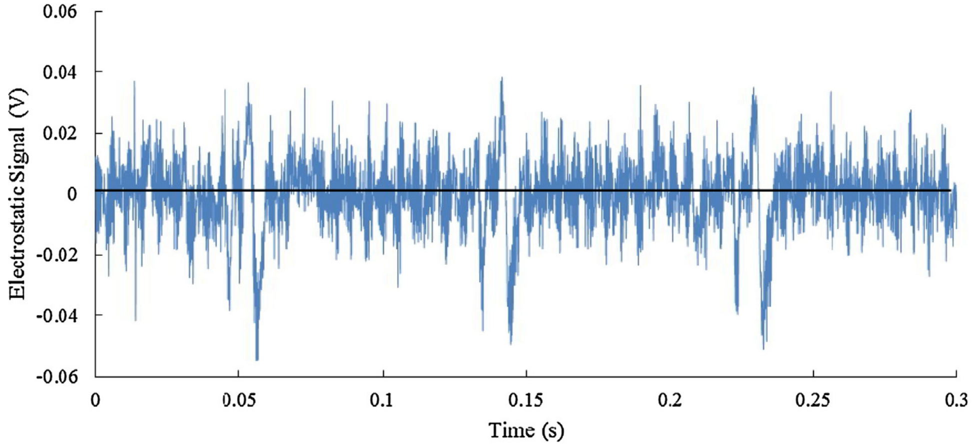

(a) Signal waveform

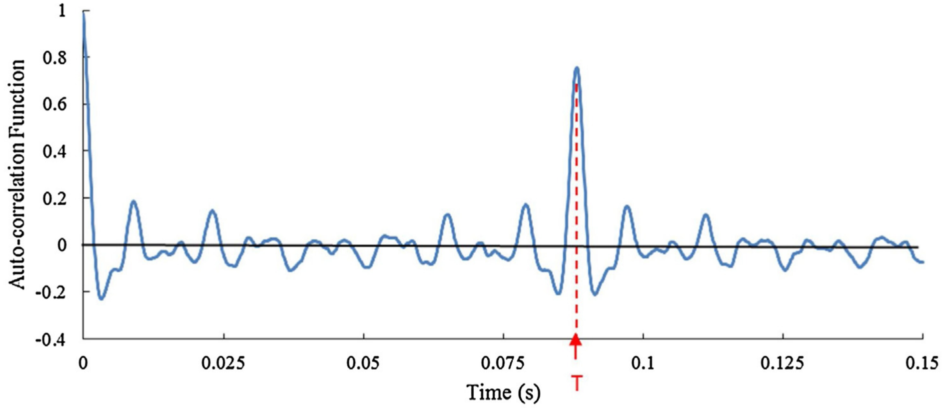

(b) Autocorrelation function of the signal

Fig. 6. Typical signal waveform from the single-sensor system and resulting auto-correlation function.

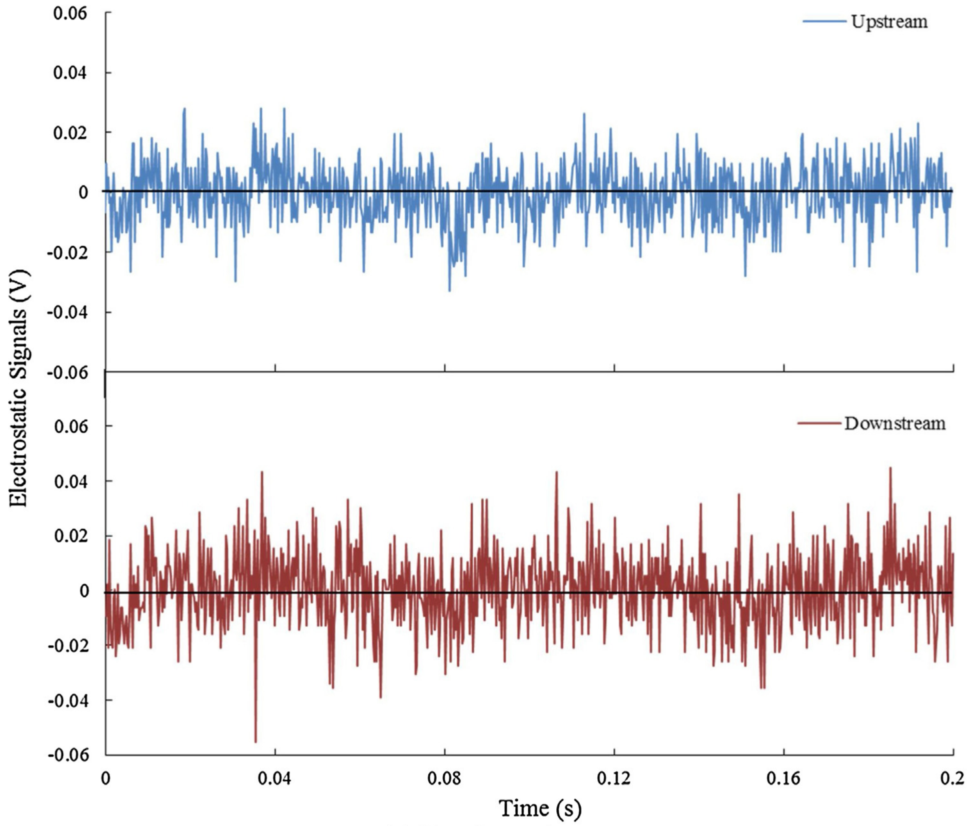

(**a**) Signal waveforms

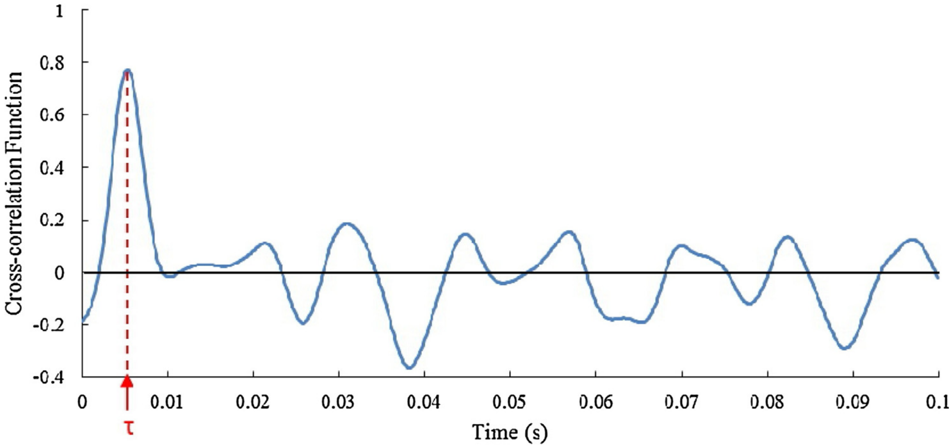

(b) Cross-correlation function of the two signals

Fig. 7. Typical signal waveforms from the double-sensor system and resulting cross-correlation function.

roughness, rotor size and rotational speed. In this study, the ambient temperature and relative humidity were set within a narrow range (Section 3.1) while the effects of rotors and operating speed on the measurement systems are investigated. Fig. 8 depicts the signal amplitude collected from the same electrostatic sensor along with corresponding signal conditioning unit for different test rotors. Each data point in Fig. 8 is a time averaged value with a standard deviation of less than 1%. The PTFE rotor generates higher electrostatic signal amplitude than the PVC and Nylon rotors for the same geometric dimension and surface roughness due to its better triboelectric characteristics and larger permittivity and resistivity. Through testing on the rotors with the same material and size, more electrostatic charge is generated on the rotors with the surface roughness of Ra 6.3. The signal amplitude of the 120 mm rotor in Fig. 8(c) is higher than that of the 60 mm rotor in Fig. 8(b) with the same material and surface roughness. This is due to the larger surface area and faster surface speed generating more electrostatic charge on the rotor surface. It can be obviously seen from Fig. 8 (a)–(c) that the RMS (Root-Mean-Square) signal amplitude for a certain rotor increases with the rotational speed because of the increased electrostatic charge on the rotor surface.

3.5. *Accuracy*

The accuracy of the electrostatic sensor based measurement systems depends on the signal –to-noise ratio of the electrostatic signals and their sampling frequency. When the rotor speed is lower than 500 rpm, limited electrostatic charge is generated on the rotor

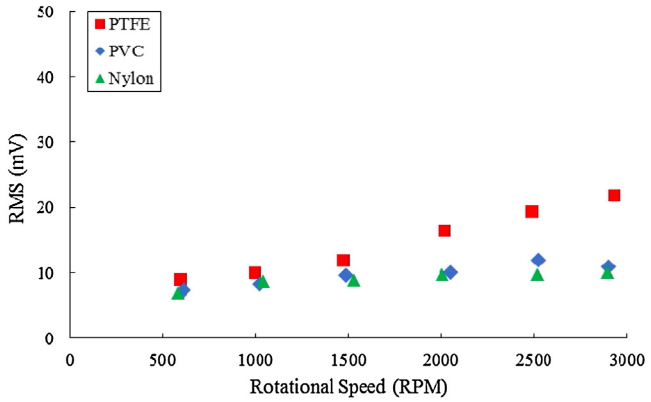

(a) D=60 mm and Ra=3.2

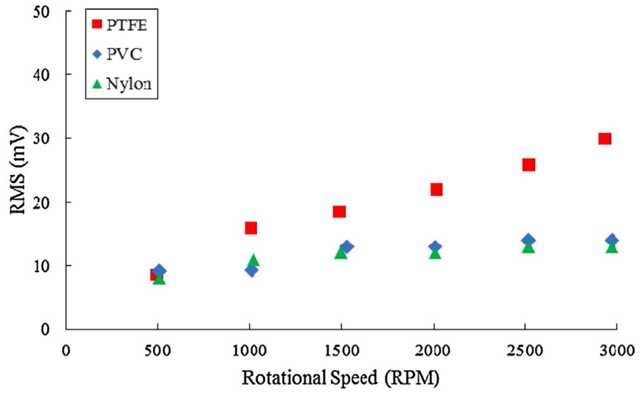

(b) D=60 mm and Ra 6.3

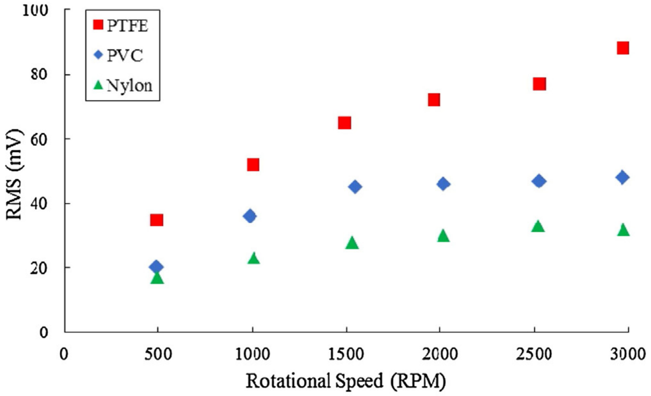

(c) D=120 mm and Ra=6.3

Fig. 8. Signal amplitude of different rotors.

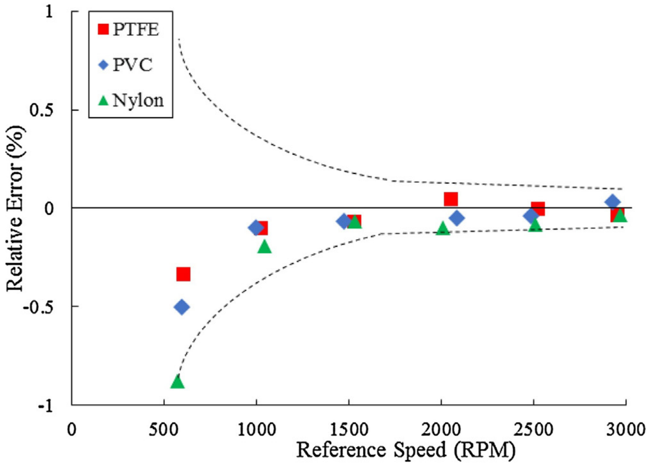

(a) D=60 mm and Ra=3.2

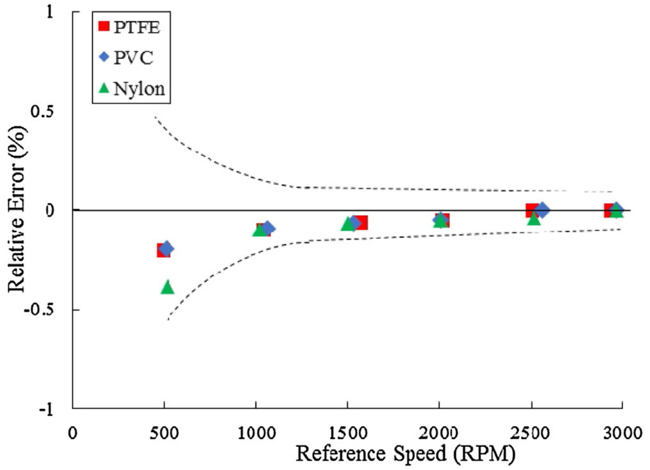

(b) D=60 mm and Ra=6.3

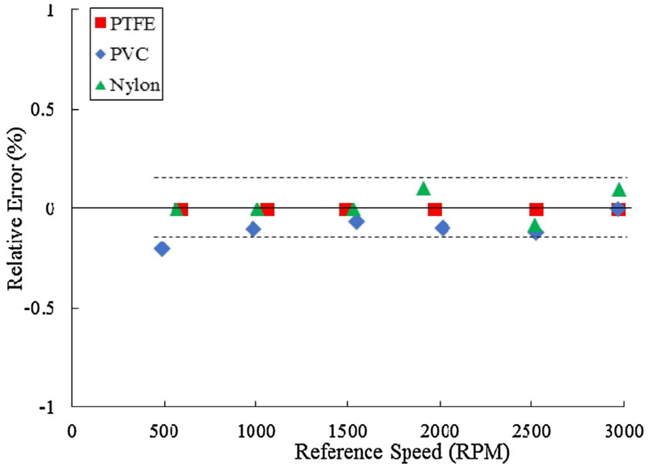

(c) D=120 mm and Ra=6.3

Fig. 9. Relative errors from the single-sensor system.

surface and discharges quickly over one revolution. In this case it is difficult to obtain valid rotational speed measurements using the single-sensor system. However, additional measures can be taken to increase electrostatic charge on the rotor. For example, a marker with better triboelectric property or even permanent charge on its surface (e.g. electret) may be used.

The relative errors of the measured rotational speed, as shown in Figs. 9 and 10, are average values with a standard deviation of less than 0.05%. The dashed lines in Figs. 9 and 10 depict the error range. It is evident that the measured speed from the single-sensor based measurement system is very close to the reference reading with a maximum error of less than ±1.5%. It can be seen from Fig. 9 that the measurement system performs better on the larger rotor and high rotational speed as more electrostatic charge generated on the rotating surface and hence high quality of signal. Moreover, the PTFE rotor outperforms the PVC and Nylon rotors in terms of accuracy. For PTFE rotors, the relative errors are always within ±0.5% over the range of 500 rpm to 3000 rpm. This outcome agrees well with the triboelectric charging series as shown in Fig. 5.

Fig. 10 shows the experimental results of comparative tests on the double-sensor system. As the rotational speed increases, more electrostatic charge is generated on the rotor surface and hence smaller relative errors. The relative error from the double-sensor system is within ±1.5% when the rotational speed ranging from

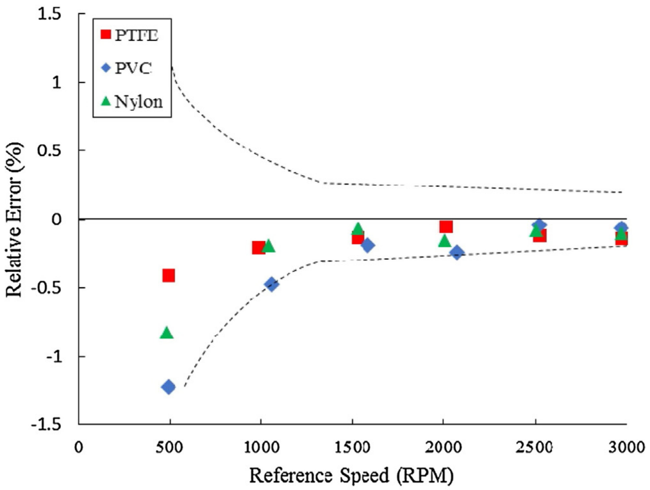

(a) D=60 mm and Ra=3.2

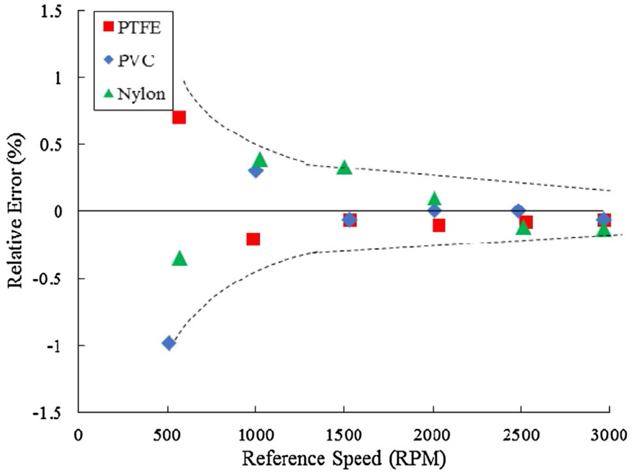

(b) D=60 mm and Ra=6.3

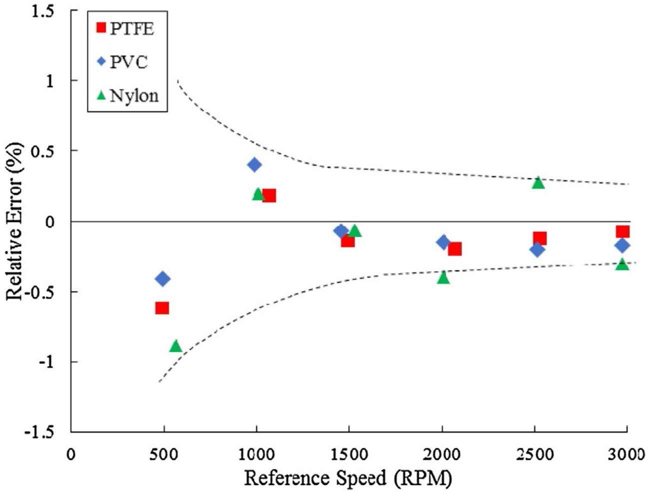

(c) D=120 mm and Ra=6.3

Fig. 10. Relative errors from the double-sensor system.

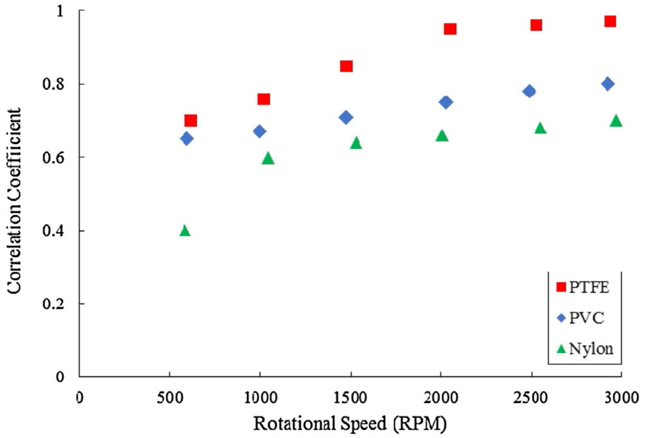

(a) D=60 mm and Ra=3.2

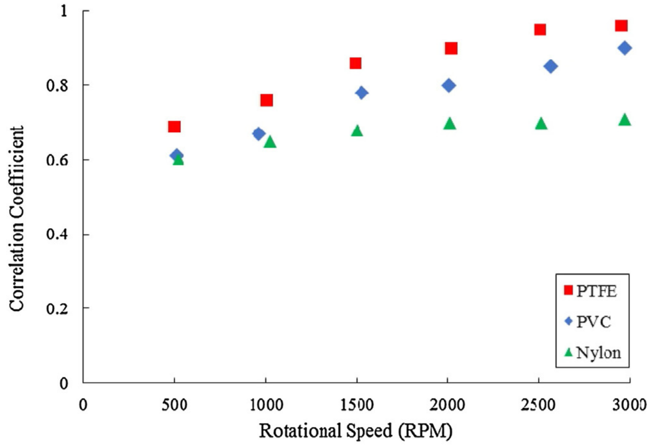

(b) D=60 mm and Ra=6.3

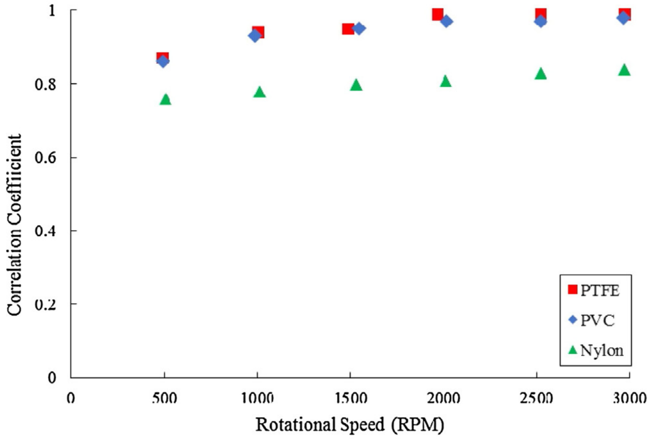

(c) D=120 mm and Ra=6.3

Fig. 11. Correlation coefficient from the single-sensor system.

500 rpm to 3000 rpm. However, the errors are relatively larger than those from the single sensor system, because the spacing between the two electrodes yields a short time delay between the two signals, which is relatively difficult to measure accurately, compared to the single-sensor system. It can be seen from Fig. 10 that the PTFE rotors yield more accurate measurement results than the PVC and Nylon rotors.

3.6. Correlation coefficient

Correlation coefficient normally represents the similarity between two signals [6] as those in the double-sensor system. In the case of the single-sensor system, the correlation coefficient represents the degree of repetitiveness or periodicity of the sensor signal due to the rotational motion. As shown in Fig. 11, the correlation

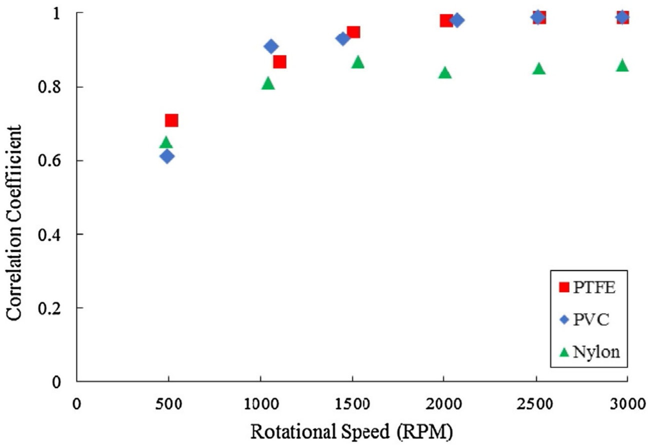

(a) D=60 mm and Ra=3.2

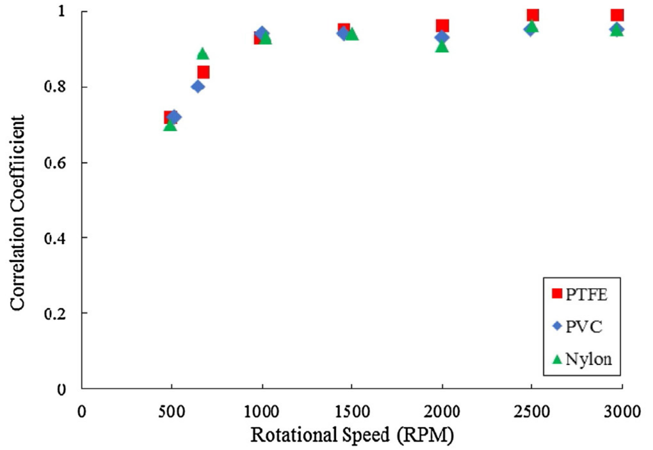

(b) D=60 mm and Ra=6.3

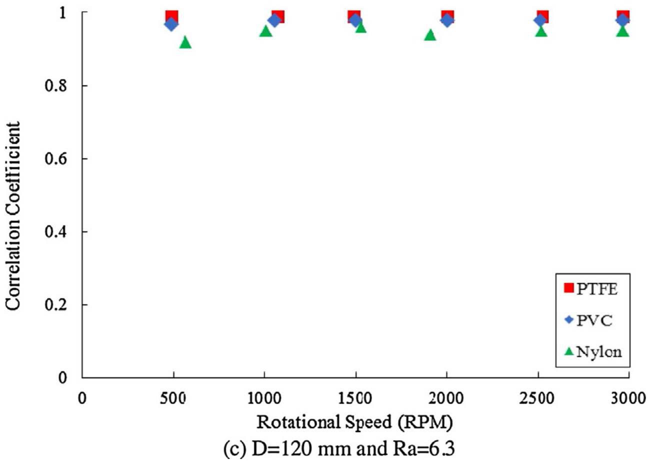

(c) D=120 mm and Ra=6.3

Fig. 12. Correlation coefficient from the double-sensor system.

coefficient obtained from the single sensor system tends to increase with the rotor speed. As expected, less electrostatic charge is generated on the Nylon rotor, resulting in lower correlation coefficient (0.4–0.8). However, the correlation coefficient of the PTFE rotor (0.7–1.0) is consistently higher than those of PVC and Nylon rotors. For larger and coarser rotors, relatively higher correlation coefficients are observed due to more electrostatic charge produced on the rotor surface.

The correlation coefficient from the double-sensor system under different test conditions is shown in Fig. 12. As the rotational speed increases, the correlation coefficient improves in general. A comparison between Figs. 11 and 12 indicate that the difference in the correlation coefficients between the three materials for the double-sensor system is much smaller than that for the single-sensor system. This outcome illustrates that the double-sensor system is less sensitive to the effect of rotor materials.

4. Conclusions

A performance comparison between the single-sensor and double-sensor systems has been conducted through experimental investigations. Experimental results have demonstrated that the single-sensor system yields a maximum error of ±1% while the double-sensor system produces an error within ±1.5% over the speed range of 500 – 3000 rpm for all tested rotors. Both measurement systems yield more reliable results for the PTFE rotor with a larger size at a higher rotational speed. Moreover, the double-sensor system is less sensitive to the effect of rotor material. Further research will be conducted to improve the signal-to-noise ratio and enhance the performance of the double-sensor system at lower rotational speed and extend the measurement range. Meanwhile, investigations into the environmental factors (i.e. ambient temperature and relative humidity) and industrial trials will be conducted in the near future.

Acknowledgements

The authors would like to acknowledge the National Natural Science Foundation of China (No. 51375163), the Fundamental Research Funds for the Central Universities (No. JB2016039) and China Postdoctoral Science Foundation (No. 2015M581045) for providing financial support for this research. The IEEE Instrumentation and Measurement Society is acknowledged for offering an IEEE Graduate Fellowship Award in relation to the research as reported in this paper.

References

[1] Y. Didosyan, H. Hauser, H. Wolfmayr, J. Nicolics, P. Fulmerk, Magneto-optical rotational speed sensor, Sens. Actuators A 106 (1–3) (2003) 168–171.
[2] C. Giebeler, D. Adelerhof, A. Kuiper, J. Zon, D. Oelgeschlager, G. Schulz, Robust GMR sensors for angle detection and rotation speed sensing, Sens. Actuators A 91 (1–2) (2001) 16–20.
[3] X. Zhang, J. Chen, Z. Wang, N. Zhan, R. Wang, Digital image correlation using ring template and quadrilateral element for large rotation measurement, Opt. Lasers Eng. 50 (7) (2012) 922–928.
[4] F. Combet, R. Zimroz, A new method for the estimation of the instantaneous speed relative fluctuation in a vibration signal based on the short time scale transform, Mech. Syst. Signal Process. 23 (4) (2009) 1382–1397.
[5] H. Lin, K. Ding, A new method for measuring engine rotational speed based on the vibration and discrete spectrum correction technique, Measurement 46 (7) (2013) 2056–2064.
[6] A. Mohanty, Machinery Condition Monitoring: Principles and Practices, CRC Press, 2014.
[7] L. Wang, Y. Yan, Y. Hu, X. Qian, Rotational speed measurement through electrostatic sensing and correlation signal processing, IEEE Trans. Instrum. Meas. 63 (5) (2014) 1190–1199.
[8] L. Wang, Y. Yan, Y. Hu, X. Qian, Rotational speed measurement using single and dual electrostatic sensors, IEEE Sens. J. 15 (3) (2015) 1784–1793.
[9] L. Wang, Y. Yan, Y. Hu, X. Qian, Effects of material type and surface roughness of the rotor on the electrostatic sensing based rotational speed measurement, in: Proceedings of the IEEE International Instrumentation and Measurement Conference, Pisa, Italy, May 11–14, 2015, pp. pp. 452–457.
[10] A. Bur, Dielectric properties of polymers at microwave frequencies: a review, Polymer 26 (7) (1985) 963–977.
[11] J. Chang, J. Kelly, J. Crowley, Handbook of Electrostatic Processes, Technology & Engineering, New York, 1995.
[12] L. Wang, Y. Yan, Mathematical modelling and experimental validation of electrostatic sensors for rotational speed measurement, Means. Sci. Technol. (25) (2014) 115101.
[13] Monarch Instruments, PLT200, 2017, Available online: http://www.monarchinstrument.com/product.php?ID=24 (Accessed on 9 February 2017).
[14] Surface Roughness, 2017, Available online: http://en.wikipedia.org/wiki/Surface_roughness (Accessed 9 February 2017).

[15] D. Taylor, P. Secker, Industrial Electrostatics: Fundamentals and Measurements, Research Studies Press, 1994.

[16] M. Silaghi, Dielectric Material, InTech Press, 2012.

[17] D. Lide, CRC Handbook of Chemistry and Physics, CRC Press, 2005.

[18] D. Davies, Charge generation on dielectric surface, J. Phys. D: Appl. Phys. 2 (11) (1969) 1533–1537.

[19] E. Groop, A. Nowicki, C. Calle, C. Buhler, J. Mantovani, Comparison of surface resistivity and triboelectric charge generation characteristics of materials, Proceedings of the 40th Space Congress (2003) p. 6, April.

Biographies

Lijuan Wang received the B.Eng. degree in computer science and technology from Qiqihar University, Heilongjiang Province, China, in 2010, and the Ph.D. degree in measurement and automation from North China Electric Power University, Beijing, China, in 2015. She is currently involved in a post-doctoral research in instrumentation and measurement with North China Electric Power University, Beijing. Her current research interests include electrostatic sensing, flow measurement and digital signal processing.

Yong Yan received the B.Eng. and M.Sc. degrees in instrumentation and control engineering from Tsinghua University, Beijing, China in 1985 and 1988, respectively, and the Ph.D. degree in flow measurement and instrumentation from the University of Teesside, Middlesbrough, U.K., in 1992. He was an Assistant Lecturer with Tsinghua University in 1988. In 1989, he joined the University of Teesside as a Research Assistant. After a short period of postdoctoral research, he was as a Lecturer with the University of Teesside from 1993 to 1996, and then as a Senior Lecturer, Reader, and Professor with the University of Greenwich, Chatham Maritime, U.K., from 1996 to 2004. He is currently a Professor of Electronic Instrumentation, the Head of Instrumentation, Control and Embedded Systems Research Group, and the Director of Research at the School of Engineering and Digital Arts, the University of Kent, Canterbury, U. K.

Kamel Reda received the B.Eng. degree in Electronics from CNAM University, Paris, France, in 2001, the M.Sc. degree in instrumentation and sensors from CNAM University, Paris, France, in 2014 and the M.B.A. degree from University Paris 1 Panthéon-Sorbonne, Paris, France, in 2004. He is currently pursuing the PhD degree in instrumentation and sensors at the University of Kent, Canterbury, U.K. His current research interests include electrostatic sensing and digital signal processing.

XXII World Congress of the International Measurement Confederation (IMEKO 2018) IOP Publishing
IOP Conf. Series: Journal of Physics: Conf. Series **1065** (2018) 072024 doi:10.1088/1742-6596/1065/7/072024

Enhancing the performance of a rotational speed measurement system through data fusion

L Wang, Y Yan[*]**, K Reda**
School of Engineering and Digital Arts, University of Kent, Canterbury, Kent CT2 7NT, UK

E-mail: y.yan@kent.ac.uk

Abstract. Electrostatic sensors with a single electrode or double electrodes have been applied for rotational speed measurement. In order to improve the performance of the rotational speed measurement system based on double electrostatic sensors, a data fusion algorithm is incorporated in the system. Two independent signals are accessible from the electrostatic sensor with double electrodes. From these signals two independent rotational speed measurements are obtained through auto-correlation processing of each signal and the third rotational speed measurement is also achieved by cross-correlating the two signals. A data fusion algorithm is then applied to optimally combine the three measurements. The system with the data fusion algorithm is capable of producing more accurate and more robust measurements than previous double-sensor system with a wider measurement range. Experimental results suggest that the relative error of the improved system is mostly within ±0.5% over the speed range of 200 rpm - 3000 rpm.

1. Introduction

Rotational speed is one of the most important variables to be measured for condition monitoring of rotating machineries. Over the past few decades a variety of tachometers based on mechanical, electrical, electromagnetic and optical principles have been developed [1-3]. These tachometers are generally classified into two types according to their sensing mode: contact and non-contact. The non-contact tachometers are superior to the contact ones due to the relief of mechanical wear and improvement in measurement accuracy. In recent years, as one of the most promising sensors for industrial applications, electrostatic sensors with single, double or quadruple electrodes have been proposed to measure rotational speed in recognition of the advantages of low-cost and suitability for a hostile industrial environment [4,5]. The single or double-electrode design is preferable over the quadruple design for practical applications due to the simpler installation of sensors [5]. However, previous experimental investigations suggest that the double-electrode system using cross-correlation between the two signals generates an error within ±1.5% in rotational speed measurement over a speed range of 500 rpm - 3000 rpm [5]. In order to improve the performance of the double-electrode system in terms of measurement accuracy, uncertainty and robustness, data fusion techniques are applied to combine the independent measurements from the individual sensors. This paper presents the principle of the proposed data fusion method along with experimental results.

---

[*] Corresponding author.

2. Measurement principle

Figure 1 shows the block diagram of the rotational speed measurement system based on a double-electrode electrostatic sensor with a data fusion algorithm. When a non-metallic rotor is in rotational motion, its surface becomes electrostatically charged due to the friction between the rotor surface and air. The double-electrode sensor is placed adjacent to the rotor surface to sense the motion of the rotor. Electrostatic charge on the rotor surface is detected by the two electrodes through electrostatic induction. After the signal conditioning unit, the amplified and filtered signals, S_1 and S_2, are converted to digital signals, $S_1(k)$ and $S_2(k)$, and processed using correlation techniques.

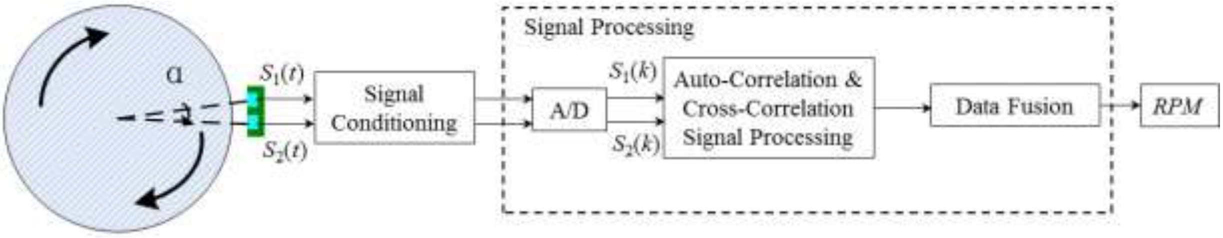

Figure 1. Block diagram of the measurement system with data fusion.

Through auto-correlation signal processing of S_1 and S_2, respectively, two independent rotational speeds, RPM_1 and PRM_2, are obtained,

$$RPM_1 = \frac{60}{\tau_1} \tag{1}$$

$$RPM_2 = \frac{60}{\tau_2} \tag{2}$$

where τ_1 and τ_2 are the periods of the rotational motion, which are determined from the auto-correlation functions of S_1 and S_2, respectively,

$$R_1(m) = \frac{\sum_{k=1}^{N} S_1(k) S_1(k+m)}{\sum_{k=1}^{N} S_1^2(k)} \tag{3}$$

$$R_2(m) = \frac{\sum_{k=1}^{N} S_2(k) S_2(k+m)}{\sum_{k=1}^{N} S_2^2(k)} \tag{4}$$

where $R_1(m)$ and $R_2(m)$ are the resulting auto-correlation functions of the two signals, respectively, and N is the total number of data points in the sampled signal during each measurement cycle. The location of the dominate peak on the time axis of each auto-correlation function is the period of the rotational motion, τ_1 or τ_2.

The third rotational speed, RPM_{12}, is determined from,

$$RPM_{12} = \frac{30\alpha}{\pi \tau_{12}} \tag{5}$$

where α is the angular spacing in radians between the two electrodes, τ_{12} is the transit time taken for the rotor moving from the upstream electrode to the downstream one, which is determined from the cross-correlation function between S_1 and S_2,

$$R_{12}(m)=\frac{\sum_{k=1}^{N}S_1(k)S_2(k+m)}{\sqrt{\sum_{k=1}^{N}S_1^2(k)}\sqrt{\sum_{k=1}^{N}S_2^2(k)}} \tag{6}$$

The time corresponding to the dominant peak in the cross-correlation function $R_{12}(m)$ is the transit time τ_{12}.

The final rotational speed, *RPM,* through data fusion, is given by,

$$RPM=\frac{c_1\times RPM_1+c_2\times RPM_2+c_{12}\times RPM_{12}}{c_1+c_2+c_{12}} \tag{7}$$

where c_1 and c_2 are correlation coefficients of the auto-correlation functions ($R_1(m)$ and $R_2(m)$) respectively, which represent the degree of periodicity of the signals due to the rotational motion, and c_{12} is the correlation coefficient of the cross-correlation function ($R_{12}(m)$) which represents the similarity between the two signals.

3. Experimental results and discussion

3.1. Test rig

As shown in figure 2, an experimental system based on the measurement principle was designed and implemented. The test rotor is made of PTFE with a diameter of 60 mm. The rotor, driven by an AC motor, provides a rotational speed up to 3000 rpm. The electrostatic sensor consists of two identical strip-type electrodes with a centre-to-centre spacing of 7 mm. Each electrode is 3 mm in width and 20 mm in length. In order to evaluate the performance of the measurement system with data fusion, a commercial laser tachometer (Monarch Instruments, PLT200 [6]) was used to provide reference speeds. During the experimental tests the ambient temperature and relative humidity were measured to be from 20 °C to 23 °C and between 30% to 35%, respectively.

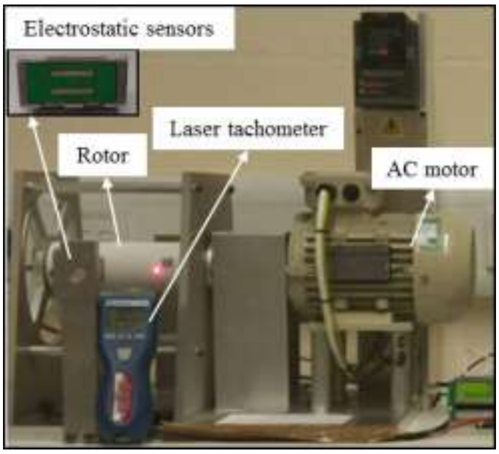

Figure 2. Rotational speed measurement system

3.2. Experimental results

Experimental tests were conducted on the test rig over the speed range of 200 rpm to 3000 rpm. For each speed, 30 measurements were recorded. The relative error of the measurement system is plotted in figure 3. The data points in figure 3 represent the average speed. The error bars indicate the maximum and minimum relative errors of the 30 measurements at each speed. Rotational speed RPM_{12} is directly obtained through cross-correlation between the two signals, while *RPM* is the final average speed through data fusion. As shown in figure 3, the average speed of RPM_{12} is very close to the averaged *RPM*. Both of the average speeds are no greater than 0.1%. In terms of maximum and minimum relative errors, the variation of *RPM* is less than RPM_{12} under all test conditions. The relative error of *RPM* is mostly within ±0.5%, which suggests the measurement results with data fusion have low uncertainty. The relatively more significant fluctuation at a lower speed is due to low signal-to-noise ratio because less electrostatic charge is generated on the rotor surface. For this reason, the system is unable to provide reliable rotational speed measurement lower than 200 rpm. As the speed increases, the relative error becomes smaller or much smaller because of the increased charge on the rotor surface. In addition, the measurement system with data fusion has better robustness. For instance, if one of the sensing channel failed, the system with sensor fusion would still be able to produce measurements through auto-correlation of the signal from the working sensor.

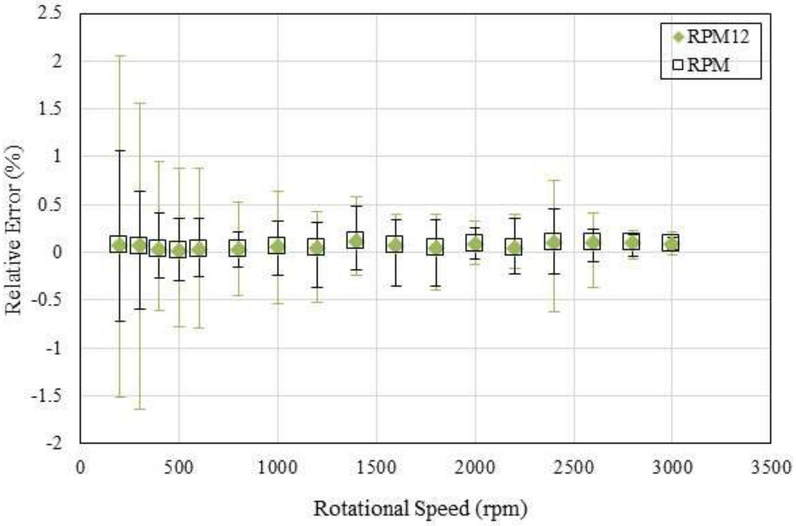

Figure 3. Relative error of the measured rotational speed

4. Conclusions

Data fusion techniques have been applied to improve and enhance the performance of the rotational speed measurement system based on a double-electrode electrostatic sensor. Experimental results have demonstrated that the measurement error has been reduced from ±1.5% to ± 0.5% due to the use of the data fusion algorithm. In addition, for this level of measurement error, the lower end of the measurement range has been extended from the previous 500 rpm to 200 rpm with reduced measurement uncertainty. Meanwhile, the robustness of the system is enhanced as the system would still be able to produce valid measurements in the case of a malfunctioning signal channel. More investigations into the effects of environmental factors (i.e. ambient temperature and relative humidity) on the measurement system and industrial trials will be conducted.

5. References

[1] Monhanty A 2014 *Machinery Condition Monitoring: Principles and Practices* (CRC Press)
[2] Chen Q, Xue L and Rao H 2017 Rotational speed measurement of ring spinning based on magnetic sensor *Meas. Sci. Technol.* **28** 115106.
[3] Guo J, Zhu C, Lu S, Zhang D and Zhang C 2016 Vison-based measurement for rotational speed by improving Lucas-Kanade template tracking algorithm *Appl. Optics* **55** 7186-94.
[4] Wang L, Yan Y, Hu Y and Qian X 2014 Rotational speed measurement through electrostatic sensing and correlation signal processing Comparison of single and double electrostatic sensors for rotational speed measurement *IEEE Trans. Instrum. Meas.* **63** 1190-99.
[5] Wang L, Yan Y and Reda K 2017 Comparison of single and double electrostatic sensors for rotational speed measurement *Sensor. Actuat. A-Phys.* **266** 46-55
[6] Monarch Instruments, PLT200, 2017 Available online: https://monarchinstrument.com/products/pocket-laser-tach-200 (Accessed on 3 March 2018)

Online Continuous Detection of an Unbalanced Metallic Shaft Using Electrostatic Sensors

Kamel Reda and Yong Yan
School of Engineering and Digital Arts
University of Kent, Canterbury, Kent CT2 7NT, UK
Email: kr314@kent.ac.uk; y.yan@kent.ac.uk

***Abstract*—Vibration detection and measurement of a rotary shaft is essential for the diagnosis and prognosis of industrial rotating machinery. However, the imbalance of a shaft, as quantified through vibration displacement, is the most common cause of machine vibration. The objective of this study is to develop a novel technique through electrostatic sensing for the on-line, continuous and non-contact detection of the imbalance fault of a rotary shaft. A mathematical model is established to extract useful information about the shaft displacement vibration from the simulated signal in the frequency domain. Experimental tests were conducted on a purpose-built test rig to detect the displacement vibration of the shaft at different rotational speeds (400, 800 and 1200 rpm). A normal shaft and an eccentric shaft were tested with the output signals from the electrostatic sensor analyzed. The effectiveness of the proposed method is verified through experimental tests and computational simulation.**

Keywords— Rotating machinery; Fault detection; Vibration; Imbalance; Displacement; Electrostatic Sensors.

I. INTRODUCTION

Vibration measurement of rotary shafts plays a significant part in the condition monitoring of rotating machinery. A variety of mechanical defects, such as shaft imbalance, coupling misalignment and bearing deterioration, may give rise to excessive vibrations that cause machine failure. Imbalance is the most common cause of vibrations of rotating machines. An unbalanced shaft makes it more susceptible to high amplitude vibrations that cause noise and incorrect functionality and thus reduces the life span of the machine.

There are a range of techniques available for shaft vibration detection through the measurement of displacement, velocity or acceleration [1, 2]. However, conventional contact type sensors, such as accelerometers and velocity transducers, are unsuitable for rotating shafts due to the impractical requirement of physical contact of the sensors with the moving surface [3, 4]. Several types of proximity sensors based on eddy current, ultrasonic, capacitive or inductive principles are often used to measure the relative vibration of a rotating shaft [5, 6]. Recently, a number of new methods have been proposed for shaft vibration detection. Tong et al [7] designed a reflective intensity-modulated non-contact optical fiber sensing system to detect radial vibration of high-speed rotating machinery. Vyroubal [8] identified the vibration signature using optical sensors through spectral analysis of phase-modulated light pulses. Okabe et al [9] described an ultrasonic sensor based method for shaft vibration detection by measuring the propagation time of the ultrasonic wave from the sensor to the shaft surface. However, the optical and acoustic sensors may not function well in a hostile environment due to the presence of dust and background acoustic noise. In addition, such instruments are prohibitively expensive to implement in routine industrial applications. Much more recently, Wang et al [10] employed electrostatic sensors for the vibration detection of rotating machinery. Later, they proposed a method for the radial vibration measurement of a shaft using electrostatic sensors and Hilbert-Huang Transform [11]. Advantages of electrostatic sensors over the conventional optical and acoustic sensors include simple structure and low cost. However, both methods were based on the amplitude of a signal resulting from electrostatic charge on the surface of a dielectric shaft, assuming that the only factor affecting the amount of induced charge and hence the signal amplitude is the distance between the electrode and the shaft. Nevertheless, the electric charge level on the dielectric shaft surface depends significantly on environmental conditions and consequently the signal amplitude varies with environmental factors such as ambient temperature and relative humidity [12, 13]. As a result, these methods cannot be used to achieve an absolute displacement measurement due to the uncertain amount of charge on the shaft surface. Moreover, these methods work only on dielectric shafts and require an array of sensors to be installed around the shaft, making the sensor installation practically difficult.

This paper presents a novel technique to detect the imbalance of a metallic shaft by applying a magnitude independent method in frequency domain and using electrostatic sensors. The proposed method is based on the frequency characteristics of the sensor signal, rather than its amplitude, in order to detect the shaft displacement. This method and hence the measurements, are independent of the level of the accumulated charge on the shaft surface, which makes the measurement system more stable and reliable in harsh industrial environments. In addition, the proposed technique can work on metallic shafts and uses only a single electrostatic sensor. Mathematical modelling is performed to study the frequency response characteristics of two metallic shafts under normal and eccentric conditions. Experiments were conducted to verify the validity and effectiveness of the proposed technique.

II. METHODOLOGY

A. Measurement Principle

Fig. 1 shows a simplified physical model of the sensing system. The physical model consists of a metallic shaft, electrically isolated point charges fixed on the shaft surface

978-1-5386-2222-3/18/$31.00 ©2018 IEEE

(e.g. points *M* and *N*), an electrostatic sensor, a signal conditioning circuit, signal processing software, and user interface.

A small marker of dielectric material with an approximate volume of 1mm^3, fixed on the metallic shaft, becomes electrostatically charged during rotational motion due to the friction between the marker and air. The insulated electrode with a suitable charge detection circuit can detect the charge on the marker and generate an output signal through electrostatic induction. Previous research [14] shows that the frequency response of the sensor output depends primarily on the circular trajectory diameter *D* of the rotating point charge *P*, the distance *s* between the point charge and the electrode, and the angular speed of the shaft. For a given point charge on the shaft, the rotational motion results in a circular trajectory of the point charge. In the case of a normal shaft, the shortest distance between any rotating point on the shaft and the electrode is constant as is its trajectory diameter, which is equal to (*D*+*s*). While each point on an eccentric shaft rotates along a different circular trajectory and results in a variation in *s*. By analyzing the frequency response of the output signal, the displacement and hence the imbalance of the shaft is then detected.

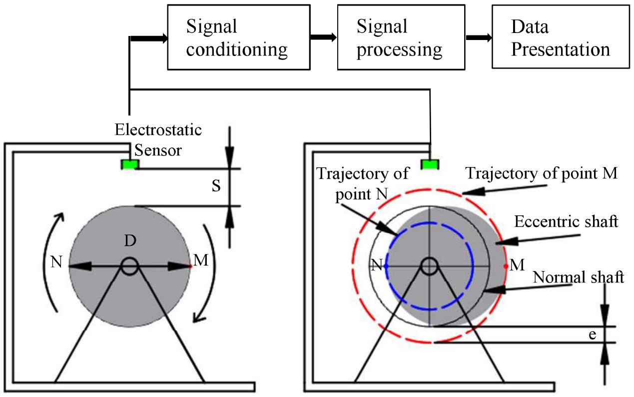

(a) Normal shaft (b) Eccentric shaft

Fig. 1: Physical model of the sensing system.

It is worth noting that the two points, *M* and *N*, correspond to the longest and shortest diameters with respect to the axis of rotation, being *(D+2e)* and *(D-2e)*, respectively, where *e* is the eccentricity of the shaft being the distance between the axis of rotation and the geometric center of the shaft.

B. *Mathematical Model*

As shown in Fig. 2, a simplified mathematical model of the electrostatic sensor for shaft displacement detection is established. The cylinder indicates a metallic rotor with a diameter *D*, on which an electrically insulated point charge is fixed. The rotational motion of the point charge at angular speed *ω* creates, in effect, an impulse input to the sensing system. A strip type electrode with dimensions *LxW*, made on a small printed circuit board with adequate insulation together with grounding around the electrode, can be regarded as a piece of perfectly conductive metal and is placed at distance *s* from the shaft.

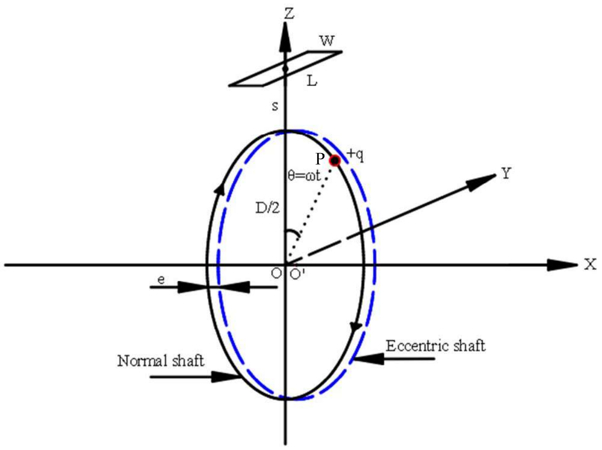

Fig. 2. Mathematical model of the sensing system.

Based on Gauss's law, the total induced charge *Q* on the surface of the electrode due to the rotating charge *q* on the shaft is given by [14]:

$$Q(t) = -\frac{q}{2\pi}\int_{-\frac{w}{2}}^{+\frac{w}{2}}\int_{-\frac{L}{2}}^{+\frac{L}{2}}\frac{(0.5D+s)-0.5Dcos\omega t}{\left(\left(x-0.5Dsin(\omega t)\right)^2+\left(0.5D+s-0.5Dcos(\omega t)\right)^2+y^2\right)^{\frac{3}{2}}}dydx \tag{1}$$

The actual current output $I_s(t)$ of the electrostatic sensor is thus:

$$I_s(t) = \frac{dQ(t)}{dt} \tag{2}$$

For an eccentric shaft where its geometric center is offset by *e* from the rotating center, the diameter of the circular trajectory of an arbitrary point on the shaft is (*D* +*2d*) and the distance *s* becomes (*s* - *d*), where d is the relative displacement of the shaft and varies in the interval [-*e*, +*e*]. The total charge becomes:

$$Q(t) = -\frac{q}{2\pi}\int_{-w/2}^{+w/2}\int_{-L/2}^{+L/2}\frac{(0.5(D+2d)+(s-d))-0.5(D+2d)cos\omega t}{((x-0.5(D+2d)sin\omega t)^2+(0.5(D+2d)+(s-d)-0.5(D+2d)cos\omega t)^2+y^2)^{3/2}}dydx \tag{3}$$

C. *Impulse Response of the Sensor*

A point charge approaching towards the electrode along a circular trajectory from infinity is equivalent to an impulse input with amplitude *q* (i.e. qδ(t)) to the sensing system, thus the impulse response $h_s(t)$ of the system is given by:

$$h_s(t) = \frac{dQ(t)}{qdt} \tag{4}$$

Fig. 3 and Fig. 4 illustrate the impulse responses of the system for the two point charges, *M* and *N*, located on the normal and eccentric shafts, respectively, for an angular speed of 60 rad/s.

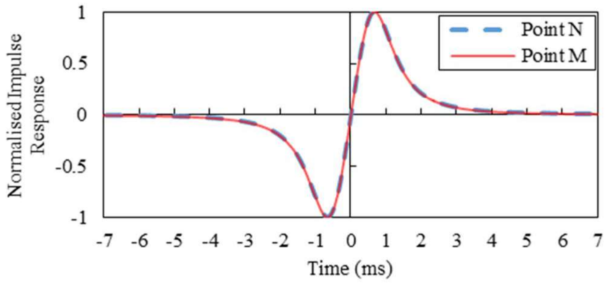

Fig. 3. Impulse responses for points N and M for normal shaft.

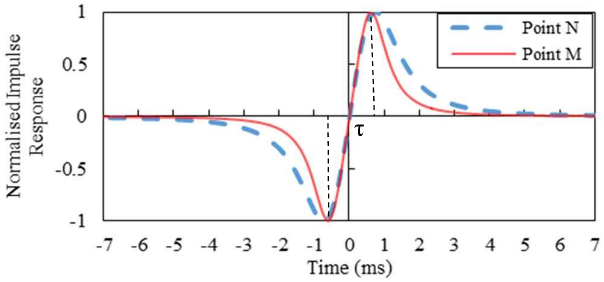

Fig. 4. Impulse responses for points N and M for eccentric shaft.

Fig. 3 shows that the impulse response curves resulting from points *M* and *N* on the normal shaft coincide with each other, while in the eccentric shaft, they do not. It is clear, that for the eccentric shaft, the time difference τ between the two peaks of the impulse response of point *N* is longer than that of point *M*, suggesting that point *N* is within the sensing region of the electrode for a longer period of time for a given angular speed (Fig. 4). The parameter *τ*, resulting from each point charge on the eccentric shaft, can then be used to identify the eccentricity of the shaft. Therefore, the eccentric shaft can be detected using the sensor output in the time domain. However, the variation of τ is relatively small, making it difficult to measure accurately.

D. Frequency Response of the Sensor

The frequency response of the sensing system can be determined from the Fourier transform of the impulse response $h_s(t)$:

$$H_s(f) = \int_{-\infty}^{+\infty} h_s(t) e^{-j2\pi f t}\, dt \tag{5}$$

By substituting $h_s(t)$ in equation (4) into equation (5), the frequency spectrum can be written as:

$$|H_s(f)| = \mathrm{F}(\omega, \mathrm{D}, \mathrm{s}, \mathrm{d}) \tag{6}$$

Equation (6) implies that the amplitude of the spectrum is a function of the angular speed *ω*, the diameter of the shaft *D*, the distance between the electrode and the shaft surface *s* and the shaft displacement *d* in case of eccentric shaft. The amplitude of the frequency response of the two impulses resulting from points *M* and *N* at rotational speed of 800 rpm for both normal and eccentric shafts are plotted in Figs. 5 and 6, respectively.

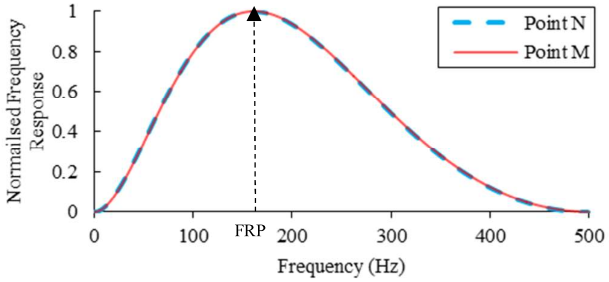

Fig. 5. Frequency responses for point charges N and M for normal shaft.

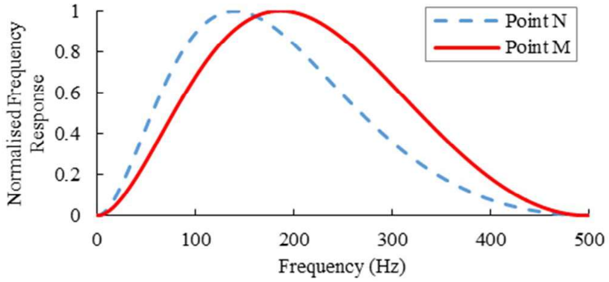

Fig. 6. Frequency responses for point charges N and M for eccentric shaft.

Simulation results in Figs. 5 and 6 indicate that the frequency responses of the system from two different point charges on the eccentric shaft are different. Moreover, the location of the Frequency Response Peak (FRP) is also different, which reflects the eccentricity of the shaft. It is evident that point *M* in a larger trajectory diameter and with the shortest distance to the electrode results in a wider bandwidth and a higher frequency at the peak than that of point *N*. When 6 identical markers were fixed around the shaft, the frequencies at the peak of the frequency responses FRP (Fig. 5) are plotted in Fig. 7.

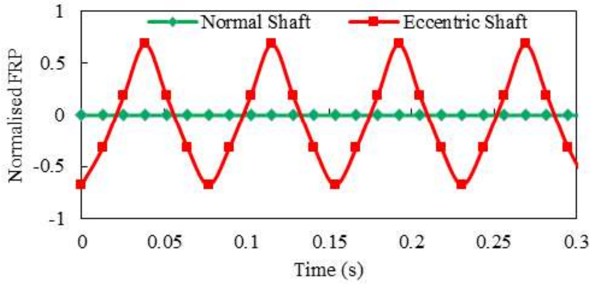

Fig. 7. Frequencies at peak of frequency responses of six point charges for normal and eccentric shafts.

It is worth noting that, the peaks and valleys in Fig. 7 correspond to the shortest and longest distance between the sensor and the shaft, respectively. Therefore, the waveform of the frequency response peak varies inversely with the spacing between the electrode and the shaft surface.

For a rigid shaft supported on rigid bearings, the shaft displacement is supposed to be independent of the shaft angular speed [3]. Previous research demonstrates that the bandwidth is proportional to the angular speed [14]. Thus, the peak frequency increases linearly with the rotational speed. For the purpose of direct comparison between the results obtained from the electrostatic sensor and that from the reference sensor, the frequency response at peaks could be normalised to the angular speed or the rotating frequency.

III. EXPERIMENTAL VALIDATION

A. *Experimental Conditions*

Experimental tests were conducted on a purpose-built test rig as shown in Fig. 8 to validate the performance of the electrostatic sensor for vibration displacement detection against a displacement sensor. The rotational speed of the motor is adjustable through the motor controller. Two metallic shafts with a diameter of 60 mm were tested. One is a normal shaft while the other is eccentric with *e* = 0.5 mm. An electrostatic sensor was placed 2 mm away from the shaft surface. To simulate two point charges on the rotor surface, two charged particles (marker) made from a 1 mm^3 cube of PTFE were fixed on each shaft. The induced current output of the sensor is derived and measured which corresponds to the impulse response. Then, the frequency response is obtained by the FFT of the impulse response. Six dielectric markers simulating six point charges are fixed evenly on the eccentric shaft. Two of them are located at the shortest and longest distance with respect to the centre of rotation. A displacement sensor, eddy current type, was used as a reference instrument to measure the relative distance to the shaft surface. All the tests were conducted in a laboratory with air conditioning (ambient temperature of 21.8°C and relative humidity of 44%).

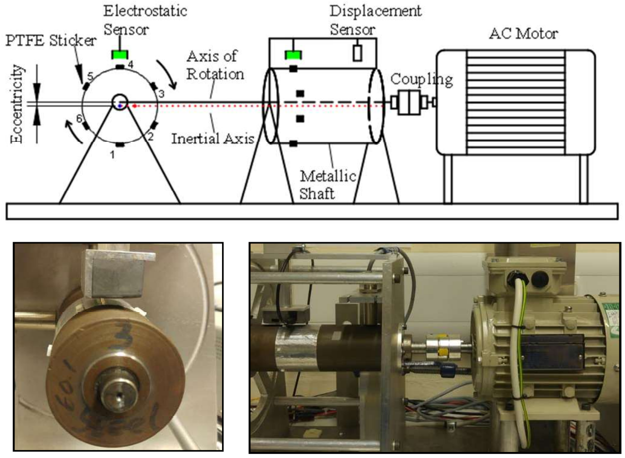

Fig. 8. Test rig.

B. *Results and Discussion*

Fig. 9 illustrates the signals from the sensors at the speed of 800 rpm from the normal and eccentric shafts. It can be seen that each signal is composed of a series of segments with six clearly identifiable impulses due to the markers on the shaft. It is clear that the amplitude of the signal, from the eccentric shaft, fluctuates due to the fluctuations of the distance between the shaft and the sensor over one revolution.

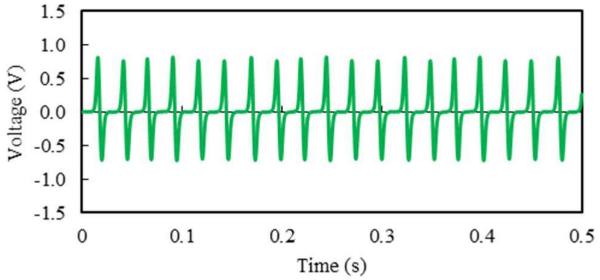

(a) Normal shaft.

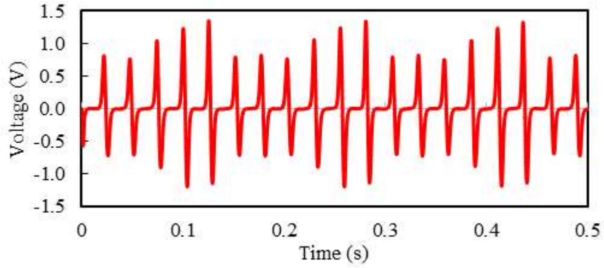

(b) Eccentric shaft.

Fig. 9. Signal output waveforms of the sensor.

The signal in fig. 9 is first decomposed into six single signals corresponding to the six point charges on the shaft. Then FFT of each signal is performed in order to extract the frequency at peak of the frequency response. Fig. 10 presents the normalised frequency response peaks of the six signals for an eccentric shaft at 800 rpm. It is obvious that the experimental results have a good agreement with the mathematical model.

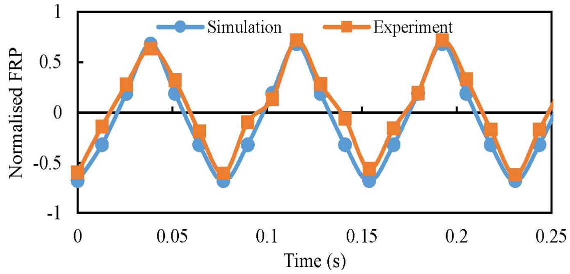

Fig. 10. Comparison between simulation and experimental data for Eccentric shaft.

Figs. 11, 12 and 13 present a direct comparison between the electrostatic sensor and the reference displacement sensor for normal and eccentric metallic shafts. The measurement from the displacement sensor in Figs. 11(b), 12(b) and 13(b) show a peak-to-peak displacement of about 1 V, independent from the rotational speed, which corresponds to 1mm. Although the measurement from the electrostatic sensor is not equal to the displacement measurement, a strong correlation and periodicity are clearly observed from both waveforms. However, the two waveforms from the two sensors exhibit nearly anti-phasing oscillatory behaviors, suggesting that the maximum displacement corresponds to the lowest bandwidth and consequently the lowest frequency at the peak of the spectrum.

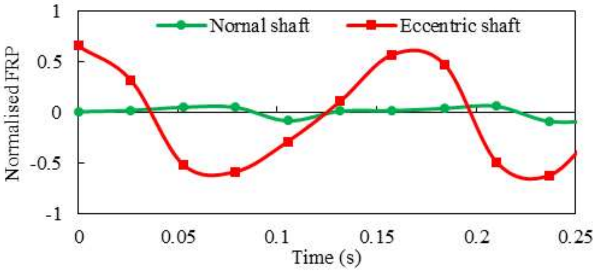

(a) Electrostatic sensor.

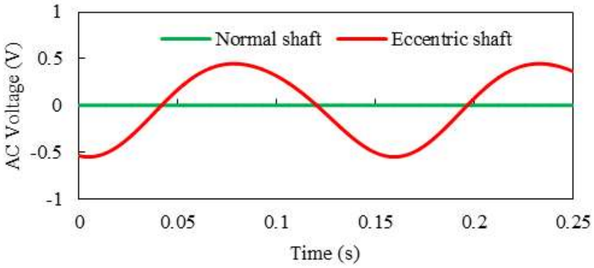

(b) Displacement sensor.

Fig. 11. Displacement measurement of the eccentric shaft at 400 RPM.

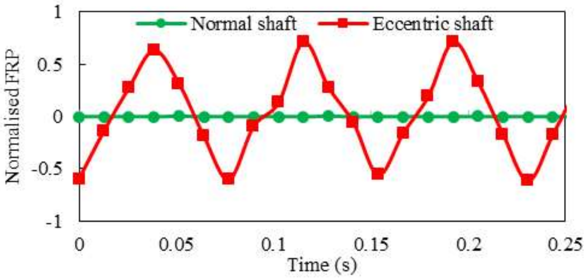

(a) Electrostatic sensor.

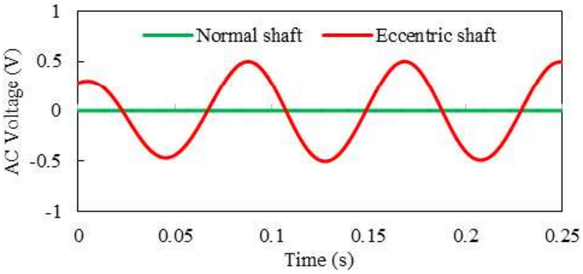

(b) Displacement sensor.

Fig. 12. Displacement measurement of the eccentric shaft at 800 RPM.

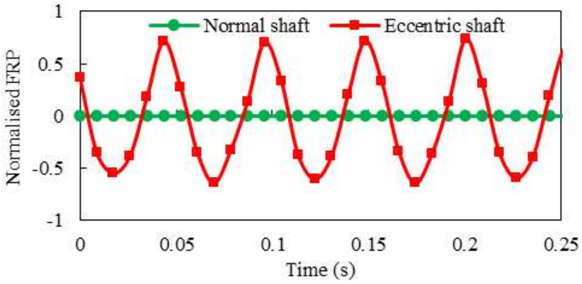

(a) Electrostatic sensor.

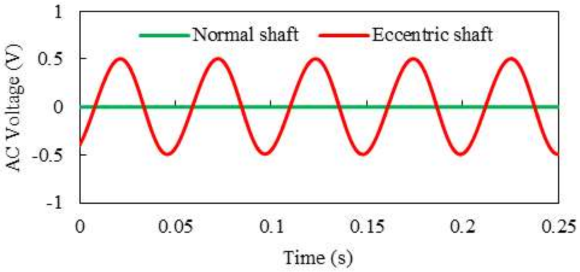

(b) Displacement sensor.

Fig. 13. Displacement measurement of the eccentric shaft at 1200 RPM.

From Fig. 11 it can be observed that the FRP of the six points fixed on the normal shaft fluctuate slightly which indicates the presence of some displacement vibrations due mainly to a minor shaft imbalance and bearings clearance.

IV. CONCLUSION

The frequency response characteristics of an electrostatic sensor have been used to detect an unbalanced shaft through displacement measurement. Six dielectric markers simulating electrically insulated point charges fixed on the shaft surface were used to generate impulsive inputs to the sensor to detect the displacement fluctuations through the variation of the frequency at the peak of frequency responses. The simulation results from the mathematical model have demonstrated the relationship between the frequency response characteristics of the electrostatic sensor and the shaft imbalance. A set of experiments has been conducted on a purpose-built test rig to validate the simulation results. The results have demonstrated that the electrostatic sensors can respond to the displacement of an eccentric shaft. Hence, an unbalanced shaft can then be identified using electrostatic sensors. This method can be developed to perform an absolute displacement measurement of an unbalanced shaft and the location of the mass imbalance can also be determined.

REFERENCES

[1] J.Z. Szabo, "Vibration diagnostic test for effect of unbalance," INES 2012-16th International Conference on Intelligent Engineering System, Lisbon, Portugal, 13-15, pp. 81–85, June 2012.

[2] W. Qiao, X. Gong, "Imbalance fault detection of direct-drive wind turbines using generator current signals," IEEE Trans. Eergy Convers. 27, pp. 468–476, 2012.

[3] M. L. Adams, "Rotating machinery vibration: From analysis to Troubleshooting," CRC Press, 2010.

[4] R. B. Randall, "State of the art in monitoring rotating machinery-Part 1," Sound Vib., vol.38, no.3, pp. 14-21, 2004.

[5] H. Chaurasiya, "Recent trends of measurement and development of vibration sensors," Int. J. Comput. Sci. Iss., vol.9, no.4, pp. 1694-0814, 2012.

[6] R. Atashkhooei, J. Urresty, S. Royo, J. Riba and L. Romeral, "Runout tracking in electric motors using self-mixing interferometry," IEEE/ASME Trans. Mech., vol.19, no.1, pp. 184-190, 2014.

[7] Q. Tong, H. Ma, L. Liu, X. Zhang and G. Li, "Key technology study on radial vibraition system of high-speed rotating machinery," Chinese Journal of Scientific Instrument, vol.5, no.32, pp. 1026-1032, May 2011.

[8] D. Vyroubal, "Optical method for instant estimate of vibration signature based on spectrum analysis of phase-modulated light pulses," IEEE Trans. Instrum. Meas., vol.53, no.1, pp. 181-185, Feb. 2004.

[9] S. Okabe and S. Tanaka, "Measurement of shaft vibration using ultrasonic sensor," in Proc. of SICE 2003 Annual Conference, pp. 1155-1158, Fukui, Japan, Aug. 2003.

[10] L. Wang, Y. Yan, Y. Hu,X. Qian, "Intelligent condition monitoring of rotating machinery through electrostatic sensing and signal analysis," in proc. of IEEE International Conference on Smart Instrumentation, Measurement and Applications (ICSIMA), Kula lumpur, Malaysia, Nov. 2013.

[11] L. Wang, Y. Yan, Y. Hu, X. Qian, "Radial vibration measurement of rotary shafts through electrostatic sensing and Hilbert-Huang transform," in proc. of Instrumentation and Measurement Technology Conference (I2MTC), pp. 867-871 Taipei, Taiwan, May 2016.

[12] J. Lowell, A. Brown, "Contact electrification of chemically modified surfaces," J. Electrostat., vol.21, pp. 69-79, 2000.

[13] W. Greason, "Investigation of a test point for triboelectrification," J. Electrostat., vol.49, pp. 245-256, 2000.

[14] L. Wang and Y. Yan, "Mathematical modelling and experimental validation of electrostatic sensors for rotational speed measurement," Meas. Sci. Technol., vol.25, no.11, pp.115101, 2014.

A Comparative Study of Different Shaped Electrostatic Sensors for Rotational Speed Measurement

Kamel Reda, Yong Yan and Lijuan Wang
School of Engineering and Digital Arts
University of Kent, Canterbury, Kent CT2 7NT, UK
Email: kr314@kent.ac.uk; y.yan@kent.ac.uk; lw400@kent.ac.uk

***Abstract*— Electrostatic sensors have been successfully used in the field of particle flow measurement due to the advantages of simple structure, robustness and low cost. Recently, advances have been made in developing electrostatic sensing techniques for rotational speed measurement. The geometric shape and size of the electrodes have significant effects on the performance of electrostatic sensors in terms of spatial sensitivity and temporal frequency response. This paper focuses on the theoretical analysis and experimental assessment of strip and butterfly shaped electrodes for rotational speed measurement of a metallic shaft. Spatial sensitivity and filtering effect of the sensors are investigated through mathematical and computational modelling. Analytical and experimental results suggest that the butterfly shaped sensor outperforms the strip sensor in terms of spatial sensitivity, power spectral density and signal bandwidth.**

Keywords—electrostatic sensors; rotational speed; spatial sensitivity; filtering effect

I. INTRODUCTION

Electrostatic sensing techniques have attracted significant attention in many industrial applications due to the advantages of simple structure, reliability and low cost. For instance, electrostatic sensors have achieved successes in metering the velocity of pneumatically conveyed particles. [1]. In recent years, further effort has been made to extend the application of electrostatic sensing techniques to rotational speed measurement [2]. Subsequently, a novel method using electrostatic sensors and Hilbert-Huang Transform has been proposed for radial vibration measurement [3]. Spatial sensitivity and spatial filtering effect are the two important factors to be considered in sensor design. Meanwhile, the geometric parameters of the electrode, including the shape and dimensions, directly affect the spatial sensitivity, frequency spectrum and bandwidth of the signals from electrostatic sensors [4].

Performance comparisons of different electrostatic sensors for flow measurement have recently been conducted [5]. However, the electrostatic electrodes used for rotational speed measurement in the previous work are all in a strip shape. Although the sensing mechanism of the strip-shaped electrode has been well studied [4], the performance of other shaped electrodes and, more importantly, how to optimize the shape of the electrode for metering rotational speed of a metallic shaft remain unknown. In order to optimize the sensor design for rotational speed and vibration measurement, it is essential to study the sensing characteristics of different shaped sensors and assess their performances. In this paper, the sensing characteristics of strip- and butterfly-shaped sensors are analysed and compared through mathematical modelling and evaluated through experimentation on a purpose-built test rig.

II. METHODOLOGY

A. *Optimal shape of the electrode*

For a given sized metallic rotor with a single electrically insulated point charge (tracer) on its surface, the electrode should have the optimal shape – the criteria for the optimal shape include the highest spatial sensitivity, the highest power spectral density and the widest signal bandwidth. The width of the strip-shaped electrode affects the signal bandwidth [4]. For the same surface area and identical width at the centre, the sensitivity of an electrode shape increases when its surface area is closer to the point charge. Since the surface area of a butterfly shape is more concentrated near the centre than that of the strip and diamond shapes where the surface area is spread out away from the centre (Fig.1), the butterfly-shaped electrode is thus proposed as the optimal shape.

Fig. 1. Different shapes of electrode.

B. *Mathematical Model*

As shown in Fig.2, a simplified mathematical model of the electrostatic sensor for rotational speed measurement is established. The cylinder indicates a metallic rotor on which an insulated point charge P is fixed - the rotational motion of P creates in effect an impulse input to the sensing system. An electrode made on a small printed circuit board with adequate insulation together with grounding around the electrode [4] can be regarded as a piece of perfectly conductive metal and is

978-1-5090-1012-7/17/$31.00 ©2017 IEEE

placed around the rotor. The distance between the sensor and the rotor surface is s.

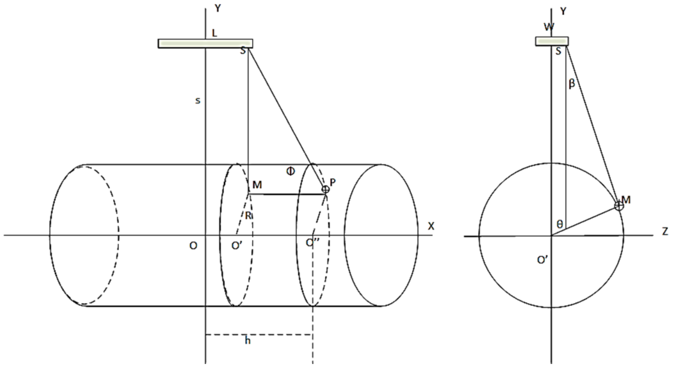

Fig. 2. Mathematical model of an electrostatic sensor.

The induced charge Q on the surface of the electrode due to the charged particle P is determined based on Gauss's law:

$$Q = \int_S \varepsilon E ds \tag{1}$$

where ε is the relative permittivity of the medium (air) and E is the electrostatic field on the surface of the electrode. S is a point on the electrode surface. In this case, E is generated due to the point charge at point P:

$$E = \frac{q}{4\pi\varepsilon|PS|^2} \tag{2}$$

The normalized electrostatic field $E_{\perp}$ is defined as:

$$E_{\perp} = Esin\varphi cos\beta = \frac{q((R+s) - Rcos\theta)}{4\pi\varepsilon|PS|^3} \tag{3}$$

where θ and R are the rotating angle of the point charge and the radius of the rotating trajectory, respectively.

$$sin\Phi = \frac{\mathrm{MS}}{\mathrm{PS}}\, ; cos\beta = \frac{(R+s)-Rcos\theta}{MS} \tag{4}$$

By substituting PS into (3) the normalized electrostatic field $E_{\perp}$ can be rewritten as:

$$E_{\perp} = \frac{q((R+s) - Rcos\theta)}{4\pi\varepsilon((x-h)^2 + (R+s-Rcos\theta)^2 + (z-Rsin\theta)^2)^{3/2}} \tag{5}$$

According to Gaussian theory, the induced charge dQ on a small surface area δ_s can be defined as :

$$dQ = -\varepsilon 2 \cdot E_{\perp}\delta_s = -\varepsilon 2 \cdot E_{\perp} dxdz \tag{6}$$

Finally, the total induced charge is equal to:

$$Q = -\frac{q}{2\pi}\int_{-w/2}^{+w/2}\int_{-l/2}^{+l/2} \frac{(R+s) - Rcos\theta}{((x-h)^2 + (R+s-Rcos\theta)^2 + (z-Rsin\theta)^2)^{3/2}} dxdz \tag{7}$$

Since $\theta = \omega t$ and $D=2R$, (7) can be rewritten as:

$$Q(t) = -\frac{q}{2\pi}\int_{-w/2}^{+w/2}\int_{-l/2}^{+l/2} \frac{(0.5D+s) - 0.5Dcos\omega t}{((z-0.5Dsin(\omega t))^2 + (0.5D+s-0.5Dcos(\omega t))^2 + (x-h)^2)^{3/2}} dxdz \tag{8}$$

where w and l are the width and length of the electrode, respectively. D and s are the diameter of the rotor and the distance between the electrode and the rotor surface, respectively. ω is the angular speed. h is the distance of the point charge along the X-axis.

The actual current output $I_s(t)$ of the sensor is:

$$I_s(t) = \frac{dQ(t)}{dt} \tag{9}$$

C. *Spatial Sensitivity*

The mathematical model in (8) is used to study the spatial sensitivity of electrostatic sensors. The spatial sensitivity $S_s(x,y,z)$ can be defined as the ratio of the induced charge over total electrical charge on the surface [4]:

$$S_s(x,y,z) = \left|\frac{Q(x,y,z)}{q(x,y,z)}\right| \tag{10}$$

where $Q(x,y,z)$ denotes the induced charge on the electrode. $q(x,y,z)$ denotes the source charge positioned at the coordinate (x,y,z). Therefore,

$$S_s = \frac{1}{2\pi}\int_{-b}^{+b}\int_{-a}^{+a} \frac{(0.5D+s) - 0.5Dcos\omega t}{\left(\left(z-0.5Dsin(\omega t)\right)^2 + \left(0.5D+s-0.5Dcos(\omega t)\right)^2 + (x-h)^2\right)^{\frac{3}{2}}} dxdz \tag{11}$$

Electrodes with two different shapes (strip and butterfly) as shown in Fig.1 are investigated in this study.

For the strip shaped electrode, the limits a and b are determined by:

$$a = \frac{l}{2};\ b = \frac{w}{2} \tag{12}$$

For the butterfly-shaped electrode, W and L being the width and the length of the shape, respectively, the limits a and b are:

$$a = \frac{l}{2};\ b = \sqrt{\frac{l^2}{4} - x^2} - \frac{(w+l)}{2} \tag{13}$$

To investigate the spatial sensitivity of the sensors, we assume W/D is a constant and equal to 1/30. The spatial sensitivities of the two shaped sensors at W/D=1/30 are illustrated in Fig.3.

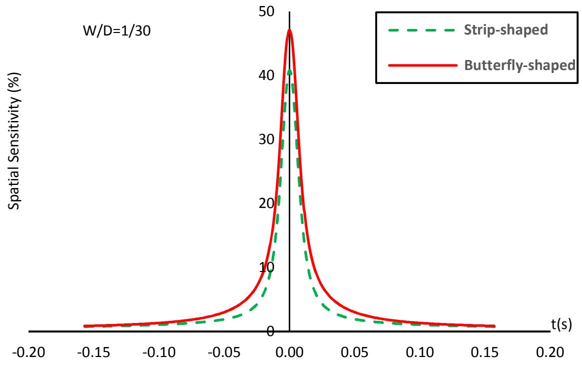

Fig. 3. Spatial sensitivity of the two electrostatic sensors of different shapes.

It is evident that the butterfly shaped sensor yields much higher sensitivity (46%) than the strip-shaped sensor (40%) for the same width and surface area.

D. *Spatial Filtering Effect*

It is known that the electrostatic sensor acts as a low-pass filter in the sensing system [4]. Frequency response is an important characteristic for electrostatic sensors. The spatial filtering effect describes an electrostatic sensor's performance in the spatial frequency domain. The frequency response of the sensing system can be determined from the power spectrum $S_h(f)$ of the impulse response $h_s(t)$:

$$S_h(f) = \int_{-\infty}^{+\infty} R_{hh}(\tau) e^{-j2\pi f t}\, d\tau \qquad (14)$$

where $R_{hh}(\tau)$ represents the autocorrelation function of $h_s(t)$:

$$R_{hh}(\tau) = \int_{-\infty}^{+\infty} h_s(t) h_s\,(t+\tau) dt \qquad (15)$$

Fig.4 depicts the power spectral densities of the two sensors for *W/D=1/30*. It is evident that the sensor system acts as a low-pass filter. The two sensors have the same bandwidth, however, the power spectral density of the butterfly-shaped sensor is higher by 15% than the strip-shaped.

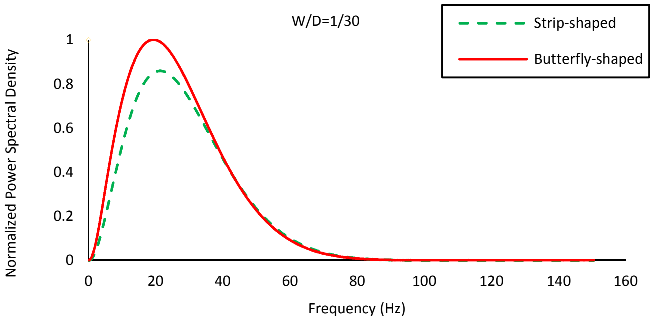

Fig. 4. Frequency characteristics of electrostatic sensors.

III. EXPERIMENTAL VALIDATION

Experimental tests were conducted on a test rig (Fig. 5). Experimental work was carried out with the strip- and butterfly-shaped sensors to verify the modelling results. The width of the strip shape is equal to the smallest width of the butterfly shape which is 2 mm. The length of the strip shape and butterfly shape are 48 and 20 mm respectively. Both shapes have the same area of 96 mm^2. To simulate a point charge on the rotor surface, a charged particle made from a 1 mm^3 cube of PTFE was fixed on a metallic rotor. The induced current output of the sensor is derived and measured. Then, the spatial sensitivity is measured by integrating the output signal (9).

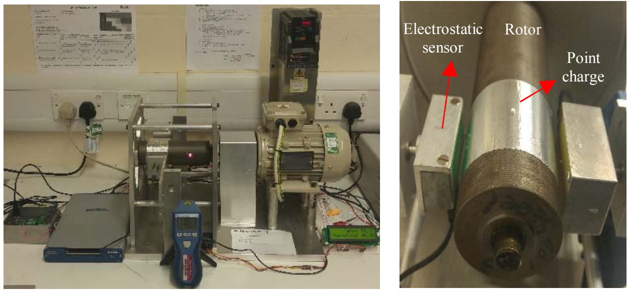

Fig. 5. Test rig for experimental assessment of the sensors

Fig. 6 illustrates the spatial sensitivity of the strip- and butterfly-shaped sensors. The experimental results show a good agreement with the mathematical model. Additional details of the experimental tests and analysis of the results will be given in the full paper.

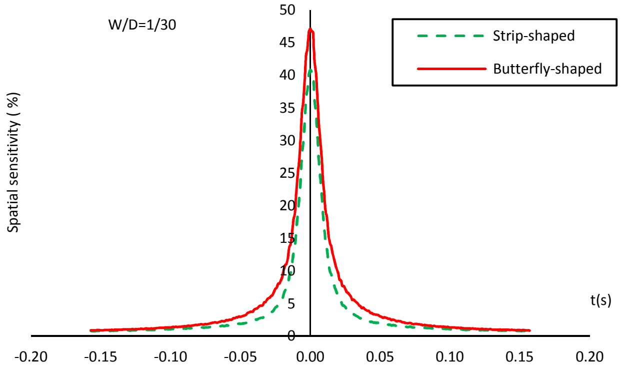

Fig. 6. Comparison between the measured spatial sensitivity of the strip- and butterfly-shaped.

IV. CONCLUSION

Investigations into the effects of the geometrical shape of the electrodes on the sensing characteristics of electrostatic sensors have been conducted through mathematical modelling and experimental validation. Theoretical models of strip- and butterfly-shaped electrostatic sensors have been numerically analysed in terms of spatial sensitivity and frequency response. In order to validate the modelling results, the butterfly- and strip-shaped electrodes with the same dimensions as in the modelling process have been manufactured and tested. It can be concluded that the butterfly-shaped sensor outperforms the strip-shaped sensors in terms of spatial sensitivity and frequency response. The geometric parameters of the butterfly shape should be also optimized in further research in addition to the accuracy and repeatability of the measurement system.

REFERENCES

[1] M. F. Rahmat and D. Y. W. Lee. "Electrostatic sensor for real-time mass flow rate measurement of particle conveying in pneumatic pipeline," Jurnal Teknologi, vol. 41, pp. 91-104, 2004.

[2] L. Wang, Y. Yan, Y. Hu, and X. Qian, "Rotational speed measurement through electrostatic sensing and correlation signal processing," IEEE Trans. Instrum. Meas., vol. 63, pp. 1190-1199, May 2014.

[3] L. Wang, Y. Yan, Y. Hu, and X. Qian, "Radial vibration measurement of rotary shafts through electrostatic sensing and Hilbert-Huang transform," in Proc. of IEEE International Instrumentation and Measurement Technology Conference, pp. 867-871, Taipei, Taiwan, May 23-26, 2016.

[4] L. Wang and Y. Yan, "Mathematical modelling and experimental validation of electrostatic sensors for rotational speed measurement," Meas. Sci.Technol., vol. 25, pp. 11510, September 2014.

[5] J. Lin, Z. Chen, Z. Hu, Y. Yang, and X. Tang, "Analytical and numerical investigations into hemisphere-shaped electrostatic sensors," Sensors, vol. 14, pp. 14021-14037, July 2014.